



ACTIVE VIBRATION CONTROL FOR A FREE  
PISTON STIRLING ENGINE WITH LINEAR  
ALTERNATOR FPSE/LA

Submitted for the Degree of Doctor of Philosophy

At the University of Northampton

**2015**

**Ali A. Hassan**

© Ali A. Hassan September 2015.

This thesis is copyright material and no quotation from it may be published without proper acknowledgement.

# 1 Abstract

New regulations introduced by the European Network of Transmission System Operators for Electricity (ENTSO) have brought further requirements for grid connected generators into action in 2013. The  $\beta$ -type Stirling engine (FPSE/LA) used for micro combined heat and power systems (MCHP) is a synchronous machine that is designed and tuned to operate at  $50\text{Hz} \pm 0.5\text{Hz}$ . This type of technology has to comply with the new regulations that imposes a wider operating envelop (47Hz-53Hz).

This engine suffers from continuous self-induced vibrations caused by the reciprocating motion of a permanent magnet attached to its piston inside a linear alternator. Currently, the damping of the vibration in the FPSA/LA is achieved with the aid of a passive tuned mass damper (TMD) tuned at 50Hz. While passive devices provide a simple and a reliable way to tackle many vibration problems, there exists distinct performance limitations associated with the use of only passive devices. As for this particular application, the main limitation of the TMD in its passive form is its narrow bandwidth of operation that cannot cope with the new bandwidth. Consequently, this could expose the engine to physical damage and failure if the excitation frequency drifts from 50Hz. For the TMD to cope with frequency changes, major modifications have to be introduced.

This research involved the design and development of an active tuned mass damper (ATMD) with the suitable control strategies to control an electromagnetic actuator, namely a linear voice coil motor (VCM). Starting with a validated vibration model of the engine based on a two degrees of freedom system (2DOF), two control techniques, Gain scheduling with zero-placement control law and Linear Quadratic (LQ) optimal control law, were investigated with numerical simulation in the frequency and time domains.

For the purpose of testing and implementation, a test rig featuring an electromagnetic shaker, a VCM, and a TMD besides an embedded system was assembled. An electromechanical

model of the test rig was also developed and simulated with the integration of the control strategies. A set of experimental tests were carried out and the concept of active vibration control was successfully illustrated. In addition to that, an in depth investigation of the effect of time delays on the control methodology was conducted. The study resulted in the identification of a time delay margin where below, stability is guaranteed. Furthermore, a set of comprehensive equations of the power and actuator force requirements to perform active damping with a VCM based on any general 2DOF system are obtained for both control strategies.

## 2 Acknowledgment

First and Foremost I thank Almighty **Allah**, the most Compassionate, and the most Merciful, who bestowed his grace upon me and helped me conduct this work.

I would like to offer my extreme thankfulness to my mother, father, and my siblings who stood by me throughout the period of my research. I dedicate my work to my father and mother who have long waited patiently for this moment.

The final completion of this work, in the first place, is attributed to the priceless support and guidance from my supervisory team, **Dr. Angel Torres-Perez**, **Prof. Stefan Kaczmarczyk**, and **Prof. Phil Picton** who I would like to express my sincere gratitude and appreciation to. I would also like thank Mr. Richard Albany-Ward who put a significant effort in the design and manufacturing of parts for the experimental setup.

I am also extremely thankful to all members of the school of Science and Technology at the University of Northampton for their continuous support throughout the research period.

I am particularly indebted to Mr. Adam Green, Dr. Dave Clark, and the engineering team at Microgen Engine Corporation who provided me with relevant engineering data and support.

### 3 Table of Contents

1	Abstract.....	ii
2	Acknowledgment.....	iv
3	Table of Contents.....	v
4	List of Figures.....	xi
5	Notations.....	xviii
1	Introduction.....	22
1.1	Introduction to Vibration.....	22
1.2	Main Contributions of this Thesis.....	25
1.3	Outline of the Thesis.....	26
2	Review of the Literature and Thesis Objectives.....	27
2.1	Structural Control.....	27
2.2	Active Control Systems.....	30
2.3	Semi-Active Control Systems.....	33
2.4	Modelling and Vibration of the Stirling Engine.....	35
2.5	Aim and Objectives.....	38
3	Basic Theoretical Concepts.....	40
3.1	Fundamentals of Vibration.....	40
3.1.1	Undamped Harmonic Oscillator.....	40
3.1.2	Damped Harmonic Oscillator.....	42
3.1.3	Vibration in Two Degrees of Freedom Systems.....	44
3.2	Concept of Vibration Control.....	47
3.2.1	Control of Natural Frequencies.....	47

3.2.2	Introduction of Damping.....	47
3.2.3	Vibration Isolation .....	47
3.2.4	Vibration Absorbers.....	50
3.3	Concept of Active vibration Control.....	50
3.4	Concept of Semi-Active vibration control .....	52
3.5	The Stirling Engine .....	53
3.6	Basics of a Voice Coil Motor (VCM).....	55
4	Passive Tuned Mass Dampers (TMD).....	58
4.1	System Analysis .....	58
4.2	TMD: RLC Electrical Analogy .....	63
4.2.1	Free Oscillation in LC circuit .....	63
4.2.2	Damped oscillation in series LRC circuit .....	64
4.2.3	Forced Oscillations in a Series LCR Circuit.....	65
4.3	Summary of the electrical-mechanical analogy .....	66
4.3.1	Impedance .....	67
4.3.2	Parallel Mechanical and Electrical Configurations.....	68
4.3.3	Series Mechanical and Electrical Configurations .....	69
4.3.4	Example with 2-DOF system.....	70
5	The FPSE/LA Analysis: Modelling, Simulation, and Validation.....	73
5.1	Modeling .....	73
5.2	Simulation .....	75
5.3	Electromagnetic Shaker V721 Characterisation .....	78
5.4	Validation.....	84

6	Active Control System Design and Simulation .....	88
6.1	Active Tuned Mass Damper (ATMD) .....	88
6.2	Gain Scheduling with Zero-Placement Feedback Control .....	89
6.2.1	Relative Measurement Feedback .....	90
6.2.2	Absolute Measurement Feedback .....	92
6.2.3	Stability .....	93
6.2.4	Frequency Domain Simulation with Gain Scheduling and Zero-Placement Control	94
6.3	Discussion .....	98
6.4	Linear Quadratic Control .....	98
6.4.1	Full-state feedback .....	99
6.4.2	State Observer Design with LQ control (LQG) .....	101
6.4.3	Frequency Domain Simulation with LQ Control .....	103
6.5	Discussion .....	106
6.6	Summary of the frequency analysis .....	107
6.7	Time Domain Simulation .....	108
6.8	Discussion .....	109
6.9	Noise and Uncertainties: Effects and Mitigation .....	112
6.9.1	Gaussian Noise .....	112
6.9.2	Noise Mitigation 1: State Observer .....	115
6.9.3	Discussion .....	117
6.9.4	Noise Mitigation 2: Butterworth Low Pass Filter .....	117
6.9.5	Discussion .....	119
6.10	Effect of Time Delays on Control Stability .....	119

6.10.1	Delays with Gain Scheduling Control .....	120
6.10.2	Delays with LQ Control.....	131
7	Experimental Setup and Implementation.....	133
7.1	Test Rig .....	133
7.2	Determination of the Helical Absorber Parameters .....	134
7.3	Test Rig Simulation and Experimental Validation .....	137
7.4	Test Rig Enhancement .....	139
7.5	Test Rig with a Voice Coil Motor (VCM) .....	141
7.5.1	Modelling with VCM.....	141
7.5.2	Model Validation Test 1: Open-Circuited VCM .....	142
7.5.3	Model Validation Test 2: Short-Circuited VCM .....	145
7.5.4	Model Validation Test 3: Powered VCM .....	146
7.6	Active Damping Control Simulation with Test Rig Model .....	148
7.7	Theoretical Study 1: Time Delays and Stability .....	152
7.7.1	Gain Scheduling with Relative Position/Acceleration and Velocity Feedback 153	
7.7.2	Time Delay Tackling with Changing the Original Tuning of the ATMD.....	155
7.8	Active Damping Control Implementation.....	157
7.8.1	Test Setup.....	157
7.8.2	Hardware and Software.....	158
7.9	Relative Position and Velocity feedback .....	160
7.9.1	Test 1: Active Damping Control Implementation .....	160

7.9.2	Test 2: Time Delays Mitigation and Characterisation of Damping Coefficient in the ATMD.....	166
7.9.3	Theoretical Study: Phase Delays Evaluation and Compensation .....	171
7.9.4	Test 3: Experimental Implementation with Phase Shift Compensation .....	175
7.10	Test 4: Absolute Position and Velocity feedback.....	179
8	Stirling Engine Active Control Analysis .....	182
8.1	Extended Model of the Stirling Engine.....	183
8.2	Simulation of the Electromechanical Model.....	186
8.3	Discussion on Power Consumption.....	187
8.4	General Equations for Active Vibration Control with a VCM .....	191
8.4.1	Gain Scheduling with Zero Placement Position & Velocity Feedback .....	191
8.4.2	Gain Scheduling with Zero Placement Acceleration & Velocity Feedback....	192
8.4.3	LQ control.....	193
9	Discussion, Future Work, and Conclusion .....	194
9.1	Discussion .....	194
9.2	Conclusions .....	199
9.3	Future Work .....	200
10	References.....	204
11	Appendix A.....	212
11.1	Passive Tuned Mass Damper (TMD) .....	212
11.2	Frequency Domain Simulation of Active Damping with Zero-Placement Control	213
11.3	Position Gain Feedback ( $\gamma$ ).....	214
11.4	Acceleration feedback ( $\alpha$ ).....	214

11.5	Position and Velocity feedback ( $\gamma\beta$ ).....	215
11.6	Acceleration and Velocity feedback ( $\alpha\beta$ ).....	216
11.7	Electrical Charge Feedback.....	217
11.8	Rate of change of the electrical current feedback.....	218
11.9	Electrical current and electrical charge feedback.....	219
11.10	Electrical current and rate of change of current feedback.....	221
12	Appendix B.....	223
12.1	Time domain Simulation of Stirling Engine with Active Control.....	223
13	Appendix C.....	224
13.1	Delay Equations with Shaker Rig Model for Feedforward Control.....	224
14	Appendix D.....	226
14.1	Experimental Testing.....	226

## 4 List of Figures

Figure 2-1 Principle of feedback control .....	28
Figure 2-2 Principle of feedforward control .....	29
Figure 3-1 SDOF Spring-mass system free body diagram (Tong, 2014) .....	41
Figure 3-2 Spring-mass system with viscous damper (Tong, 2014) .....	42
Figure 3-3 Two degrees of freedom spring-mass system with viscous damping (Tong, 2014) .....	44
Figure 3-4 SDOF representation of an isolation system with rigid foundation (Rao, 1990)...	48
Figure 3-5 The variation of transmissibility with frequency .....	49
Figure 3-6 General active vibration suppression with feedback control (Tong, 2014) .....	51
Figure 3-7 Semi-active damping based on manipulating damper properties (Tong, 2014) ....	52
Figure 3-8 Stirling Engine (Microgen Engine Corporation, ).....	53
Figure 3-9 Working principle of a $\beta$ -type Stirling engine, (Microgen Engine Corporation ) .	54
Figure 3-10 Conventional construction of a VCM (Kimco Magnetics) .....	55
Figure 3-11 Basic Lorentz force law .....	56
Figure 4-1 2DOF TMD system (Tong, 2014).....	58
Figure 4-2 Normalised amplitude of vibration of the primary mass expressed as a function of the frequency ratio for different damping ratios and mass ratio $\mu=0.05$ .....	61
Figure 4-3 An LC electrical circuit.....	63
Figure 4-4 LRC circuit.....	64
Figure 4-5 Driven LRC circuit.....	65
Figure 4-6 Parallel mechanical tuned mass damper configuration .....	68
Figure 4-7 Parallel analogous electrical configuration .....	68
Figure 4-8 Series mechanical tuned mass damper configuration .....	69
Figure 4-9 Series analogous electrical configuration.....	70

Figure 4-10 Example of a 2-DOF mechanical-electrical analogy .....	71
Figure 4-11 Impedance .....	71
Figure 4-12 Transmissibility.....	72
Figure 5-1 Dynamic model of the $\beta$ -type Stirling engine showing a casing .....	73
Figure 5-2 Frequency response from excitation force to engine case and absorber displacements.....	76
Figure 5-3 Photo of the electromagnetic shaker used in the experiment (Bruel & Kjaer) .....	78
Figure 5-4 V721 series vibrator with PA1000L amplifier and FPS10L field power supply (Bruel & Kjaer).....	78
Figure 5-5 Schematic of the design of an electrodynamic actuator (Preumont, 2011).....	79
Figure 5-6 V721 LDS shaker operating range (Bruel & Kjaer) .....	81
Figure 5-7 V721 Shaker current frequency response for a swept sine (Bruel & Kjaer).....	81
Figure 5-8 Frequency response of the electrical current for the proposed VDS721 shaker model.....	83
Figure 5-9(a) $\beta$ -type Stirling engine, courtesy of Microgen Engine Corporation (MEC) and (b) Rig of the TMD.....	84
Figure 5-10 Theoretical simulation and experimental validation of the engine .....	85
Figure 5-11 Schematic model of the absorber test.....	86
Figure 5-12 Theoretical Vs. Experimental data of the absorber transmissibility. The value of $c_2 = 2.7 \text{ Ns/m}$ is determined by reverse fitting of the theoretical data with the experimental data.....	87
Figure 6-1 ATMD with a 2-DOF system.....	88
Figure 6-2 Operation principle of the proposed control strategy.....	89
Figure 6-3 Required values of gains $\gamma$ and $\alpha$ to produce a frequency shift of 10 Hz bandwidth .....	92

Figure 6-4 SIMULINK model used to simulate the control of the engine vibration with ATMD.....	96
Figure 6-5 Frequency response from excitation force to primary mass displacement with $\beta = 0$ .....	97
Figure 6-6 Frequency response from excitation force to primary system displacement with $\beta = -c2$ .....	97
Figure 6-7 Operation principle of the LQ control.....	99
Figure 6-8 Schematic representation of LQ control state space system (Messner and Tilbury, ) .....	101
Figure 6-9 Closed loop state observer design (Messner, Tilbury 2015).....	103
Figure 6-10 Frequency response of the engine case displacement with LQ control .....	105
Figure 6-11 Engine case displacement with original system Vs. LQG control.....	106
Figure 6-12 Simulation results with gain scheduling control (position feedback) .....	108
Figure 6-13 Simulation results with LQG control (based on estimated states).....	109
Figure 6-14 SIMULINK with addition of Gaussian noise.....	113
Figure 6-15 Probability density function of noise distribution.....	114
Figure 6-16 Effect of noise on the actuator force with each control strategy.....	115
Figure 6-17 State observer with noise .....	116
Figure 6-18 Noise mitigation with of state observer on noisy signals.....	116
Figure 6-19 Noise Filtering.....	117
Figure 6-20 Noise mitigation with of low pass filtering of noisy signals.....	118
Figure 6-21 Percentage error between the original delay function and its Taylor series expansion approximation.....	120
Figure 6-22 System poles variation with position and velocity feedback showing unstable pole after 50Hz.....	122

Figure 6-23 SIMULINK model for delayed actuator force with position and velocity feedback .....	123
Figure 6-24 Time domain response of the control force with acceleration and velocity feedback with positive time delay showing system instability after 50Hz for different time delays .....	124
Figure 6-25 System pole variation with acceleration and velocity feedback showing unstable pole before 50Hz.....	125
Figure 6-26 SIMULINK model for delayed actuator force with acceleration and velocity feedback .....	126
Figure 6-27 Time domain response of the control force with acceleration and velocity feedback with time delay .....	127
Figure 6-28 SIMULINK model with delay represented as per Taylor approximation.....	128
Figure 6-29 Time domain response with Taylor representation of time delay .....	128
Figure 6-30 System pole variation with acceleration and velocity feedback ignoring the unstable pole before 50Hz .....	129
Figure 6-31 Time domain response of the control force with acceleration and velocity feedback .....	130
Figure 6-32 System poles variation with LQ control.....	131
Figure 6-33 Time domain response of the control force with LQ control.....	132
Figure 7-1 Initial test rig .....	133
Figure 7-2 Helical spring used in the design of an ATMD.....	135
Figure 7-3 Test results .....	136
Figure 7-4 Theoretical model results vs experimental results without the VCM.....	138
Figure 7-5 Lateral Vibration .....	140
Figure 7-6 Shaker with absorber and VCM test rig.....	141

Figure 7-7 Theoretical model results vs experimental results with open circuited VCM .....	143
Figure 7-8 Updated theoretical model results vs experimental results with open circuited VCM ( $c_2 = 7 \text{Ns/m}$ ).....	144
Figure 7-9 Model verification with short circuited VCM.....	145
Figure 7-10 Short-circuited VCM with damping $c_2 = 20.5 \text{Nm/s}$ .....	146
Figure 7-11 Updated theoretical model results vs experimental results with short circuited VCM .....	147
Figure 7-12 Control system representation.....	150
Figure 7-13 Time domain simulation results for the active damping control of the designed rig.....	151
Figure 7-14 Position of the closed-loop poles with gain scheduling control: position and velocity feedback control with ATMD tuned at 50Hz.....	153
Figure 7-15 Position of the closed-loop poles with gain scheduling control: Acceleration and velocity feedback control with ATMD tuned at 50Hz.....	154
Figure 7-16 ATMD tuned at 55Hz with Position control.....	155
Figure 7-17 ATMD tuned at 55Hz with Acceleration control.....	156
Figure 7-18 Active damping shaker-absorber rig .....	157
Figure 7-19 Active damping control model.....	161
Figure 7-20 Test1: Shaker table excitation and acceleration.....	162
Figure 7-21 Test1: VCM voltage and Current with active control.....	163
Figure 7-22 Test1: VCM Real power consumption with active control.....	163
Figure 7-23 Velocity gain against excitation frequency .....	167
Figure 7-24 Results of Test 2.....	168
Figure 7-25 Response of the shaker table acceleration with ATMD (originally tuned at 55Hz) vs TMD (originally tuned at 50Hz) .....	169

Figure 7-26 VCM voltage and Current with TMD tuned at 55Hz .....	169
Figure 7-27 VCM Active power consumption with TMD tuned at 55Hz.....	170
Figure 7-28 Low pass Butterworth filter response with cut-off frequency of 200Hz .....	172
Figure 7-29 High pass Butterworth filter response with cut-off frequency of 1Hz.....	173
Figure 7-30 Schematic Diagram of the control model of Test 3 .....	175
Figure 7-31 Shaker table excitation and acceleration with TMD tuned at 50Hz with delay cancellation .....	177
Figure 7-32 VCM voltage and Current with TMD tuned at 50Hz with delay cancellation ..	178
Figure 7-33 VCM power consumption with TMD tuned at 50Hz with delay cancellation ..	178
Figure 7-34 Schematic Diagram of the control model of Test 4 .....	179
Figure 7-35 Shaker table excitation and acceleration .....	180
Figure 7-36 VCM voltage and Current of Test 4.....	181
Figure 7-37 VCM real power consumption of Test 4.....	181
Figure 8-1 Schematic model diagram for the active damping control of the Stirling engine	185
Figure 8-2 Simulation results of the active damping control for the Stirling engine .....	187
Figure 8-3 Close-up view of the real power consumption of the VCM for 1kN and 3kN excitation forces.....	188
Figure 8-4 Real power consumption of the VCM for 3kN excitation force and VCM motor constant $k_{vcm} = 51.6 [N/A]$ .....	190
Figure 11-1 Normalised amplitude of vibration of the primary mass as a function of the frequency ratio for several values of damping ratios assuming negligible damping in the primary mass and $\mu=0.2$ .....	212
Figure 11-2: Normalised amplitude of vibration of the primary mass as a function of the frequency ratio for several values of mass ratios assuming negligible damping in the primary mass and $\zeta=0$ .....	212

Figure 11-3 SIMULINK model used to simulate the control of the engine vibration with ATMD.....	213
Figure 11-4 Frequency response of the primary mass displacement with position feedback.....	214
Figure 11-5 Frequency response of the primary mass with acceleration feedback .....	214
Figure 11-6 Frequency response of the primary mass displacement with position and negative velocity feedback .....	215
Figure 11-7 Frequency response of the primary mass displacement with position and with positive velocity feedback.....	216
Figure 11-8 Frequency response of the primary mass displacement with acceleration and negative velocity feedback.....	216
Figure 11-9 Gain scheduling control strategy for the analogous electrical circuit with electrical charge feedback.....	217
Figure 11-10 Frequency response of the electrical analogous system with electrical charge (Q) feedback.....	217
Figure 11-11 Frequency Response with current rate of change feedback gains.....	218
Figure 11-12 Multisim Model with electrical charge and electrical current gain scheduling control strategy.....	219
Figure 11-13 Frequency response with charge feedback and with positive current feedback gain.....	219
Figure 11-14 Frequency response with charge and negative current feedback gain .....	220
Figure 11-15 Multisim Model with rate of change of electrical charge and electrical current scheduling control strategy .....	221
Figure 11-16 Frequency response with rate of current and with positive rate of change of current feedback gain.....	221

Figure 11-17 Frequency response with current and negative rate of change of current feedback .....	222
Figure 12-1 Time domain simulation results of the primary mass displacement .....	223
Figure 14-1 LabVIEW FPGA code .....	226
Figure 14-2 LabVIEW Real time front panel .....	227
Figure 14-3 LabVIEW Real time block diagram.....	228
Figure 14-4 VCM parameters GVCM-051-051-01 .....	229

## 5 Notations

As a general rule in this thesis, lowercase letters represent scalars, bold lower case letters represent vectors and bold upper case letters represent matrices.

### Abbreviations

FPSA/LA	Free piston Stirling engine with linear alternator
MCHP	Micro combined heat and power
TMD	Tuned mass damper
ATMD	Active tuned mass damper
VCM	Voice coil motor
SDOF	Single degree of freedom
LQ	Linear quadratic
SISO	Single-input Single-output
MIMO	Multiple-input Multiple-output
EMF	Electromotive force
AC	Alternating current
DC	Direct Current
PID	Proportional-Integral-Derivative
ARE	Algebraic Riccati equation
FPGA	Field programmable gate array
RT	Real time

## Mathematical Conventions

$x$	Scalar
$\mathbf{x}$	Vector
$\mathbf{X}$	Matrix
$x(\cdot)$	Scalar function
$\mathbf{x}(\cdot)$	Vector function
$\dot{x}, \ddot{x}$	First and second time derivatives of $x$
$\mathbf{X}^T$	Transpose of a matrix
$\mathbf{X}^{-1}$	Inverse of a matrix
Rank ( $\mathbf{X}$ )	Rank of a matrix
Det ( $\mathbf{X}$ )	Determinant of a matrix $\mathbf{X}$
$j$	Complex number $j^2 = -1$
$\omega$	Excitation frequency of a sinusoidal function
$t$	Time
$e$	Error
$f(t)$	Function of time
$s$	Laplace complex number
$F(s)$	Laplace function
$\phi, \varphi$	Phase
$\omega$	Excitation frequency of a sinusoidal function
$f_n, \omega_n$	Natural frequency
$\tau$	Time delay
$\tau_n$	Normalised time delay

## Sub-super scripts

$x_0, x_i(0)$	Initial value of $x$
$\hat{x}$	Observer state
$x_i$	$i^{\text{th}}$ state of a system
$\omega_i$	Natural frequency of $i^{\text{th}}$ system
$a_i$	Denominator function coefficients
$b_i$	Numerator function coefficients

## Mechanical

$m_i$	Mass of $i^{\text{th}}$ body
$k_i$	Stiffness of $i^{\text{th}}$ spring
$c_i$	Damping in $i^{\text{th}}$ body

## Electrical

$R_i$	Resistance of $i^{th}$ resistor
$L_i$	Inductance of $i^{th}$ inductor
$C_i$	Capacitance of $i^{th}$ capacitor
$v_i$	Input voltage
$q_i$	Electrical charge

## Voice Coil Motor

$F$	Force
$k$	Motor constant
$B$	Magnetic flux density
$I, i$	Electrical Current
$v$	Speed
$L$	Length of motor coil (conductor)
$N$	Number of conductor turns
$E, V$	Voltage

## System and Control

$A$	State system matrix
$B$	Input matrix
$C$	Output matrix
$D$	Feedforward matrix
$Q$	State penalty matrix with LQ control
$R$	Input penalty matrix with LQ control
$K$	Gain matrix with LQ control

$F(t)$	Excitation force
$f(t)$	Control force
$F_{sha}$	Shaker Excitation force
$k_{sha}$	Shaker motor constant
$R_{sha}$	Resistance in shaker coil
$i_{sha}$	Shaker current
$V_{sha}$	Shaker voltage
$L_{sha}$	Shaker coil inductance
$q_{sha}$	Charge in shaker coil
$f_{act}$	Actuator force
$m_{VCM}$	Mass of the VCM base
$m_{coil}$	Mass of the VCM coil
$V_{vcm}$	VCM voltage
$i_{vcm}$	VCM current

$L_{vcm}$	VCM coil inductance
$k_{vcm}$	VCM motor constant
$R_{vcm}$	Resistance in VCM coil
$q_{vcm}$	Actual charge in VCM coil
$i_{ref}$	Reference current for VCM
$q_{ref}$	Reference charge for VCM
$\alpha$	Acceleration feedback gain
$\beta$	Velocity feedback gain
$\gamma$	Position feedback gain

### **Simulation and Implementation**

$T$	Simulation time
$T_s$	Sampling time
$f$	Frequency
$f_{HP}$	High pass cut-off frequency
$f_{LP}$	Low pass cut-off frequency

# 1 Introduction

## 1.1 Introduction to Vibration

A lot of human activities incorporate vibration in one form or another. We hear due to the vibration of our eardrums, we see due to light waves undergoing vibration, and we speak due to the oscillatory motion of our larynxes and tongues (Rao, 1990). Vibration can be utilised in several industrial applications, such as for hoppers, conveyers, sieves, and drills etc. While vibration is useful in some areas, it is often not desired in other due to adverse effects, not only to structures but also to humans. Vibration and noise are very common problems that occur in most dynamic systems, thus it was established that effective control of those phenomena is required (Harris and Beyer, 1988). If not controlled, excessive vibration and noise in structures such as airplanes, cars, machinery, and buildings can cause damages or radiate unwanted noise (Simpson and Schweiger, 1998).

The suppression and control of harmful vibration can be achieved within three main categories: passive, active, and semi-active (Liu, 2004). Passive vibration suppression comprises the use of materials with predefined parameters that are able to perform attenuation over a range of frequencies without the need of an external power supply. Traditionally, the isolation of a vibrating system has always been achieved by designing passive systems based on compliant materials such as rubber that isolates the equipment dynamics from the source of vibration (Mead, 1999). Up until 1990, passive vibration suppression techniques were generally the most considered for engineering systems. Harris and Beyer (Harris and Beyer, 1988) presented an extensive theoretical study in the field of shock and vibration in addition to their reduction techniques. Since conventional passive damping is performed with the use of materials that can only have fixed properties, its performance is thus limited, justifying the need for better methods. While passive devices

could provide a simple and reliable way to tackle many vibration problems, there exists distinct performance limitations associated with the use of only passive devices (Hansen and Snyder, 1997). Franchek et al (Franchek et al., 1996) state that better vibration isolation can be achieved with the aid of materials that possess adaptable features that can be altered in response to varying excitation characteristics. Changing the characteristics of a material can be facilitated with the use of active control techniques that are capable of achieving greater performance than passive techniques. The concept of using active control involves the use of actuators that either add or dissipate energy from a system with the aid of a control system. While active vibration techniques have been proved to exhibit a superior performance to that of the best possible passive systems, this superiority comes at a high cost in most cases. External power supply that involves the use of power amplifiers in addition to complex control is needed. Active vibration techniques have been used explored, but their use is limited to areas where the performance benefits outweigh the costs. By evaluating both, the benefits and the limitations of active suppression techniques, a new concept of vibration control has been developed, known as the semi-active damping (Karnopp et al., 1974). Unlike active vibration control, the concept of semi-active vibration control is based on utilising materials that possess variable properties that do not require significant amount of external power in order to function. Altering of the materials properties is achieved by employing a technique that is capable of changing the mechanical properties of a material such as damping, stiffness, resistance, etc., through a feedback system. While the implementation of semi-active control is considered more economic than fully active control systems, its performance is still limited and its suitability is subject to many other key factors. New vibration control designs introduced new types of materials known as smart materials. Amongst those are the electrorheological (ER), magnetorheological (MR) fluid, and piezoelectric materials that can be utilised to mitigate vibration problems efficiently. In fact,

the vast majority of research in smart damping considers the use of piezoelectric transducers (Qiu et al., 2009). Piezoelectric transducers have been the focus of intense research in the area of vibration suppression for over four decades (Moheimani, 2003). Certain drawbacks are associated with the use of those materials. For example, piezoelectric transducers operate in the range of micrometres, and they can fail to control the amplitude precisely due to the hysteresis effect as well as the increase in the difficulty of their control due to the presence of a feedback controller (Fan et al., 2006).

The use of electromagnetic actuators for vibration control has been receiving a considerable attention recently. This category of actuators possesses some advantageous features such as cleanliness, speed, compactness, type variety (linear, rotary), and control availability etc. Furthermore, Electromagnetic devices can be used as actuators, sensors or both (Boldea and Nasar, 1999). Electromagnetic actuators have been used extensively used for applications where rapid and controlled motions of devices are required. In principle, when an electric current flows through the terminals of an electromagnetic device, a force or a torque is obtained. Alternatively, if an electromagnetic device is moved with a velocity, a voltage proportional to the speed is induced across the terminals of the transducer. In fact, their properties make them a good target to be used in vibration suppression such as car suspension systems (Kim et al., 2001) and isolation platforms (Jinsiang Shaw, 1999). However, as previously mentioned, while active vibration incurs the use of external power and more expensive devices, electromagnetic devices can also be implemented within a semi-active vibration suppression system utilising the use of shunted electronics circuit (de Marneffe, 2007). Among the electromagnetic devices that can be invested in vibration suppression are electromagnetic rotary motors and electrical linear motors. One of the linear electrical motors is the Voice Coil Motor (VCM) which acts as a linear drive motor, comprising a permanent coil winding and a magnet that produce a force proportional to the flowing electrical current.

This research discusses a mitigation technique of the vibration problem within the  $\beta$ -type free piston Stirling engine with linear alternator by converting its existing passive vibration damping technique into an active one with the aid of an electromagnetic actuator.

## **1.2 Main Contributions of this Thesis**

1. Modeling, simulation, design, and implementation of the concept of active vibration control using an ATMD within the field of machine induced vibrations, precisely for a free piston Stirling engine with linear alternator FPSE/LA. There have different attempts to tackle this problem using various approaches, however according to the author's knowledge of reported research; this work is the first attempt to tackle the problem with active control. Furthermore, considering that most of the research that has been done on active control of vibration is focused in civil structures operating at low frequencies, for this work the operating frequencies are considered high while taking into account the resulting inertias exhibited by the system.
2. A novel method for characterising the mass and natural frequency of a single DOF spring-mass system using a vibratory platform.
3. A novel experimental technique of characterising the damping of the composite ATMD system using active vibration control.
4. An in-depth study on the effect of time delays on the stability of the active control system was carried out based on a 2DOF system. Time delays were found to affect stability after a delay margin which is defined depending on the operational frequency. Two solutions for mitigating the effect of time delays were proposed and tested.
5. Derivation of the equations for the required force, current, power consumption to perform active vibration control using a VCM and relevant control technique based on a 2DOF electromechanical system.

### **1.3 Outline of the Thesis**

In Chapter 2 of this thesis, a review of the literature is presented on structural control and the vibration of the Stirling engine. The aim and objectives of the thesis are clearly stated at the end of this chapter.

Chapter 3 presents the basic concepts of vibration in SDOF and MDOF systems. A definition and explanation on the operation of Stirling engine is included in this chapter. The basics of electromagnetic voice coil motors are also introduced. Finally, the concepts of active and semi active vibration are explained.

In Chapter 4, the concept of passive tuned mass damper (TMD) is discussed from a mechanical perspective and its analogous electrical representation is also illustrated.

Chapter 5 considers the modeling, simulation and model validation of the Stirling engine under study from a vibration perspective.

In Chapter 6, the design and simulation of active vibration control techniques for the Stirling engine are performed and analysed in the frequency and time domains. A detailed study is followed considering the effect of noise and effect of delays on the control performance.

In Chapter 7, the experimental setup and implementation of the active vibration control are demonstrated, analysed, and discussed using a lab test rig.

In Chapter 8, a simulation of the Stirling engine based on an electromechanical model is performed. A discussion is presented on how to reduce the power consumption in the VCM upon implementation in the Stirling engine.

Finally, Chapter 9 includes a discussion and a conclusion of this research. In addition to that, it considers future research trends.

## 2 Review of the Literature and Thesis Objectives

### 2.1 Structural Control

Generally speaking, structural control is associated with controlling the dynamic characteristics and behaviour of a structure or system with the aid of a control system that is programmed to perform suitable algorithms. In the field of active and semi-active control of vibration, various control algorithms have been proposed and tested for their efficiency by both, numerical simulations and laboratory experiments. In this section, the analysis of different control schemes is defined in the chronological order (Jianjun Liu et al., 2009):

The first classification dates back before 1950s, known as classical control. Control analysis in classical control mainly comprised frequency domain analysis of transfer functions that are eventually converted to time response. Laplace transforms, transfer functions, Bode plots, Nyquist stability plots, Routh-Hurwitz, and root-locus were techniques used extensively to perform the analysis. The classical control approach has many drawbacks. First of all, the frequency domain analysis is restricted to LTI systems and zero initial conditions. The conversion from time domain to frequency domain and vice versa incurs reduction in accuracy. Moreover, solutions of MIMO systems were approximated on the basis of SISO systems.

In the late 1950s, the era of modern control set off; systems can now be dealt with in the time domain by employing state-space analysis with variables expressed as vectors and equation expressed in matrix form. The advances in computational power capabilities during that period allowed for easier and highly accurate analysis of MIMO systems that are not restricted to being linear and having zero initial conditions.

The third control development occurred in the period from 1970s-1990s with the inclusion of robust control that incorporates both classical and modern control, i.e. benefiting from the

frequency-domain analysis in classical control with state-space models from modern control. Robust control is designed to operate with uncertainties, i.e. a robust controller is capable of functioning well under varying set of assumptions.

More control laws have been derived from previous available control methods. In the last few decades, some advanced control laws have been developed such as optimal and adaptive control. In terms of optimal control, the algorithm is used to adjust system variables in such a way that the overall performance indices of the system under control are optimised (Dorf and Bishop, 1998). In adaptive control, the desired response is achieved by benefiting from a set of known system dynamics and then adjusting the relevant parameters in a mathematical procedure. Amongst the most widely used algorithms in real structure applications, fuzzy logic algorithms (FL), artificial neural networks (ANN), and genetic algorithms (GA) are examples of adaptive control algorithms that demonstrated significant enhancement in the overall dynamic response.

In terms of vibration control, the techniques function based on two main control pathways, namely, Feedback and feedforward control or a combination of both (der Poel, 2010). Various types of control architectures ranging from classic control, optimal control, and adaptive control have relied on feedback/feedforward control to achieve the desired system response. The following introduces the general basics of feedback and feedforward control.

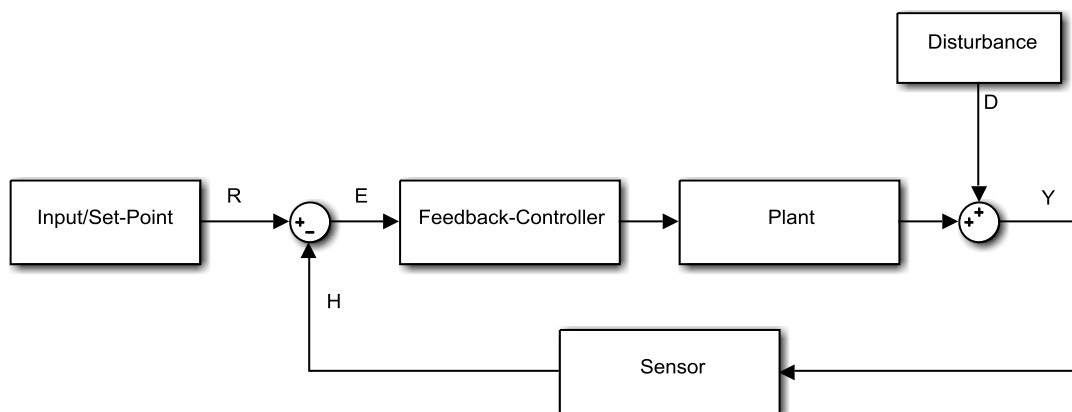


Figure 2-1 Principle of feedback control

Referring to Figure 2-1 on feedback control,  $E = R - H$  is the error and is generated from the comparison operation of the feedback signal  $H$  of the system and the desired input  $R$ . The error is processed with feedback controller and then applied to the plant. The process of designing the suitable controller is obtained by employing techniques that are available for the different types of control systems such as root-locus, stability analysis, Nyquist plots etc. The aim is to achieve the desired performance without causing instability of the closed-loop system.

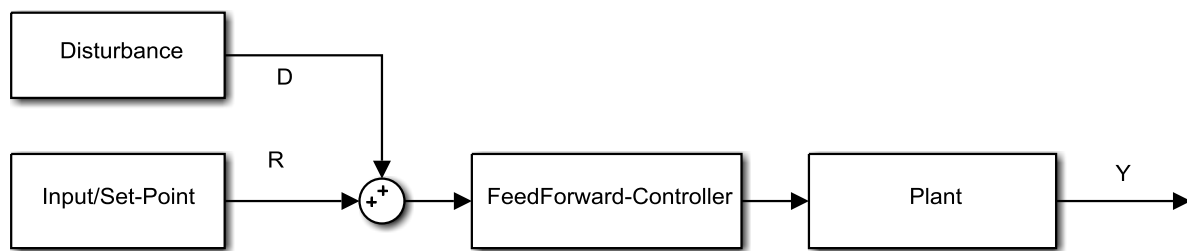


Figure 2-2 Principle of feedforward control

Figure 2-2 shows the principle of feedforward control. This technique is significantly beneficial whenever there is availability or quantitative measurement of the disturbance acting on a system. For example, a feedforward adaptive filter for disturbance rejection may be implemented for controlling the vibration generated in rotating machines. Vibration in this type of systems is usually associated with angular frequency of the rotor which can be measured using a suitable sensor such as a tachometer. According to (Fuller et al., 1997), the feedforward method was initially used with noise control but eventually was adapted for vibration control. In the most ideal scenario, by having accurate knowledge of the disturbance, it becomes possible for the feedforward control to completely mitigate the effect of the disturbance. Regarding the rotary system vibration, the adaptive filter manipulates the measured signal from disturbance and then outputs a control signal to a suitable actuator. The actuator generates a counteracting force that minimises the vibration in the structure. This however doesn't necessarily ensure that the global response of the system is controlled for all

locations, which could be viewed as a drawback of this method. If the system is not dominated by a single mode, the actuation might introduce higher levels of vibration in other parts of the structure whilst reducing the vibration at the point of error; thus the technique is considered to be local compared to the feedback method which is more global. Despite being local, the feedforward technique can be made effective for any disturbance frequency. The approach has seen many applications in the cancellation of narrowband disturbances as well as broadband applications (Vipperman et al., 1993). The major restriction in this method is the accessibility to a reference signal correlated to the disturbance.

## **2.2 Active Control Systems**

Historically, passive vibration isolation methods were dominant in the area of mechanical vibration control. In more detail, the isolation was achieved by introducing rubber materials in machine mounts on foundations (Harris, 1988), or by adding passive tuned mass dampers (TMD) to structures (Soong and Dargush, 1997). In sight of the limitations in passive vibration isolation techniques on one side and amid recent advances in control strategies and digital signal processing (DSP) techniques on the other, active vibration control attracted all the attention (Meirovitch, 1990).

Active vibration isolation control is a broad engineering field which incorporates interdisciplinary technologies, mainly relying on the interaction between mechanical and electronic devices that are integrated and controlled through a computer/microprocessor (Alkhatib and Golnaraghi, 2003). Various active control techniques have been proposed and tested for mitigating vibration problem across a wide spectrum of engineering fields. Nowadays, there exists a considerable amount of published work that discusses vibration isolation in a wide range of domains, specifically seismic (Karnopp, 1995), machinery (Watters et al., 1988, Jenkins et al., 1993), and aerospace & transportation (Spanos et al., 1993), etc.

Harris (Harris, 1988) dedicated five chapters that included the concepts of passive and active vibration isolation designs for both SDOF and MDOF vibratory systems. Von Flotow (Von Flotow, 1988) reviewed the principles of active and hybrid (active/passive) vibration control techniques. Von Flotow discussed the way active vibration isolation tackles problems that passive vibration isolation is limited to overcome. In his publication, Soong (Soong, 1987) reviewed the various structural active control systems that were proposed and implemented up until 1990. Karnopp (Karnopp, 1995) reviewed the historical development of vibration isolation and also indicated to the influence of control theory and active control since 1960s. Karnopp applied the principles of active control to seismic vibrations and also to automotive suspension systems. Furthermore, (Housner et al., 1997) presented another review on structural control. More recently, Datta (Datta, 2003) reviewed the research in active structural control with particular emphasis on active control of structures under earthquake excitations. Alkhatib and Golnaraghi (Alkhatib and Golnaraghi, 2003) published a review that covered the key issues associated with designing active control systems for vibration. They derived a generic procedure for designing such systems. A very recent extensive review presented by Korkmaz (Korkmaz, 2011) covered a similar overview to the previous with focus of new advances that facilitate the application of active structural control in addition to the existing challenges.

Electromagnetic actuators have been widely used in active vibration control. Liu and Wu (Liu and Wu, 2013) used a VCM with velocity feedback law to provide control at low frequencies (2-6 Hz) for highly sensitive instruments by producing a sky-hook damper. Chen et al (Chen et al., 2013) developed a control method to attenuate the milling vibration by using voice coil motors and laser displacement detectors. Fan et al (Fan et al., 2006) employed a VCM to achieve the vibration isolation for a fabrication system of miniature parts.

In terms of the control architectures implemented in active structural control, many algorithms have been implemented ranging from classical control concepts using displacement, velocity, and acceleration feedback to optimal control concepts with linear quadratic regulator (LQR) and linear quadratic Gaussian (LQG) techniques (Ram and Inman, 1999, Chung et al., 1989). Adaptive control with least mean squares, fuzzy logic, and artificial neural networks (Battaini et al., 1998) has also been used. These are not the only control algorithms used by they are the most common.

A wide variety of active control structures have been used to tackle numerous vibration problems. Active cable and tendon control systems exert the active control force through cables. The cables are used to manipulate the stiffness in the structure under control on one end and to reduce geometric uncertainty resulting from gaps in the structure (Guo et al., 2012). This control technique has been applied to civil structures such as in suspended bridges as well as in aeronautical applications. Abdel-Rohman proposed this technique (Abdel-Rohman and Leipholz, 1983) to actively control the sway in tall building instead of using an ATMD. It was observed that following this approach, more efficient control is obtained but larger forces were required. Chung (Chung et al., 1988) controlled an SDOF system using tendons connected to a servo-hydraulic actuator with an optimal closed-loop control scheme that minimizes a performance index to obtain the optimal response from a structure subjected to large-scale seismic excitation. Chang (Chang and Yu, 1998) controlled the vibration of a structure subject to white noise excitation using an optimal pole placement technique. In their research project, Bani-Hani et al (Bani-Hani et al., 1999) controlled a hydraulic actuator with a neural network control law. The actuator was attached to a tendon system that performs structural control on a quarter scaled model of a three-storey steel frame. Preumont et al (Preumont et al., 2000) also used active tendons employing piezoelectric transducers within an integral force feedback control law to control a cable

structure. Similarly, Liu (Luo et al., 2002) minimized the vibration of a cable structure subjected to unknown excitation by adopting a sliding mode decentralized controller.

An ATMD is built by adding a control mechanism to a passive TMD system. The concept of ATMD in civil engineering was first flagged by Yao (Yao, 1972). The first theoretical attempt to improve control performance of a TMD actively was done in the work of Morrison and Karnopp (Morrison and Karnopp, 1973) by which a linear quadratic optimum regulator was employed to specify the feedback gains for controlling the system. A drawback of optimal control at that point was the lack of intuitiveness in comprehending the physical meaning of the feedback gains of the optimal control as stated by Karnopp. Chang and Soong (Chang and Soong, 1980) implemented an ATMD with a classical feedback controller for structural control. Their numerical analysis showed that an ATMD can achieve significant improvement in the reduction of vibration amplitudes. Furthermore, other research (Chang and Yang, 1995, Yan et al., 1999, Nagashima, 2001, Li et al., 2003) considered using ATMD systems employing classical feedback control methods including displacement, speed, and acceleration feedback. Wang and Lin (Wang and Lin, 2007) proposed two kinds of controllers based on adaptive control and fuzzy sliding mode control for a building employing an ATMD. The simulation showed that under earthquake induced excitation, both methods were successful however the fuzzy sliding mode controller was found to be more economical and practical due to a smaller control force requirement associated.

### **2.3 Semi-Active Control Systems**

Another category of active control systems is known as semi-active control systems. These systems require lower energy consumption than that of a fully active system. Under normal circumstances, semi-active control systems do not possess the capability of destabilising the system under control for bounded input force. This type of control combines features from both passive and active control systems (Spencer and Soong, 1999, Housner et al., 1997).

Research work on semi-active control has been applied in many areas of engineering such as the work done by Karnopp (Karnopp, 1990). Symans (Symans and Constantinou, 1999) presented an in depth review which focused on the description of the dynamic behaviour of different semi-active systems. Spencer and Nagarajaiah (Spencer Jr and Nagarajaiah, 2003) published a review study which focused on the concept and implementation of semi-active control devices and their categories. Recent contributions in new concepts of control and their application were presented by Rodellar et al (Rodellar et al., 1999). Soon and Cimerallo (Soong and Cimellaro, 2009) focused on the design for integration of control with structural systems.

Adaptive control techniques such as fuzzy logic control and neural network were also used for semi-active control as in the work presented by carter et al (Carter, 1998, Fang and Chen, 1999). It was previously mentioned that an ATMD can achieve a wider bandwidth and a better performance than the passive ones but with more complexity and a relatively high cost of operation (Chang and Soong, 1980). By recognising the performance benefits and the limitation of ATMD systems, the concept of semi-active tuned mass dampers (STMD) has been introduced (Pinkaew and Fujino, 2001). The work done by Hrovat et al (Hrovat et al., 1983) investigated the performance of an STMD for attenuating wind-induced vibrations.

A wide variety of devices can be employed in semi-active control. They can be of various types ranging from electromagnetic, electrorheological (ER), magnetorheological (MR), stiffness control devices, hydraulic dampers, to friction control devices. The following discusses some of the commonly applied semi-active devices with their control strategies. ER dampers comprise micro-sized dielectric particles that are contained within a hydraulic as a fluid substance. These particles resist or allow the flow in response to variations to a strong electric field. Magnetorheological devices (MR) operate in a similar fashion to ER dampers, however they respond to magnetic field. Both ER and MR materials are capable of changing

from a fully free-flowing fluid to a semi-solid state in time scale of few milliseconds (Symans and Constantinou, 1999). This type of material has been studied by many researchers in many areas such as seismic vibration (Ehrgott and Masri, 1999, Makris et al., 1995), (Spencer Jr et al., 1996, Gordaninejad et al., 1998). Wu and Griffin (Wu and Griffin, 1997) reduced the effect of shocks on suspension seats by employing an ER damper. Jeon et al (Jeon et al., 1999) studied the performance of MR for vibration isolation using an on-off control strategy for a system subjected to harmonic disturbances. There is also a considerable amount of reported research in the literature that considered the use of electromagnetic devices for semi active control. In his work, Karnopp (Karnopp, 1989) explored semi-active control for vehicle suspension using permanent magnet linear motors. The motors were exploited as dampers that can rapidly change their damping coefficients in response to varying the external resistance connected the motor terminals. Cheng and Ho (Cheng and Oh, 2009) studied the suppression of vibration in cantilever beams with the aid of an electromagnetic actuator.

## **2.4 Modelling and Vibration of the Stirling Engine**

Section 3.5 contains a detailed definition and a description of operation of the Stirling engine. The development of the Stirling engine technology has been ongoing continuously for the past several decades paving the way for new concepts, designs, and models (Ross, 1995). The domestic Stirling engine generator is particularly an interesting machine of promising future (Berchowitz, 1983). The development of this technology is perceived as a time-consuming trial-and-error process associated with huge costs. Thus modeling of the engine is considered as one of the alternative solutions. Cheng and Yu (Cheng and Yu, 2010) reviewed some numerical models that have been developed for different Stirling engine technologies. They also proposed a theoretical model for a  $\beta$ -type Stirling engine that drives a crank shaft via a rhombic-drive mechanism.

The Stirling engine used in this work is a 1kW  $\beta$ -type Stirling engine fitted with a linear alternator FPSE/LA provided by Microgen Engine Corporation (MEC). This type of engine is subject to forced vibration due to the interaction of its internal components. The cancellation of the vibrations due to internal excitation in the FPSE/LA is currently done by employing a passive TMD tuned at 50Hz. The current technique works very well when the engine is grid-connected at 50 Hz only. If this frequency varies from 50Hz, the absorber will not be capable of cancelling the vibration.

Research within the area of active vibration control for free piston Stirling machines has been mainly industry-led. As a result, there is not much academic research available within this topic. Nevertheless, there have been some attempts made to find a solution for the vibration problem of the Stirling engine for wider frequency bandwidths. Rauch ([Rauch], 1983) claimed the conceptual design of a low-cost and low-maintenance absorber that self-adjusts its gas spring constants to tune its natural frequency at all engine frequencies. In other words, the vibration absorber spring follows the engine working gas mean pressure created by the displacer and changes the absorber frequency as the engine frequency changes. It has to be remembered that the vibration in the engine is due to the piston displacement and not the displacer and there exists a phase shift, ideally 90 degrees, between the two. The phase difference between the piston and displacer is not accurately 90 degrees and is subject to slight variation depending on the pressure, temperature and damping factor. Rauch's method is based on the gas pressure that is moved by the displacer which originally, according to the above explanation, does not fully represent the vibration frequency of the engine. Rauch built his work upon the basis of an improved design of the engine which is done by Sunpower, Inc. (Beale et al., 1980) who accomplished a full synchronisation between the engine and the displacer natural frequencies with proper phase. Although theoretically this method is ideal

and low cost to cancel the vibration of the engine at all operating frequencies, this concept has never become a working product.

Dr. Dave Clark (personal communication, April 23, 2015), application manager at Microgen Engine Corporation (MEC), considers the concept presented by Rauch as “could be very difficult to work in reality because frequencies change and engine temperatures change.” He adds “...adding another gas spring is probably a very difficult control parameter. The pressure wave will have/add a time lag and a magnitude related to engine/piston frequencies and temperatures/pressures and may be difficult to control especially during transient conditions.” He continues “...adding extra volume and pressure channels will inevitably lead to pressure and damping losses and will add to the tuning. A free piston engine when linked to grid, the grid frequency dominates, when off grid the natural frequencies usually have more effect. The engine will want to operate at frequencies depending on how cold the engine is – we see this, an engine at low power off grid will run at frequencies down as low as 47Hz as power and temperatures increase this will rapidly increase towards 50Hz and at higher temperatures will rise above 50 Hz.” He concludes “Off grid controlling the engine frequency would not need an active absorber. I doubt you would ever consider this method nowadays with modern fast and efficient electronics.”

More recently, few patents in this area still continue to come out. Some of them suggest control of the amplitude and phase of the piston or displacer and the engine case motion such as the control algorithm in (Qiu et al., 2005). Latest patented solution in (Holliday, 2014) uses the concept of adaptive filtering to balance the vibrating machine at the fundamental operating frequency of the machine and at selected harmonics of that operating frequency. A motion sensor that measures the amplitude and phase of the vibration is required. In terms of other Stirling-type applications, Ross (Ross Jr, 2003) provided an overview of the vibration characteristics of typical linear-drive space cryo-coolers outlining the history of development

and typical performance of the various active and passive vibration suppression systems being used. Ross considers that work done by Sievers and Von Flotow (Sievers and von Flotow, 1992) and others on active vibration control in 1990 became visible to the cooler community. Recently, Johnson (Johnson et al., 2012) worked on developing embedded active vibration cancellation of a Piston-Driven cryo-cooler or nuclear spectroscopy applications.

For other Stirling type applications, Bin-Nun (Bin-Nun, 2008) presented a study of the self-induced vibration problem in rotary Stirling cycle coolers that are used in the IR imaging systems and methods to reduce the magnitudes of those vibrations.

Considering the different attempts of solving the vibration problem in Stirling applications in general and free piston Stirling engine in particular, the outcome is significantly enough to warrant a solution that comprises active vibration control.

## **2.5 Aim and Objectives**

Aim: Broadening the operating envelop of the Stirling engine from 50Hz to 47Hz-53Hz by mitigating its vibration problem.

The main objectives in this thesis are stated below

1. To run initial simulations for passive, active, and semi-active vibration control
  - As an initial step, it was required to perform adequate modeling and simulations in order to develop an understanding of how the three different types of vibration control strategies behave. Matlab/Simulink and NI Multisim software kits were used to perform simulations and a comprehensive understanding of the different control strategies was developed.
2. To model and characterise experimentally the existing TMD and compare it to the simulation results

- A simplified model of the synchronous generator and the existing damper were developed to represent the real system as two degrees of freedom system. Simulations results were validated with experimental data obtained from the manufacturer and from experiments carried out at the university's mechanical labs.
3. To design and convert the passive damper into an active one by including linear actuators (such as VCMs).
    - A design of the active damper was proposed alongside a set of appropriate control strategies. A comprehensive model of the full 2DOF system in addition to a VCM has been simulated using Simulink/Simscape. A handful of useful data was obtained and will be used for the implementation stage. Studies towards the effect of noise and delays were performed to check the robustness of the system against instability.
  4. To characterise the active damper experimentally
    - This is part of the implementation stage where an actuator is connected to perform the active damping using a scaled test rig.
  5. To design, simulate, and test suitable control system to perform different control strategies for active damping
    - A set of simulations have been performed and propositions have been made in order to identify the required hardware and software that will carry out the active damping.
  6. Active damping implementation on a scaled rig.

## 3 Basic Theoretical Concepts

### 3.1 Fundamentals of Vibration

For the purpose of reducing the vibration in machines, it is crucial to understand the basics of vibration. Generally, machine vibrations can be classified into two main types: synchronous or sub-synchronous (Tong, 2014). The first type is associated with vibrations that follow a dominant frequency that matches the excitation of the machine itself, for instance the speed of rotation of a rotor. The second type corresponds to vibration at frequencies below the operating frequency, for instance, resonant frequency of a rotating shaft during the start-up and shut-down of the machine. While most mechanical systems in the real world are considerably complicated, the analysis of those systems undergoes a simplification process that allows performing theoretical studies with them. In terms of vibration analysis, a matrix notation of a mechanical MIMO system could be expressed as follows

$$\mathbf{M}\ddot{\mathbf{x}} + \mathbf{C}\dot{\mathbf{x}} + \mathbf{K}\mathbf{x} = \mathbf{f} \quad 3-1$$

In here,  $\mathbf{M}$ ,  $\mathbf{C}$  and  $\mathbf{K}$  represent the mass, damping, and stiffness matrices respectively.  $\ddot{\mathbf{x}}$ ,  $\dot{\mathbf{x}}$  and  $\mathbf{x}$  represent vectors of acceleration, velocity, and displacement respectively. The external forces exerted on the system are represented by the force vector  $\mathbf{f}$ .

#### 3.1.1 Undamped Harmonic Oscillator

In general, systems that comprise a mass and an elastic member are capable of undergoing free vibration that occurs without the need of continuous external forcing. The natural frequency of oscillation is considered as one of the primary interests in such systems. The natural frequency of oscillation in this type of systems depends upon the mass and the stiffness possessed in the elastic member (Thomson and Dahleh, 1981).

A basic vibration model of a simple oscillatory system featuring a mass and a spring is shown in Figure 3-1. The force associated with the spring stiffness is defined by a linear relationship following Hooke's law,  $F = kx$ , where  $k$  is stiffness of the spring measured in Newton per meter (N/m) and  $x$  is the displacement exhibited by the spring.

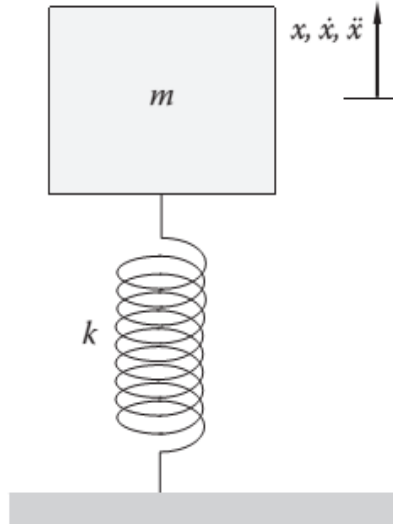


Figure 3-1 SDOF Spring-mass system free body diagram (Tong, 2014)

It is assumed that the above system is restricted to free movement in the vertical direction only. Therefore, since the motion of this system can be fully described by a single coordinate  $x$ , it is said to have a single degree of freedom (SDOF). By applying Newton's second law and incorporating Hooke's law, the equations of motion of the above system can be derived as follows

$$F = m\ddot{x} = -kx \quad 3-2$$

The force  $F$  is defined as the restoring force contained in the spring and the mass  $m$  is the mass of the body. The quantity  $x$  represents the offset displacement from the equilibrium position. By assuming a sinusoidal solution of the resulting differential equation, the displacement of the body mass can be expressed with respect to time as follows

$$x(t) = A \cos(\omega t + \phi) \quad 3-3$$

In the solution,  $A$  is the amplitude of oscillation,  $\omega$  is the frequency of oscillation, and  $\phi$  the phase angle. In other words, once excited, the system exhibits an oscillation at its natural frequency  $f_n$ , which is a feature of the system. It is defined by

$$\omega_n = \sqrt{\frac{k}{m}} \quad \text{or} \quad f_n = \frac{1}{2\pi} \sqrt{\frac{k}{m}} \quad 3-4$$

The velocity and acceleration of the body are

$$\begin{aligned} v &= \dot{x}(t) = -A\omega \sin(\omega t + \phi) \\ a &= \ddot{x}(t) = -A\omega^2 \cos(\omega t + \phi) \end{aligned} \quad 3-5$$

### 3.1.2 Damped Harmonic Oscillator

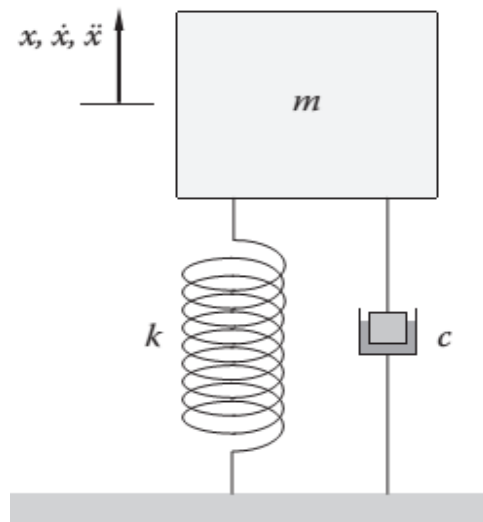


Figure 3-2 Spring-mass system with viscous damper (Tong, 2014)

The damping that exists in a mechanical system can be perceived as the ability of the system to dissipate energy in such a way that reduces the amplitude and duration of vibration. A damping element is generally represented by a dashpot symbol. One of the different types of damping is called viscous damping and is equated to a force proportional to velocity by a damping coefficient usually denoted by  $c$  and measured in  $(Ns/m)$ . The equation of motion of the system presented in Figure 3-2 may be written as

$$m\ddot{x} + c\dot{x} + kx = 0 \quad 3-6$$

A dimensionless quantity of the damping is introduced, denoted by zeta ( $\zeta$ )

$$\zeta = \frac{c}{2\sqrt{mk}} \quad 3-7$$

The natural frequency of this system is similar to the one defined in previous section and the equation of motion is now rewritten as follows

$$\ddot{x} + 2\zeta\omega_n\dot{x} + \omega_n^2x = 0 \quad 3-8$$

Assuming initial conditions for the displacement  $x_0$  and velocity  $v_0$ , the solution is assumed represented in the exponential form as follows

$$x(t) = e^{rt} \quad 3-9$$

Where

$$r_{1,2} = \omega_n(-\zeta \pm \sqrt{\zeta^2 - 1})$$

A general solution of equation can be expressed as a combination of two exponential components

$$x(t) = C_1e^{r_1t} + C_2e^{r_2t} \quad 3-10$$

Depending on the value of  $\zeta$ , four different scenarios are identified as shown below

- $\zeta = 0$  : Completely undamped system. This is exactly the same as if damping element was removed from the system.
- $0 < \zeta < 1$  : underdamped system with oscillation that dies after a period of time. The closer  $\zeta$  to 1, the lower the duration of oscillation. This is also evident in the solution presented in 3-10 in which the imaginary part is not zero.
- $\zeta = 1$  : Critically damped system where the system response settles to equilibrium within the minimum possible duration. In this case the solution is real and no oscillation is present.

- $\zeta > 1$  : An overdamped system where the system response does not have oscillations at all, but takes longer time to settle into equilibrium than a critically damped system. In this case the solution is also real.

### 3.1.3 Vibration in Two Degrees of Freedom Systems

In this section, the analysis of the free and forced vibration of a 2DOF system is considered

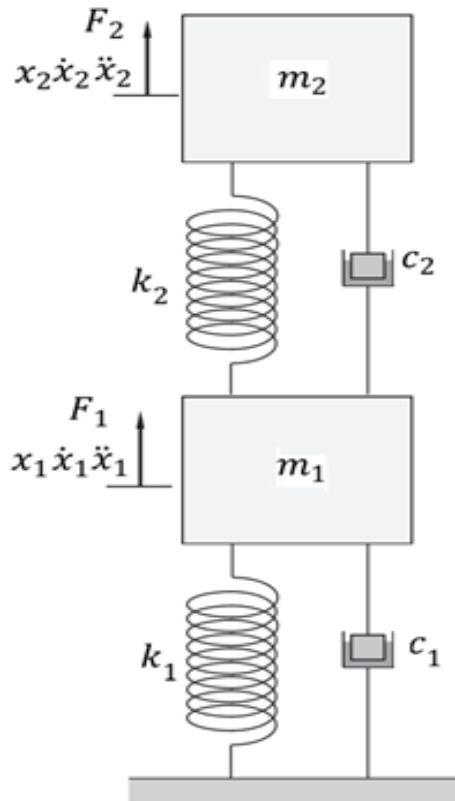


Figure 3-3 Two degrees of freedom spring-mass system with viscous damping (Tong, 2014)

The system shown in Figure 3-3 is assumed to have viscous damping. The motion of the system is restricted to the vertical direction only and is fully described by the coordinates  $x_1$  and  $x_2$  that define the motions of masses  $m_1$  and  $m_2$  at any time from the equilibrium position respectively. Masses  $m_1$  and  $m_2$  are subjected to external forces  $F_1$  and  $F_2$  respectively. By applying Newton's second law of motion, the equation of motion describing each mass is expressed as shown below

$$\begin{aligned}
m_1\ddot{x}_1 + (c_1 + c_2)\dot{x}_1 - c_2\dot{x}_2 + (k_1 + k_2)x_1 - k_2x_2 &= F_1 \\
m_2\ddot{x}_2 + c_2(\dot{x}_2 - \dot{x}_1) + k_2(x_2 - x_1) &= F_2
\end{aligned}
\tag{3-11}$$

Equation system 3-11 represents two coupled second order differential equations due to involvement of terms relating two masses physically. In other words, the motion of each mass is influenced by the other. The matrix form representation of 3-11 is presented as follows

$$\mathbf{M}\ddot{\mathbf{x}} + \mathbf{C}\dot{\mathbf{x}} + \mathbf{K}\mathbf{x} = \mathbf{f}
\tag{3-12}$$

The mass, damping, and stiffness matrices and are expressed as follows

$$\mathbf{M} = \begin{bmatrix} m_1 & 0 \\ 0 & m_2 \end{bmatrix} \quad \mathbf{C} = \begin{bmatrix} c_1 + c_2 & -c_2 \\ -c_2 & c_2 \end{bmatrix} \quad \mathbf{K} = \begin{bmatrix} k_1 + k_2 & -k_2 \\ -k_2 & k_2 \end{bmatrix}$$

The vectors  $\mathbf{x}$ ,  $\dot{\mathbf{x}}$ ,  $\ddot{\mathbf{x}}$  and  $\mathbf{f}$  are the displacement, velocity, acceleration and force vectors respectively and are given by

$$\mathbf{x} = \begin{Bmatrix} x_1 \\ x_2 \end{Bmatrix} \quad \dot{\mathbf{x}} = \begin{Bmatrix} \dot{x}_1 \\ \dot{x}_2 \end{Bmatrix} \quad \ddot{\mathbf{x}} = \begin{Bmatrix} \ddot{x}_1 \\ \ddot{x}_2 \end{Bmatrix} \quad \mathbf{f} = \begin{Bmatrix} F_1 \\ F_2 \end{Bmatrix}$$

It can be seen that the system becomes uncoupled when  $k_2 = c_2 = 0$ , which means that the two masses are not physically connected. For arbitrary forces  $F_1$  and  $F_2$  the analytical solution of the equations becomes difficult to obtain, mainly due to the coupling of variables  $x_1$  and  $x_2$ . The solution of the system involves four constants of integration that can be obtained from the initial conditions of displacements and velocities of the two masses that are specified at  $x_1(0)$ ,  $x_2(0)$ ,  $\dot{x}_1(0)$  and  $\dot{x}_2(0)$ . The free vibration analysis of the system can be obtained while assuming the damping is negligible, i.e.  $c_1 = c_2 = 0$ . The system can then be reduced to

$$\begin{aligned}
m_1\ddot{x}_1 + (k_1 + k_2)x_1 - k_2x_2 &= 0 \\
m_2\ddot{x}_2 - k_2x_1 + k_2x_2 &= 0
\end{aligned}
\tag{3-13}$$

One solution of the above system can be expressed as presented in system

$$\begin{aligned}
x_1 &= X_1 \cos(\omega t + \phi) \\
x_2 &= X_2 \cos(\omega t + \phi)
\end{aligned}
\tag{3-14}$$

It is assumed that the system can oscillate harmonically with the same frequency and phase angle but with different amplitudes. Assuming that  $X_1$  and  $X_2$  are constants that denote the maximum amplitudes of  $x_1$  and  $x_2$  and  $\phi$  is the phase angle. By substituting the solution in the system, the following set of equations can be obtained

$$\begin{aligned} [(-m_1\omega^2 + k_1 + k_2)X_1 - k_2X_2]\cos(\omega t + \phi) &= 0 \\ [-k_2X_1 + (-m_2\omega^2 + k_2)X_2]\cos(\omega t + \phi) &= 0 \end{aligned} \quad 3-15$$

The system in 3-15 represents two simultaneous equations with unknowns  $X_1$  and  $X_2$ . The above equalities are satisfied for  $X_1 = X_2 = 0$  which implies no vibration. A nontrivial solution of the system is possible if the following condition is met

$$\det \begin{bmatrix} -m_1\omega^2 + (k_1 + k_2) & -k_2 \\ -k_2 & -m_2\omega^2 + k_2 \end{bmatrix} = 0 \quad 3-16$$

By equating to zero, the determinant in 3-16 yields the natural frequencies of the system expressed as follows

$$-m_1m_2\omega^4 + \{(k_1 + k_2)m_2 + k_2m_1\}\omega^2 + k_1k_2 = 0 \quad 3-17$$

Yields

$$\omega_1^2, \omega_2^2 = \frac{1}{2} \left\{ \frac{(k_1 + k_2)m_2 + k_2}{m_1m_2} \right\} \pm \left[ \frac{1}{2} \left\{ \frac{(k_1 + k_2)m_2 + k_2m_1}{m_1m_2} \right\}^2 - 4 \frac{k_1k_2}{m_1m_2} \right]^{1/2} \quad 3-18$$

The solution indicates to two natural frequencies associated with this system each correspond to a vibration mode. The nontrivial solution for  $X_1$  and  $X_2$  in 3-15 depends on each frequency as follows

$$r_n = \frac{X_2^{(n)}}{X_1^{(n)}} = \frac{k_2}{-m_1\omega_n^2 + (k_1 + k_2)} \quad 3-19$$

Hence equation system 3-14 is expressed as

$$\begin{aligned} x_1^{(n)} &= X_1^{(n)} \cos(\omega_n t + \phi_n) \\ x_2^{(n)} &= r_n X_1^{(n)} \cos(\omega_n t + \phi_n) \end{aligned} \quad 3-20$$

## **3.2 Concept of Vibration Control**

There are several methods used for controlling the vibration of a structure (Rao, 1990). Some important techniques are considered below

### **3.2.1 Control of Natural Frequencies**

This technique involves altering the natural frequency of a system in such a way to avoid resonance. This happens when the excitation frequency matches the natural frequency of a particular system. Generally, resonance of a mechanical structure must be avoided as it could lead to system failure. The natural frequencies can be altered by manipulating either the stiffness or the mass.

### **3.2.2 Introduction of Damping**

If a system is under excitation, its vibration amplitude would be larger if it possesses no damping. Generally, the presence of damping in a system limits its vibration. The previous concept in 3.2.1 is suitable when the excitation frequency is known however it is limited when the system excitation frequency varies during operation. In such cases, damping may be introduced into the system to control its vibration amplitudes over a wider range of excitation frequencies.

### **3.2.3 Vibration Isolation**

This method involves the insertion of an isolator, a flexible member comprising stiffening and a damping element, between the vibrating structure and the source of vibration so that it reduces the dynamics response of that structure within specified conditions of excitation. The following example explains the conditions for successful isolation for a general sdof system.

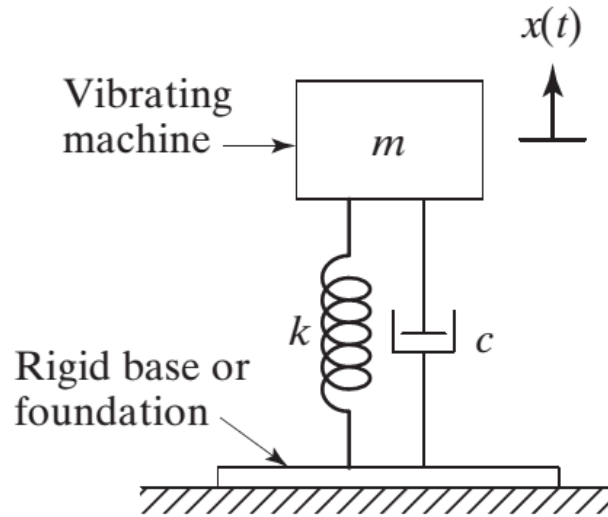


Figure 3-4 SDOF representation of an isolation system with rigid foundation (Rao, 1990)

Referring to Figure 3-4, the operation of the system gives rise to a harmonically varying force  $F(t) = F \sin(\omega t - \varphi)$ , the equation of motion according to Newton's second law can be expressed as follows

$$m\ddot{x} + c\dot{x} + kx = F \sin(\omega t - \varphi) \quad 3-21$$

The general solution can be assumed to be harmonic and can be written as

$$x(t) = X \sin(\omega t - \varphi) \quad 3-22$$

With  $X$  representing the steady state amplitude of the response and expressed as follows

$$\frac{F}{X} = [(k - m\omega^2)^2 + \omega^2 c^2]^{\frac{1}{2}} \quad 3-23$$

By associating the solution into the equation, the transmitted force,  $F_t(t)$ , to the foundation can then be expressed as

$$F_t(t) = kx(t) + c\dot{x}(t) = X[k\sin(\omega t - \varphi) + c\omega\cos(\omega t - \varphi)] \quad 3-24$$

The magnitude of the transmitted force,  $F_t$ , is then given by

$$F_t = [(kx)^2 + (c\dot{x})^2]^{\frac{1}{2}} = X(k^2 + \omega^2 c^2)^{\frac{1}{2}} \quad 3-25$$

The transmission ratio of the isolator, denoted by transmissibility ( $T_r$ ) is defined as the ratio of the magnitude of the transmitted force to the exciting force

$$T_r = \frac{F_t}{F} = \left( \frac{k^2 + \omega^2 c^2}{(k - m\omega^2)^2 + \omega^2 c^2} \right)^{1/2} = \left( \frac{1 + (2\zeta r)^2}{[1 - r^2]^2 + (2\zeta r)^2} \right)^{1/2} \quad 3-26$$

The quantity  $r = \frac{\omega}{\omega_n}$  is the frequency ratio and  $\zeta = \frac{c}{2m\omega_n}$  is the damping ratio.  $\omega$  is the frequency of excitation and  $\omega_n$  is the resonant frequency or natural frequency of the system.

Note that the derived equations also apply when the foundation is the source of excitation.

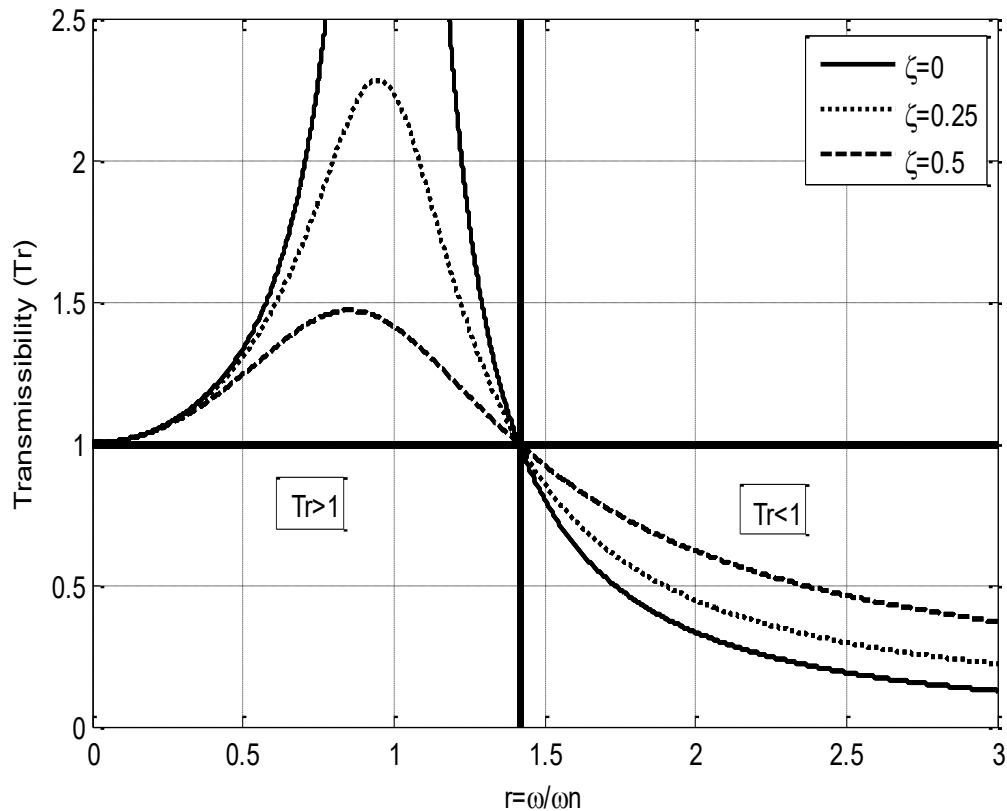


Figure 3-5 The variation of transmissibility with frequency

By examining the graphs of Figure 3-5, the reduction of the transmitted force can be achieved by either lowering the natural frequency of the system or by increasing the damping ratio.

Note that for successful isolation of vibration  $r$  must be greater than  $\sqrt{2}$ , but the machine would still pass resonance during start up and stopping. Hence, some damping is required to avoid large amplitudes at resonance.

### **3.2.4 Vibration Absorbers**

In cases where the system undergoes an excitation of known constant frequency, a vibration absorber may be employed in order to neutralise the vibration of the system. A vibration absorber is designed in such a way that when it is added to the system, the vibration is reduced at certain frequencies and the resulting natural frequencies of the combined system are away from that of the excitation.

### **3.3 Concept of Active vibration Control**

Active control uses an external adjustable device called an actuator to provide a force to the structure or machine whose vibrations are to be manipulated. Many types of actuators can be employed including hydraulic piston, piezoelectric device, electric motor, etc. The force that the actuator delivers to the structure can be determined based on the response of the system. The actuators are programmed and controlled to oppose the vibration and hold the isolated mass nearly motionless by counteracting the response of the vibrating force. The force of actuation, directed by a controller/processor in the feedback loop avoids the need of supplementary mass, stiffness or damping adjustments. Due to the fact that a force is added to the system, control instability becomes a potential problem. It should be noted that semi-active isolation systems are considerably less complicated and do not cause system instability for bounded input force, and their operating performance has shown to be very effective, nearly matching active isolation results (Harris et al., 2002). Figure 3-6 shows an adjustable force actuator within an active control configuration.

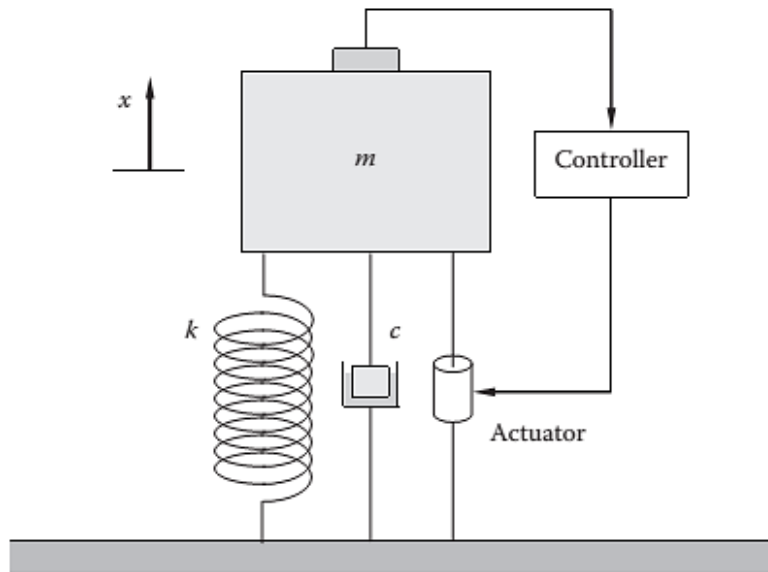


Figure 3-6 General active vibration suppression with feedback control (Tong, 2014)

Control methods for active isolation are usually based on response measurement but can also be based on input variables. Other techniques compare input and response and adjust gains accordingly. There are numerous control strategies implemented in active isolation configuration comprising the use of feedback and feedforward control. Classical control strategies have been used with several implementations such as the proportional-integral-derivative control (PID). Linear optimal control has also been used including linear quadratic controller (LQC) and linear quadratic regulators (LQR). In addition to that, adaptive control has been used including implementation of fuzzy logic and adaptive neural networks.

### 3.4 Concept of Semi-Active vibration control

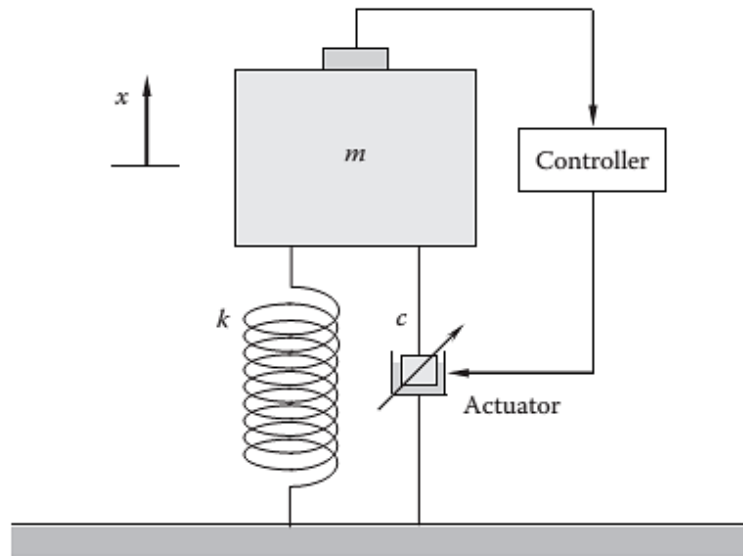


Figure 3-7 Semi-active damping based on manipulating damper properties (Tong, 2014)

Figure 3-7 illustrates the concept of semi-active damping. Semi-active isolation involves the use of devices with properties that can be manipulated based on the implementation of control strategies that do not require a significant amount of energy input. One way realising this law is by controlling the damping factor of a particular actuator. The variable device with its controller and electronics can be mounted separately or used with the passive isolator to operate as an integrated assembly. As mentioned previously, many types of devices can be implemented as energy dissipaters/storage to achieve the semi-active control scheme (Liu, 2004). When using the device for varying the damping in the system, the magnitude of the dissipating force depends on the relative velocity across the device. Altering the damping in the system is performed by a controller performing the appropriate control strategy in such a way that controls the dissipating force.

Karnopp (Karnopp, 1973) designed the first semi-active control strategy by which the force generated by a passive device is varied to approximate the force that would be generated by a damper connected to an inertial reference denoted by skyhook damper.

### 3.5 The Stirling Engine

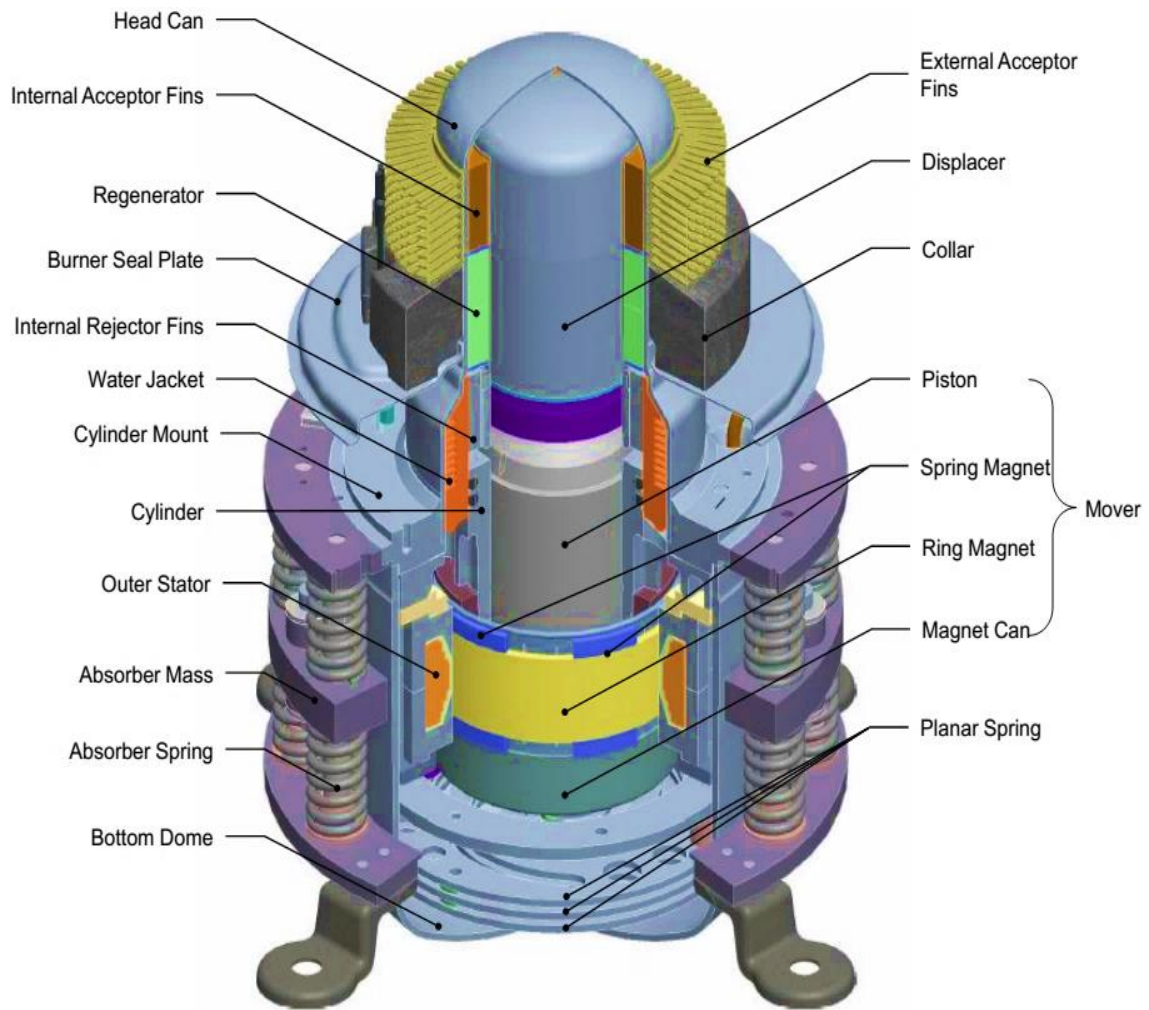


Figure 3-8 Stirling Engine (Microgen Engine Corporation, )

Reverend Robert Stirling invented the Stirling engine in 1816 and William Beale developed the Free-Piston Stirling engine concept in 1970 (Microgen Engine Corporation, ). This type of thermodynamic machines is designed to operate within a closed thermodynamic cycle, where cyclic compression and expansion of the working fluid at different temperature occurs between the top and the bottom of the engine (Walker, 1980). Air, nitrogen, helium or hydrogen can be used as the working fluid inside the engine and a variety of heat sources including natural gas, solar energy, waste heat, and fossil fuels can be utilised to heat the gas at the top of the engine and water can used to cool the gas at the bottom. A piston called the displacer is fitted inside the engine cylinder to move the gas between the cold and hot ends of

the engine. The process of expansion and compression of the gas when heated and cooled respectively powers the engine with efficiency similar to that of the Carnot efficiency, around 30%. A piston fitted with permanent magnet is driven up and down at a defined rate in cycles per second. In general, there are three types of configuration for Stirling engines (Ross, 1993):

1.  $\alpha$ -type: featuring two pistons in two separate cylinders
2.  $\beta$ -type: featuring a piston and a displacer fitted in one cylinder
3.  $\gamma$ -type: featuring a piston and a displacer, each in its own cylinder

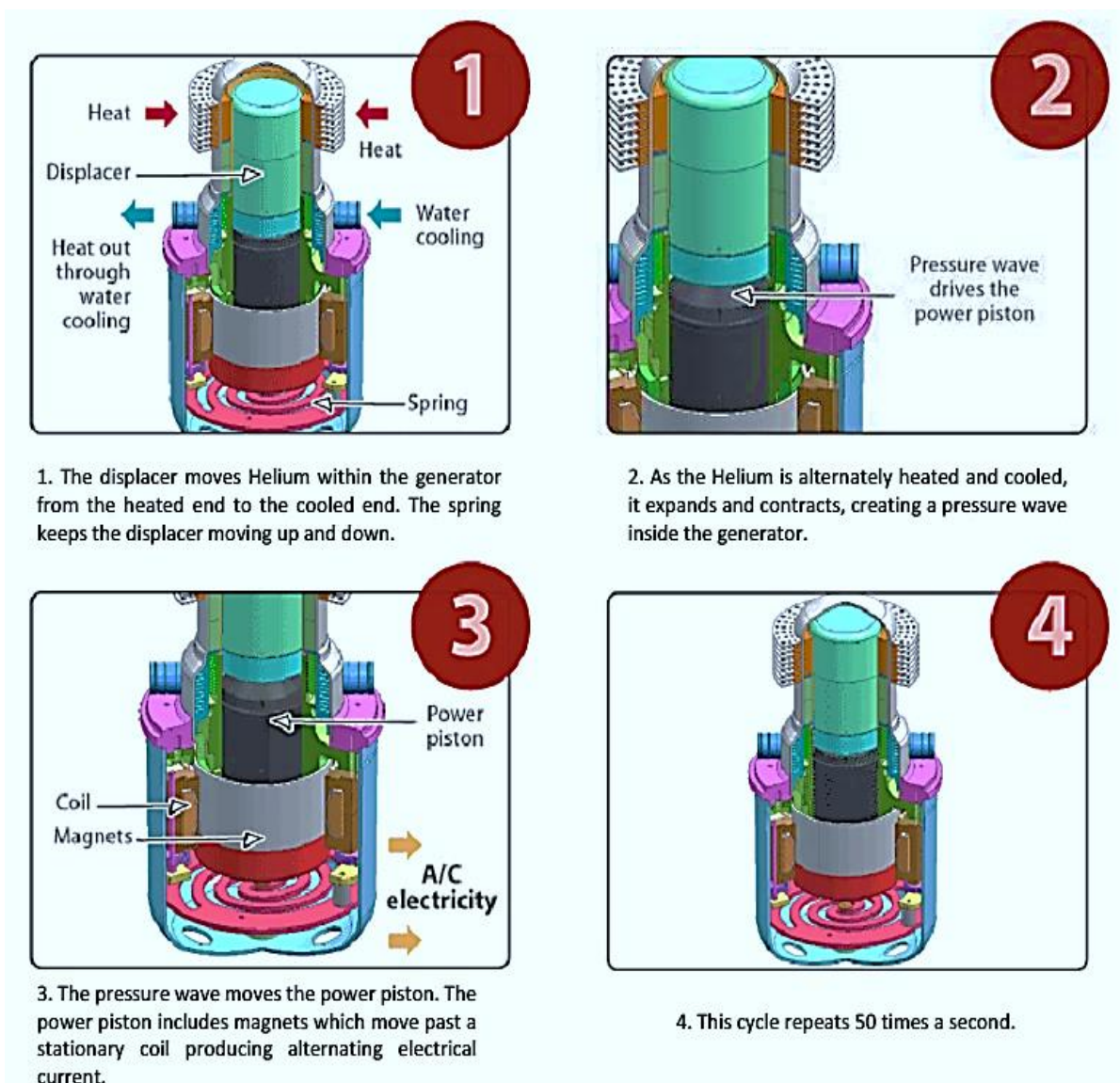


Figure 3-9 Working principle of a  $\beta$ -type Stirling engine, (Microgen Engine Corporation )

### 3.6 Basics of a Voice Coil Motor (VCM)

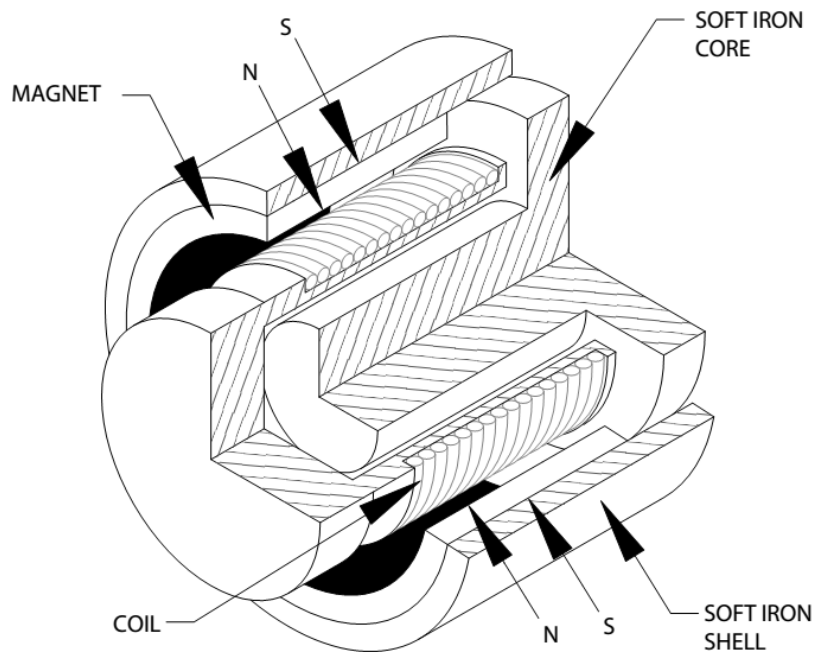


Figure 3-10 Conventional construction of a VCM (Kimco Magnetics)

VCMs are linear motion transducers fitted with a coil winding moving through a permanent magnet as shown in Figure 3-10. The flow of electrical current in the motor terminals generates a force of magnitude proportional to that current (Black et al., 1993). Originally used in radio loud speaker, those actuators have received considerable attention with applications that require accurate feedback control. The capability of operating at high acceleration and high frequencies ranges made them desired actuators for use.

A VCM converts its input electrical energy into an output mechanical energy according to Lorentz Force law. If an electrical current flows through a conductor in the presence of a magnetic field, the conductor exhibits an electromagnetic force as shown in Figure 3-11.

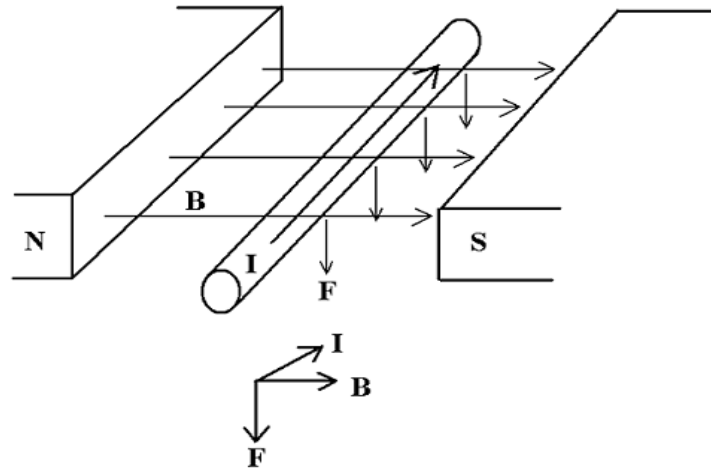


Figure 3-11 Basic Lorentz force law

The electromagnetic force, measured in Newton (N), is determined by

$$\vec{F} = KLN\vec{B} \times \vec{I} \quad [N] \quad 3-27$$

Where  $K$  represents a constant related to the physical design and materials of the motor,  $B$  the magnetic flux density measured in Tesla,  $I$  the current in A,  $L$  the length of the conductor in meters, and  $N$  is the number of conductor turns. As the formula states, the electric current and magnetic field directions determine the direction of the force. Mathematically speaking, the direction of the force vector is determined by taking the cross product of the other two vectors. The direction of the force reverses if either the direction of the current or the magnetic field is reversed while keeping the other constant. By assuming a constant magnetic field and a constant number of conductor turns, i.e. same length, the force is said to be directly proportional to the input. According to Faraday's law, the same moving conductor will see an induced voltage across its terminals governed by the following equation

$$\vec{E} = KLN\vec{B} \times \vec{v} \quad [V] \quad 3-28$$

The quantity  $v$  is the velocity of the conductor. In simpler terms, it can be stated that a VCM is a device comprising a permanent magnet and a coil moving inside the magnet field that generates a force proportional to the electrical current through its coil and a voltage proportional to the relative velocity of its coil and the permanent magnet. Electromagnetic

actuators are suitable to develop active and semi-active control configurations. For use in semi-active mode, if the terminals of the motor are shorted or connected to an external resistor, the device acts as a mechanical damper of variable damping dependent on the resistance of the external load. Assuming no external resistor is connected, the damping is null when the circuit is open, and reaches maximum when the coil is shorted.

## 4 Passive Tuned Mass Dampers (TMD)

This chapter considers the analysis of tuned mass dampers TMDs based on 2DOF vibration system. The analysis is carried out both from a mechanical engineering perspective and the analogous electrical engineering view is also considered. Two different software tools, Matlab/Simulink and MultiSim are used to verify the results.

### 4.1 System Analysis

The working principle of a TMD is based on coupling an auxiliary mass to a primary structure with a spring as depicted in Figure 4-1. For a TMD to function properly, the tuned natural frequency of the TMD, anti-resonant frequency as seen by the primary structure, and the excitation frequency of the vibrating structure have to be synchronized. The auxiliary mass should exert an inertial force that is out-phased with the displacement of the primary structure at the excitation frequency. The modeling of a TMD is shown below

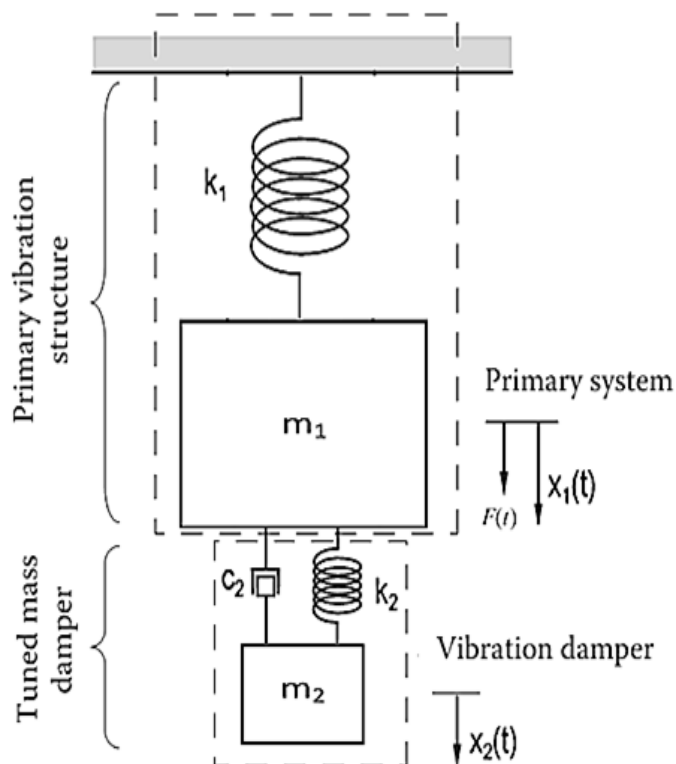


Figure 4-1 2DOF TMD system (Tong, 2014)

The auxiliary mass  $m_2$  is connected to a primary mass  $m_1$  via a spring of stiffness  $k_2$ , and damper of damping coefficient  $c_2$ . The composite system  $m_1 + m_2$  is connected to a fixed end through spring of stiffness  $k_1$ . The equations that describe the system of Figure 4-1 may be derived as follows (Den Hartog, 1985)

$$\begin{aligned} m_1 \ddot{x}_1 + k_1 x_1 + k_2(x_1 - x_2) + c_2(\dot{x}_1 - \dot{x}_2) &= F(t) \\ m_2 \ddot{x}_2 + k_2(x_2 - x_1) + c_2(\dot{x}_2 - \dot{x}_1) &= 0 \end{aligned} \quad 4-1$$

The matrix representation of the system 4-1 is shown in 4-2

$$\begin{bmatrix} m_1 & 0 \\ 0 & m_2 \end{bmatrix} \begin{bmatrix} \ddot{x}_1 \\ \ddot{x}_2 \end{bmatrix} + \begin{bmatrix} c_1 + c_2 & -c_2 \\ -c_2 & c_2 \end{bmatrix} \begin{bmatrix} \dot{x}_1 \\ \dot{x}_2 \end{bmatrix} + \begin{bmatrix} k_1 + k_2 & -k_2 \\ -k_2 & k_2 \end{bmatrix} \begin{bmatrix} x_1 \\ x_2 \end{bmatrix} = \begin{bmatrix} F \\ 0 \end{bmatrix} \quad 4-2$$

The matrices  $\mathbf{M}$ ,  $\mathbf{C}$  and  $\mathbf{K}$  are of dimension  $2 \times 2$  whose elements are the known masses, damping, and stiffnesses of the system. If the excitation force is assumed to be harmonic of the shape  $F(t) = F \sin \omega t$ , the solutions of the equations of motion may follow the form

$$\begin{aligned} x_1(t) &= X_1 \sin(\omega t) \\ x_2(t) &= X_2 \sin(\omega t) \end{aligned} \quad 4-3$$

The equations 4-3 yield the solutions for the primary system and the TMD systems in 4-4

$$\begin{aligned} x_1(j\omega) &= \frac{(k_2 - m_2\omega^2 + j\omega c_2) F \sin \omega t}{[(k_1 - m_1\omega^2)(k_2 - m_2\omega^2) - m_2 k_2 \omega^2] + j\omega c_2(k_1 - m_1\omega^2 - m_2\omega^2)} \\ x_2(j\omega) &= \frac{(k_2 + j\omega c_2) F \sin \omega t}{[(k_1 - m_1\omega^2)(k_2 - m_2\omega^2) - m_2 k_2 \omega^2] + j\omega c_2(k_1 - m_1\omega^2 - m_2\omega^2)} \end{aligned} \quad 4-4$$

The solution of the denominator of 4-4 yields the resonant frequencies of the composite system,  $\omega_1, \omega_2$

$$\omega_{1,2}^2 = \frac{1}{2} \left\{ \frac{(k_1 + k_2)m_2 + (k_2)m_1}{m_1 m_2} \right\} \pm \left[ \frac{1}{2} \left\{ \frac{(k_1 + k_2)m_2 + k_2 m_1}{m_1 m_2} \right\}^2 - 4 \left\{ \frac{(k_1 + k_2)(k_2 + k_3) - k_2^2}{m_1 m_2} \right\} \right]^{1/2} \quad 4-5$$

The main interest is the motion of the primary mass and it is useful to express it in a dimensionless form. For this purpose the following dimensionless quantities are introduced

$\mu = m_2/m_1$ : Mass Ratio = absorber mass/primary mass

$\delta_{st} = F/k_1$ : Static deflection

$\omega_2^2 = k_2/m_2$ : Natural frequency of the absorber squared

$\omega_1^2 = k_1/m_1$ : Natural frequency of the primary mass squared

$f = \omega_2/\omega_1$ : Ratio of frequencies

$g = \omega/\omega_1$ : Forced frequency ratio

$c_c = 2m_2 \omega_1$ : Critical damping constant

The dimensionless form of the amplitude of the main mass can be written as

$$\delta_t = \frac{X_1}{\delta_{st}} = \left[ \frac{(2\zeta g)^2 + (g^2 - f^2)^2}{(2\zeta g)^2 (g^2 - 1 + \mu g^2)^2 + \{\mu f^2 g^2 - (g^2 - 1)(g^2 - f^2)\}^2} \right]^{1/2} \quad 4-6$$

The plot of the normalised primary mass displacement against normalised excitation frequency is shown below for different damping ratios  $\zeta$  while the mass ratio  $\mu = 0.05$  is fixed.

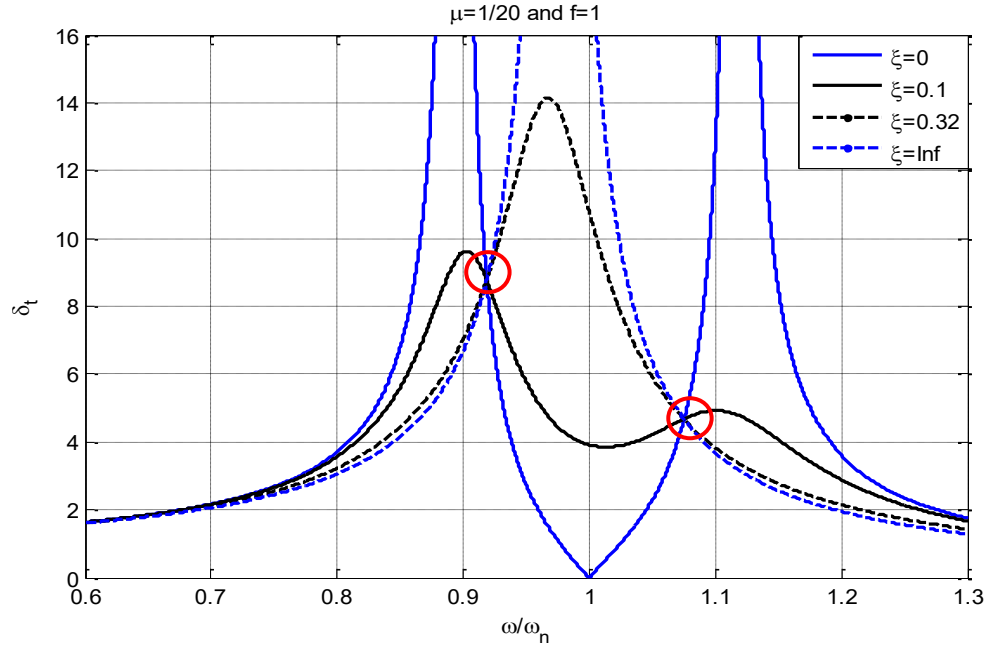


Figure 4-2 Normalised amplitude of vibration of the primary mass expressed as a function of the frequency ratio for different damping ratios and mass ratio  $\mu=0.05$

The graphs of Figure 4-2 depict frequency response of the normalised displacement of the primary mass of a 2DOF system comprising a primary and an auxiliary mass. The auxiliary mass is chosen 20 times smaller than the primary mass. Generally, by adding an isolator to the system the aim is to bring the amplitude at the resonant peaks down to an acceptable level. However, this research is associated with the operation of a TMD, particularly when the frequency ratio is chosen as  $f = 1$ . The analysis for the case of an isolator was presented earlier in subsection 3.2.3 and the case of the TMD is emphasised in this subsection.

By examining the graphs of Figure 4-2, the composite 2DOF system exhibits two peaks associated with two modes of vibration. Those frequencies are determined according to equation 4-5. It can be said that higher the mass ratio  $\mu$ , the further the resonant frequencies go apart. Damping is a crucial property of the system and the following analysis is based on the damping factor  $\zeta$  which is directly proportional to the damping coefficient in the TMD  $c_2$ . When damping the TMD is assumed null ( $\zeta = 0$ ), the peak amplitude of the primary mass displacement at both resonant frequencies of the composite system is virtually infinite. Now

by considering the case when  $\zeta$  is infinite, the two masses are virtually clamped together and the system behaves as an SDOF with a mass  $m_1 + \frac{1}{20}m_1$ , a stiffness  $k_1$ , and a damping coefficient  $c_1$ . If the intention is to design a TMD that cancels the vibration of the primary mass at a particular frequency, the best outcome is to completely cancel the vibration by matching resonant frequency of the TMD to the forcing frequency. This case coincides with  $\zeta = 0$ . This approach guarantees the maximum attenuation, however, it is associated with a huge risk of damaging the system if the excitation frequency drifts and matches any of the resonant modes. This type of TMD is very sensitive to minimal drifts in the excitation frequency. By increasing  $\zeta$ , the peak amplitude of the primary mass vibration at resonant modes will be reduced but at the same time the amplitude of vibration of the primary mass would not be completely attenuated at the anti-resonant frequency (natural frequency of the TMD). For an optimum TMD, one might consider keeping  $\zeta = 0$  whereby setting the composite system resonant frequencies further apart. In fact by modifying the frequency ratio  $f$  or the mass ratio  $\mu$ , the position of the two resonant frequencies of the composite system can be altered.

Now if the aim is to design an optimal dynamic absorber that attenuates the vibration as well as the amplitude peaks at resonance, Den Hartog observed a remarkable peculiarity concerning the graphs of Figure 4-2; that all four curves always intersect in two points independent of damping. Realising that the most favourable solution is obtained when the curve passes with a horizontal tangent to those points, Hartog derived a solution based on defining an expression of the optimum frequency ratio and optimum damping ratio given by

$$f_{opt} = \frac{1}{1 + \mu} \quad 4-7$$

$$\zeta_{opt} = \sqrt{\frac{3\mu}{8(1 + \mu)^3}} \quad 4-8$$

## 4.2 TMD: RLC Electrical Analogy

Analogies can be very useful when trying to explore new fields. By means of analogies, an unexplored system may be compared to another which is well understood. Electrical systems have been widely studied as vibrating systems. By means of analogies, the knowledge of electrical circuits may be applied to solving problems in mechanical and acoustic systems (Olson, 1958). In this procedure, a mechanical system is converted into an analogous electrical circuit. For the purpose applying electrical analogies to mechanical vibration system, we shall visit the relevant electrical analogous models of the mechanical TMD studied previously. Showing this analogy addresses readers who are somewhat more familiar with AC systems. The equivalence can be set by deriving the Kirchhoff voltage equation of the electrical circuit.

### 4.2.1 Free Oscillation in LC circuit

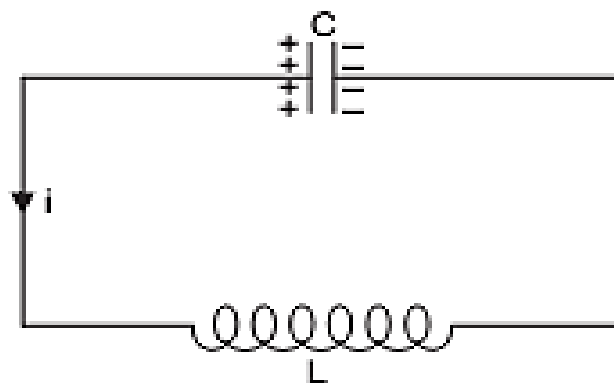


Figure 4-3 An LC electrical circuit

A simple schematic of an LC electrical circuit is shown Figure 4-3. It features an inductor of inductance  $L$  and a capacitor of capacitance  $c$ . The capacitor is assumed to have an initial charge that is allowed to discharge in the inductor. The following definitions are then made

- The voltage across the capacitor terminals at any time is  $V_c = \frac{q}{c}$
- The voltage across the inductor terminals at any time is  $V_L = -L \frac{di}{dt} = -L \frac{d^2q}{dt^2}$

The electrical charge stored in the capacitor is denoted by  $q$  and the electrical current flowing in the circuit is denoted by  $i$ , which is also the rate of flow of electrical charge in time.

Applying Kirchhoff's voltage law yields the following differential equation

$$L \left( \frac{d^2q}{dt^2} \right) + \frac{q}{c} = 0 \quad 4-9$$

It can be said that a pure  $LC$  circuit is an electrical analogue of the undamped simple harmonic mass oscillator, i.e. a mass connected to a fixed end via a spring. In the case of the simple undamped harmonic oscillator, the mechanical energy interchanges repeatedly between a kinetic energy and potential one while being conserved. In the electrical case, energy changes back and forth between an electrical form stored in the capacitor and a magnetic form around the inductor. The natural frequency of oscillation of the electrical system can be expressed as  $\omega_n = \frac{1}{\sqrt{LC}}$

#### 4.2.2 Damped oscillation in series LRC circuit

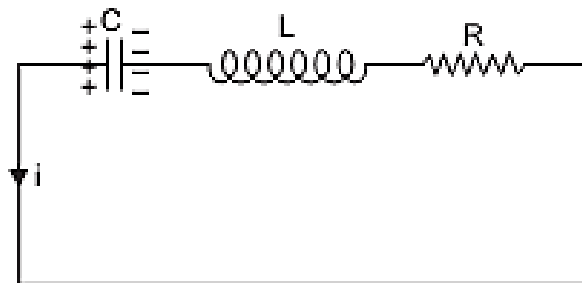


Figure 4-4 LRC circuit

Referring to Figure 4-4, the capacitor in the RLC circuit has an initial charge which can discharge with a current flowing in both the inductor and the resistor. The same definitions for the voltage across the capacitor and inductor apply, with the addition of the voltage across the resistor defined as  $V_R = Ri = R \frac{dq}{dt}$ . Then by applying Kirchhoff's voltage law, the following is obtained

$$\frac{d^2q}{dt^2} + \frac{R}{L} \frac{dq}{dt} + \frac{q}{LC} = 0 \quad 4-10$$

$$\omega_n^2 = \frac{1}{LC} \quad \text{and} \quad \zeta = \frac{R}{2L\omega_n} = \frac{R}{2} \sqrt{\frac{C}{L}}$$

The variation of electrical charge with time  $q$  ( $i = dq/dt$ ) is analogous to variation of displacement with time in mechanical systems. It follows the electrical current is analogous to the velocity experienced by the damper and the spring. Similarly, the values of  $\zeta$  determine if the response type is underdamped, critically damped, or overdamped.

### 4.2.3 Forced Oscillations in a Series LCR Circuit

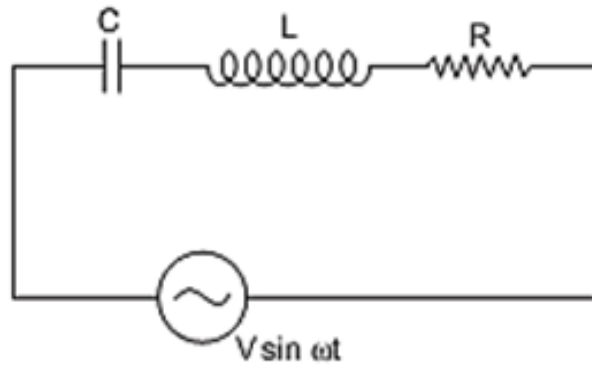


Figure 4-5 Driven LRC circuit

Figure 4-5 shows an RLC circuit connected in series to a voltage source that drives an alternating current in the circuit with  $v(t) = V \sin \omega t$ .

By applying Kirchhoff's law, the following differential equation is obtained

$$\frac{d^2q}{dt^2} + \frac{R}{L} \frac{dq}{dt} + \frac{q}{LC} = \frac{V}{L} \sin \omega t \quad 4-11$$

If the steady state solution of the above linear differential equation is assumed to be sinusoidal,  $q(t) = Q \sin(\omega t + \phi)$ , the amplitude  $Q$  is obtained as follows

$$Q = \left| \frac{I}{j\omega} \right| = \left| \frac{V}{j\omega(R + j(\omega L - \frac{1}{\omega C}))} \right| = \frac{V}{[(1/C - L\omega^2)^2 + \omega^2 R^2]^{\frac{1}{2}}} \quad 4-12$$

### 4.3 Summary of the electrical-mechanical analogy

The conversion of the mechanical part of a system into the electrical domain allows the entire system to be analysed as a unified whole. The mathematical behaviour of a simulated electrical system is identical to the mathematical behaviour of the represented mechanical system. Each element in the mechanical system has a corresponding element in the electrical one and the differential equations of the two systems are similar. Circuit laws such as Kirchhoff's laws, Thévenin, and Norton are applied for electrical systems to describe the behaviour of the system. Table 4-1 contains a summary of the mechanical quantities alongside their electrical analogous representation.

Table 4-1 Analogy between electrical and mechanical quantities

Electrical Quantity	Electrical Expression	Mechanical Analogy	Mechanical Expression
Resistor	$V_R = Ri$	Damper	$F_d = cv$
Inductor	$V_L = L \frac{di}{dt}$	Mass	$F_m = m \frac{dv}{dt} = ma$
Capacitor	$V_c = \frac{1}{C} \int i dt$	Spring	$F_k = k \int v dt = kx$
Power Supplied	$P = Vi$	Power Supplied	$P = Fv$
Power (resistor)	$P = Ri^2 = \frac{V_R^2}{R}$	Power (Damper)	$P = cv^2 = \frac{F_d^2}{c}$
Magnetic Energy	$E = \frac{1}{2} Li^2$	Kinetic Energy	$E = \frac{1}{2} mv^2$
Electric Energy	$E = \frac{1}{2} CV_c^2$	Potential Energy	$E = \frac{1}{2} \frac{F_k^2}{k}$

### 4.3.1 Impedance

The electrical impedance  $Z_e$  of the system shown in Figure 4-5 is defined as the ratio of the driving voltage to the current flowing through a circuit with the assumption that the voltage varies with frequency.

$$Z_e = \frac{V}{I} = R + j(\omega L - \frac{1}{\omega C}) \quad 4-13$$

In electrical circuits, when two elements are in series, their individual impedances add up. They exhibit different voltage drops across them but same amount of current flows through them. For parallel connection, components exhibit same voltage across them and different amount of electrical current flowing through them. In general, measurement of impedance of a system can be used to predict the behaviour of the system. The electrical impedance can be extended to analyse a mechanical system based on the analogy that exists between mechanical system and electrical systems shown in Table 4-1.

The mechanical impedance  $Z_m$  for a spring mass damper system is equivalent to the RLC circuit impedance, and is expressed as

$$Z_m = \frac{F}{v} = c + j(\omega m - \frac{k}{\omega}) \quad 4-14$$

In mechanical systems, the impedance is defined as the ratio of the force to speed. Similar to the electrical system, two connected mechanical components that have the same velocity are said to be connected in series and their individual impedances add up. However, when two elements carry the same force, they are said to be in parallel and their combined impedance is defined as the product of their individual impedance upon their sum.

### 4.3.2 Parallel Mechanical and Electrical Configurations

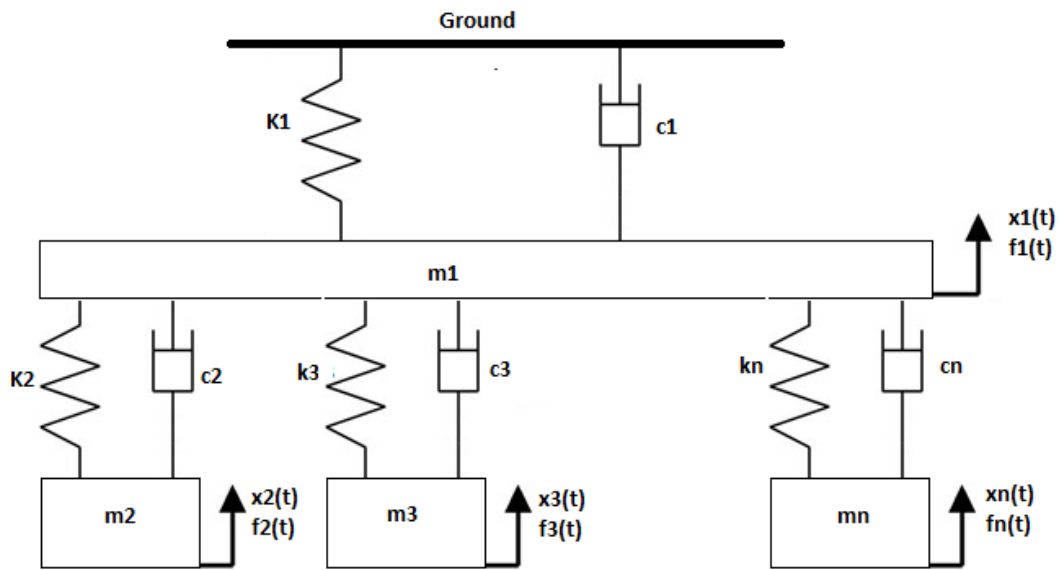


Figure 4-6 Parallel mechanical tuned mass damper configuration

$$m_1 \ddot{x}_1 + c_1 \dot{x}_1 + k_1 x_1 + \sum_{m=2}^n c_m (\dot{x}_1 - \dot{x}_m) + \sum_{m=2}^n k_m (x_1 - x_m) = f_1$$

4-15

$$m_i \ddot{x}_i + c_i (\dot{x}_i - \dot{x}_1) + k_i (x_i - x_1) = f_i$$

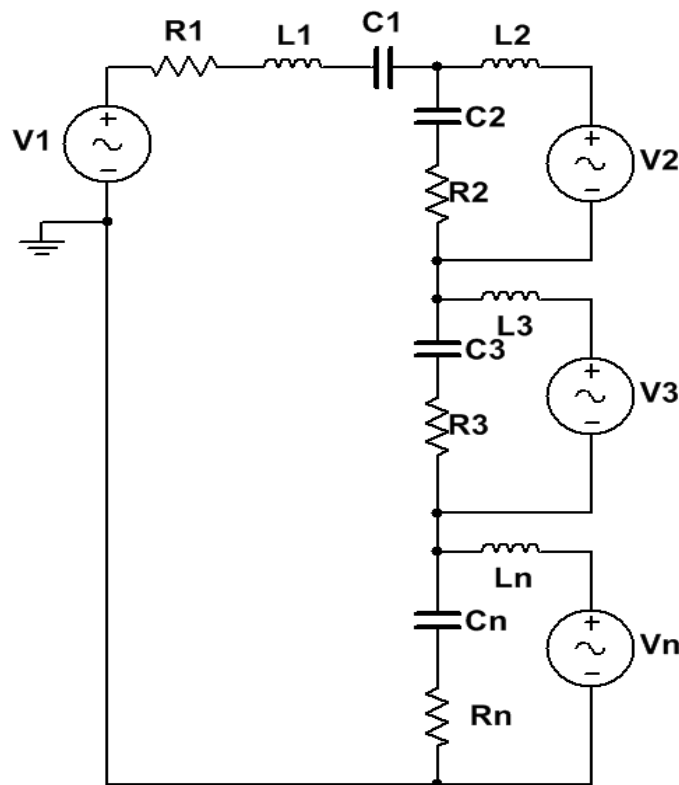


Figure 4-7 Parallel analogous electrical configuration

$$L_1 \ddot{q}_1 + R_1 \dot{q}_1 + \frac{1}{c_1} q_1 + \sum_{m=0}^n R_m (\dot{q}_1 - \dot{q}_m) + \sum_{m=0}^n \frac{1}{c_m} (q_1 - q_m) = v_1$$

4-16

$$L_i \ddot{q}_i + R_i (\dot{q}_i - \dot{q}_1) + \frac{1}{c_i} (q_i - q_1) = v_i$$

where  $n$  represents the number of electrical/mechanical branch and  $i = [2; n]$

### 4.3.3 Series Mechanical and Electrical Configurations

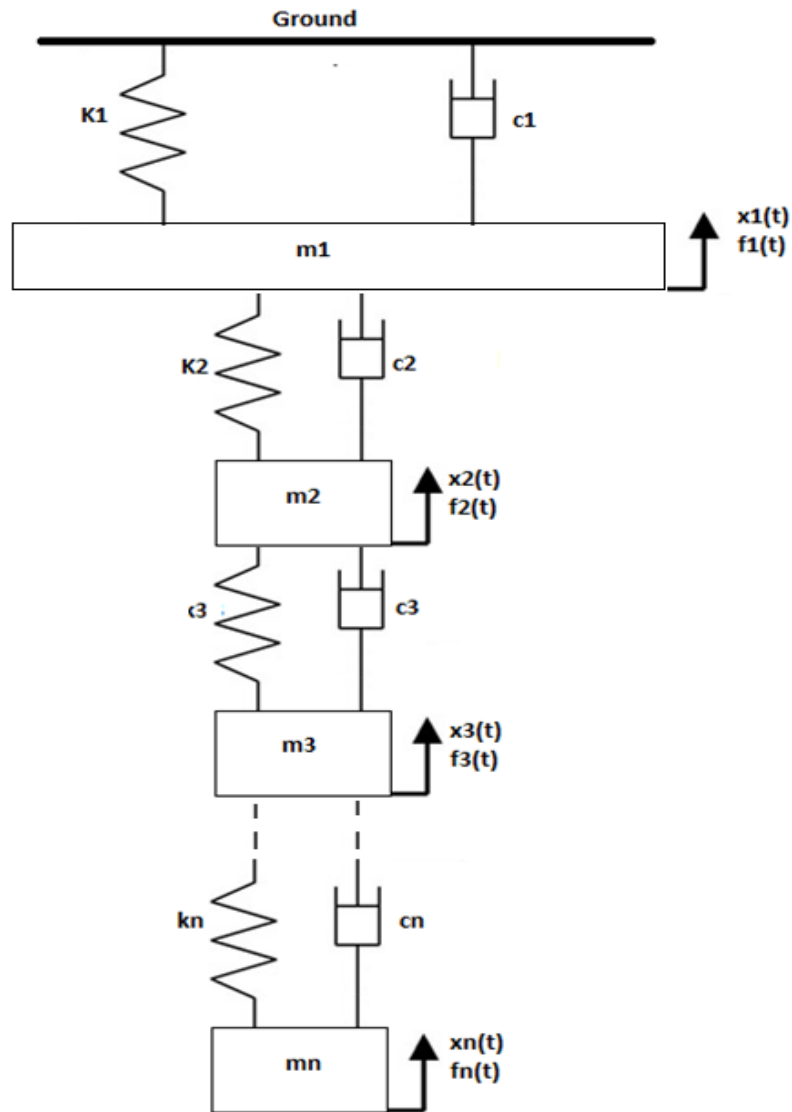


Figure 4-8 Series mechanical tuned mass damper configuration

$$m_i \ddot{x}_i + c_i (\dot{x}_i - \dot{x}_{i-1}) + k_i (x_i - x_{i-1}) + k_{i+1} (x_i - x_{i+1}) + c_{i+1} (\dot{x}_i - \dot{x}_{i+1}) = f_i$$

4-17

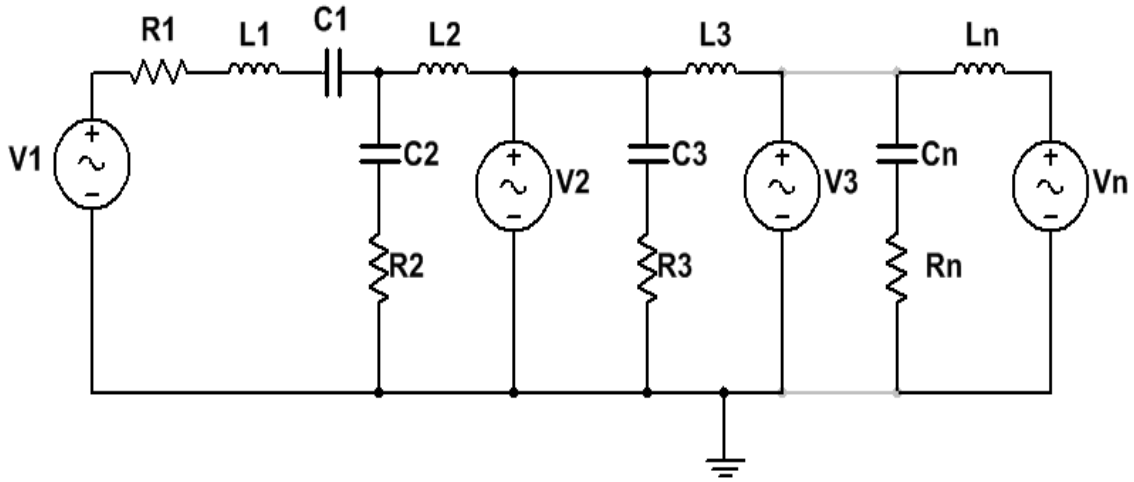


Figure 4-9 Series analogous electrical configuration

$$L_i \ddot{q}_i + R_i(\dot{q}_i - \dot{q}_{i+1}) + \frac{1}{c_i}(q_i - q_{i-1}) + R_{i+1}(\dot{q}_i - \dot{q}_{i+1}) + \frac{1}{c_{i+1}}(q_i - q_{i+1}) = v_i \quad 4-18$$

Where  $i = [1; n]$

#### 4.3.4 Example with 2-DOF system

The numerical example illustrates the concept of mechanical-electrical analogy based on a 2-DOF system. The mechanical system features a TMD that is represented with an LRC electrical circuit. A simulation is carried out using values adopted in Table 4-2 and with different values of the damping ratio  $\zeta$ . The results are shown in Figure 4-10.

Table 4-2 Numerical Example

Mechanical	Electrical
$m_1 = 40 [kg]$	$L_1 = 40 [H]$
$k_1 = 1579 [N/m]$	$C_1 = 633.257[\mu F]$
$c_1 = 0.1 [Ns/m]$	$R_1 = 0.1 [\Omega]$
$m_2 = 4 [kg]$	$L_2 = 4 [H]$
$k_2 = 394788.788 [N/m]$	$C_2 = 2.533[\mu F]$
$c_2 = 0 - 220 [Ns/m]$	$R_2 = 0 - 220 [\Omega]$
$f = 0 - 100 [Hz]$	$f = 0 - 100 [Hz]$

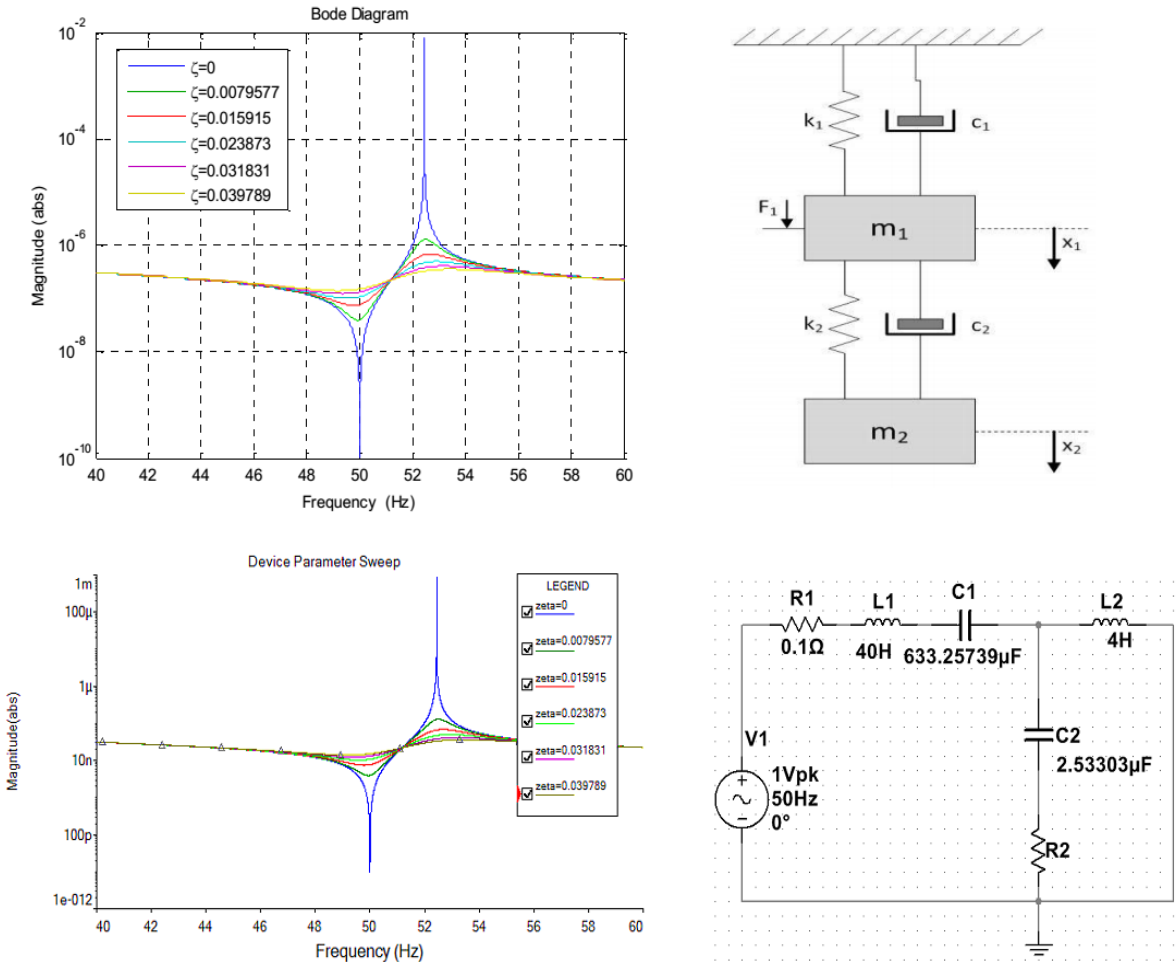


Figure 4-10 Example of a 2-DOF mechanical-electrical analogy

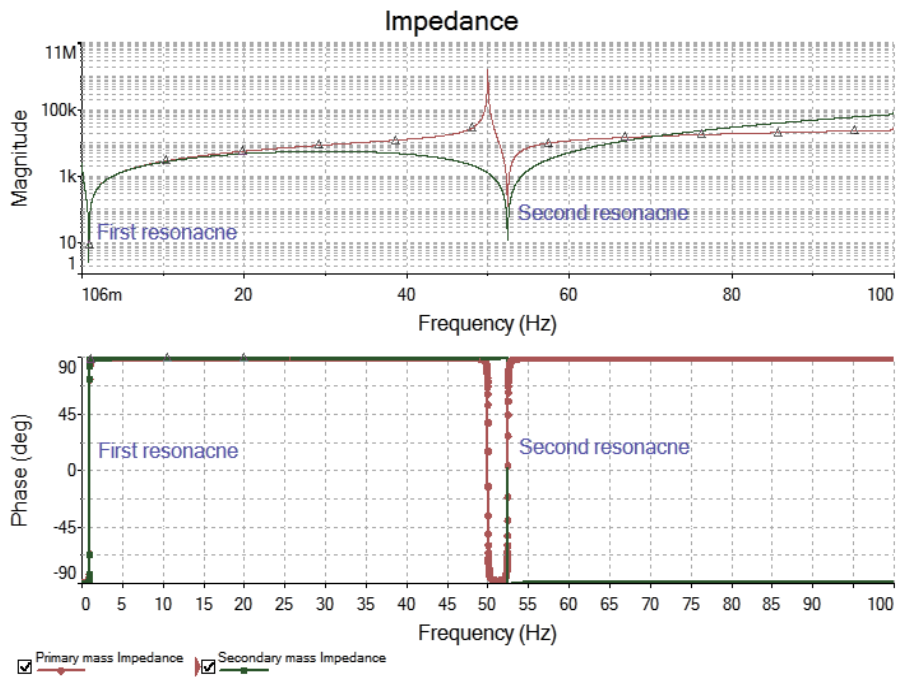


Figure 4-11 Impedance

The graphs of Figure 4-11 show the analogous electrical impedance of the above 2DOF mechanical system simulated with an electrical software kit. The combined system exhibits two resonant peaks at 1Hz and 54Hz respectively. At resonance, the current (velocity) and the voltage (force) are in phase. The electrical current is limited by the resistance (damping) in the system. The displacement of the primary system is approximately zero at 50Hz because the secondary system is tuned at 50Hz.

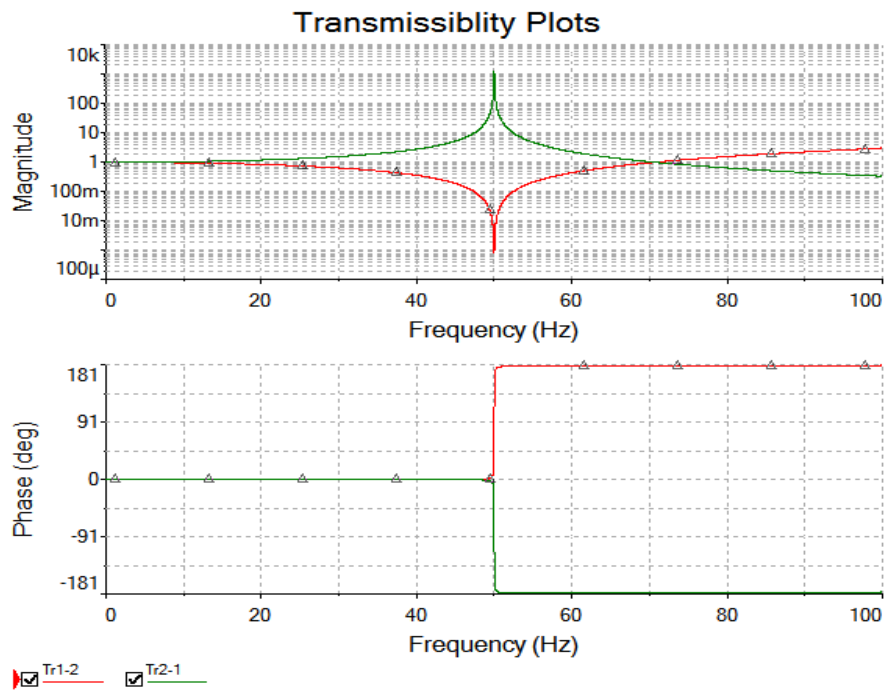


Figure 4-12 Transmissibility

In Figure 4-12, the graphs indicate that at 50Hz, the supplied energy is transferred to the secondary mass completely and the primary mass is motionless at this frequency.

## 5 The FPSE/LA Analysis: Modelling, Simulation, and Validation

### 5.1 Modeling

A Stirling engine is a complex machine and its behavioural description requires a multidisciplinary approach. An accurate FPSE/LA dynamic model involves a complex multiphysics problem that couples thermodynamics, electromagnetism and mechanics. However, this type of model could be cumbersome to handle. Therefore, the use of simpler models is desired from a dynamic point of view. The following diagram shows a schematic of the proposed vibration model of the Stirling engine under study.

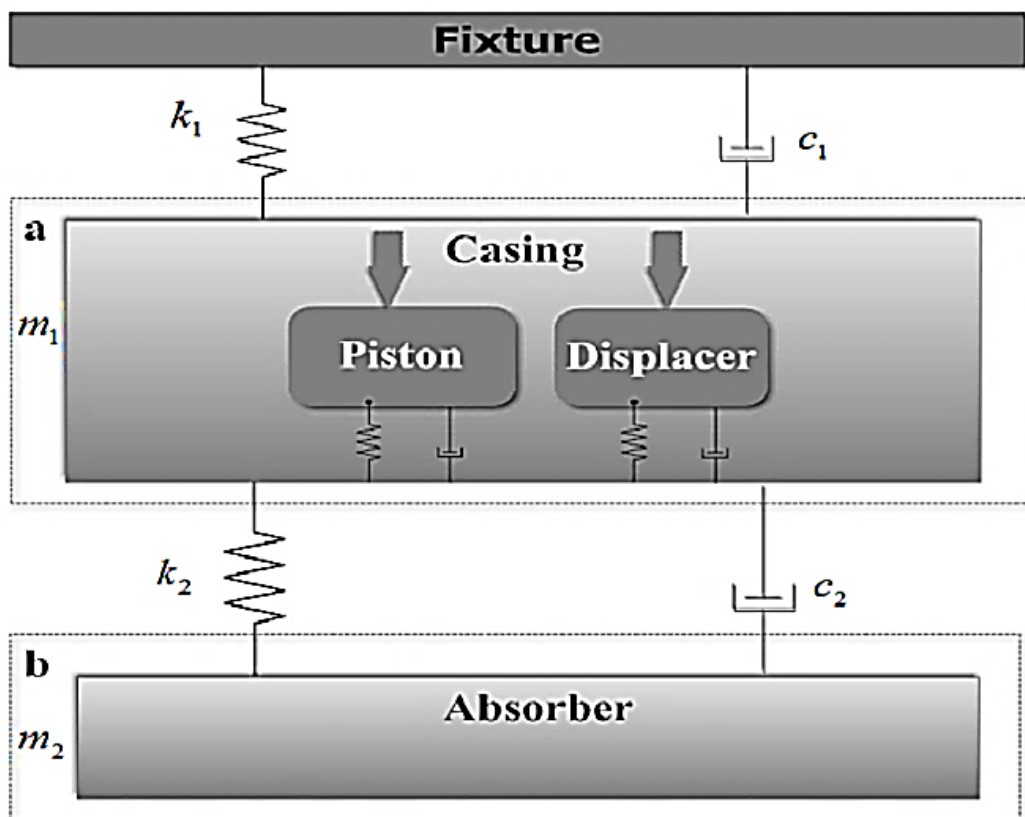


Figure 5-1 Dynamic model of the  $\beta$ -type Stirling engine showing a casing

The subsystem (a) of Figure 5-1 represents the casing of the Stirling engine which forms the main system that contains a displacer and a piston modeled as spring-mass-damper system. Subsystem (b) represents that of the TMD. The piston and the displacer move approximately

90° out of phase. When the gas inside the engine is heated, the displacer moves it from the hot end to the cool end creating a pressure wave that exerts on the piston. The displacer movement is maintained at 50Hz via tuned spring connections. The power piston is fitted with magnets that move past the alternator and cause vibration to the engine case. Since the piston motion causes the vibration of the engine case at 50Hz, and the mass of the displacer is neglected with comparison to the piston plus the engine case mass, the internal dynamics between the piston and displacer are deemed unnecessary.

By neglecting the internal dynamics of the piston and the displacer and by assuming that the piston movement is causing a sinusoidal excitation in the casing, a vibration model of the Stirling engine system is proposed by approximating it as a 2DOF system. The mass  $m_1$   $m_1$  is connected through a damping element of coefficient  $c_1$  and spring of stiffness  $k_1$  to a fixed ground on one end and to a passive absorber via another spring of stiffness  $k_2$  and another damping element of coefficient  $c_2$  on the other end. The equations of motion that describe the system are expressed in a state-space model as follows

$$\begin{aligned} \dot{\mathbf{x}} &= \mathbf{Ax} + \mathbf{Bu} \\ \mathbf{y} &= \mathbf{Cx} + \mathbf{Du} \end{aligned}$$

$$\begin{bmatrix} \dot{x}_1 \\ \dot{x}_2 \\ \dot{x}_3 \\ \dot{x}_4 \end{bmatrix} = \begin{bmatrix} 0 & 0 & 1 & 0 \\ 0 & 0 & 0 & 1 \\ \frac{-(k_1 + k_2)}{m_1} & \frac{k_2}{m_1} & \frac{-(c_1 + c_2)}{m_1} & \frac{c_2}{m_1} \\ \frac{k_2}{m_2} & \frac{-k_2}{m_2} & \frac{c_2}{m_2} & \frac{-c_2}{m_2} \end{bmatrix} \begin{bmatrix} x_1 \\ x_2 \\ x_3 \\ x_4 \end{bmatrix} + \begin{bmatrix} 0 \\ 0 \\ 1 \\ 0 \end{bmatrix} F(t) \quad 5-1$$

$$\begin{bmatrix} y_1 \\ y_2 \\ y_3 \\ y_4 \end{bmatrix} = \begin{bmatrix} 1 & 0 & 0 & 0 \\ 0 & 1 & 0 & 0 \\ 0 & 0 & 1 & 0 \\ 0 & 0 & 0 & 1 \end{bmatrix} \begin{bmatrix} x_1 \\ x_2 \\ x_3 \\ x_4 \end{bmatrix} + \begin{bmatrix} 0 \\ 0 \\ 0 \\ 0 \end{bmatrix} F(t)$$

The state variables  $x_1, x_2, x_3$  and  $x_4$   $x_1, x_2, x_3, \text{ and } x_4$  represent the engine case and TMD's displacements and velocities respectively. The engineering data of this particular engine are obtained from the manufacturer. For the purpose of analysing the system theoretically, it is assumed that a sinusoidal excitation force  $F(t)$  of magnitude 1000N with nominal frequency

of 50Hz acts on the engine case. The magnitude of the excitation force can be obtained by measuring the absorber displacement amplitude when the engine is harmonically excited at 50Hz. The passive TMD is tuned to minimise the vibration of the engine case at the nominal excitation frequency, hence at this frequency, the excitation from the engine is transferred totally to the absorber. The TMD displacement corresponding to 1000N excitation is around 1.15mm at 50Hz.

## 5.2 Simulation

Table 5-1 contains the engine's dynamic information that used for simulation. The data are obtained from Microgen Engine Corporation (MEC), the engine manufacturer. The value of  $c_2$  is assumed to be zero in this the simulation and is identified later in the validation section.

Table 5-1 Engine Manufacturer's Data

Engine Parameters
$m_1 = 41.38 [kg]$
$m_2 = 8.862 [kg]$
$c_1 = 200 [Ns/m]$
$c_2 = 0 [Ns/m]$
$k_1 = 8369.4 [N/m]$
$k_2 = 874640 [N/m]$
$F(t) = 1000 \sin 100\pi t [N]$

The plots below show the theoretical frequency response from the excitation force to the engine case motion and the absorber mass motion respectively.

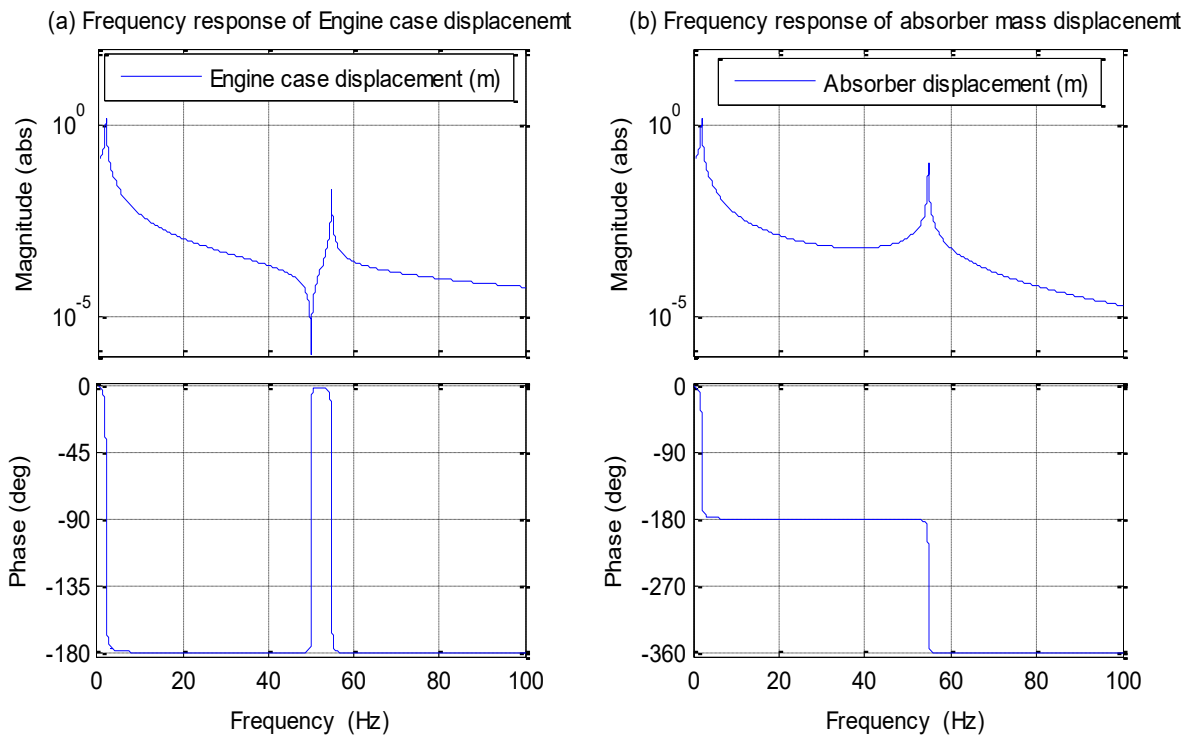


Figure 5-2 Frequency response from excitation force to engine case and absorber displacements

According to the theoretical analysis covered in section 3, a 2DOF system exhibits two resonant modes. For the given engine parameters, the two resonant frequencies occur at approximately 2Hz and 54.8Hz. The curves in Figure 5-2 show two peak values corresponding to the natural resonance of the combined system. In Figure 5-2 (a), the dip at 50Hz is associated with the operation of the TMD that is tuned to resonate naturally at 50Hz or the “anti-resonant” frequency as far as the engine case is concerned. By examining the phase plot of the absorber mass and engine case, it can be seen that both masses are in phase with the excitation force for excitation frequency below 2Hz. At 2Hz, the first resonance occurs causing both the engine case and the absorber mass to become  $90^0$  out of phase with respect to the excitation force at resonance. After the first resonance, both of the masses switch to  $180^0$  out of phase behind the excitation force until the natural resonance of the TMD at 50Hz.

At 50Hz, the engine case switches back to  $90^0$  out of phase with the excitation force and the TMD remains  $180^0$  out of phase with respect to the excitation force. As a result, at the

nominal operation of the engine at 50Hz, the TMD will be  $90^{\circ}$  out of phase with respect to the engine case, thus counteracting its vibration. For frequencies beyond 50Hz, the engine case becomes in phase with excitation and the TMD continues  $180^{\circ}$  out of phase with respect to excitation. The second resonance of the combined system occurs at 54.8 Hz where beyond, the engine case phase switches from  $0^{\circ}$  to  $180^{\circ}$  again behind the excitation force. After that point, the TMD becomes in phase with excitation and  $180^{\circ}$  out of phase with respect to the engine case. Although after the second resonance the engine case and the absorber are  $180^{\circ}$  out of phase. It is observed that the maximum attenuation of the engine case vibration occurs at 50 Hz only despite being  $180^{\circ}$  out of phase with the TMD after 54.8Hz.

Now examining the engine and TMD functionality, since the nominal operating frequency range of the  $\beta$ -type Stirling engine is 50Hz the first peak can be neglected as it only affects the engine on start-up and shut-down for a very small period of time and at low frequency. In fact, the higher risk exists around the second peak which is very close to the nominal operating range. According to the results, if the frequency fluctuates above 50Hz, the vibration of the composite system grows to large magnitudes because the absorber becomes less efficient. According to MEC's specification, the max allowed displacement of the engine case is  $20\mu\text{m}$  at 50Hz (Microgen Engine Corporation, 2016). For an optimal design of the absorber parameters, Den Hartog (Den Hartog, 1985) states that those parameters can be calculated based on finding an optimal frequency and damping ratios. It can be argued that a larger damping coefficient  $c_2$  of the TMD system is capable of broadening the bandwidth of operation of the TMD however there is a trade-off between damping and attenuation. That is to say, a higher damping in the TMD yields less attenuation on the primary mass at the tuned frequency of the TMD. Higher damping may be more desired in the design of vibration isolators however it doesn't serve the purpose of the TMD in this application.

### 5.3 Electromagnetic Shaker V721 Characterisation

In order to perform the tests on the engine absorber, an electromagnetic shaker was used to provide a sinusoidal swept profile. This type of signal excitation is appropriate for testing the TMD at hand thus it is important to understand the dynamics of the electromagnetic shaker in use. Therefore, this section considers the mathematical modeling of the V721 shaker dynamics shown in Figure 5-3.



Figure 5-3 Photo of the electromagnetic shaker used in the experiment (Bruel & Kjaer)

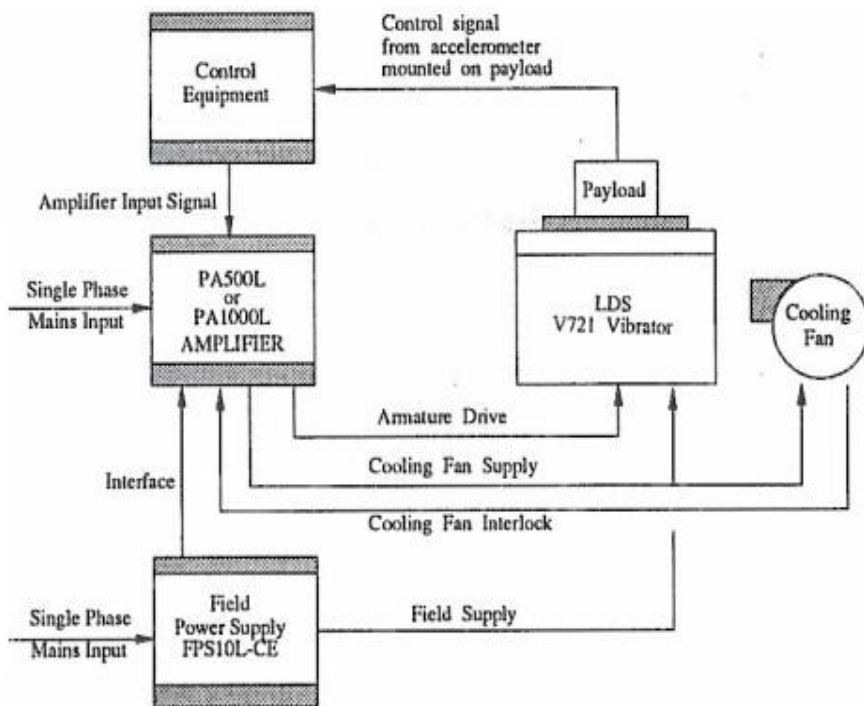


Figure 5-4 V721 series vibrator with PA1000L amplifier and FPS10L field power supply (Bruel & Kjaer)

Figure 5-4 depicts a schematic of the V721 power-up connections. The V721 LDS shaker system consists of an electromagnet that produces a magnetic flux density normal to the gap and of an armature coil that is free to move axially within the gap. It has a field power supply that supplies current to the electromagnet to create a magnetic field. A power amplifier is also connected to provide current to the armature coil. By ignoring the electromagnetic dynamics, the electromagnetic shaker may be modeled as an SDOF system comprising a spring, a mass, and a damper. According to Lorentz law, the force acting on the moving armature coil  $f$ , is equivalent to the product between the shaker motor constant  $k_{sha}$  and the current delivered by amplifier  $i$ .

In order to derive a mathematical model of the electrodynamic shaker, a model is proposed based on an SDOF system depicted in Figure 5-5. Originally, the shaker table mass and axial stiffness are known from the product data sheet. In addition to that, data obtained from tests done by the manufacturer are also used.

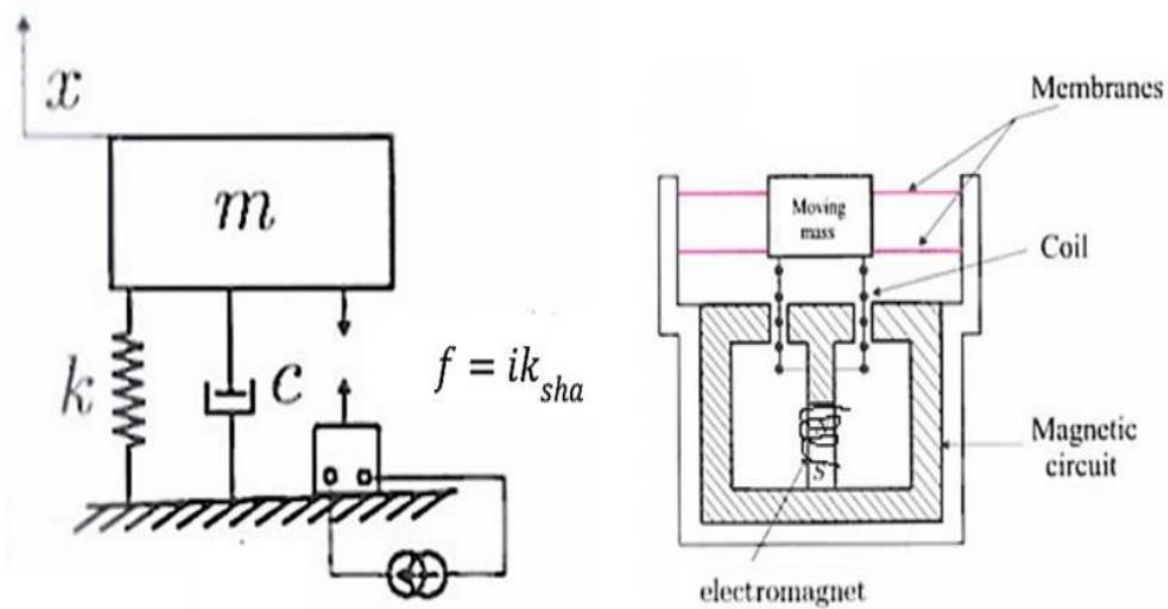


Figure 5-5 Schematic of the design of an electrodynamic actuator (Preumont, 2012)

By applying Newton's second law of motion, the equations of motion can be written down and the Laplace domain transfer functions that describe the states of the system can be derived as follows

$$m\ddot{x} + c\dot{x} + kx = k_{sha}i = f \quad 5-2$$

Where  $\ddot{x}$ ,  $\dot{x}$ , and  $x$  represent the acceleration, velocity and displacement of the shaker moving mass. In the Laplace domain, the displacement, velocity, and acceleration of the armature mass  $m$  can be written as

$$X(s) = \frac{k_{sha}I(s)}{ms^2 + cs + k}$$

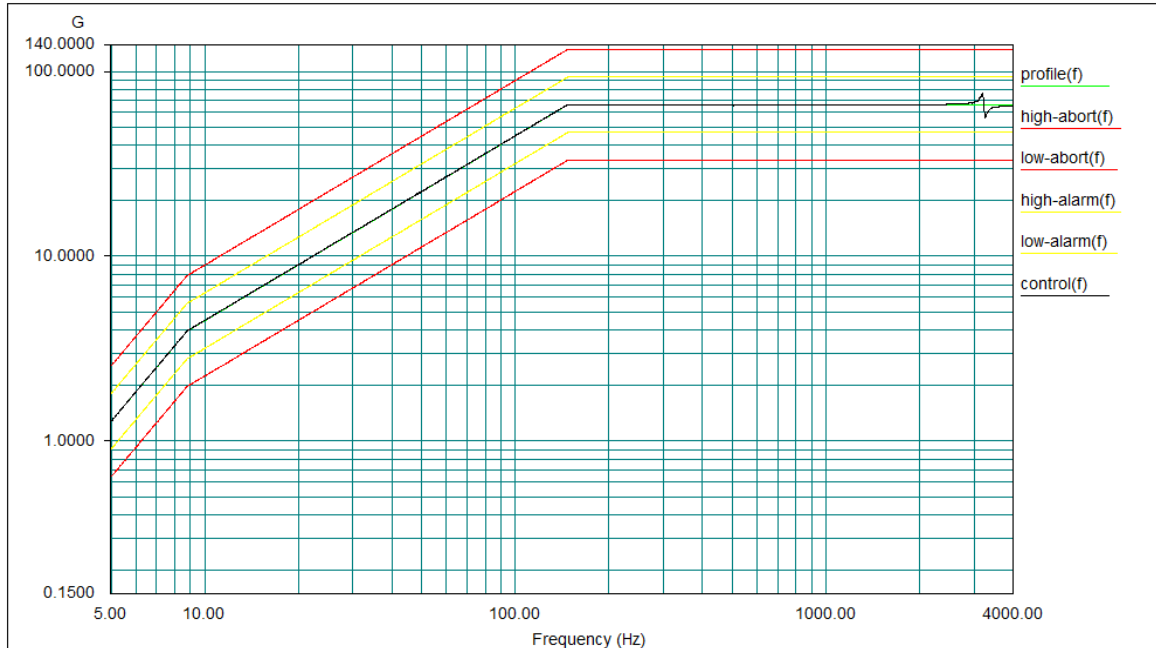
$$V(s) = sX(s) = s \frac{k_{sha}I(s)}{ms^2 + cs + k} \quad 5-3$$

$$A(s) = s^2X(s) = s^2 \frac{k_{sha}I(s)}{ms^2 + cs + k}$$

The term  $k_{sha}$  represents the shaker motor constant measured in Newton per Amp ( $N/A$ ) and  $i$  represents the electrical current flowing in the armature coil measured in Amps (A). Once the model parameters are identified, the model of the shaker can be integrated within the model of TMD once attached to it. The aim of performing system identification is to understand the behaviour and propose a model of the dynamic shaker so it can be integrated within the model of another system attached to it. The system identification is done based on reverse fitting of the proposed model parameter so that the theoretical simulation results of the resulting model match with the obtained experimental results. The experimental data are obtained by running the shaker in open loop and measuring the acceleration and current of the shaker table to the armature current. The graphs below show the armature drive current frequency response for a sweep type between 5Hz-4000Hz as per Bruel & Kjaer for the V721 series vibrator. The results show that the current varies as the frequency changes which implies that the force acting on the armature moving mass is not constant.

V721 PA1000L CE  
10004/1

Project File Name: BARE TABLE CAPABILITY.pj  
Profile Name: BARE TABLE CAPABILITY 25.4mm/0.7m/s/66g 5-4000Hz Test Type: Swept Sine Run Folder: \Run1



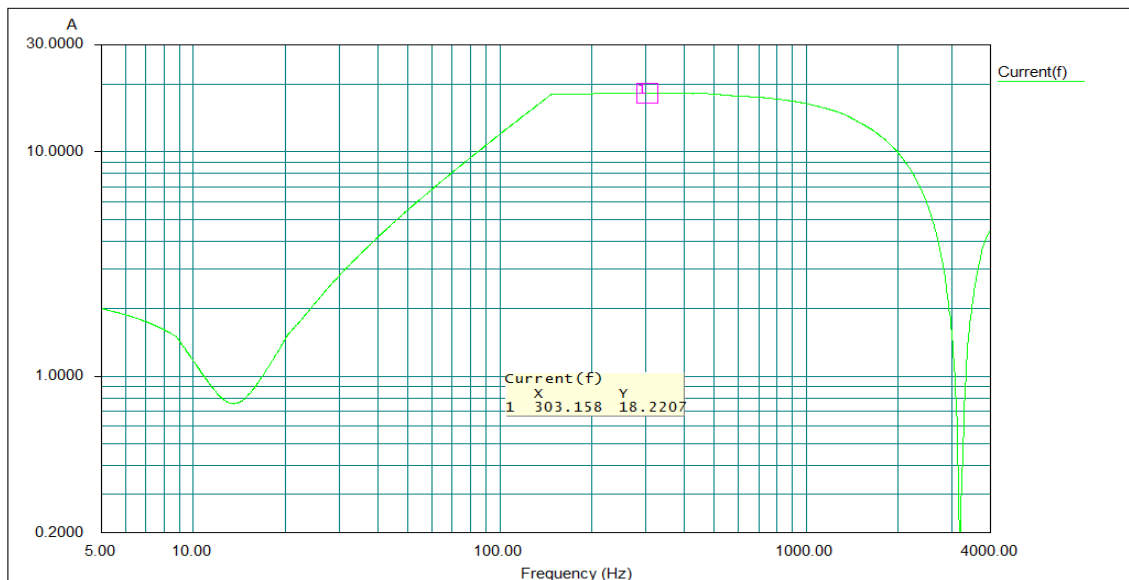
Level: 0 dB Control Peak: 65.483551 G Full Level Time: 00:09:39 Sweep Type: Logarithmic  
Frequency: 3999.800293 Hz Demand Peak: 65.955238 G Time Remaining: 00:00:00 Sweep Rate: 1 Oct/Min

Data saved at 04:57:32 PM, Monday, January 30, Report created at 04:57:33 PM, Monday, January 30, 2006

Figure 5-6 V721 LDS shaker operating range (Bruel & Kjaer)

V721 PA1000L CE  
10004/1

Project File Name: BARE TABLE CAPABILITY.pj  
Profile Name: BARE TABLE CAPABILITY 25.4mm/0.7m/s/66g 5-4000Hz Test Type: Swept Sine Run Folder: \Run1



Level: 0 dB Control Peak: 65.483551 G Full Level Time: 00:09:39 Sweep Type: Logarithmic  
Frequency: 3999.800293 Hz Demand Peak: 65.955238 G Time Remaining: 00:00:00 Sweep Rate: 1 Oct/Min

Data saved at 04:57:31 PM, Monday, January 30, 2006 Report created at 04:57:33 PM, Monday, January 30, 2006

Figure 5-7 V721 Shaker current frequency response for a swept sine (Bruel & Kjaer)

The graphs of Figure 5-6 show the operating range for controlling the shaker with respect to frequency. It is shown that at low frequencies up to 9Hz, a position control is applied to maintain displacement amplitude of 25.4mm. At frequencies from 9Hz up to approximately 150Hz, velocity control is applied to maintain a velocity of 0.7m/s. For frequencies that are higher than 150Hz, acceleration control is applied to maintain an acceleration of 66g. The graph in Figure 5-7 shows the frequency response of the shaker electrical current with position, velocity, and acceleration control between 5Hz - 4kHz. The knowledge of the values of the current and the input allows finding the parameters of the proposed SDOF model. The mass and stiffness of the armature moving mass can be extracted from the shaker's technical information sheet. The motor constant,  $k_{shaker}$ , and the damping coefficient,  $c$ , have to be chosen so that the response of the proposed model matches that of the electrical current in Figure 5-7. The estimated transfer functions representing the shaker system in the Laplace domain are listed below. Based on the previous, the proposed model was simulated and the transfer function parameters were reverse fitted to match the experimental data. The transfer functions of the shaker electrical current are determined for three discrete intervals as shown below

Control type	Transfer Function	Frequency Interval (Hz)
Shaker current to position $I(s) = \frac{ms^2 + cs + k}{k_{sha}}$	$\frac{4.41s^2 + 170s + 31500}{159}$	5 – 8.8
Shaker current to speed $I(s) = \frac{ms^2 + cs + k}{sk_{sha}}$	$\frac{4.41s^2 + 170s + 31500}{159s}$	8.8 – 150
Shaker current to acceleration $I(s) = \frac{ms^2 + cs + k}{s^2k_{sha}}$	$\frac{4.41s^2 + 170s + 31500}{159s^2}$	150 – 4000

The following graph shows the estimated model response of the electrical current in the armature after system identification.

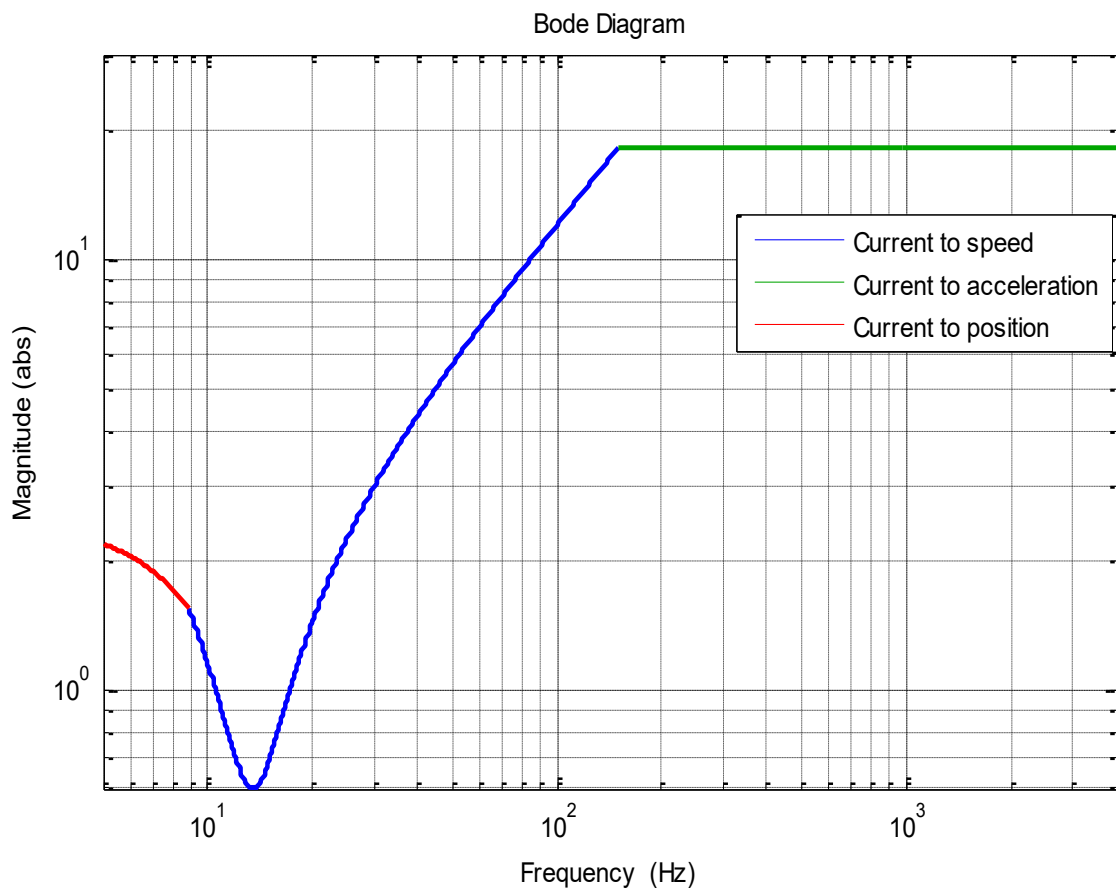


Figure 5-8 Frequency response of the electrical current for the proposed VDS721 shaker model

The current curve of Figure 5-8 shows a dip at 13.5Hz corresponding to the first resonant frequency of the shaker table. This matches the experimental results provided by the manufacturer in Figure 5-7. There exists a discrepancy between the graphs at 3 kHz where the experimental data shows a dip in the current corresponding to a resonance of the shaker table which doesn't exist in the simulation results of the proposed model. This difference is related to the existence of some dynamics not incorporated in the proposed model. These dynamics can occur due to further resonant mode at this frequency. At this stage, the modeling of these dynamics will not be considered and we will suffice with the operating range up to 1 kHz.

## 5.4 Validation

For the absorber, an electromagnetic shaker is used to shake the absorber and the data were recorded using acceleration sensors. For the engine, acceleration data of the engine were collected from a test performed at the company site.



Figure 5-9(a)  $\beta$ -type Stirling engine, courtesy of Microgen Engine Corporation (MEC) and (b) Rig of the TMD Test 1 setup for the engine model validation is shown in Figure 5-9 (a). The engine case  $m_1$  is fixed to the wall via four springs and four rubber dampers that correspond to stiffness  $k_1$  and damping coefficient  $c_1$ . The absorber is mounted internally to the engine with dynamic mass that correspond to  $m_2$ . The absorber features an additional mass comprising the holding rings and part of the springs that contribute to the mass  $m_1$ . An inverter is used to excite the engine with a sinusoidal excitation and varying frequency between 49-51 Hz. The model presented in section 5.1 is used for the comparison between the theoretical and experimental data.

Vibration Data were collected and averaged from four MEMS accelerometers with dynamic range  $\pm 2g$ , bandwidth 1 kHz and sensitivity of 350mv/g placed in four different locations to detect the vertical vibration.

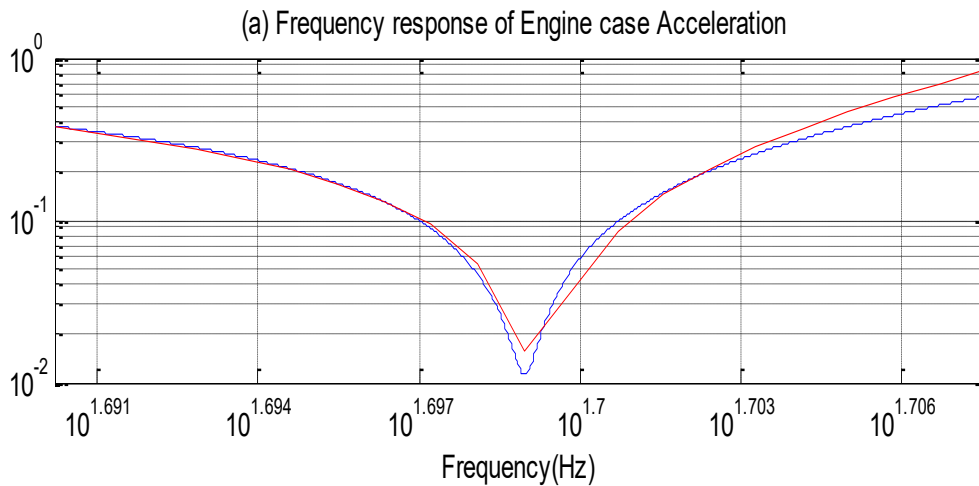


Figure 5-10 Theoretical simulation and experimental validation of the engine

The theoretical and experimental results of the engine case acceleration are shown in Figure 5-10. It is revealed that the engine case acceleration is attenuated at 50Hz due to the resonance of the TMD. After 50Hz the amplitudes of the acceleration grow larger due to the second resonance of the combined system. There appears to be a difference between both sets of data as the experimental acceleration grows larger than the theoretical one after 50Hz. The cause of this difference is attributed to the excitation force amplitude which is assumed to be around 1000N in theory however in reality the magnitude of this force varies depending on frequency and loading of the engine.

Test 2 setup for the TMD is shown in Figure 5-9 (b). In this test, the absorber was separated from the engine and then mounted vertically on an electrodynamic shaker V721 series from Bruel & Kjaer. The shaker is controlled with an LDS USB vibration controller. Acceleration data from the dynamic mass of the absorber and the shaker table were collected from two accelerometers of 100 mv/g sensitivity and 70g max dynamic range interfaced with the 24-bit input stage of the vibration controller. This test was performed using a sinusoidal profile between 40Hz to 80Hz in open loop. Generally a closed loop test is used to maintain a reference position, speed or acceleration of the shaker table. In this case, an open loop is used because the vibration of the shake table will be damped by the absorber at its tuning

frequency. Originally the absorber is designed with minimal damping however a small amount of frictional damping is expected due the existence of internal guiding rods. Since the value of the damping coefficient of the absorber mass is not known beforehand, a reverse fitting technique is used to align the theoretical simulation results of the absorber model with the real test results obtained in this experiment. The schematic in Figure 5-11 represents the model of the absorber validation test.

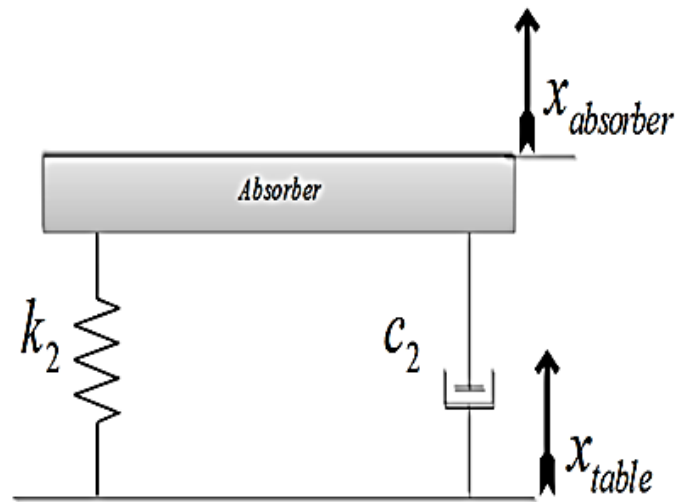


Figure 5-11 Schematic model of the absorber test

The idea is to measure the acceleration of both the absorber dynamic mass and shaker table then plot the transmissibility from the shaker to the absorber. The theoretical transmissibility is expressed in the following equation according to the above model

$$TR(s) = \frac{A(s)_{absorber}}{A(s)_{shakertable}} = \frac{s^2 X(s)_{absorber}}{s^2 X(s)_{shakertable}} = \frac{c_2 s + k_2}{m_2 s^2 + c_2 s + k_2} \quad 5-4$$

The test results are plotted against the simulation results and then the graphs are aligned by changing the value of  $c_2$  accordingly.

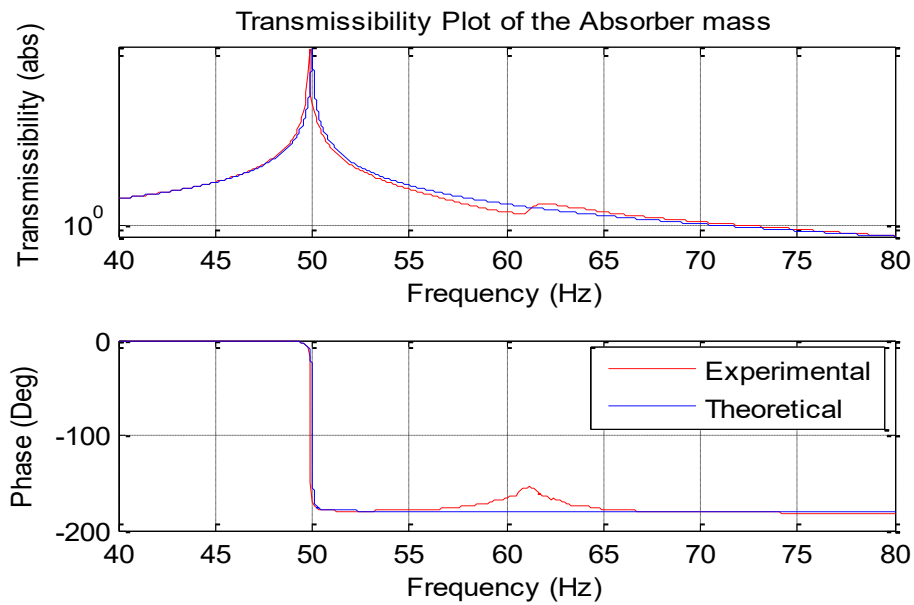


Figure 5-12 Theoretical Vs. Experimental data of the absorber transmissibility. The value of  $c_2 = 2.7 \text{ Ns/m}$  is determined by reverse fitting of the theoretical data with the experimental data

The real response of the absorber shows some dynamics around 63 Hz which didn't exist in simulation. The root cause of this discrepancy is linked to the second resonance of the combined system consisting of shaker table mass and the absorber mass which was not part of the simulated model. The value of damping in the absorber system is determined as  $c_2 = 2.7 \text{ Nm/s}$ .

## 6 Active Control System Design and Simulation

### 6.1 Active Tuned Mass Damper (ATMD)

An active mass damper (ATMD) system is a versatile system that uses an additional forcing function on an auxiliary mass to perform a broad range of disturbance attenuation by feedforward, feedback or a hybrid form of control (Pare, 1999). In the case where the external disturbances can be assessed reliably, gain scheduling control with zero placement feedback can provide a more effective disturbance rejection for the ATMD (Anthony and Elliott, 2000). In here, the control of an ATMD is explained thoroughly with emphasis on the 2DOF model of the Stirling engine. A generic actuator is assumed to be located between the two masses providing a generic force  $f(t)$  as shown in the figure below.

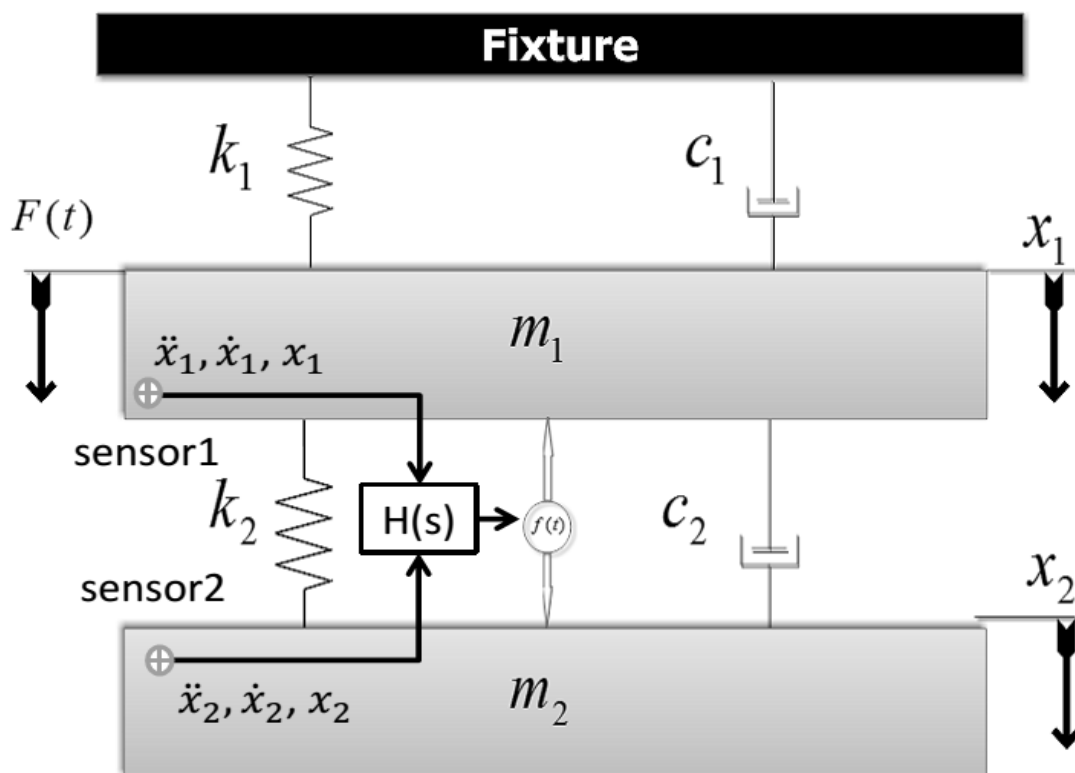


Figure 6-1 ATMD with a 2-DOF system

The physical arrangement of the system is illustrated in Figure 6-1. The main mass  $m_1$  is subjected to a sinusoidal excitation force  $F(t)$ . The actuator provides a force  $f(t)$  that is

proportional to the control signal. Any inherent stiffness or damping associated with the actuator can be added in with that of the TMD before the control is applied. Ideally, three separate sensors will be used to measure the acceleration, velocity, and displacement. In practice it depends on the type of control strategy; often a single transducer is available to measure the acceleration then analog or digital integrators are employed to derive signals proportional to velocity and displacement depending on the type of the controller. The following discusses the proposed control strategies for the active control of the vibration problem in the Stirling engine with the aid of the validated models presented in the previous section.

## 6.2 Gain Scheduling with Zero-Placement Feedback Control

In this technique, the actuator control force is achieved based on two sets of information

1. Prior knowledge of the excitation frequency input to the controller.
2. Measured response of the system: Relative or Absolute.

The following figure provides an overview of the concept of operation in this control strategy

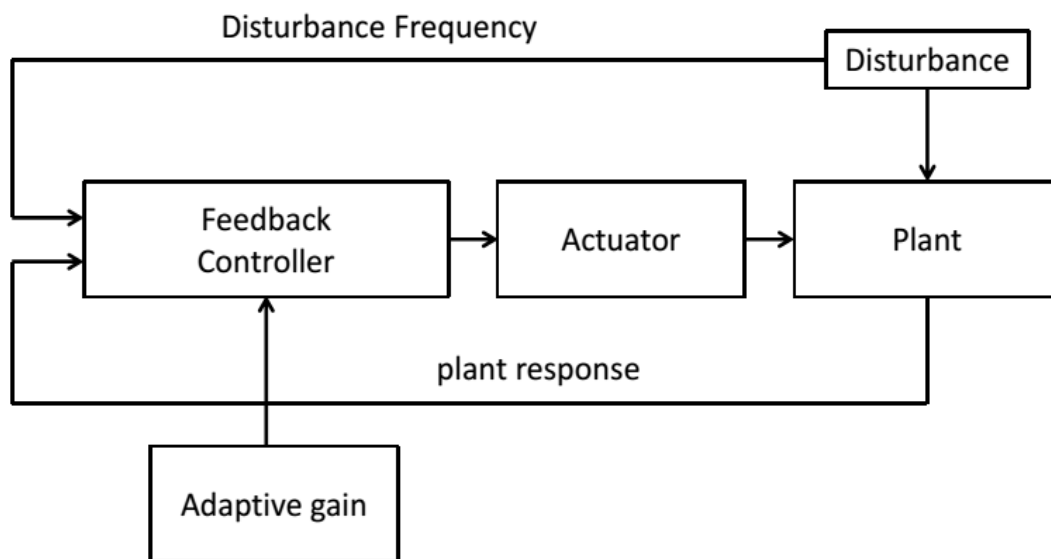


Figure 6-2 Operation principle of the proposed control strategy

The plant response holds dynamic data about the system such as acceleration, velocity, and displacement. Data are measured by employing appropriate sensors such as vibration accelerometers. For this application, relative and absolute measurements are considered for analysis. In this type of control, the automation of the control strategy can be achieved by providing a prior knowledge of changes in the excitation frequency without the need of an accurate model for the entire system. The Stirling engine is connected to the national grid in its normal operation hence it follows the grid frequency which can be measured and used as input to the control system.

### 6.2.1 Relative Measurement Feedback

The working principle of this control strategy is based on re-tuning of the ATMD so its natural resonant frequency tracks that of the excitation one. The equations of motion of the system in Figure 6-1 with the insertion of the actuator force  $f(t)$  is derived as follows

$$\begin{aligned} m_1\ddot{x}_1 + k_1x_1 + c_1\dot{x}_1 + k_2(x_1 - x_2) + c_2(\dot{x}_1 - \dot{x}_2) &= F(t) - f(t) \\ m_2\ddot{x}_2 + k_2(x_2 - x_1) + c_2(\dot{x}_2 - \dot{x}_1) &= f(t) \end{aligned} \quad 6-1$$

Assuming that a set of sensors is available to provide data about the response of the system, the actuator may then deliver a force that is associated with the feedback of the system response. Therefore, the actuator force  $f(t)$  may take the following generic form (Marques et al., 2001)

$$f(t) = [\alpha(\ddot{x}_1 - \ddot{x}_2) + \beta(\dot{x}_1 - \dot{x}_2) + \gamma(x_1 - x_2)] \quad 6-2$$

The terms  $\alpha$ ,  $\beta$ , and  $\gamma$  represent the acceleration, velocity, and displacement feedback gains respectively. By associating equation 6-2 in equation 6-1, the system with control incorporated may be expressed as follows

$$\begin{aligned} \begin{bmatrix} m_1 + \alpha & 0 \\ 0 & m_2 + \alpha \end{bmatrix} \begin{bmatrix} \ddot{x}_1 \\ \ddot{x}_2 \end{bmatrix} + \begin{bmatrix} c_1 + c_2 + \beta & -c_2 + \beta \\ -c_2 + \beta & c_2 + \beta \end{bmatrix} \begin{bmatrix} \dot{x}_1 \\ \dot{x}_2 \end{bmatrix} \\ + \begin{bmatrix} k_1 + k_2 + \gamma & -k_2 + \gamma \\ -k_2 + \gamma & k_2 + \gamma \end{bmatrix} \begin{bmatrix} x_1 \\ x_2 \end{bmatrix} &= \begin{bmatrix} F \\ 0 \end{bmatrix} \end{aligned} \quad 6-3$$

Equation 6-4 represents the Laplace domain closed-loop transfer function that relates the primary mass displacement to the excitation force. It is obtained by model reduction of the MIMO system into a SISO one.

$$W(s) = \frac{X_1(s)}{F(s)} = \frac{(m_2 + \alpha)s^2 + (c_2 + \beta)s + (k_2 + \gamma)}{a_4s^4 + a_3s^3 + a_2s^2 + a_1s + a_0} \quad 6-4$$

$$a_4 = m_2\alpha + m_1(m_2 + \alpha)$$

$$a_3 = (m_1 + m_2)(c_2 + \beta) + c_1(m_2 + \alpha)$$

$$a_2 = k_1(m_2 + \alpha) + c_1(c_2 + \beta) + (k_2 + \gamma)(m_1 + m_2)$$

$$a_1 = c_1(k_2 + \gamma) + k_1(c_2 + \beta)$$

$$a_0 = k_1(k_2 + \gamma)$$

By observing equation 6-4, the gains  $\alpha$ ,  $\beta$ , and  $\gamma$  can be perceived as mass, damping, and stiffness variations. Assuming that the TMD system has no damping ( $c_2 = 0$ ), the math

shows that  $W(s)$  has a zero equal to  $\sqrt{-\frac{k_2+\gamma}{m_2+\alpha}}$ . It follows that it is possible to cancel the

harmonic vibration of the engine case by proper choice of the acceleration or displacement feedback gains. If the TMD inherently possesses damping, the damping coefficient term will appear in the numerator of  $W(s)$ . The original zero of  $W(s)$  will be the same if the feedback gain  $\beta$  is chosen to cancel the damping ( $c_2 + \beta = 0$ ). In fact, by substituting ( $s = j\omega$ ), the

zero of  $W(s)$  is called an antiresonant frequency  $\omega_2 = \sqrt{\frac{k_2+\gamma}{m_2+\alpha}}$ . The antiresonant frequency

$\omega_2$  is actually the tuned frequency of the TMD. Hence by proper choice of the gain  $\gamma$  or  $\alpha$  it is possible to alter the natural resonant frequency of the TMD. Based on the previous analysis, it can be generalized that for the above system, a feedback force associated with the relative displacement or acceleration of the two masses has the capability of altering the natural frequency of the TMD. If the feedback force is proportional to relative velocity, it cannot alter the tuned frequency of the absorber but only the quality factor of the TMD which

is directly proportional to the damping coefficient of the TMD. The formulae that relate the required gain  $\gamma$  and  $\alpha$  to produce a frequency shift to the absorber frequency ( $\omega_2$ ) so it tracks the excitation one  $\omega$  are shown in 6-5

$$\gamma = m_2(\omega^2 - \omega_2^2) \quad \alpha = m_2\left(\frac{\omega_2^2}{\omega^2} - 1\right) \quad 6-5$$

The following graphs show the required gain  $\alpha$  or  $\gamma$  in order to generate 5Hz shift on either side of the 50Hz for the Stirling engine. The determined gains are valid for the engine data provided in Table 5-1.

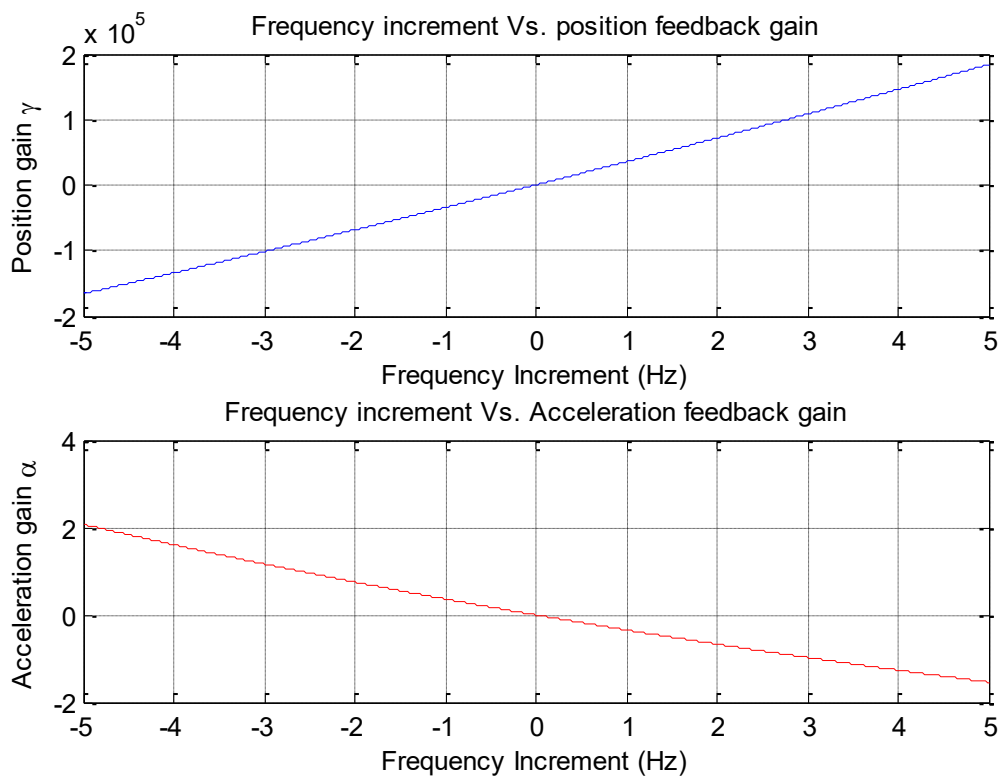


Figure 6-3 Required values of gains  $\gamma$  and  $\alpha$  to produce a frequency shift of 10 Hz bandwidth

### 6.2.2 Absolute Measurement Feedback

In this section it will be shown that the numerator of the transfer function  $W(s)$  doesn't change if absolute measurement of TMD response only is considered instead of relative measurement. This means that the zeros of  $W(s)$  will be the same and therefore it is still possible to cancel the vibration of the engine case by measurement of the TMD response

only. To prove that, let's assume that the actuator force takes the following shape in the absolute measurement configuration

$$f(t) = -[\alpha\ddot{x}_2 + \beta\dot{x}_2 + \gamma x_2] \quad 6-6$$

The transfer function  $W(s)$  is then

$$W(s) = \frac{X_1(s)}{F(s)} = \frac{(m_2 + \alpha)s^2 + (c_2 + \beta)s + (k_2 + \gamma)}{a_4s^4 + a_3s^3 + a_2s^2 + a_1s + a_0} \quad 6-7$$

Where

$$a_4 = m_1\alpha + m_1m_2$$

$$a_3 = c_2(m_1 + m_2) + c_1(m_2 + \alpha) + \beta m_1$$

$$a_2 = k_1(m_2 + \alpha) + c_1(c_2 + \beta) + k_2(m_1 + m_2) + \gamma m_1$$

$$a_1 = c_1(k_2 + \gamma) + k_1(c_2 + \beta)$$

$$a_0 = k_1(k_2 + \gamma)$$

In addition to providing a less complex solution, the use of absolute measurement of the system response allows controlling the system without the need of sensors to measure the response of the main mass. This is a much simpler and more cost effective, however in some cases the physical layout of the system allows for relative measurement. Despite the fact that absolute measurement is equally possible, in the following chapters the analysis will be carried out based on relative measurement.

### 6.2.3 Stability

Assuming that the original system without control is inherently stable, the stability of the system after adding the actuator force will be dependent upon the control force gains. . In order to study the stability of the integrated system with the control force, the Routh-Hurwitz criterion is applied to the characteristic equation of the transfer function  $W(s)$  for stability analysis (Ogata, 2010).

$$1. A = \frac{a_3 a_2 - a_4 a_1}{a_3} > 0$$

$$2. B = \frac{a_1 A - a_3 a_0}{A} > 0$$

The first condition yields

$$\alpha > \frac{-m_1 m_2}{m_1 + m_2} \quad \beta > -c_2 - \frac{c_1 m_2^2}{(m_1 + m_2)^2} \quad \gamma > -k_2 - \frac{k_1 m_2^2}{(m_1 + m_2)^2}$$

Since the parameters  $m_1$ ,  $m_2$ ,  $c_1$ ,  $c_2$ ,  $k_1$ ,  $k_2$  are all positive and  $m_1 > m_2$ , the inequalities of  $\alpha$ ,  $\beta$ , and  $\gamma$  can be simplified to obtain the following inequalities as presented by Marques (Marques et al., 2001)

$$\alpha > -m_2$$

$$\beta > -c_2$$

$$\gamma > -k_2$$

The second condition can be checked by associating the obtained inequalities of  $\alpha$ ,  $\beta$ , and  $\gamma$

$$A = k_2 m_2 > 0 \quad B = 0$$

Following the results obtained from the stability check, the actuator force gains must follow the inequalities displayed above for stability to be ensured. It was also found that the same inequalities obtained above guarantee stability when using absolute measurement feedback.

#### 6.2.4 Frequency Domain Simulation with Gain Scheduling and Zero-Placement Control

This section demonstrates the simulation results with the ATMD. The following table contains the values that are adopted for the primary system and the purely passive TMD.

Table 6-1 Model parameters

Parameter	Value	Unit
$m_1$	41.38	[kg]
$m_2$	8.862	[kg]
$c_1$	200	[Ns/m]
$c_2$	2.7	[Ns/m]
$k_1$	8369.4	[N/m]
$k_2$	87464	[N/m]
$F(t)$	1000 sin $\omega t$	[N]

The purely passive TMD is tuned at a natural frequency of  $\omega_2 = 100\pi \text{ rad/s}$  matching that of the nominal excitation. It was shown in section 4 that a purely undamped TMD is fully effective when the excitation matches its natural frequency leading to complete vibration suppression (when  $c_2 = 0 \text{ Ns/m}$ ). It was also observed that when the excitation frequency doesn't match that of the TMD, the vibration of the engine case exhibits larger amplitudes, particularly at the second resonant mode. By introducing an active element to convert the TMD into an ATMD controlled with relative displacement/Acceleration and velocity feedback, the idea is to determine the gains accordingly so that the ATMD frequency tracks that of the excitation. The ATMD with the zero-placement technique provides a relatively simple control in the sense that the gains are simpler to obtain and are tuned in real-time. For this, typical tuning procedure must include an automatic identification of the excitation frequency from the source. To illustrate the ATMD system with the Stirling engine, a SIMULINK model, whose block diagram is presented below, was built.

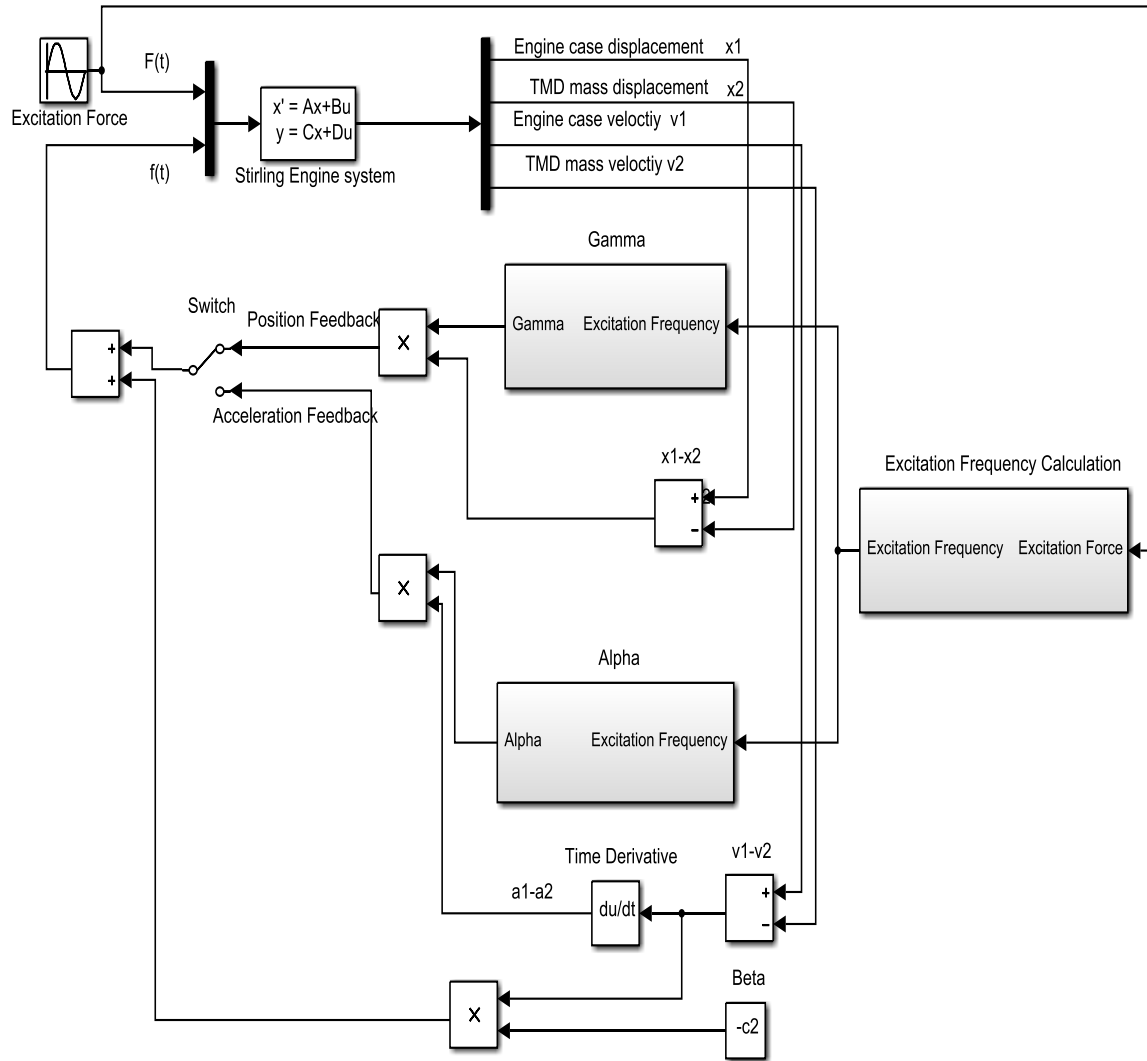


Figure 6-4 SIMULINK model used to simulate the control of the engine vibration with ATMD

In this model, the combined Engine and TMD are represented in a state-space form. The excitation frequency is varied from 45Hz to 55Hz in steps of 1Hz. Although the ATMD is capable to track any frequency, in here the simulation is performed with 11 excitation frequencies from 45Hz to 55Hz in steps of 1Hz. Assuming that the excitation frequency is not output from the readily made “Sine” Simulink Block, it is calculated based on the counting the number of zero crossings from the excitation source. The simulation results of the system presented in Figure 6-4 (or equation 6-4 with  $\alpha=0$ ) are plotted in the figures below for different values of feedback gains that alter the ATMD frequency accordingly.

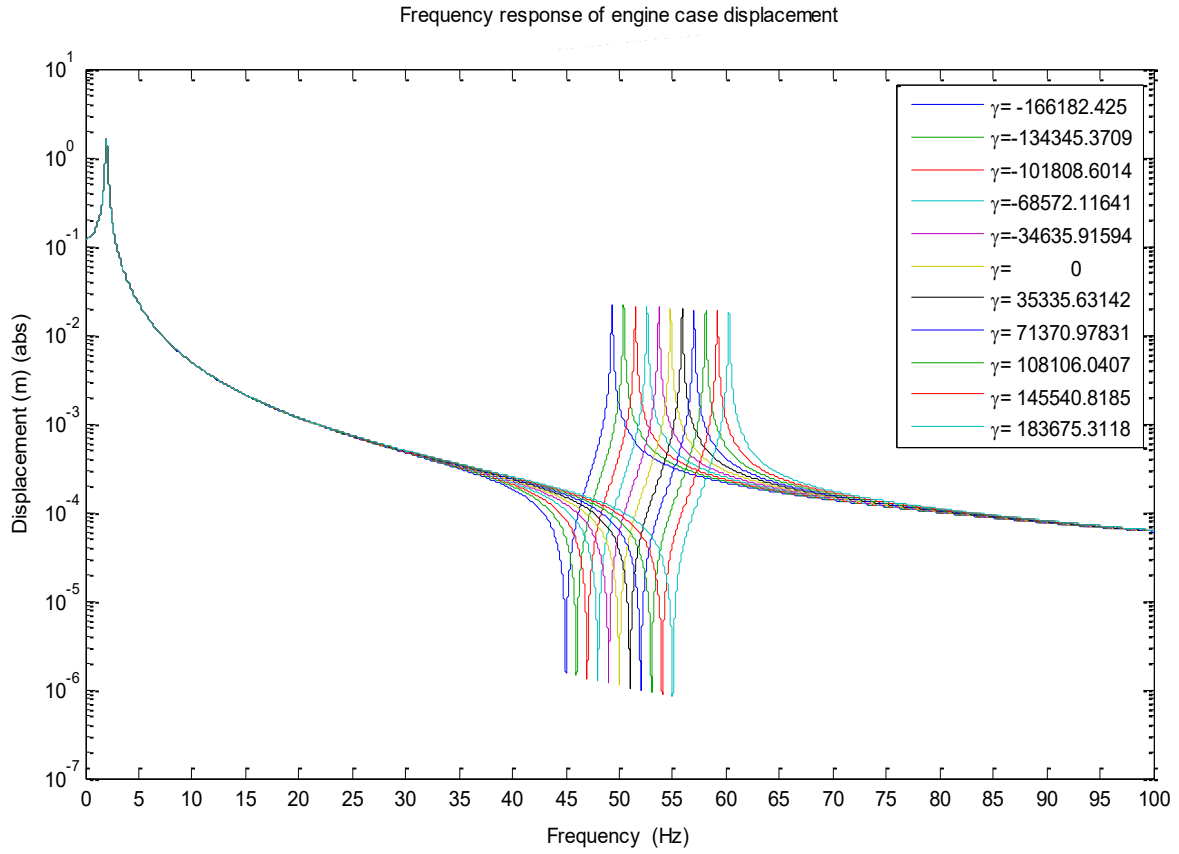


Figure 6-5 Frequency response from excitation force to primary mass displacement with  $\beta = 0$

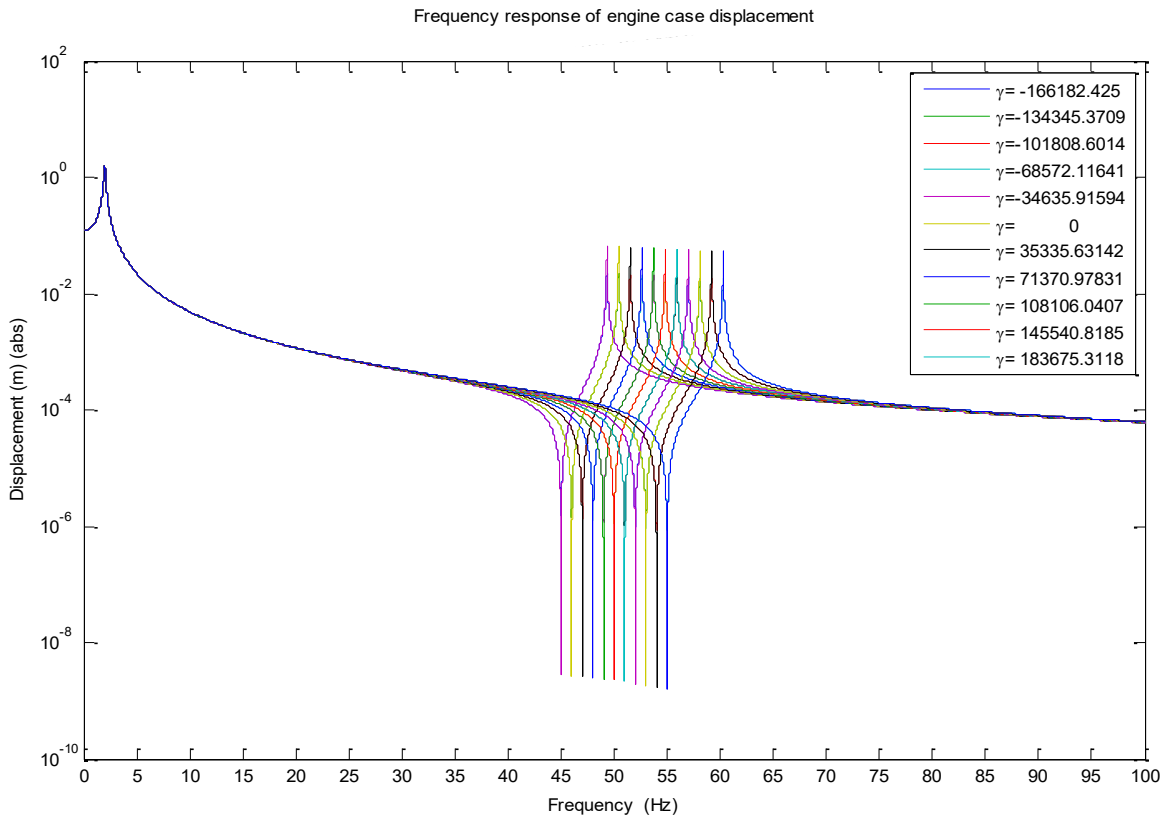


Figure 6-6 Frequency response from excitation force to primary system displacement with  $\beta = -c_2$

### 6.3 Discussion

The Bode plots in Figure 6-5 and Figure 6-6 represent the frequency response of the engine case displacement with the effect of relative position and velocity feedback gains on the ATMD for the cases when  $\beta = 0$  and  $\beta = -c_2$  respectively. Examining the first case, it has been observed that as the excitation frequency varies, the feedback gain  $\gamma$  is updated accordingly so the ATMD tracks the excitation frequency. According to the results, the ATMD does not only alter the resonant frequency of the passive TMD, but it also shifts the second resonant mode of the composite system. The first resonant mode that occurs at approximately 2Hz is not affected by the operation of the ATMD. Since the ATMD has damping of value  $c_2$ , a negative velocity feedback gain equal to  $-c_2$  is incorporated to achieve a better attenuation level as revealed in Figure 6-6. From a Frequency domain point of view, this technique succeeds in minimising the vibration of the engine for a wider frequency range.

### 6.4 Linear Quadratic Control

In this control technique, accurate knowledge of the system behaviour is crucial. The idea is to obtain an optimal gain in such a way that achieves the best performance of the system response at a minimal cost. It can be viewed as a technique that benefits from the available knowledge of the system dynamics to generate an optimal feedback gain multiplied with the system response. The following figure gives an overview of the working principle of this control technique.

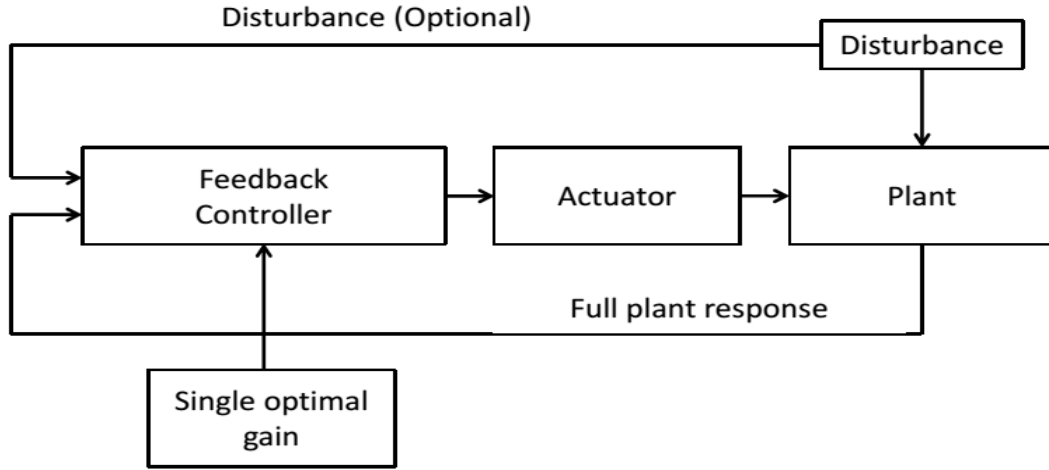


Figure 6-7 Operation principle of the LQ control

### 6.4.1 Full-state feedback

For the purpose of deriving the LQ control dynamics, the state space model can be defined as

$$\begin{aligned}
 \dot{\mathbf{x}} &= \mathbf{Ax} + \mathbf{Bu} \\
 \mathbf{y} &= \mathbf{Cx} + \mathbf{Du}
 \end{aligned}$$

$$\dot{\mathbf{x}} = \begin{bmatrix} 0 & 0 & 1 & 0 \\ 0 & 0 & 0 & 1 \\ \frac{-(k_1 + k_2)}{m_1} & \frac{k_2}{m_1} & \frac{-(c_1 + c_2)}{m_1} & \frac{c_2}{m_1} \\ \frac{k_2}{m_2} & \frac{-k_2}{m_2} & \frac{c_2}{m_2} & \frac{-c_2}{m_2} \end{bmatrix} \begin{bmatrix} x_1 \\ x_2 \\ x_3 \\ x_4 \end{bmatrix} + \begin{bmatrix} 0 & 0 \\ 0 & 0 \\ \frac{1}{m_1} & \frac{-1}{m_1} \\ 0 & \frac{1}{m_2} \end{bmatrix} \begin{bmatrix} F(t) \\ f(t) \end{bmatrix} \quad 6-8$$

$$\mathbf{y} = \begin{bmatrix} 1 & 0 & 0 & 0 \\ 0 & 1 & 0 & 0 \\ 0 & 0 & 1 & 0 \\ 0 & 0 & 0 & 1 \end{bmatrix} \begin{bmatrix} x_1 \\ x_2 \\ x_3 \\ x_4 \end{bmatrix}$$

The optimal control method achieves the optimal solution by calculating the feedback gains that result from the reduction of a cost function based on previous knowledge of the system (Preumont, 2012). The cost function is quadratic and it penalizes the states of the system. In other words, the feedback gains are optimized in order to achieve a control  $u(t)$  that minimizes the cost function expressed in equation 6-9

$$J = \int_0^{\infty} (\mathbf{x}^T \mathbf{Q} \mathbf{x} + \mathbf{u}^T \mathbf{R} \mathbf{u}) dt = \sum_{i=1}^n \sum_{j=1}^n \mathbf{Q}_{ij} x_i x_j + \sum_{i=1}^p \sum_{j=1}^p \mathbf{R}_{ij} u_i u_j \quad 6-9$$

The matrix  $\mathbf{Q}(n \times n)$  is the state penalty matrix and is positive semi-definite. The matrix  $\mathbf{R}(p \times p)$  is the control penalty matrix and it is a positive definite matrix. The quantity  $n$  represents the number of system states and the quantity  $p$  represents the inputs to the system. The scalar quantity  $\mathbf{x}^T \mathbf{Q} \mathbf{x}$  is quadratically related to the outputs of the system under control with  $\mathbf{x}$  a  $n \times 1$  vector. The scalar quantity  $\mathbf{u}^T \mathbf{R} \mathbf{u}$  is quadratically dependent on the control effort being input by the actuator with  $\mathbf{u}$  a  $p \times 1$  vector. Initially, a first choice for the matrix coefficients may be obtained based on Bryson's rule which estimates the coefficients of the LQ matrices as follows

$$Q_{ii} = \frac{1}{\max(x_i^2)} \quad R_{ii} = \frac{1}{\max(u_i^2)}$$

The steady state solution of the optimal problem that determines the required actuator force becomes

$$\mathbf{f}(t) = -\mathbf{K} \mathbf{x} \quad 6-10$$

The vector  $\mathbf{x}$  is a full state-feedback vector that has all the states and  $\mathbf{K}$  is a constant gain matrix determined by solving a non-linear Algebraic Riccati equation (ARE) as follows

$$\mathbf{K} = -\mathbf{R}^{-1} \mathbf{B}^T \mathbf{P} \quad 6-11$$

The matrix  $\mathbf{P}$  represents a solution obtained from the nonlinear Algebraic Riccati equation (ARE) expressed as

$$\mathbf{A}^T \mathbf{P} + \mathbf{P} \mathbf{A} - \mathbf{P} \mathbf{B} \mathbf{R}^{-1} \mathbf{B}^T \mathbf{P} + \mathbf{Q} = 0 \quad 6-12$$

The state-feedback control law results in a closed-loop system of the form

$$\begin{aligned} \dot{\mathbf{x}} &= \mathbf{A}_{cl} \mathbf{x} \\ \mathbf{y} &= \mathbf{C} \mathbf{x} + \mathbf{D} \mathbf{u} \end{aligned} \quad 6-13$$

A crucial property of the LQR controller design is the closed-loop system stability that is guaranteed when the eigenvalues of  $\mathbf{A}_{cl}$  have negative real parts. The controllability and observability matrices must have a full rank and are defined by

$$\mathbf{C}tl = [\mathbf{B} \mathbf{A} \mathbf{B} \mathbf{A}^2 \mathbf{B} \mathbf{A}^3 \mathbf{B} \mathbf{A}^{n-1} \mathbf{B}] \quad \mathbf{O}bv = [\mathbf{C} \mathbf{C} \mathbf{A} \mathbf{C} \mathbf{A}^2 \mathbf{C} \mathbf{A}^3 \mathbf{C} \mathbf{A}^{n-1}]^T$$

The following block diagram describes the state space model of the full-state feedback LQ control.

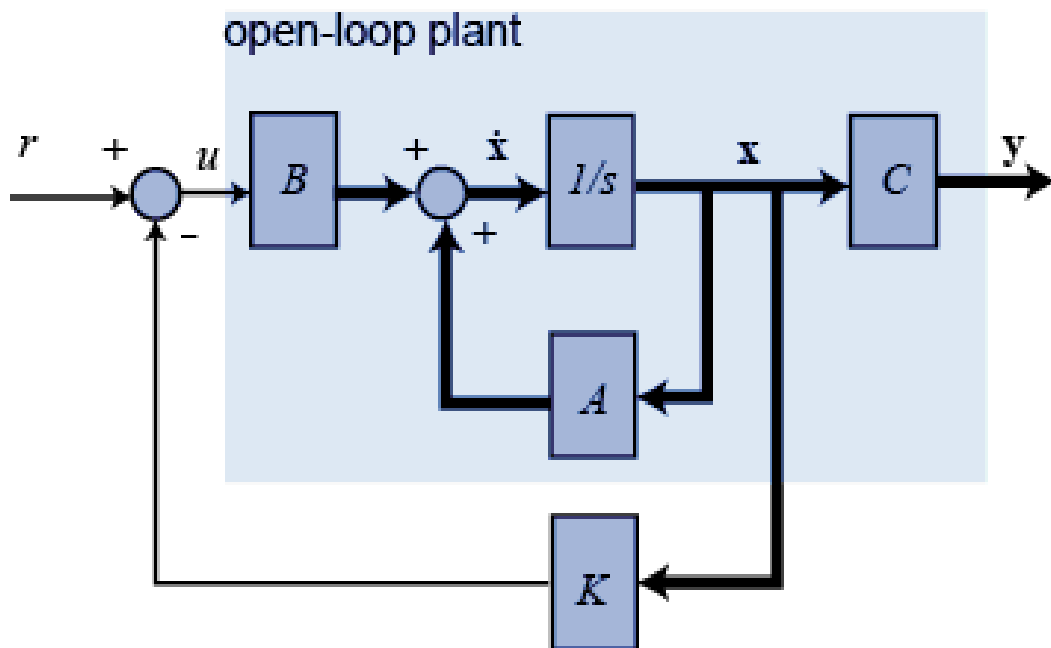


Figure 6-8 Schematic representation of LQ control state space system (Messner and Tilbury, )

#### 6.4.2 State Observer Design with LQ control (LQG)

The previous discussion is based on full-state feedback which assumes that all states can be measured. The minimization of equation 6-9 leads to an optimal gain for the controller and the procedure is referred to as the linear quadratic regulator (LQR). Two major drawbacks arise with the LQ control strategy. First of all, accurate model of the dynamics is required for better estimation of the gain matrices. In fact, inaccurate modelling may result in poor control performance due to many factors such as spill-over that are related to dynamics that are not incorporated in the model. Secondly, the LQ control requires access to the full-state variables which is not always possible mainly due to physical limitations regarding the number of sensors that can be used. Practically speaking, it is either not feasible or prohibitively expensive to measure all the states, thus feedback control design often requires state variable estimation. In this situation, an estimator may be designed to estimate the states of the system. The optimal solution of the estimator problem is known as a Kalman-Bucy filter

(Sciulli, 1997). The combination of the optimal estimator and controller is referred to as the linear quadratic Gaussian (LQG) regulator problem.

An observer is a dynamic system with control inputs and measured responses, and an output that estimates the state vector. A feedback correction element with a gain  $L$  is added as an extra input to the system. Consider the general form a state-space representation of a dynamics system as expressed in 5-1. In order to design an observer of the system, an observability check is required. The MATLAB command “obsv” is employed to construct the observability matrix and the rank command to check its rank. It was found the observability matrix of the engine model is full rank. An estimated dynamical system of this system is expressed as

$$\hat{\dot{\mathbf{x}}} = \mathbf{A}\hat{\mathbf{x}} + \mathbf{B}\mathbf{u} + \mathbf{L}(\mathbf{y} - \hat{\mathbf{y}}) \quad 6-14$$

The last term in the equation corrects the state estimate based on the difference between the actual output  $\mathbf{y}$  and the estimated output  $\hat{\mathbf{y}}$ . The equation that describes the error between the estimated and original systems is defined as in 6-15

$$\dot{\mathbf{e}} = \dot{\mathbf{x}} - \dot{\hat{\mathbf{x}}} = (\mathbf{A}\mathbf{x} + \mathbf{B}\mathbf{u}) - (\mathbf{A}\hat{\mathbf{x}} + \mathbf{B}\mathbf{u} + \mathbf{L}(\mathbf{C}\mathbf{x} - \mathbf{C}\hat{\mathbf{x}})) \quad 6-15$$

Therefore

$$\dot{\mathbf{e}} = (\mathbf{A} - \mathbf{L}\mathbf{C})\mathbf{e} \quad 6-16$$

By examining the change in the error function, if the matrix  $\mathbf{A} - \mathbf{L}\mathbf{C}$  is stable, the error should converge to zero for a bounded input. Therefore  $\hat{\mathbf{x}}$  eventually converges to  $\mathbf{x}$  as time extends to infinity. The speed of convergence depends of the poles of the estimator (eigenvalues of  $\mathbf{A} - \mathbf{L}\mathbf{C}$ ). Since the interest is to use the estimated states as inputs to the LQ control system, it is desired to estimate the states as fast as possible or at least faster than the controller poles. Common guideline is to make the estimator poles 4-10 times faster than the slowest controller pole (Messner and Tilbury, ).

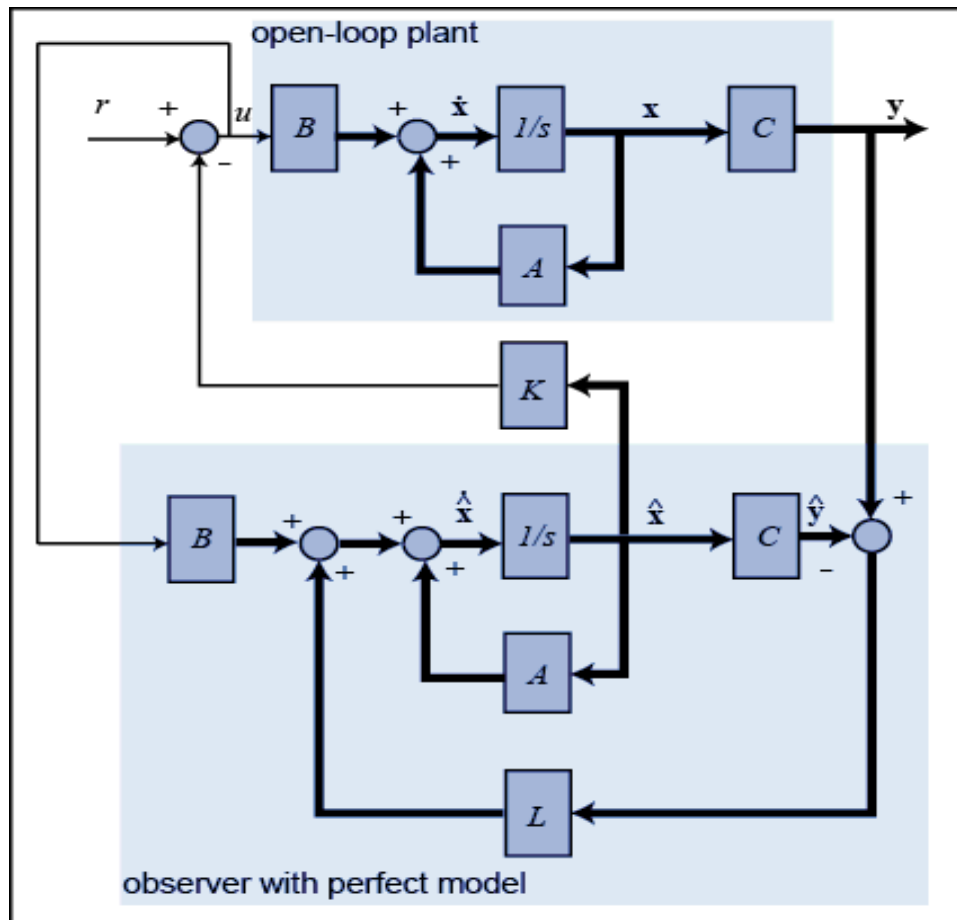


Figure 6-9 Closed loop state observer design (Messner and Tilbury, )

The state equations of the closed loop system presented in **Error! Reference source not found.** are presented as follows

$$\begin{aligned} \dot{x} &= Ax - BK\hat{x} + Br \\ \dot{\hat{x}} &= (A - LC)\hat{x} + B(r - K\hat{x}) + LCx \end{aligned} \quad 6-17$$

The state equation in a vector space model form is shown below

$$\begin{aligned} \begin{bmatrix} \dot{x} \\ \dot{\hat{x}} \end{bmatrix} &= \begin{bmatrix} A & -BK \\ LC & A - LC - BK \end{bmatrix} \begin{bmatrix} x \\ \hat{x} \end{bmatrix} + \begin{bmatrix} B \\ B \end{bmatrix} r \\ y &= [C \quad 0] \begin{bmatrix} x \\ \hat{x} \end{bmatrix} \end{aligned} \quad 6-18$$

### 6.4.3 Frequency Domain Simulation with LQ Control

The engine parameters used in this simulation are adopted from Table 5-1. In the state-space representation presented in system 6-8 ,  $A$  is  $4 \times 4$ ,  $B$  is  $4 \times 2$ ,  $C$  is  $4 \times 4$ , and  $D$  is  $4 \times 2$  .

The coefficients of matrices  $Q$  and  $R$  are chosen following Bryson's rule. This method is

used to identify an initial guess of  $\mathbf{Q}$  and  $\mathbf{R}$  coefficients relative to the expected magnitude of the output states and of the control force by which the displacement and velocity of the engine case are penalised. The TMD states are not penalised. The coefficients of matrix  $\mathbf{R}$  were chosen in such a way to allow for a limited control action relative to the excitation force based on trial and error. The choice of matrix  $\mathbf{R}$  has to be considered carefully because it comprises a gain related to the control force that has to be regulated in order to reduce the vibration of the primary mass. As for matrix  $\mathbf{Q}$ , the first and third diagonal coefficients are chosen to be much larger than the rest of the diagonal items indicating that the first and third states (primary mass displacement & velocity) are penalised most. The off-diagonal items are not considered in this case, but it is possible to use them in order to penalise a combination of two states with a single coefficient. Once the matrices  $\mathbf{Q}$  and  $\mathbf{R}$  are defined, the gain matrices  $\mathbf{K}$  and  $\mathbf{L}$  are calculated using Matlab commands ‘LQR’ and ‘PLACE’ respectively. The ‘LQR’ command calculates the optimal gain matrix  $\mathbf{K}$  such that the feedback force  $\mathbf{u} = -\mathbf{K}\mathbf{x}$  minimizes the cost function in equation 6-9. In this case, the control force vector  $\mathbf{u}$  becomes scalar value after multiplication. The ‘PLACE’ command computes the gain matrix  $\mathbf{L}$  in such a way that the eigenvalues of  $\mathbf{A} - \mathbf{L}\mathbf{C}$  are placed as desired by the specified user input. The coefficients of  $\mathbf{Q}, \mathbf{R}$  are presented in Table 6-2

Table 6-2 LQ and state observer control parameters

Simulation Parameters				
$\mathbf{Q} =$	$\begin{bmatrix} 1e11 & 0 & 0 & 0 \\ 0 & 0 & 0 & 0 \\ 0 & 0 & 1e10 & 0 \\ 0 & 0 & 0 & 0 \end{bmatrix}$	$\mathbf{R} =$	$1e - 6$	

The **Q** and **R** matrices are used to obtain the LQ control gain **K** using matlab command “LQR”. The resulting system with LQ control can be expressed in the following state space model

$$\begin{aligned}\dot{x} &= [A - BK][x] + Bu \\ y &= [C][x]\end{aligned}\tag{6-19}$$

The matrices **A** and **B** are obtained referring to Table 6-1 and system 6-8. The response of the system 6-19 is shown below.

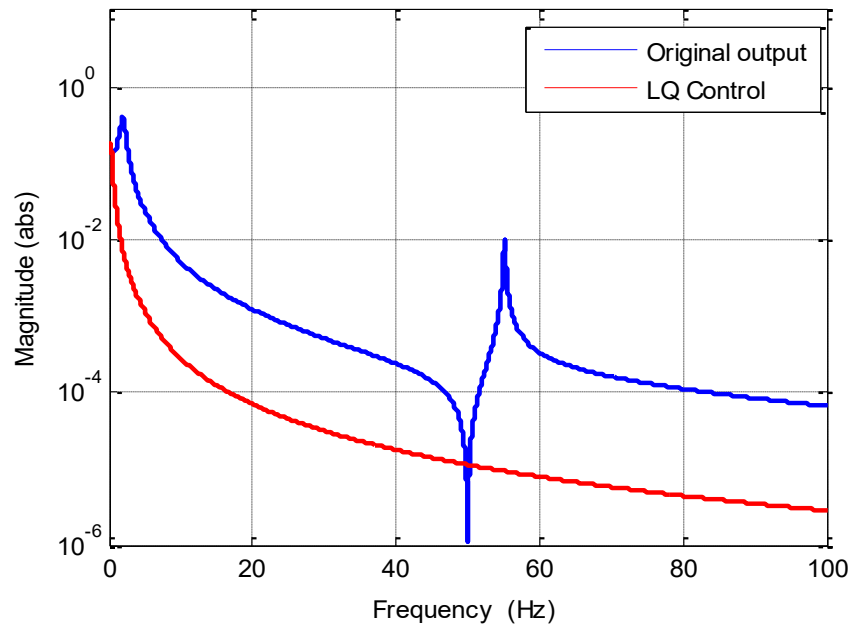


Figure 6-10 Frequency response of the engine case displacement with LQ control

According to the graphs of Figure 6-10, the frequency response of the engine case displacement shows that the LQ controller succeeds in reducing the vibration of the engine case to amplitudes below  $20\mu\text{m}$  for the range of excitation frequencies between 45Hz and 55Hz. For state estimation, an observer is designed based on the system provided in equation 6-18. The gain **L** is obtained following using matlab “PLACE” command in such a way that the eigvalues of **A – LC** are 4 times larger than those of **A – BK**. The graph of Figure 6-11 shows frequency response of the engine case displacement with the effect of LQG control- that is the LQ control with full state feedback of the observed states.

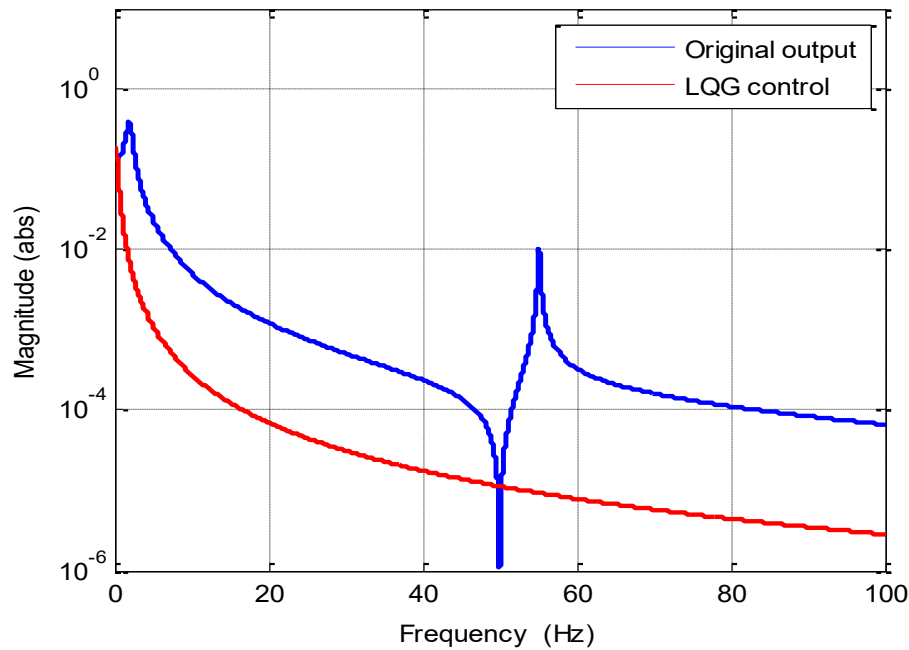


Figure 6-11 Engine case displacement with original system Vs. LQG control

## 6.5 Discussion

The LQ control is capable of reducing the vibration of the engine case not only at 50Hz but also for the intended range. This type of control is more complicated than the gain scheduling control because it requires more computational power as well as accurate knowledge of the system under control. In addition to that, it was shown that for the full-state feedback LQ control, an observer system is required because it is not always feasible to obtain measurements of the full-state variables. In systems where the dynamics of the system do not change with time, real-time tuning of the gain matrix is not required since only one solution of the ARE is required. This allows for less computational power requirements since the gain matrix can be obtained beforehand. Unlike the case where the system dynamics change with time, the system becomes more complex and real-time tuning of the gain matrix is required, warranting the need for more computational resources. The practical implementation of LQG

control requires knowledge of the main system inputs and certainly more computational power is required since the states are estimated instantaneously.

## **6.6 Summary of the frequency analysis**

Two control strategies were investigated for the mitigation of the vibration problem in the Stirling engine. The theoretical simulation revealed that both the LQ control and the gain scheduling with zero placement succeeded in reducing the vibration of the engine case despite the fact that their principle of operation is different. The LQ control requires detailed knowledge of the model dynamics and the full-state variables whether by measurement or by estimation. The gain scheduling control only requires knowledge of some system dynamics, which make it relatively easier method to implement, compared to the LQ control.

For known excitation frequencies, gain scheduling with zero-placement control approach can achieve greater performance with relatively straightforward determination of the feedback gains. Following this control law, the tuning of the gains is achieved adaptively following a known equation based on measurement of the excitation frequency whereas a single gain is used with LQ control determined offline providing that system dynamics do not change. The matrix gain of the LQ control is less intuitive to obtain and requires solving the algebraic Riccati equation. The gains matrix is obtained after determining the coefficients of the state and input matrices.

For the gain scheduling technique, the simulation showed that a feedback force proportional to either relative or absolute position/acceleration is capable of altering the resonant frequency of the ATMD so it tracks a desired frequency. In comparison, relative/absolute velocity feedback does not alter the resonant frequency of the ATMD, but it can modify its damping. The LQ control strategy provides a more robust control across a wider range of frequencies. It is particularly useful when knowledge of the excitations is not available and requires full accessibility to the output states either by measurement or with the aid of a state

observer. From a computational power perspective, active control of vibration with gain scheduling and pole placement control can be achieved with more flexibility considering the number of sensors that can be used and the required computational power. A state estimator is often required with LQ control because full-state access is required and it is not always possible to obtain. The observer requires good knowledge of the model dynamics and its inputs as well as more computational power.

## 6.7 Time Domain Simulation

The parameters of Table 6-1 and Table 6-2 are adopted in this section. The simulation is performed for a total time of 55 seconds with excitation frequency varied from 45Hz to 55Hz in steps of 1Hz. The frequency increments are implemented by using a switch mechanism that passes through sinusoidal input signals with different frequencies. Figure 6-12 and Figure 6-13 present the simulation results for gain scheduling and LQ control respectively.

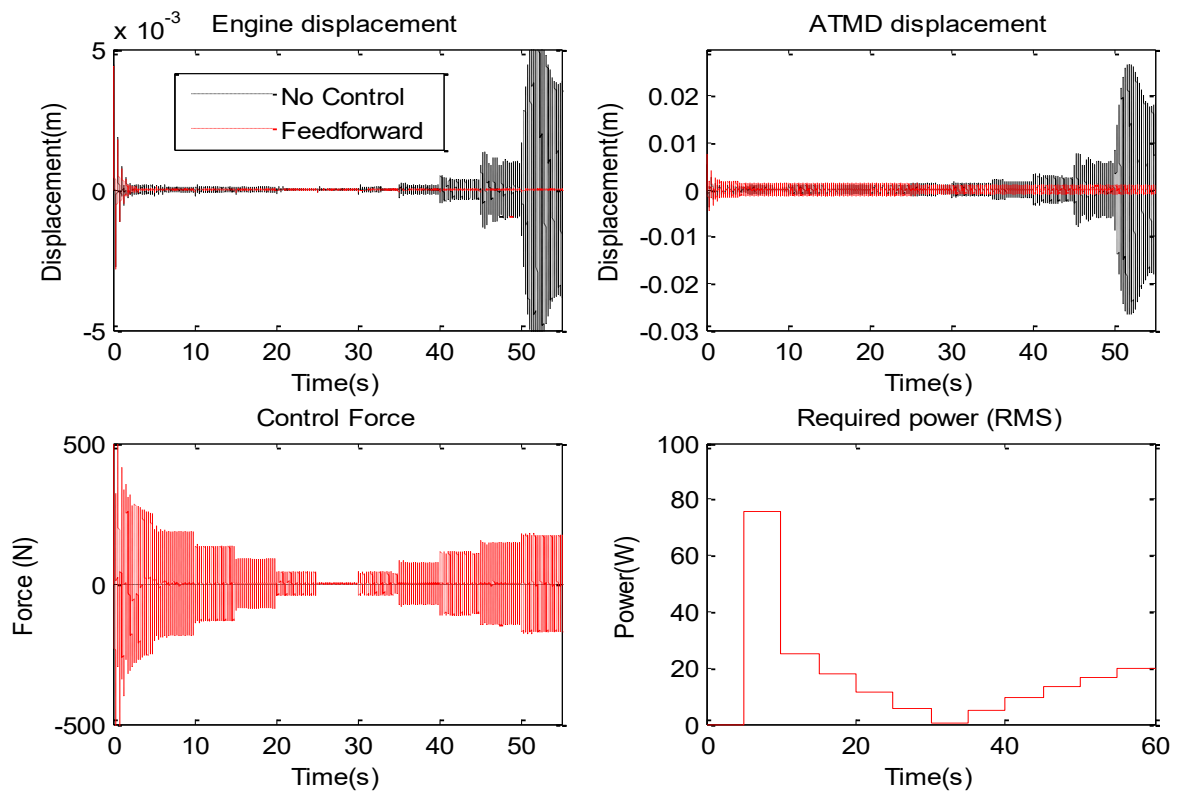


Figure 6-12 Simulation results with gain scheduling control (position feedback)

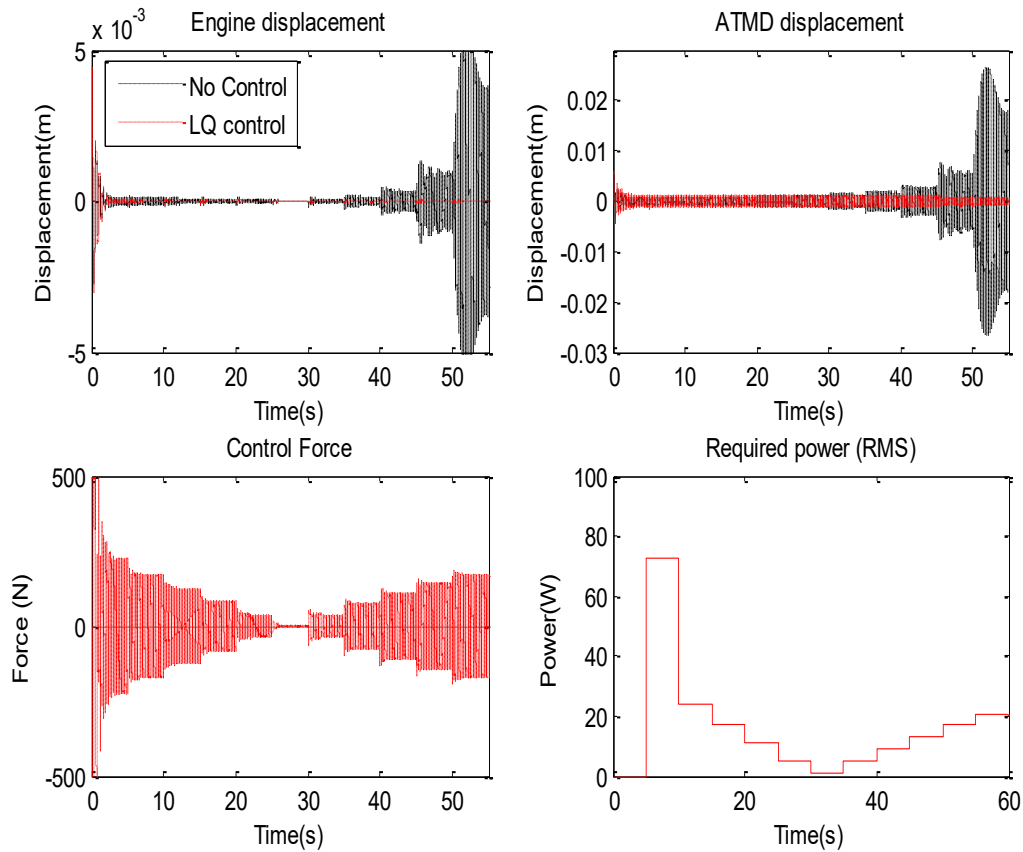


Figure 6-13 Simulation results with LQG control (based on estimated states)

For the gain scheduling control, the simulation is performed while assuming position and velocity feedback. The position feedback gain is determined in real time and the velocity feedback gain is chosen equal to  $-c_2$ . For the LQ control, a state observer is used for state estimation and the gain matrix is determined prior to simulation based on the chosen coefficients of  $\mathbf{R}$  and  $\mathbf{Q}$  matrices.

## 6.8 Discussion

The engine case displacement, ATMD displacement (actuator stroke), required actuation force, and power consumption are shown for each control technique. The analysis is carried out by comparing the cases of no control, gain scheduling control, and LQG control.

a. No control

The vibration of the engine case is attenuated only when the excitation is at 50 Hz which is the anti-resonant frequency of engine case as an effect of the passive TMD. When the excitation frequency drifts on either side from 50Hz, the vibration of the engine case grows larger exceeding the maximum allowed magnitude. In fact, as the excitation frequency shifts rightwards from 50Hz, the amplitudes of the vibration become much larger than the case of shifting leftwards. The larger amplitudes for frequencies above 50Hz were expected. The frequency domain simulation showed that second resonant mode of the composite system occurs at approximately 54.8 Hz. It is evident now that a drift in the excitation frequency would cause the amplitudes of the engine case vibration to exceed the limits drastically that may lead to detrimental consequences such as damaging the physical system.

b. Gain scheduling Control:

In this case, relative position and relative velocity feedback gains are used to alter the tuning of the ATMD so its frequency tracks that of the excitation as well as to reduce the damping from the ATMD system. The excitation frequency is compared to the current tuning frequency of the ATMD and a gain is generated automatically then multiplied by the relative position. The value of the negative velocity feedback gain is constant and equal to the damping coefficient in the ATMD. For the latter to be correct, it is assumed that damping in the ATMD is constant and does not change with frequency. In practice, this assumption might not be very accurate because damping can change depending on several factors such as frequency and strokes, as well as the type of actuator used. Damping in the ATMD is studied thoroughly in the implementation stage. Furthermore, by using a velocity feedback gain  $\beta = -c_2$ , the system is actually marginally stable as shown in the stability study. Practically, slight

amount of damping should be allowed  $\beta > -c_2$  in the system to avoid marginal stability situations. The aim of including a velocity gain is to reduce the effect of damping introduced by the ATMD system because it was shown previously that the existence of damping in the absorber reduces the vibration attenuation level in the engine case at the resonant frequency. Referring to Figure 6-12, the results reveal that when control is on, the vibration amplitudes of the engine case is reduced to less than  $20\mu\text{m}$  for all the frequencies between 45Hz and 55Hz indicating to a successful vibration reduction. In fact, thanks to the velocity feedback gain, the damping from the system is removed causing the ATMD to achieve far more attenuation than the passive TMD at 50Hz. The simulation shows that there exists a transient time of approximately two seconds at 45Hz. This long transient is caused by excitation at 45Hz which caused the control to immediately shift the resonant frequency of ATMD from 50Hz to 45Hz. In fact, this doesn't happen in reality because the grid frequency never fluctuates from 50Hz quickly. For small frequency changes, settling time of this transient is very small and this can be seen in the graphs when the excitation frequency is increments in steps of 1Hz after 45Hz.

The graph also shows the actuator stroke, force, and power requirements to achieve the active damping between 45Hz and 55Hz. These quantities represent the requirements from an actuator irrespective of its type. From the force and power curves, it can be seen their quantities change quadratically with frequency as they are proportional to the relative position gain which was shown to change quadratically as frequency changes. Being max at 45Hz, the force and power values gradually decrease to reach the minimum value at 50Hz then increase again after that. Of course the requirements at 45Hz are not similar to those at 55Hz because the quantities vary quadratically with frequency rather than linearly.

c. LQG control:

Similar results to the previous are obtained with the LQG control despite the two different ways of operation. The vibration of the engine case is reduced and the actuator strokes, power and force requirements are very close to the ones obtained with the gain scheduling control. The comparison of the results obtained with LQ control to the gain scheduling control, it was observed that it is possible to achieve similar control action to the gain scheduling control with position and velocity feedback when proper tuning of the gain matrix of the LQG control is performed.

## **6.9 Noise and Uncertainties: Effects and Mitigation**

### **6.9.1 Gaussian Noise**

Noise can deteriorate the performance of a control system. In this section, the effect of noise on each control technique is investigated and a comparison is made based on the performance. The time domain simulation in the previous section considered ideal scenarios assuming that the sensor measurements are noise-free. In reality sensor readings could be contaminated with noise due to many different factors such as electromagnetic and radio frequency interference. In this simulation, noise with Gaussian type distribution of different magnitudes is added for each measured signal. Gaussian noise generators are added to the model and noise is generated based on specifying the variance and the mean of the distribution. For the system under study, the position and velocity measurements of the engine case and absorber mass are contaminated with noise. The following figure depicts the SIMULINK model of the simulation with noise.

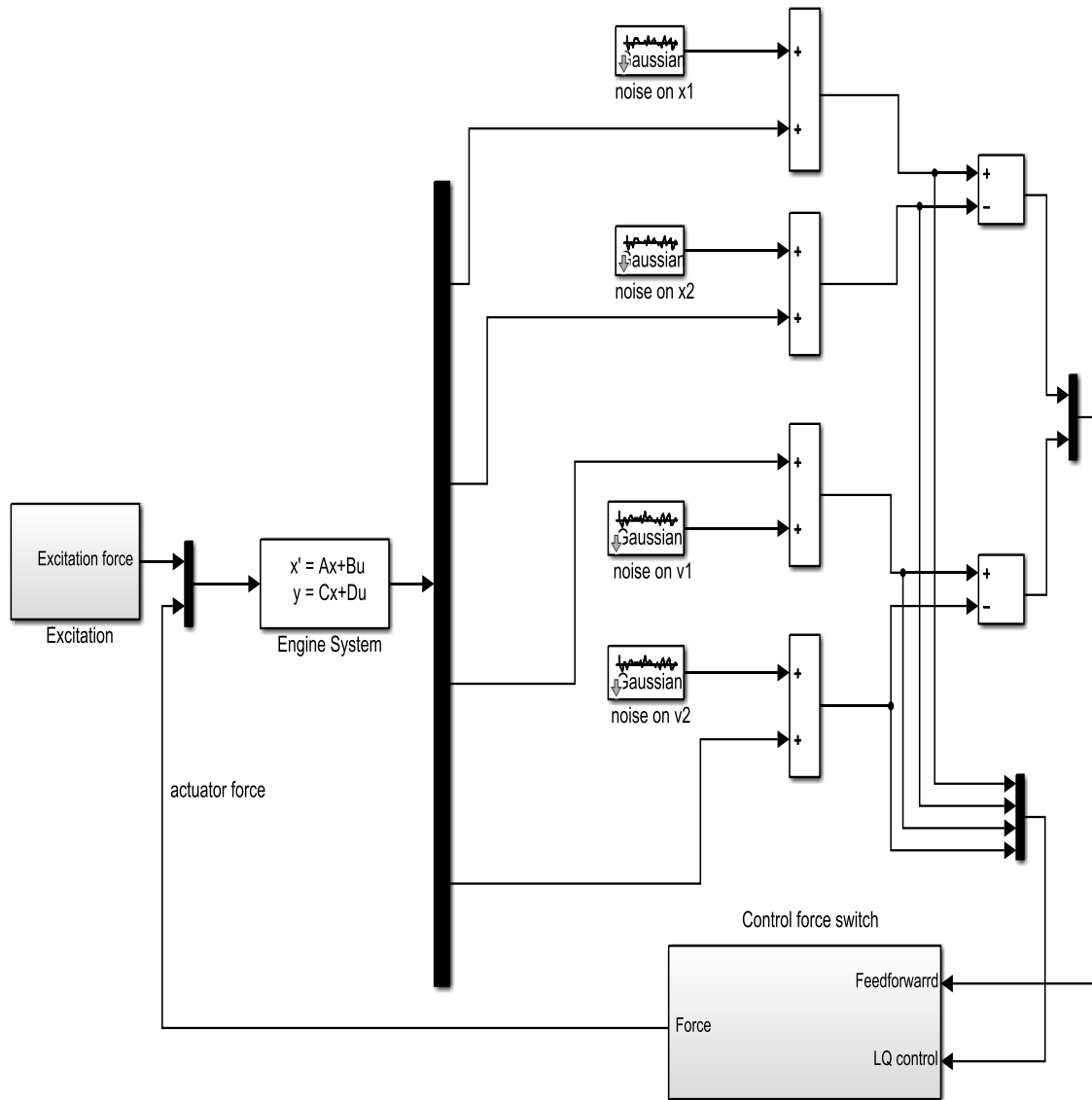


Figure 6-14 SIMULINK with addition of Gaussian noise

The value of presented in Table 6-3 are adopted for the simulation.

Table 6-3 Gaussian noise parameters

Signal	Noise Distribution Variance
<b>Engine displacement</b>	5e-12
<b>Absorber displacement</b>	0.25e-6
<b>Engine velocity</b>	2e-6
<b>Absorber velocity</b>	1e-2

The graphs depicted in Figure 6-15 represent the noise distribution for each signal. They reveal that 99.9% of noise values fall within  $\pm 3\sqrt{\text{Variance}}$  shown in each level.

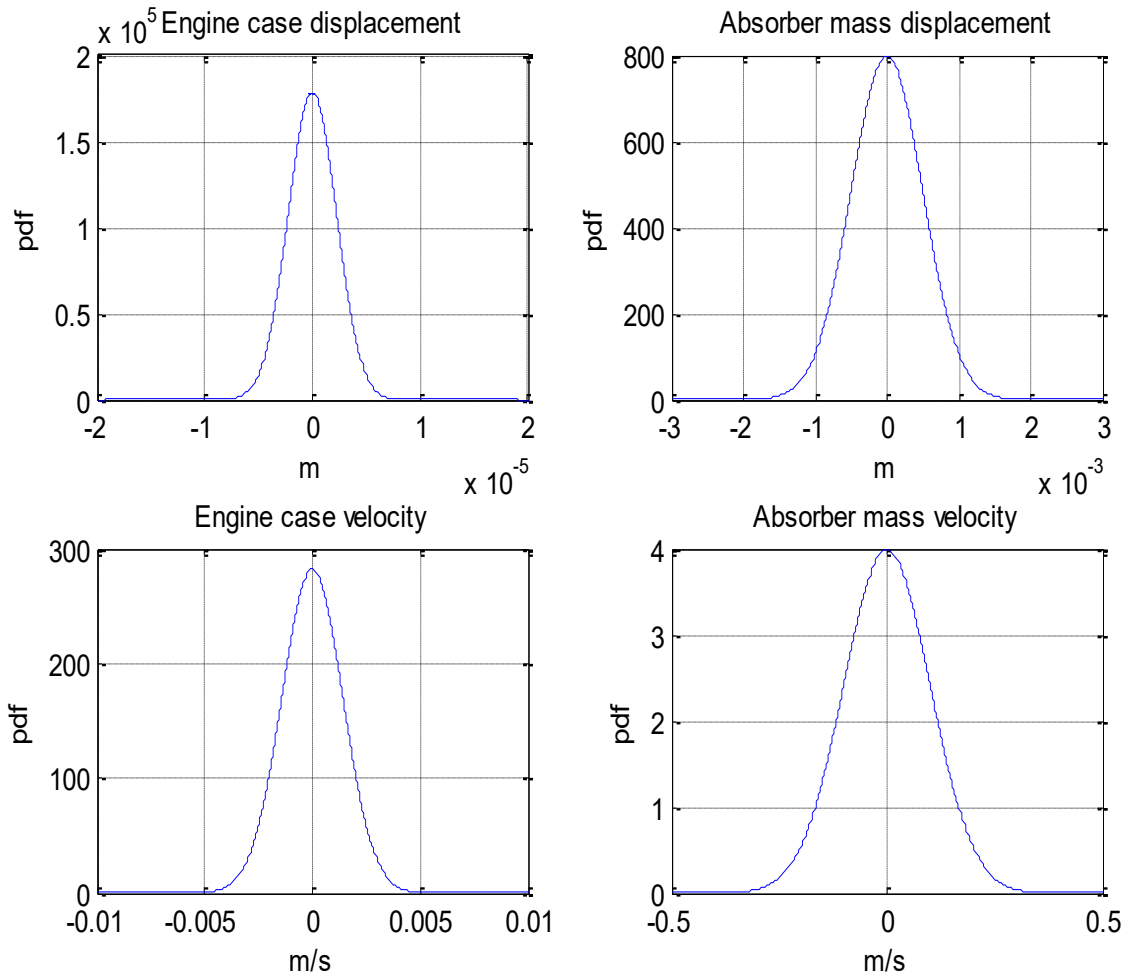


Figure 6-15 Probability density function of noise distribution

The idea is to study how noise in measurement signals deters the control action with particular emphasis on the actuator force. The graphs of Figure 6-16 show a comparison between the cases with and without noise for both the gain scheduling and LQ control. The graph reveals that for both control methods when signal measurements are contaminated with noise, the actuator force curves are rough and chirpy for all the frequency range compared to the case when measurements are free of noise. In addition to that, it is revealed that the actuator force is more sensitive with the gain scheduling control than it is with the LQ control. This can be attributed to the fact that LQ control gains are calculated based on knowledge of the system dynamics unlike the gain scheduling control law.

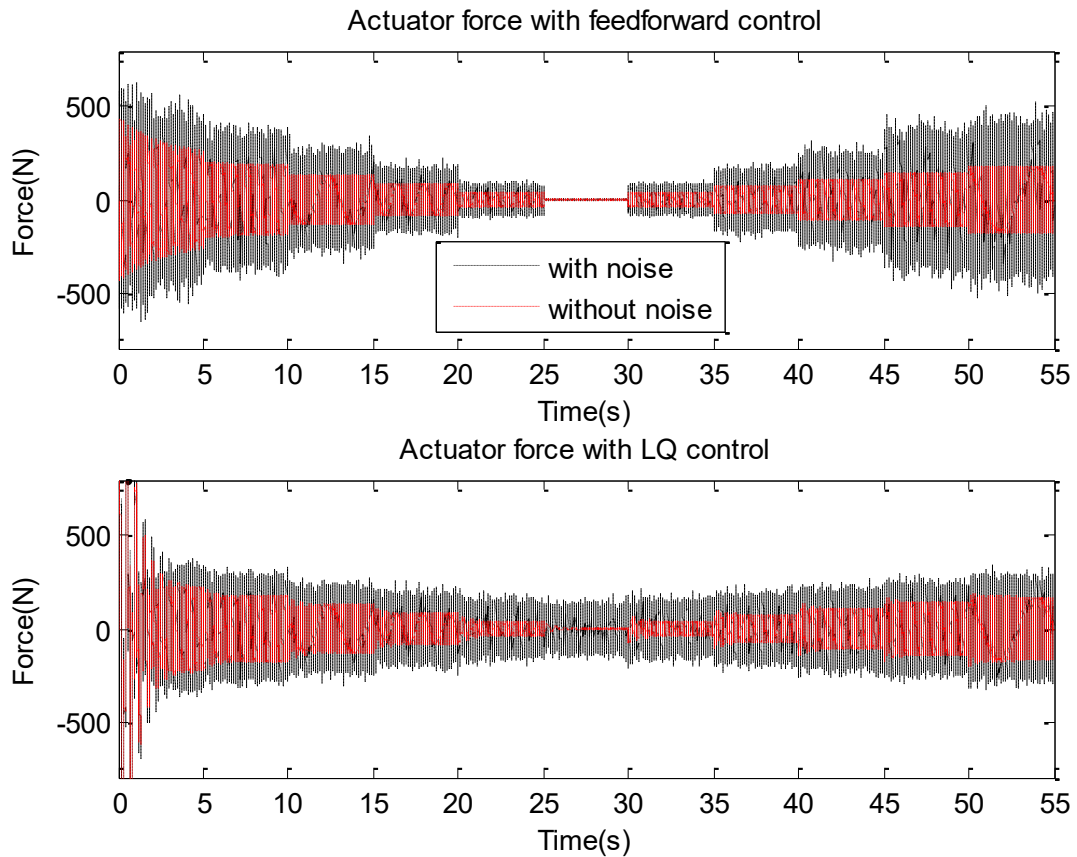


Figure 6-16 Effect of noise on the actuator force with each control strategy

### 6.9.2 Noise Mitigation 1: State Observer

Having a good knowledge of the system model could be beneficial in situations where noisy measurements exist. The idea here is to estimate the system outputs instead of measuring them based on knowledge of the dynamics of that system. This could be achieved by introducing a state observer that estimates the system states based on the good knowledge of the system dynamics as depicted in Figure 6-17. The observer gain  $L$  is chosen such as the eigenvalues of matrix  $A-LC$  are 4 times larger than those of matrix  $A$ . The observer state space system block contains the following model

$$\begin{aligned} \dot{\hat{x}} &= (A - LC)\hat{x} + B \begin{bmatrix} F \\ f \\ \hat{x}_1 - x_1 \end{bmatrix} \\ y &= c\hat{x} \end{aligned} \quad 6-20$$

With  $A_{4 \times 4}$ ,  $B_{4 \times 3}$ ,  $C_{4 \times 4}$ .

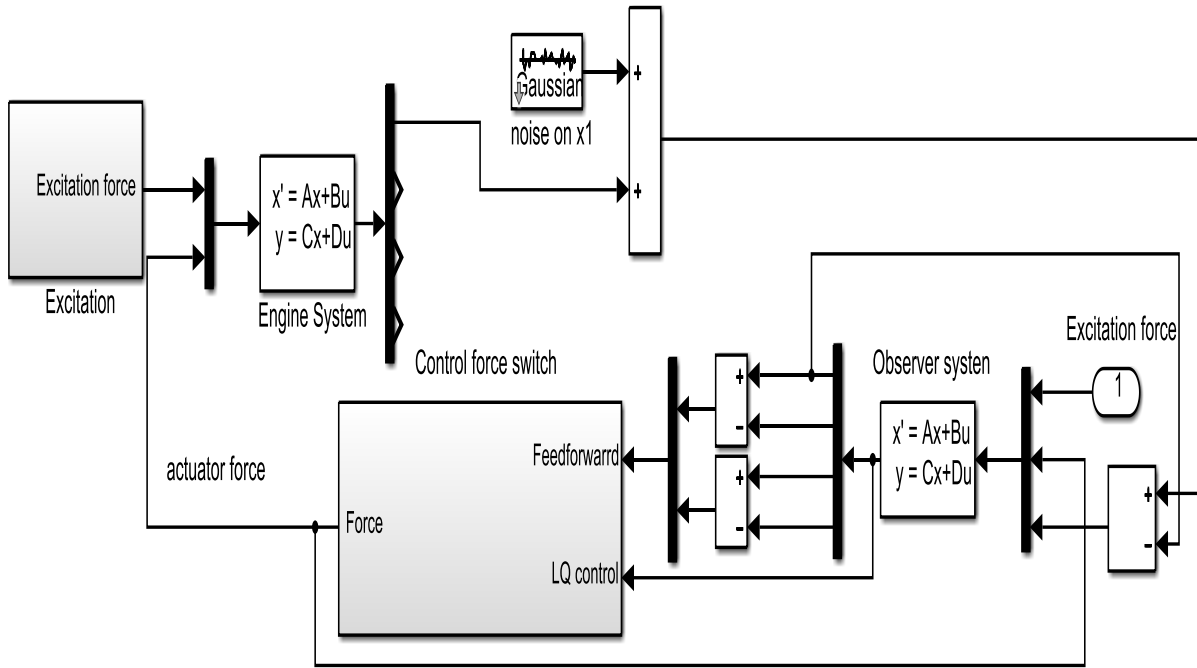


Figure 6-17 State observer with noise

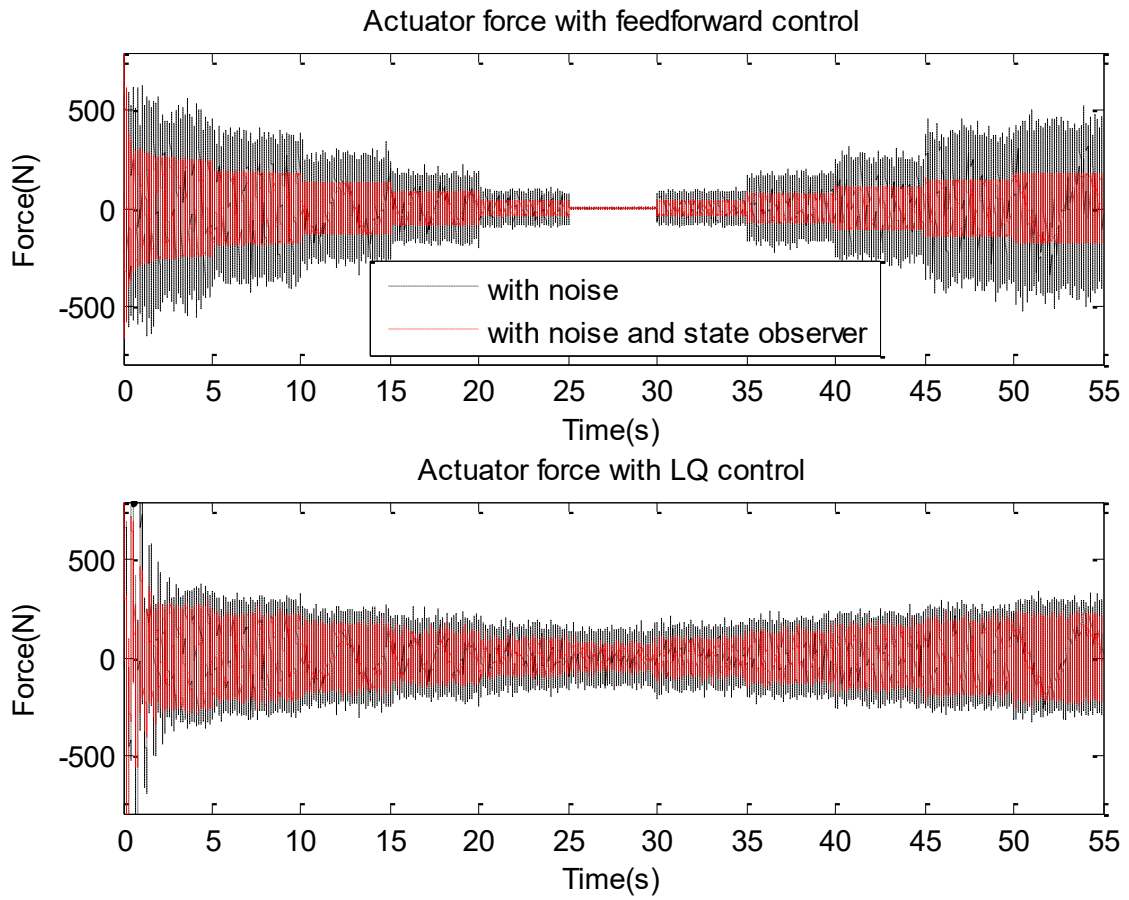


Figure 6-18 Noise mitigation with of state observer on noisy signals

### 6.9.3 Discussion

Referring to the graphs of Figure 6-18, it is revealed that the addition of a state observer to estimate the system states has succeeded in removing the effect of noise in both of the control strategies. Although the observer system can provide a good remedy in such situations, certain drawbacks are associated with following this method. First of all, in order for the observer system to estimate the states accurately, an accurate knowledge of the system whose states to be estimated must be available otherwise the observer would not be able to account for spill over and other missing dynamics. The second issue is concerned with the computational power requirement which will certainly increase with the increase of computations that a state observer adds.

### 6.9.4 Noise Mitigation 2: Butterworth Low Pass Filter

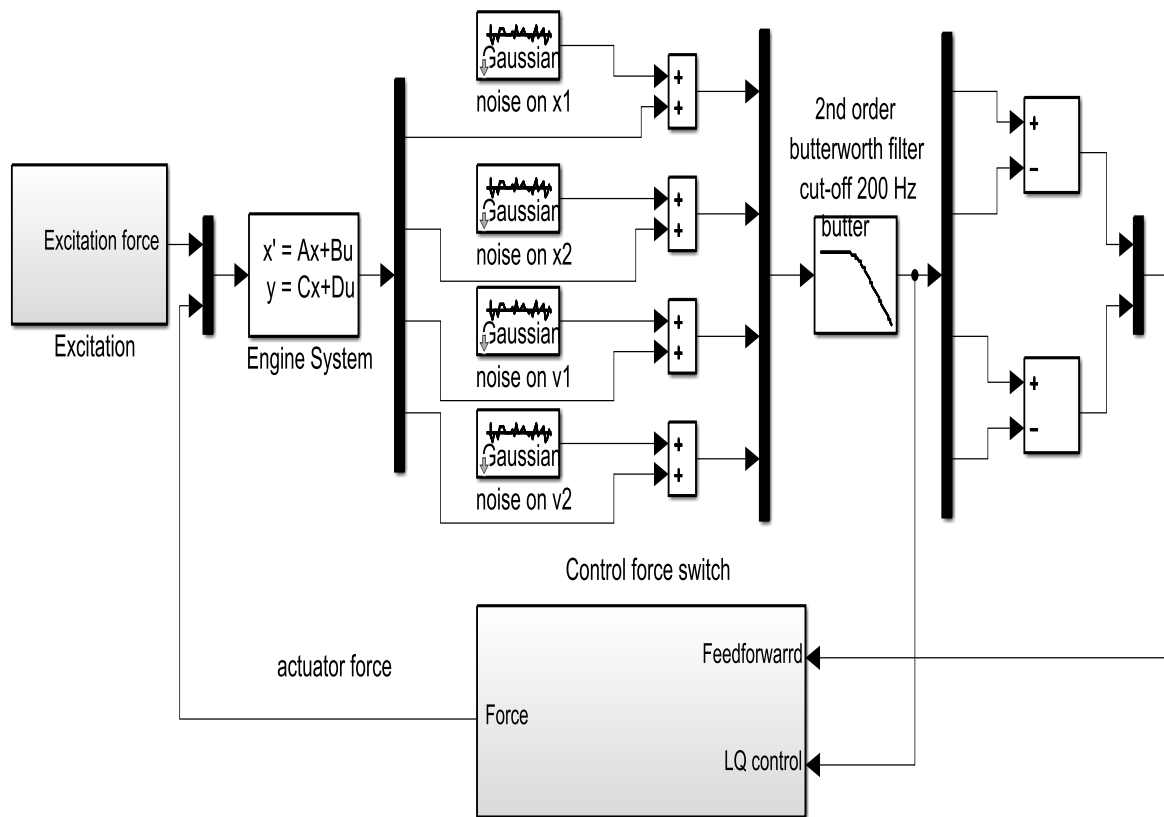


Figure 6-19 Noise Filtering

The use of a state observer has succeeded in reducing the effect of noisy measurements. The increase in complication and computational requirements that the observer system introduces make this approach less desirable particularly when other methods can be more efficient with lower costs. This section is dedicated to the investigation of a different approach for noise mitigation. The proposed solution is based on implementing a low pass filter stage that is capable of removing the noise from the sensor measurements to an acceptable level.

Referring to the model presented in Figure 6-19, a second order Butterworth low pass filter with a 200Hz cut-off frequency is introduced after the noise-contaminated signals measurement. A simulation is carried out in the time domain and the actuator force response with the two different control techniques is observed. Figure 6-20 depicts the response of the actuator force requirement for both gain scheduling/feedforward and LQ control in the presence of noise and a low pass filter.

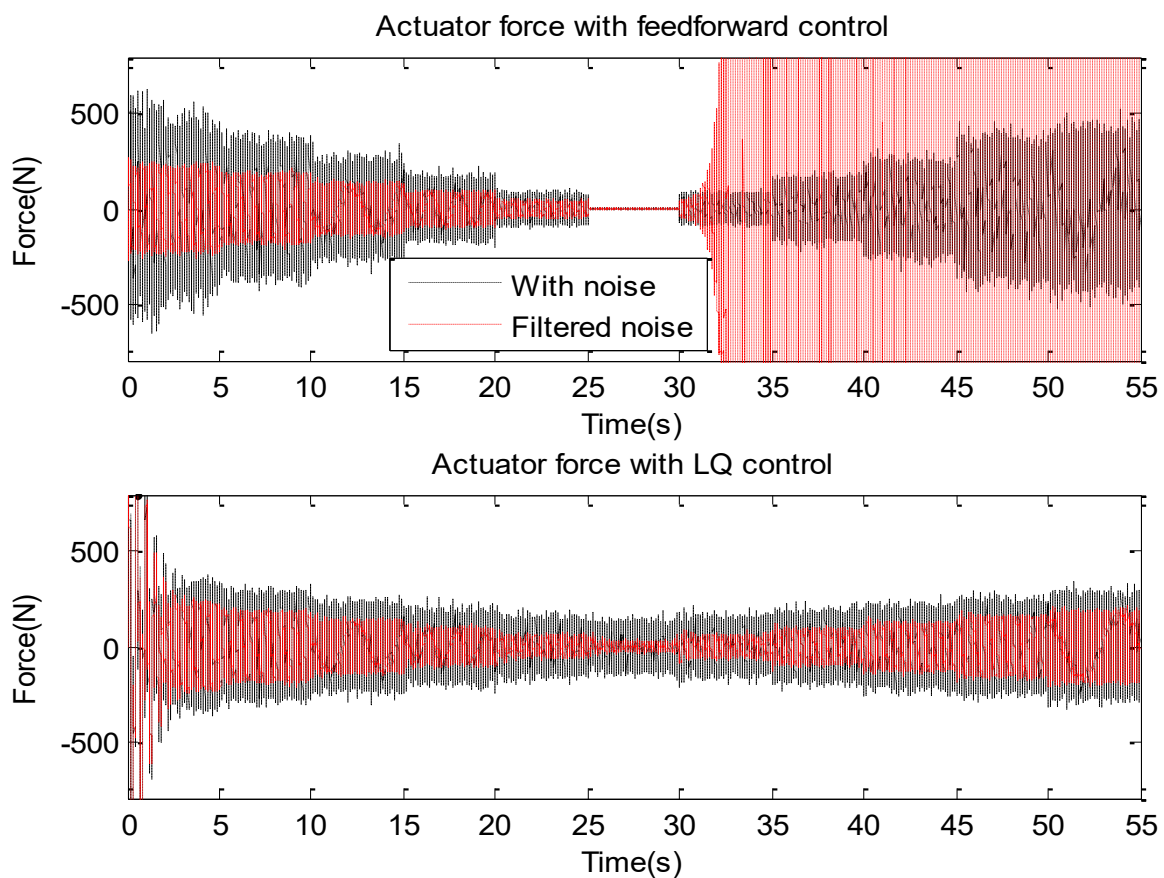


Figure 6-20 Noise mitigation with of low pass filtering of noisy signals

### 6.9.5 Discussion

The graphs reveal that for the LQ control, filtering has reduced the effect of noise on the actuator force amplitude between 45Hz and 55Hz. For the gain scheduling control, filtering has improved the signals for the frequencies between 45Hz and 50Hz. However after 50Hz, the actuator force suffers a significant growth of amplitude. The sudden growth of amplitude indicates to instability in the control system. The source of instability is attributed to the introduction of a low pass filter which introduced delays. Thus the following section is dedicated to the investigation of control stability with time delays for the two control techniques.

### 6.10 Effect of Time Delays on Control Stability

A time delay  $d(t - \tau)$  can be expressed by  $e^{-\tau s}$  in the Laplace domain. The term  $\tau$  is defined as the amount of time delay in seconds. The idea is to analyse the position of the closed-loop poles of the transfer function that relates the displacement of the primary mass to the excitation force after model reduction. The model reduction incorporates the control force into the transfer function. The exponential term of the delay has to be transformed into a rational form. The most obvious polynomial expansion of the exponential is the Taylor series. The first order of Taylor approximation assuming a sinusoidal force of period  $T$  in the frequency domain becomes

$$e^{-\tau s} \xrightarrow{s=j\omega} e^{-j\tau\omega} = e^{-j\tau\frac{2\pi}{T}} = e^{-j2\pi\tau_n} \quad 6-21$$

$$e^{-\tau s} \approx 1 - \tau s \xrightarrow{\text{yields}} e^{-j2\pi\tau_n} \approx 1 - j2\pi\tau_n$$

where  $\tau_n$  is the normalised delay and defined as  $\tau_n = \frac{\tau}{T}$ , the relative error is defined as

$$e_r = \left| \frac{e^{-j2\pi\tau_n} - (1 - j2\pi\tau_n)}{e^{-j2\pi\tau_n}} \right| \times 100 \quad [\%] \quad 6-22$$

Assuming that the excitation is sinusoidal, Figure 6-21 shows the error percentage with Taylor approximation as a function of the normalized delay.

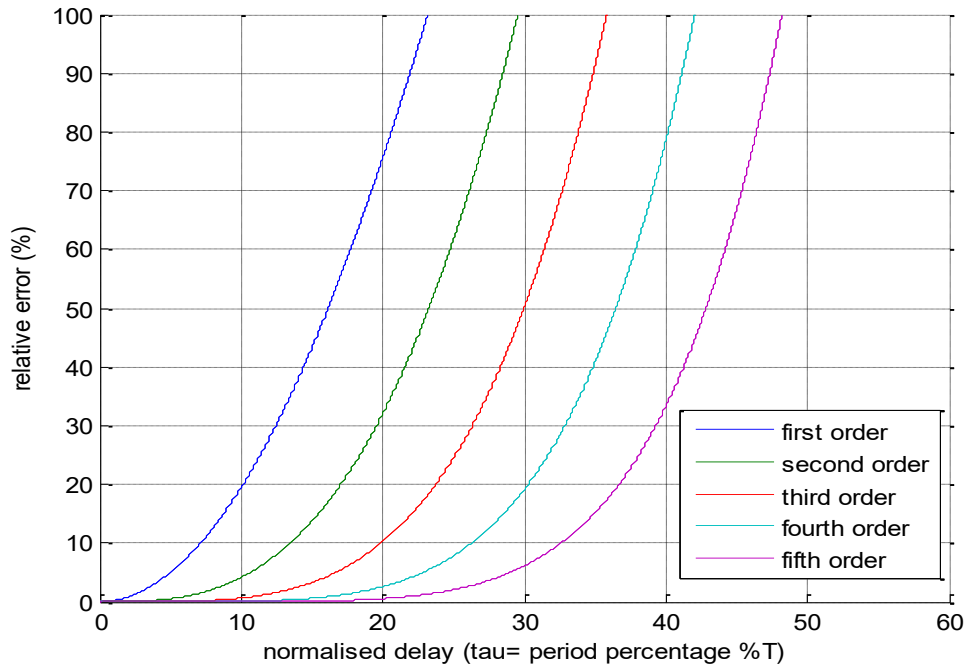


Figure 6-21 Percentage error between the original delay function and its Taylor series expansion approximation. It is revealed that for the Taylor approximation to be at least 90% accurate, the amount of time delay should not exceed 6% of the value of the operating period  $T$  with the first order approximation whereas it can be up to 15% with second order approximation. For the purpose of the application in this research, the first order Taylor approximation is considered.

### 6.10.1 Delays with Gain Scheduling Control

The general form of the actuator force can be extended to incorporate time delays in the control signal assuming relative measurement feedback. The expression that represents the control force with time delays can then be expressed as follows

$$f_{act}(t - \tau) = d(t - \tau)[\alpha(\ddot{x}_1 - \ddot{x}_2) + \beta(\dot{x}_1 - \dot{x}_2) + \gamma(x_1 - x_2)] \quad 6-23$$

By associating the actuator force equation into the equations of motion of the Stirling engine model,  $W(s)$  becomes

$$W(s) = \frac{X_1(s)}{F(s)} = \frac{\alpha\tau s^3 + (\beta\tau - m_2 - \alpha)s^2 + (\gamma\tau - c_2 - \beta)s - \gamma - k_2}{a_0s^5 + a_1s^4 + a_2s^3 + a_3s^2 + a_4s + a_5} \quad 6-24$$

Where

$$a_5 = \alpha\tau(m_1 + m_2)$$

$$a_4 = -\alpha(m_1 + m_2) - m_1m_2 + \alpha\tau c_1 + \beta\tau(m_1 + m_2)$$

$$a_3 = -\beta(-\tau c_1 + m_1 + m_2) - c_1m_2 - c_2(m_1 + m_2) - \alpha(c_1 + \tau k_1) + \gamma\tau(m_1 + m_2)$$

$$a_2 = -c_1(-\gamma\tau + c_2 + \beta) - \gamma(m_1 + m_2) - k_2(m_1 + m_2) - k_1(-\beta\tau + \alpha + m_2)$$

$$a_1 = -k_1(-\gamma\tau + \beta + c_2) - c_1(k_2 + \gamma)$$

$$a_0 = -k_1(\gamma + k_2)$$

The existence of time delay  $\tau$  in the denominator of the closed loop transfer function  $W(s)$  indicates that the system poles include delay terms. Assuming the original system before the addition of delays is stable, the idea is to examine how varying the amount of time delay affects the system poles as the excitation frequency is varied. A solution of the above system is obtained numerically at each frequency between 45Hz-55Hz as time delay is varied from 0 to 0.5ms.

#### 6.10.1.1 Gain Scheduling Control with Position and Velocity Feedback

Figure 6-22 depicts the variation of the system poles as a function of time delays for excitations between 45Hz and 55Hz with position and velocity feedback. In this case, the relative acceleration feedback gain  $\alpha = 0$ , the relative velocity feedback gain  $\beta = -c_2$ , and the relative position feedback gain  $\gamma$  is determined adaptively for each frequency.

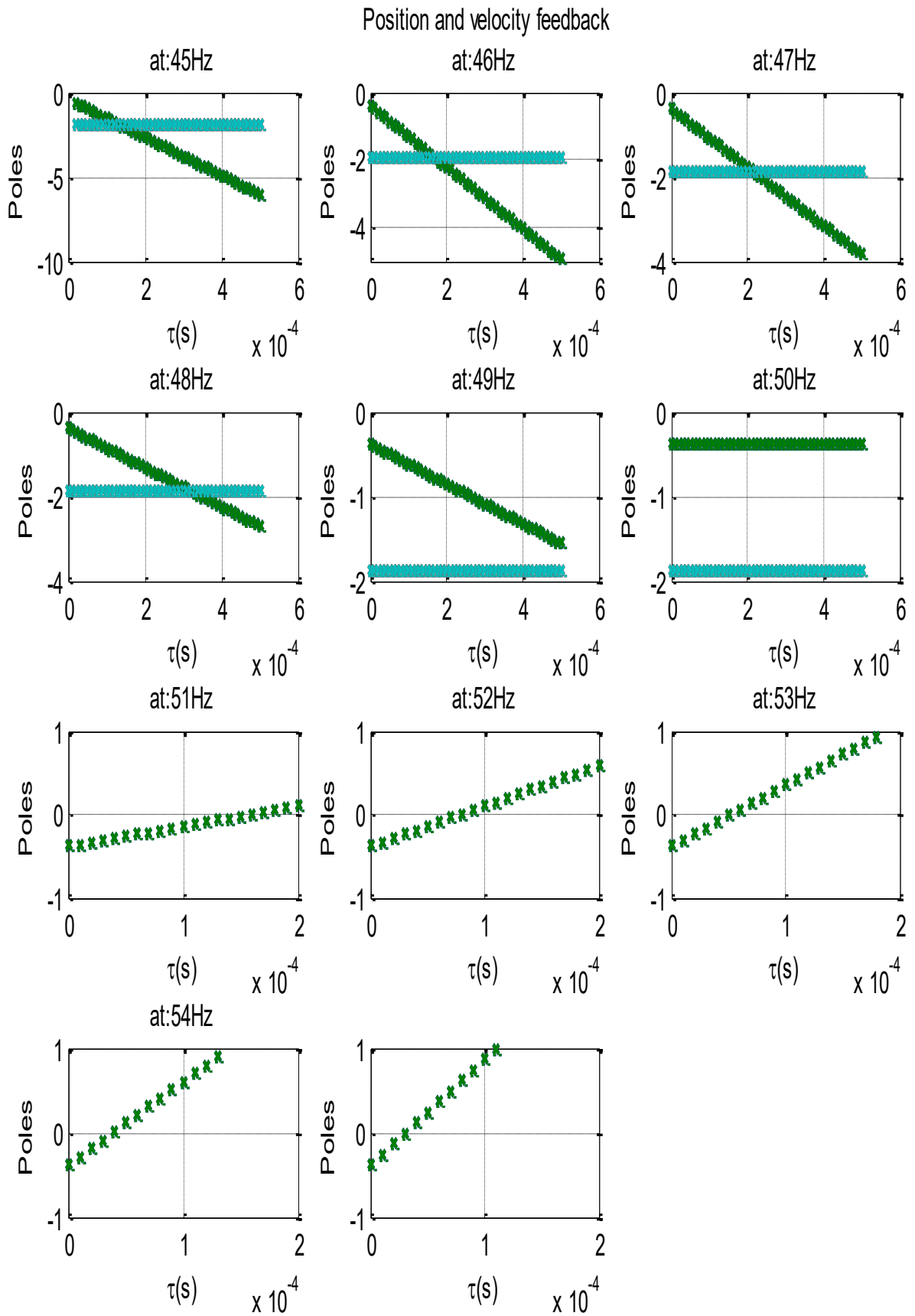


Figure 6-22 System poles variation with position and velocity feedback showing unstable pole after 50Hz

For stability to be ensured, all the system poles must exist in the left-hand side of the S-plane. According to Figure 6-22, it is revealed the system is stable before 50Hz which is the original tuning of the ATMD. After 50Hz, the real part of two complex poles changes from negative to positive after some time delay denoted by critical time delay margin. As delay increases, the poles move gradually to the right along the real axis causing system instability when becoming positive. It is revealed that as the excitation frequency is increased, the unstable poles move at a faster rate, thus decreasing the value of the critical time delay margins. These results support the findings obtained in section 6.9.4 when filtering caused delays that consequently destabilised the system as explained here.

In order to illustrate the effect that time delays have on the stability of the control system from a time domain perspective, the time domain response of the actuator force is plotted with excitation varying between 45Hz and 55Hz for five different time delays. Figure 6-23 shows a SIMULINK model that represents the active control with position and velocity feedback and delayed actuator force.

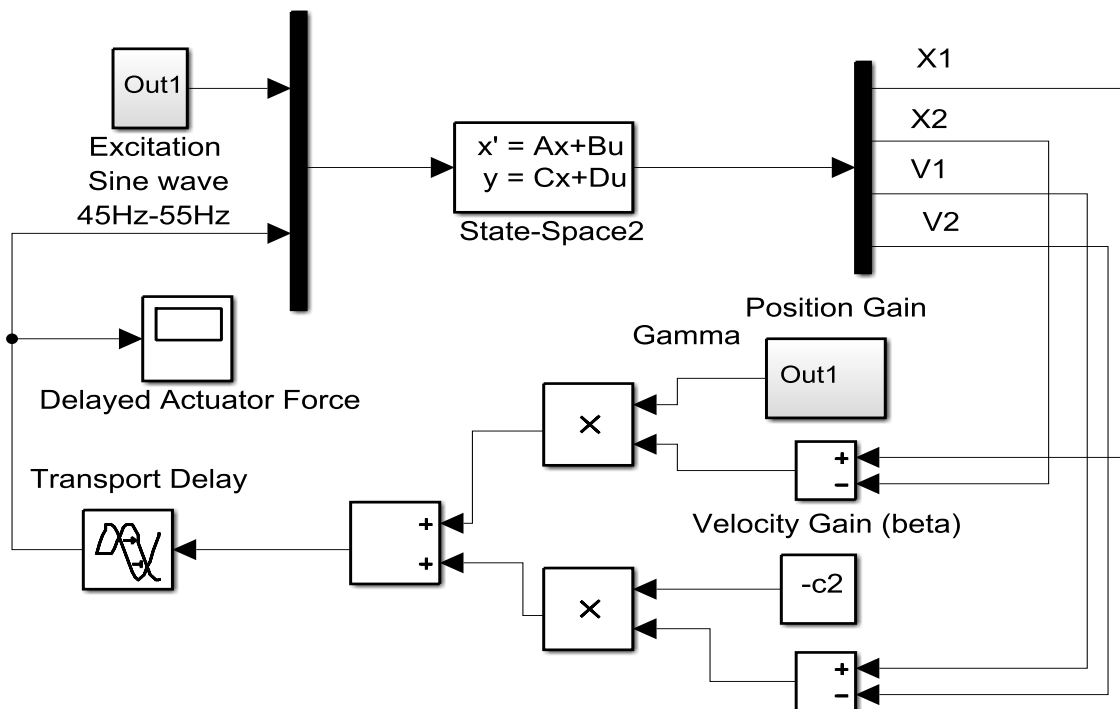


Figure 6-23 SIMULINK model for delayed actuator force with position and velocity feedback

Figure 6-24 depicts the results of the time domain simulation of the model represented in Figure 6-23. The simulation is carried out for 55 seconds for sinusoidal excitation with frequency that is varied from 45Hz to 55Hz in steps of 1Hz every 5 seconds for different values of time delay. The simulation results demonstrate that delays above a certain time margin destabilise the control system when excitation frequency is above 50Hz, proving the correctness of the results presented in Figure 6-22.

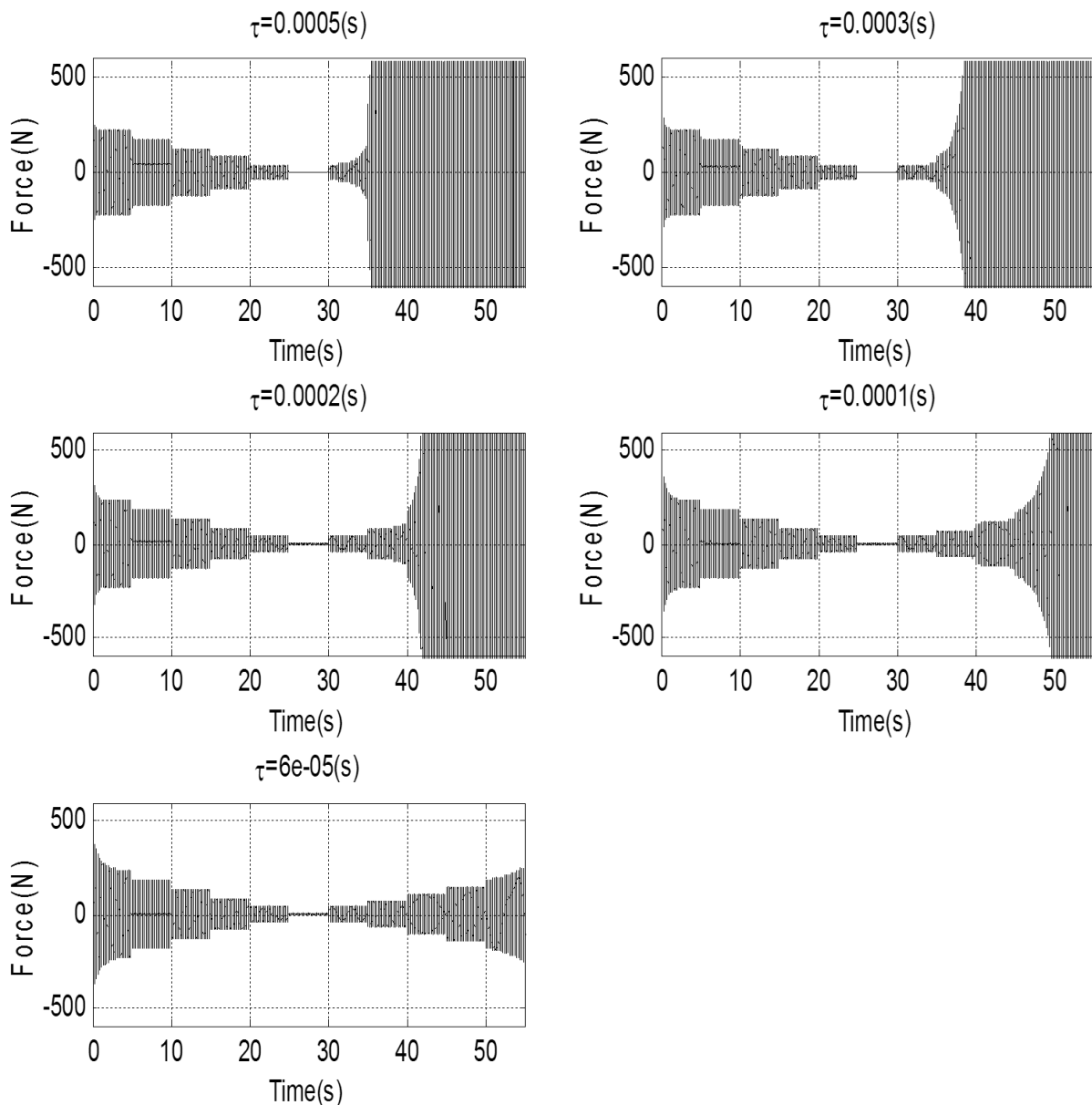


Figure 6-24 Time domain response of the control force with acceleration and velocity feedback with positive time delay showing system instability after 50Hz for different time delays

### 6.10.1.2 Acceleration and Velocity Feedback

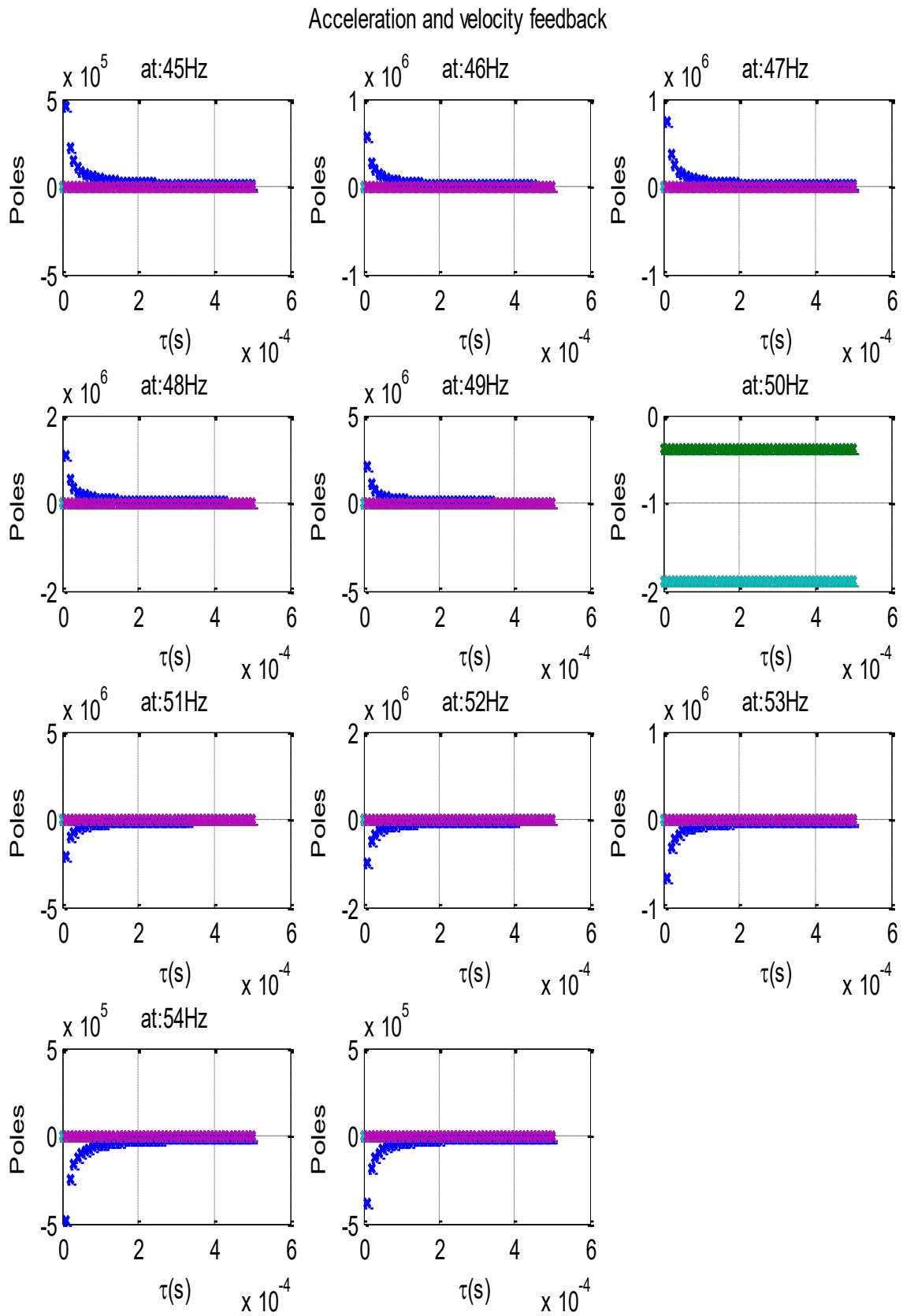


Figure 6-25 System pole variation with acceleration and velocity feedback showing unstable pole before 50Hz



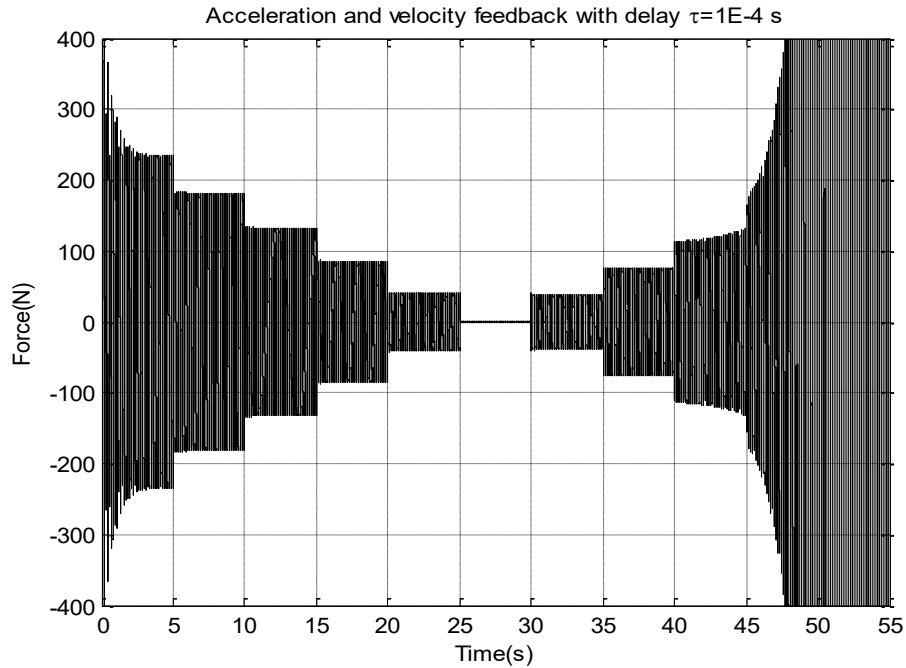


Figure 6-27 Time domain response of the control force with acceleration and velocity feedback with time delay. According to the findings presented in Figure 6-25, the system should suffer instability any time delay before 50Hz. By examining the graph of Figure 6-27, the system response is stable before 50Hz (0-25 seconds) despite the existence of time delay. This is clearly contrasting the stability results shown above. In fact the time domain simulation reveals that the system exhibits similar response to the position feedback case and the system becomes unstable at 53Hz (40 seconds). The findings from the time domain simulation have called for a further investigation into this major discrepancy. Referring to the SIMULINK model in Figure 6-26, the delay is introduced by a “Transport Delay” block. In the stability study that was carried out separately, the delay term was converted from an exponential function  $e^{-\tau s}$  to a rational function,  $1 - \tau s$ , using the first Taylor approximation. In fact, it was found that the operation of the “Transport Delay” block in SIMULINK differs from the Taylor approximation term where the latter is showing an unstable pole. In order to demonstrate the concept, the same simulation is carried out again whereby a transfer function representing the delay with Taylor approximation is used instead of the SIMULINK ready block as shown in the model of Figure 6-28. The time domain response is shown in Figure 6-29.

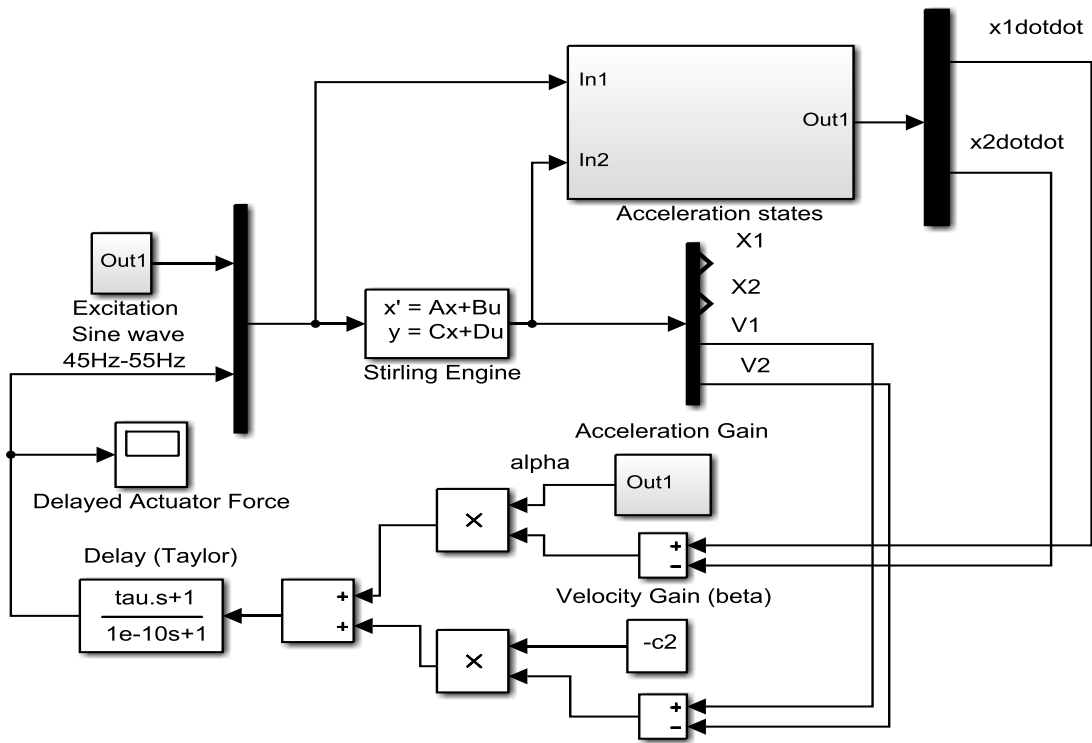


Figure 6-28 SIMULINK model with delay represented as per Taylor approximation

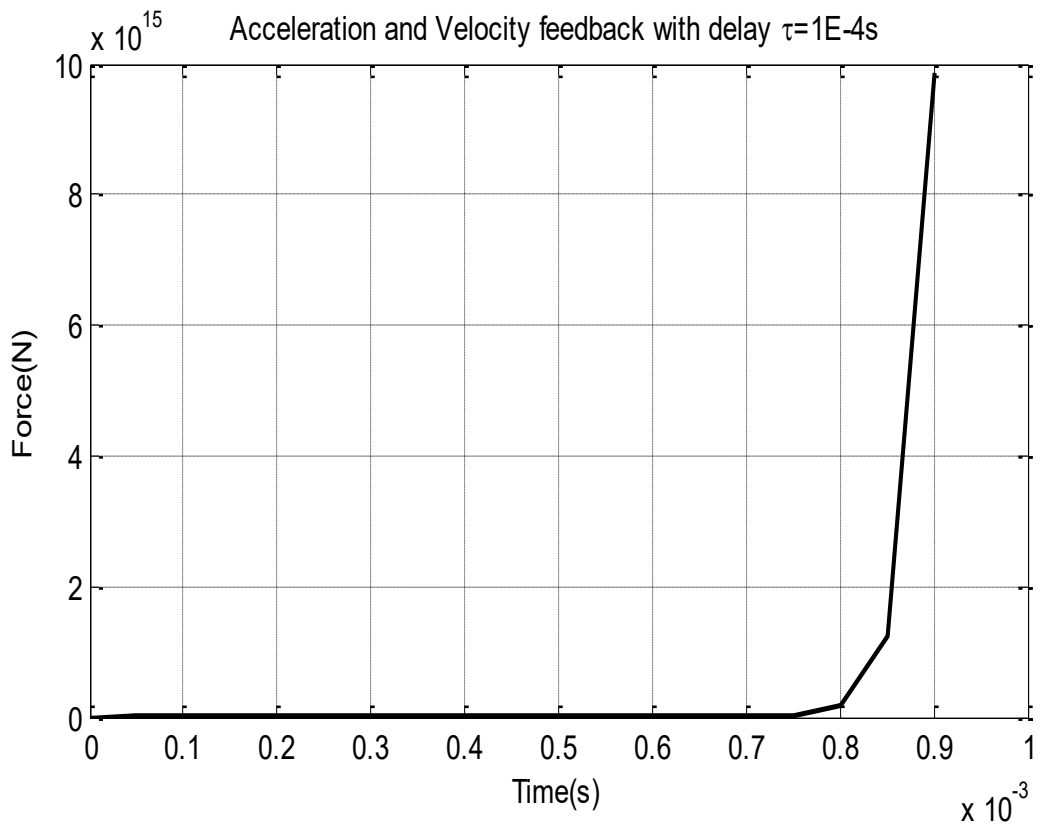


Figure 6-29 Time domain response with Taylor representation of time delay

The simulation reveals that the system becomes unstable if Taylor approximation is used to represent the delay in time simulation. While the first Taylor approximation is accurate enough for approximating small time delays, it introduces an additional pole corresponding to a higher order characteristic equation with acceleration feedback. For this reason, the stability is checked again with ignoring the first unstable pole and the following is obtained.

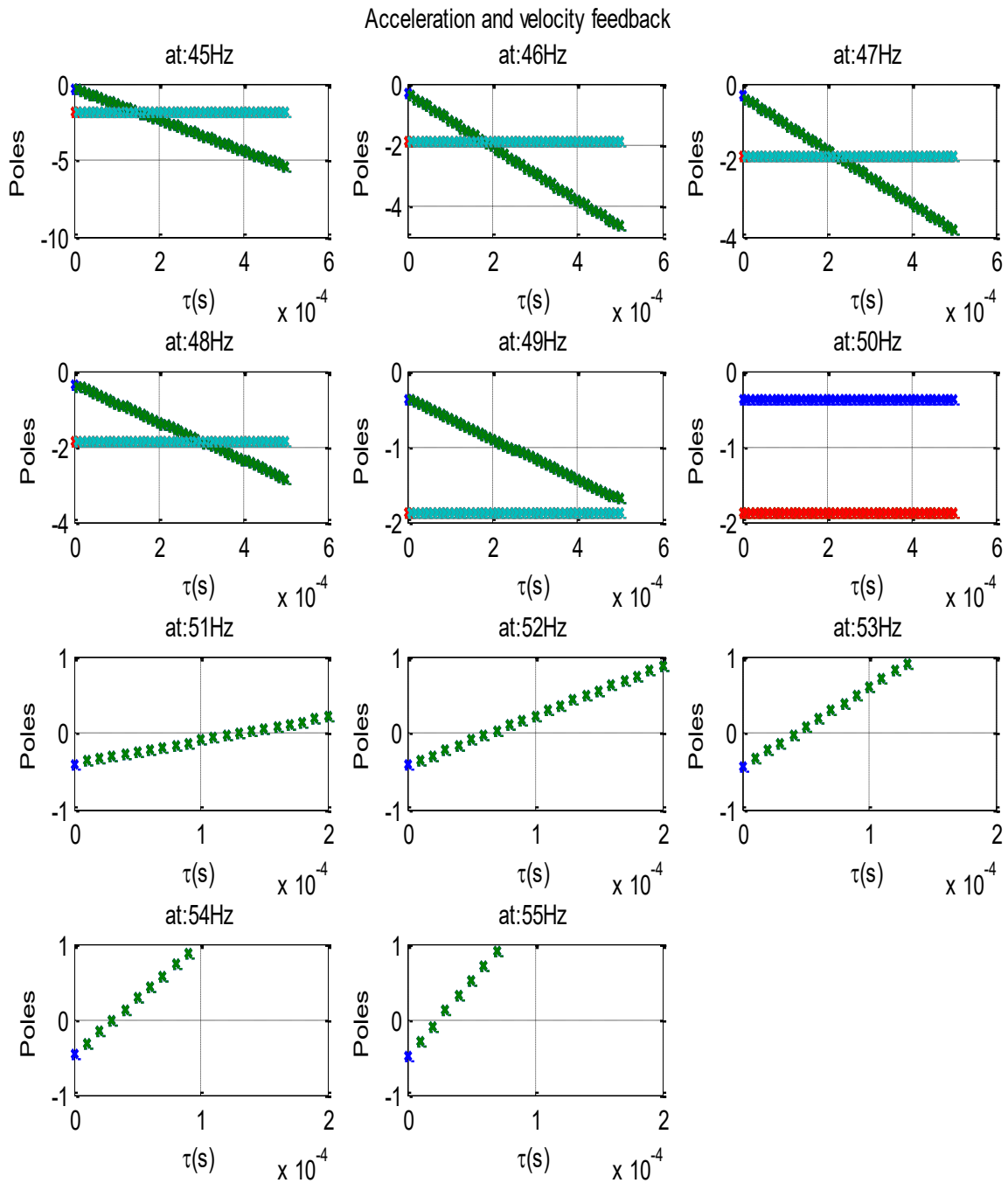


Figure 6-30 System pole variation with acceleration and velocity feedback ignoring the unstable pole before 50Hz

The results of the new stability conditions are shown in Figure 6-30 and they are similar to those of the position and velocity feedback in Figure 6-22. The new stability condition shows that the system is stable for excitations frequencies below 50Hz and becomes unstable after a certain time margin that decreases with increase in excitation frequency. To illustrate the finding, Figure 6-31 shows the time domain simulation results for different time delays. The results clearly match up with the stability conditions presented in Figure 6-30.

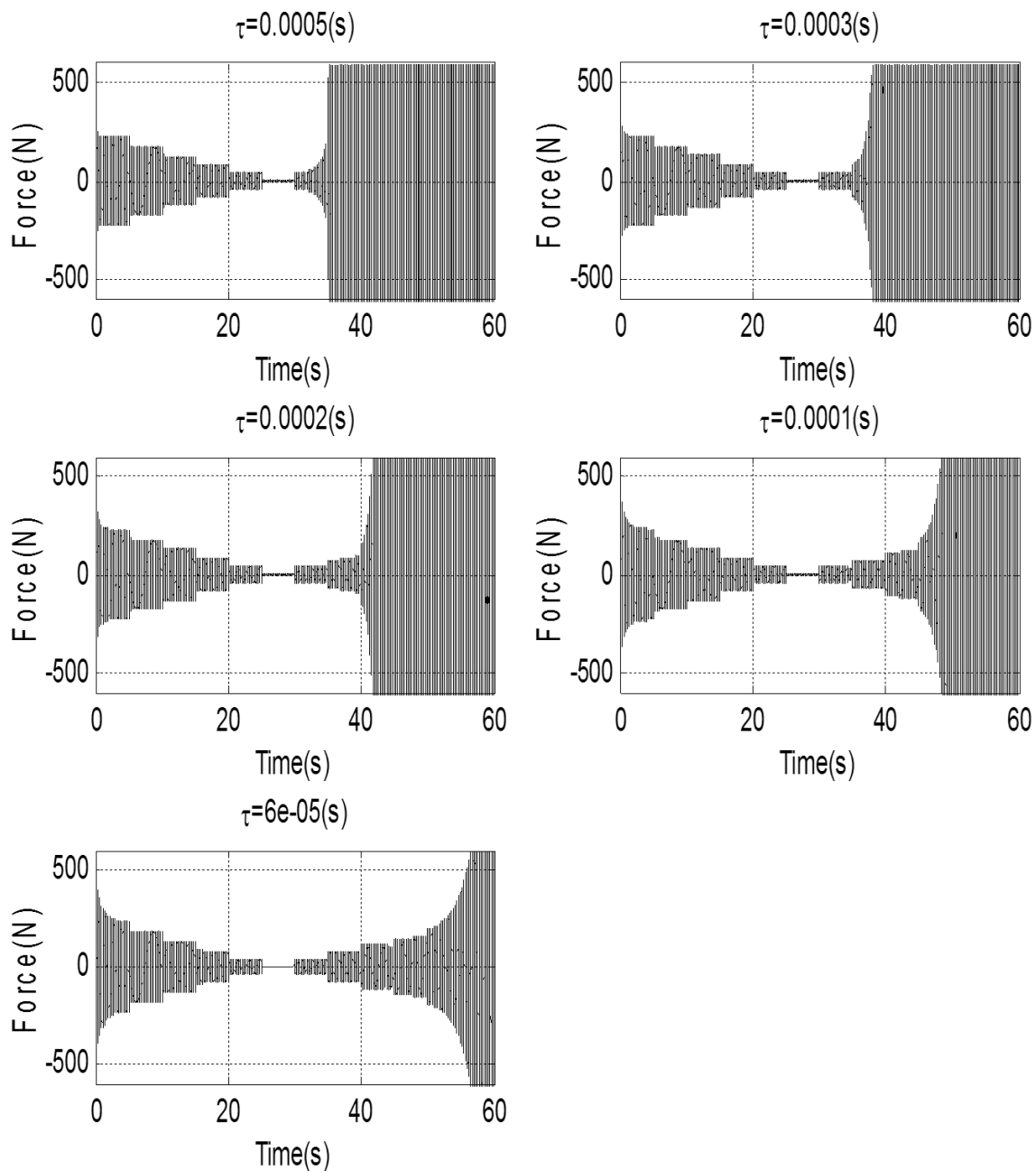


Figure 6-31 Time domain response of the control force with acceleration and velocity feedback

### 6.10.2 Delays with LQ Control

The actuator force with LQ control and time delay is expressed as follows

$$f_{act}(t - \tau) = -\mathbf{K}d(t - \tau)\mathbf{x} \quad 6-25$$

The closed-loop transfer function  $W(s)$  with LQ full-state feedback control strategy is expressed as

$$W(s) = \frac{X_1(s)}{F(s)} = \frac{(K_4\tau - m_2)s^2 + (K_2\tau - K_4 - c_2)s - k_2 - K_2}{a_0s^4 + a_1s^3 + a_2s^2 + a_3s^1 + a_4} \quad 6-26$$

$$a_0 = K_4m_1\tau - K_3m_2\tau - m_1m_2$$

$$a_1 = K_3m_2 - c_2m_1 - c_2m_2 - c_1m_2 - K_4m_1 + K_4c_1\tau - K_1m_2\tau + K_2m_1\tau$$

$$a_2 = K_1m_2 - c_1K_4 - k_1m_2 - k_2m_1 - k_2m_2 - c_1c_2 - K_2m_1 + K_2c_1\tau + K_4k_1\tau$$

$$a_3 = K_2k_1\tau - c_2k_1 - K_2c_2 - K_4k_1 - c_1k_2$$

$$a_4 = -K_2k_1 - k_1k_2$$

With LQ control, the gain matrix  $\mathbf{K}$  is determined following the procedure presented previously. The parameter  $K_i$  represents the element at index  $i$  of the LQ gain matrix. The delays expression is rationalised with first order Taylor approximation.

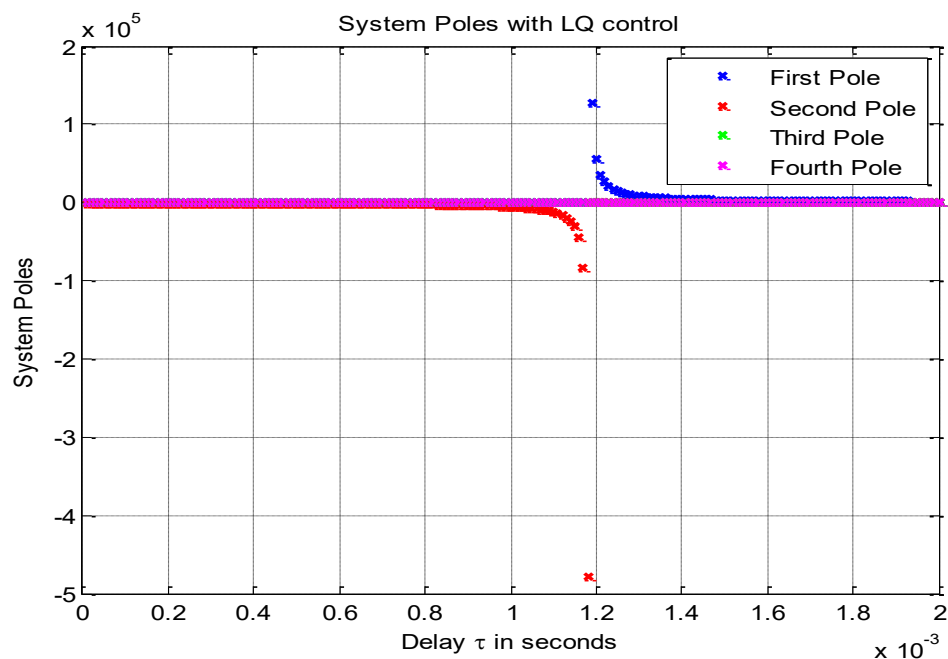


Figure 6-32 System poles variation with LQ control

According to the above graph, for the chosen  $K$  matrix, stability with LQ control is affected by time delays as one of the poles become unstable. Unlike with gain scheduling control, the LQ control allows for a larger delay margin as depicted in Figure 6-32. The first pole becomes unstable after almost 1.2ms.

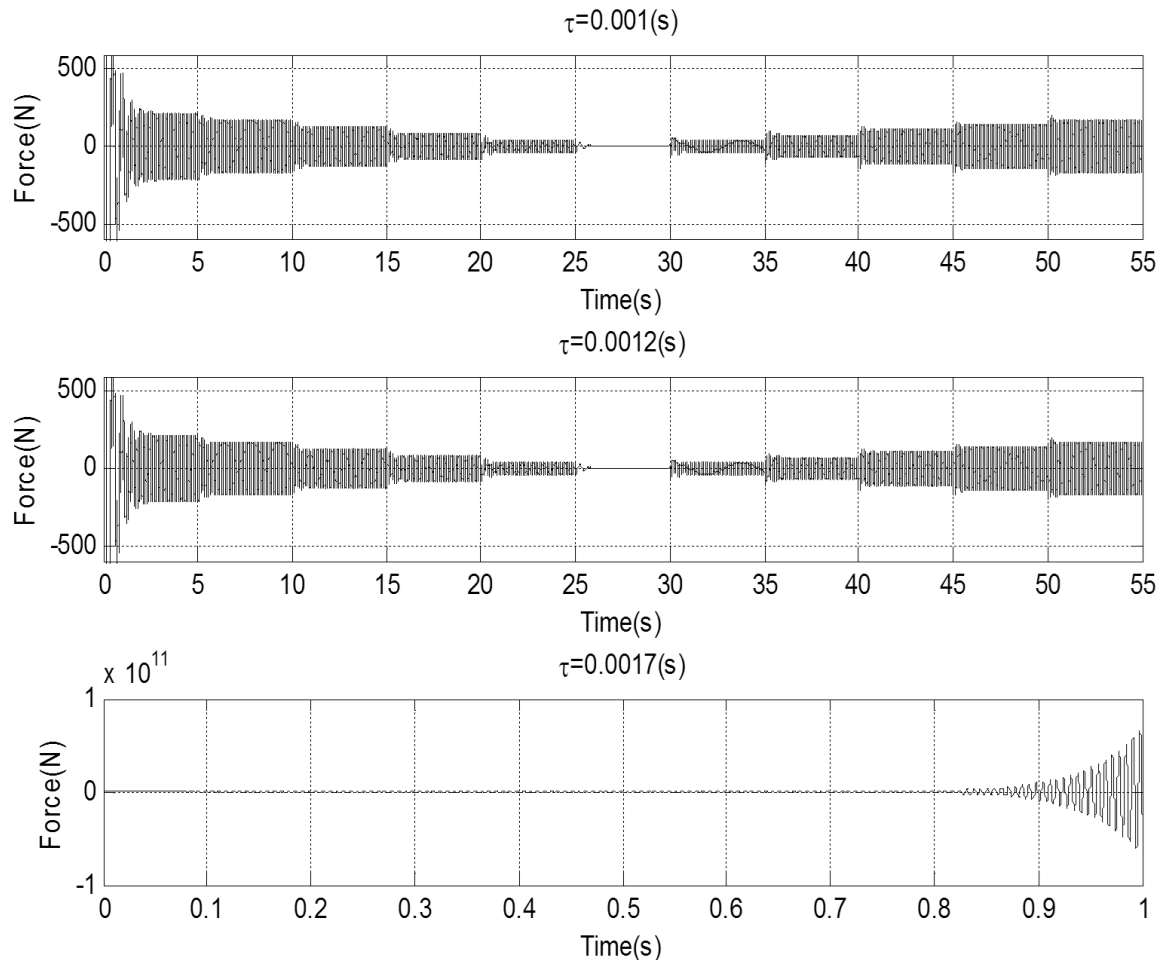


Figure 6-33 Time domain response of the control force with LQ control

The graphs of Figure 6-33 depict the time domain response of the actuator force with LQ control for different values of time delay. By examining the second graph, the time domain response is stable however, according to Figure 6-32 which reveals that the time delay margin is around 1.19ms, the response should be unstable for the value of time delay (1.2ms) because it is greater than the critical time delay margin. This discrepancy is attributed to the fact that for large values of delays, the Taylor approximation becomes less accurate, which is the case in encountered.

## 7 Experimental Setup and Implementation

### 7.1 Test Rig

A test rig emulating the behaviour of the Stirling engine is built for the purpose of demonstrating the concept of active damping experimentally. An electrodynamic shaker (V406) from B&K is mounted as shown in the Figure 7-1. The shaker acts as the source of sinusoidal excitation to the shaker table which, in turn, is fitted with a helical spring absorber originally tuned at 50Hz that acts as a TMD. The TMD consists of a mass and a helical spring attached horizontally on top of the shaker table. The mass ratio,  $\mu$ , is chosen carefully to match that of the Stirling engine. In its passive form, the absorber should attenuate the vibration of the shaker table at its tuned resonant frequency. The intention is to insert a voice coil actuator between the shaker table and the dynamic mass of the absorber to perform the active damping. The following diagram shows the initial test rig alongside its equivalent vibration model.

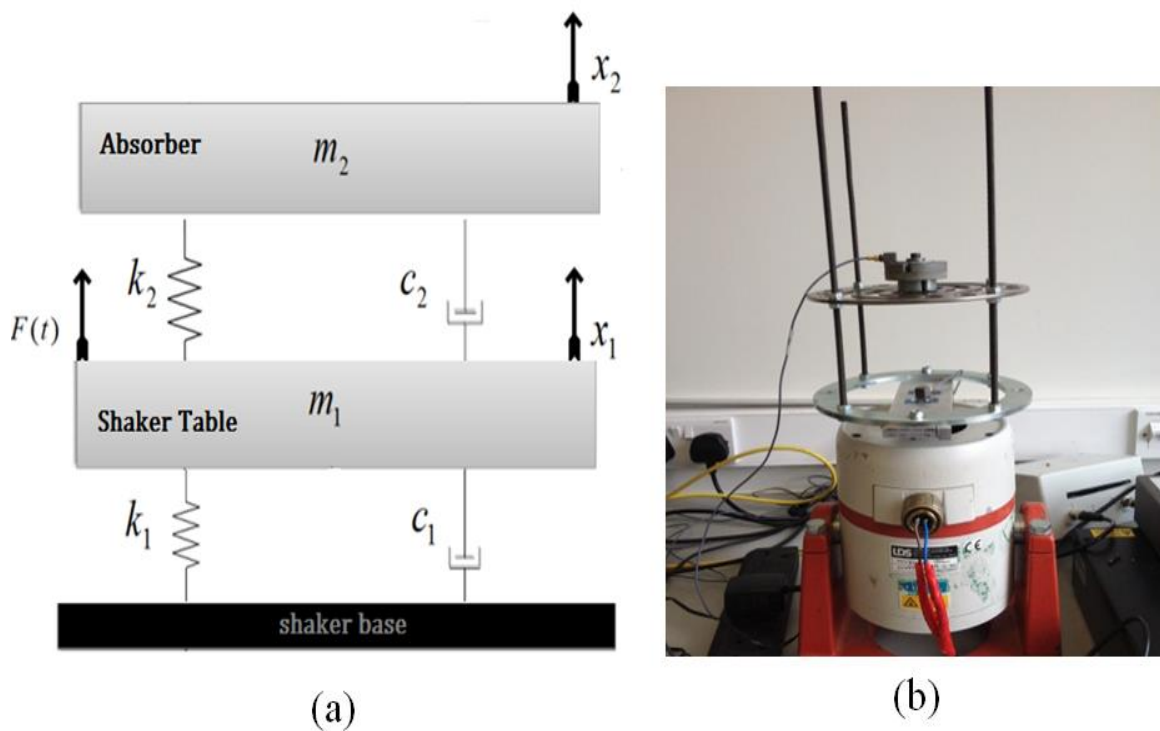


Figure 7-1 Initial test rig

In the model of Figure 7-1 (a), the mass  $m_1$  consists of the shaker table mass, studs, holding ring, and the stationary mass of the TMD. The dynamic mass  $m_2$  consists of the moving part of the helical spring (yet to be determined) in addition to an extra mass added for tuning. The availability of a mathematical model of the above rig allows for a better prediction of the system response before control implementation. In addition to that, the required actuator specification to perform the active damping, such as force, strokes, voltage, current, bandwidth, and power consumption, will be extracted and a suitable actuator will be chosen based on the test rig model simulation.

## 7.2 Determination of the Helical Absorber Parameters

Accurate data about the dynamic mass and the spring stiffness of the helical spring is not available. This section presents a heuristic procedure to estimate the stiffness and dynamic mass of the helical TMD based on an experimental set of tests using the shaker rig. An optimisation technique is followed for finding the TMD parameters based on a parameter fitting process of the experimental results. The only available information is that the natural resonant frequency of the bare helical TMD is around 100Hz and that the damping in the helical spring is negligible.

Assuming that the TMD behaves as an SDOF system, the idea is to utilise the shaker rig to excite the TMD system with a frequency sweep from 5Hz to 150Hz with different dynamic masses for each sweep. By measuring the transmissibility from shaker table acceleration to the TMD acceleration, the resonant frequency of the TMD,  $\omega_n$ , at which maximum transmissibility occurs, is recorded. The resonant frequency of the TMD varies according to  $\omega_n^2 = k/(m + m_n)$  where  $k$  represents the unknown stiffness coefficient of the helical spring,  $m$  the dynamic mass and  $m_n$  the added mass. The equation can then be transposed to show that  $k = \omega_n^2(m + m_n)$  and  $m = \frac{k}{\omega_n^2} - m_n$ . The idea is to follow a parameter fitting

technique based on a reverse optimisation process. Before each frequency sweep of the shaker table, a known mass is added to the dynamic mass of the helical spring and the resonant frequency is recorded during the sweep. The optimisation function aims to find the values of  $k$  and  $m$  for a set of added masses  $m_n$  and their associated frequencies  $\omega_n$  in such a way that would minimize a function  $Z$  shown in 7-1. Matlab function “FMINSEARCH” is used to find the minimum of  $Z$  starting with initial estimates of  $m$  and  $k$ . This is generally referred to as unconstrained nonlinear optimization.

$$Z = \sum_{i=0}^{N-1} \sum_{j=i+1}^N \left[ [\omega_i^2(m + m_i) - \omega_j^2(m + m_j)]^2 + \left[ \left( \frac{k}{\omega_i^2} - m_i \right) - \left( \frac{k}{\omega_j^2} - m_j \right) \right]^2 \right] \quad 7-1$$

Where  $i$  is the index for the current test and  $j$  the index for the previous test.  $N$  is the total number of tests.  $\omega_i$  and  $\omega_j$  are the recorded natural frequencies at each test.



Figure 7-2 Helical spring used in the design of an ATMD

Each frequency sweep involves adding some known mass to the dynamic mass where the frequency at which the maximum transmissibility occurs is measured. The chart of Figure 7-3 shows the measured frequencies for the different added masses at which maximum transmissibility occurs.

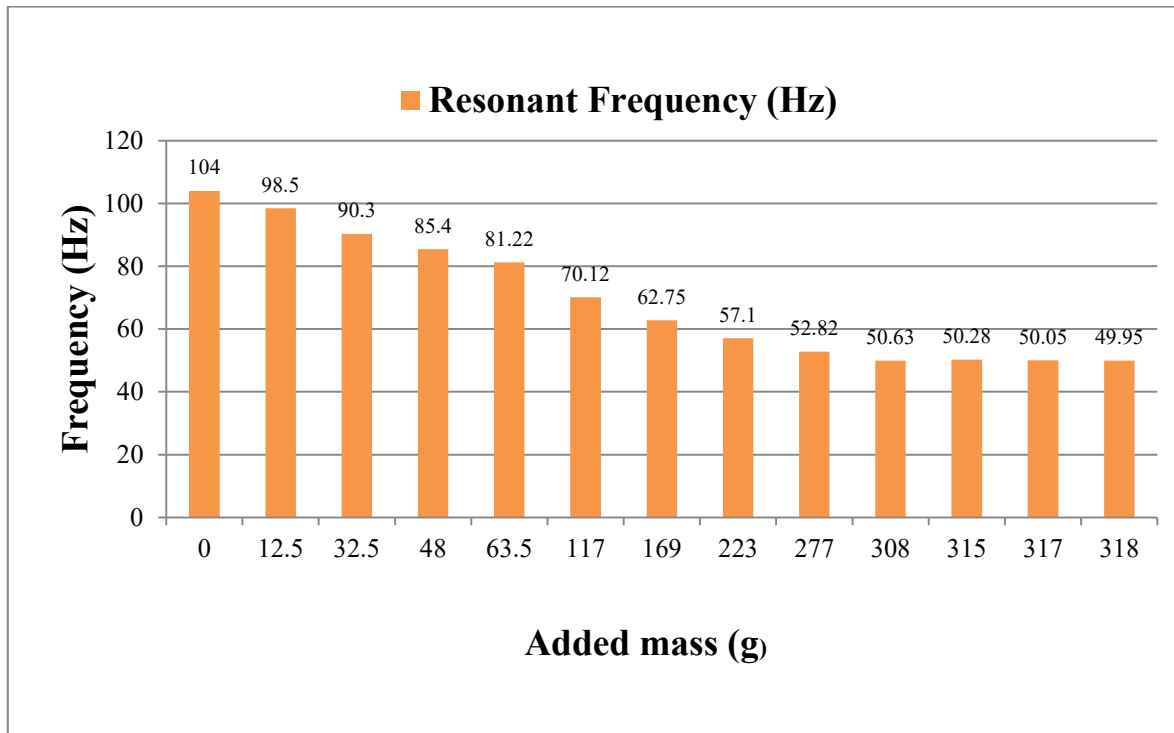


Figure 7-3 Test results

Based on the optimisation problem, the values of the stiffness and mass were determined as  $k = 40714 \text{ N/m}$  and  $m = 0.0946 \text{ kg}$ .

The aim is now to add the proper mass to the TMD that would make it resonate at 50Hz. The dynamic mass for the TMD to be tuned at 50Hz is calculated following this equation  $m_n = \frac{k}{\omega_n^2}$  which yields  $m_n = 0.4125 \text{ kg}$ . Thus the mass to be added to the absorber is  $m = 0.3179 \text{ kg}$ .

### 7.3 Test Rig Simulation and Experimental Validation

This section is dedicated to modeling and validating a proposed model of the test rig. The idea is to perform simulations with the integration of the control system. A set of simulations and experimental tests will be carried out and the results from both will be compared for validation. In the proposed model, the equations that relate the dynamic mechanical system to the electrical system of the dynamic shaker for the above test rig are presented in 7-2

$$\begin{cases} m_1\ddot{x}_1 + k_1x_1 + c_1\dot{x}_1 + k_2(x_1 - x_2) + c_2(\dot{x}_1 - \dot{x}_2) = F_{sha} \\ m_2\ddot{x}_2 + k_2(x_2 - x_1) + c_2(\dot{x}_2 - \dot{x}_1) = 0 \\ V_{sha} = R_{sha}i_{sha} + L_{sha}\frac{di_{sha}}{dt} + k_{sha}(\dot{x}_1) \\ F_{sha} = k_{sha}i_{sha} \end{cases} \quad 7-2$$

The shaker system is modelled as an RL system with  $V_{sha}$ ,  $I_{sha}$  representing the voltage across and the current through the shaker terminals. The terms  $R_{sha}$ ,  $L_{sha}$ ,  $k_{sha}$  represent the motor coil's inductance, resistance, and the motor constant of the shaker respectively. Table 7-1 contains the parameters of the rig that are used. Those parameters will be used to perform a simulation of the proposed model using MATLAB/SIMULINK software. The simulation results will be compared with test results for the purpose of validating the proposed test rig model.

Table 7-1 Test rig parameters

Mechanical	Electrical
$m_1 = 1.80 [kg]$	$V_{sha} = 3 \sin(2\pi ft)[V]$
$m_2 = 0.4125 [kg]$	$L_{sha} = 1.8 [mH]$
$c_1 = 5 [Ns/m]$	$R_{sha} = 1.2 [\Omega]$
$c_2 = 0.5 [Ns/m]$	$k_{sha} = 11.1 [N/A]$
$k_1 = 12300 [N/m]$	$f = [5 - 100][Hz]$
$k_2 = 40714 [N/m]$	$T = 55 [s]$

The first test is carried out to verify the proposed model against experimental results. In this test, the shaker controller is commanded with a 3 Volts sinusoidal excitation in open-loop with a frequency range 5Hz-100Hz. The shaker controller is actually a 24-bit vibration control system connected to a linear power amplifier (PA 100 E). Two accelerometers with dynamic range of  $\pm 71g$  located in the middle of the shaker table and the TMD mass are employed for measuring the acceleration in the axial direction. The sensors are connected to the shaker controller for recording. In addition to that, current and voltage sensors were used to measure the electrical current and the voltage in the shaker coil.

In this test, the relevant mass is added to the TMD to tune its resonant frequency at 50Hz. The shaker table is attached to a spring with axial stiffness  $k_1$  which tunes the composite system at around 11.8 Hz. The graphs of Figure 7-4 show the theoretical simulation response of the proposed model alongside the experimental test results.

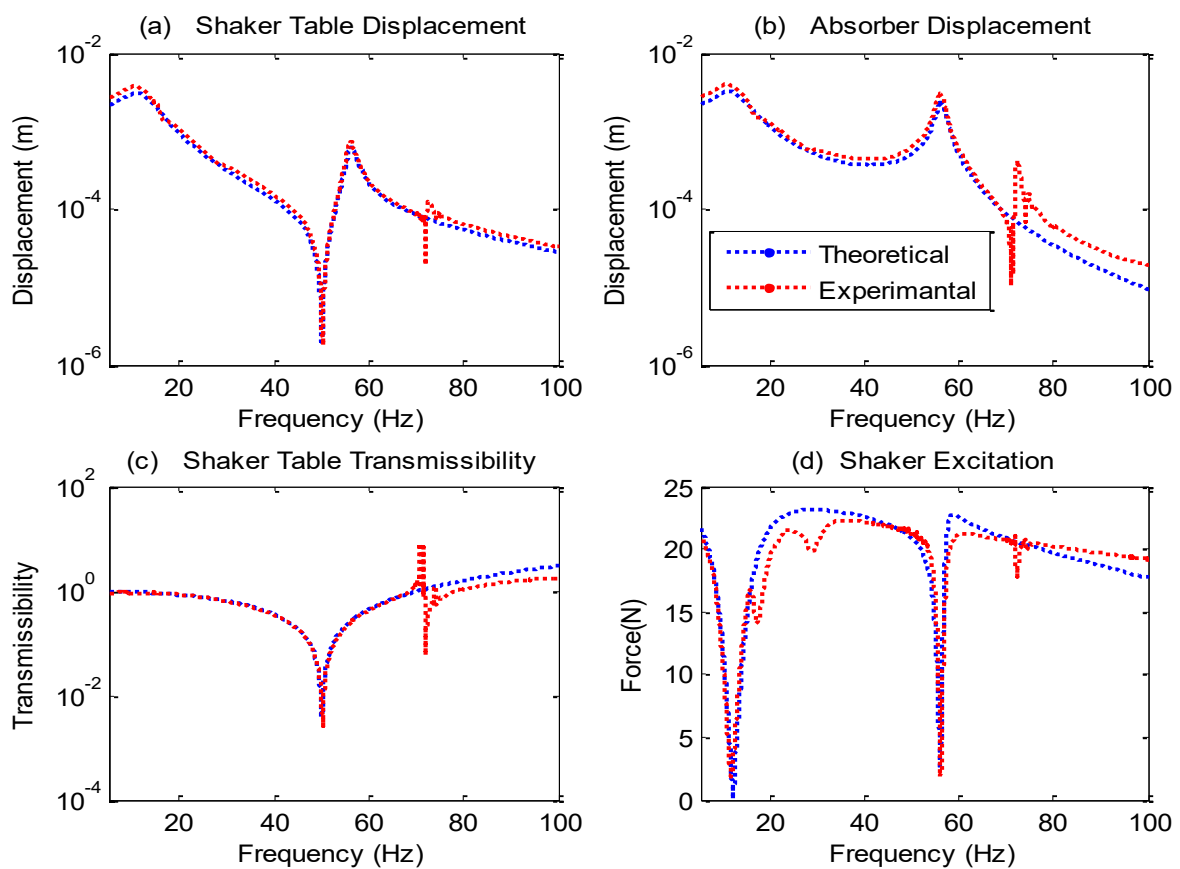


Figure 7-4 Theoretical model results vs experimental results without the VCM

The graphs reveal that the theoretical results match very well with the test results. The plot in (a) shows the curves of the displacement of the shaker table with two peaks between 5-100Hz corresponding to the two resonant modes of the composite system. At 50Hz, it is observed the displacement of the shaker table is attenuated to a minimum value due to the effect of the TMD. This is also implied in (c) where the excitation force is transmitted completely from the shaker table to the TMD mass at this frequency. The shaker excitation force plot depicted in (d) is obtained by measuring the shaker electrical current and taking the result of its product with the shaker motor constant  $k_{sha}$ . It is revealed that the shaker virtually requires no driving force in order to excite the system at its natural resonances. The experimental results also show that there exist dynamics at 70Hz that do not appear in the theoretical model. The existence of those dynamics is related to some other resonance in the real system related to the design of the rig where the theoretical model did not cater for. The design of the rig has undergone improvements as explained in the following section.

#### **7.4 Test Rig Enhancement**

Upon further examination of the rig while under test, it was found that the long studs that appear in Figure 7-1 exhibit lateral vibration at around 70Hz. It was then implied that the long studs possess a natural resonance around this frequency. This justifies the dynamics that appeared around this frequency in the test results shown in Figure 7-4. For this reason the studs were cut short and the dynamics have disappeared. Figure 7-7 further illustrates the results after cutting the studs short and adding a VCM. Furthermore, it was observed that both the shaker table and the TMD exhibit some lateral motion which may have an adverse effect on the actuator when connected between the shaker table and the absorber. Specifically, if a linear VCM is added, the motor coil may exhibit an eccentric motion relative to the motor base which results in an unbalance in the air gap and therefore less efficient actuation force. In order to investigate the lateral motion occurring on the shaker

table and the absorber mass, a test was carried out while placing the two accelerometers in the centre of the shaker table and the centre of the TMD facing horizontally to detect lateral vibrations. The shaker is excited using sinusoidal signal with 1.5V amplitude and frequency range between 5Hz-100Hz in open-loop. The test results of Figure 7-5(a) show that the difference in lateral vibration of the two structures is significant at some frequencies and insignificant at others. The RMS value of the error between the two accelerations is determined and found to be 3.3. As a remedy, the test rig was modified by adding rigid hollow rods to support the stud that connect the shaker table to the absorber mass. In addition to that, extra washers were inserted for each nut to level the absorber mass accurately. The same test was carried out after the rig enhancement and the results are presented in Figure 7-5(b). It is implied that the enhancement has improved the performance of the rig and that the lateral vibration of the two structures is not only reduced at all frequencies, but also match closely. The RMS error after enhancement was reduced to 0.8.

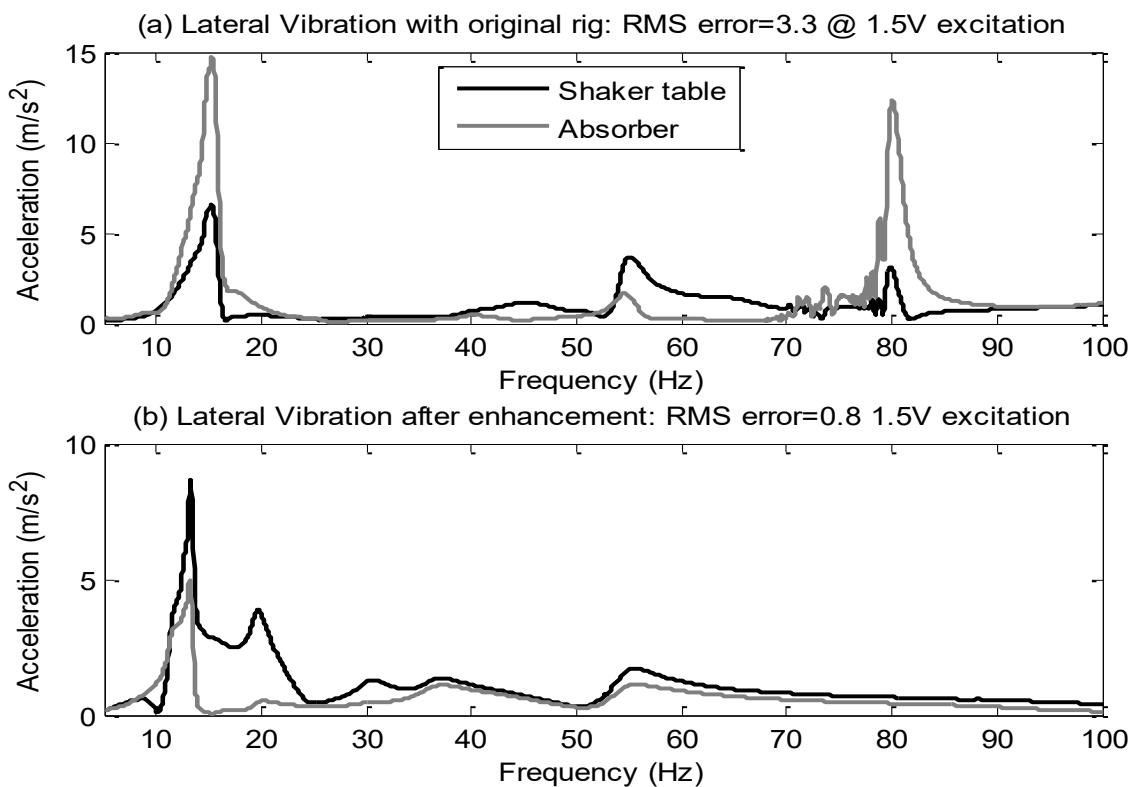


Figure 7-5 Lateral Vibration

## 7.5 Test Rig with a Voice Coil Motor (VCM)

### 7.5.1 Modelling with VCM

The previous section presented the verification of the theoretical model with experimental results without an actuator connected between the shaker table and the absorber's dynamic mass. In this section, an off-shelf voice coil motor (VCM) from Moticon (GVCM-051-051-01) is connected to the shaker rig as depicted in Figure 7-6. The validated model from the previous section is now extended to include the dynamics of the VCM in addition to the feedforward gain scheduling with zero-placement control equations. The TMD will be referred to as an ATMD after the addition of the VCM.



Figure 7-6 Shaker with absorber and VCM test rig

The coupling equations of the electrodynamic shaker, the absorber, and the VCM are derived following Newton's second law of motion and Lorentz law as shown in equation system 7-3.

$$\begin{cases} m_1\ddot{x}_1 + k_1x_1 + c_1\dot{x}_1 + k_2(x_1 - x_2) + c_2(\dot{x}_1 - \dot{x}_2) = F_{sha} - f_{act} \\ m_2\ddot{x}_2 + k_2(x_2 - x_1) + c_2(\dot{x}_2 - \dot{x}_1) = f_{act} \\ V_{vcm} = R_{vcm}i_{vcm} + L_{vcm}\frac{di_{act}}{dt} + k_{vcm}(\dot{x}_1 - \dot{x}_2) \\ f_{act} = k_{vcm}i_{vcm} \\ V_{sha} = R_{sha}i_{sha} + L_{sha}\frac{di_{sha}}{dt} + k_{sha}(\dot{x}_1) \\ F_{sha} = k_{sha}i_{sha} \end{cases} \quad 7-3$$

The model from the previous section is extended with the addition of an RL circuit equation with a back EMF element to represent the VCM. The terms  $V_{act}$  and  $i_{act}$  represent the voltage across and the current through the VCM terminals.  $R_{vcm}$ ,  $L_{vcm}$ ,  $k_{vcm}$ , represent the VCM coil's inductance, resistance, and motor constant respectively. In the new model, the mass  $m_1$  constitutes the shaker table, holding ring, studs and rods, and the VCM stationary base. The mass  $m_2$  comprises the dynamic mass of the TMD, an addition mass added for tuning, and the motor coil. The values of the back EMF constant and the motor constants for both the shaker and the VCM actuator are used as per the manufacturer's data sheets. The equations are derived as follows

For the frequency domain simulation with the VCM, the values of Table 7-1 are adopted in addition to the parameters of the VCM that are presented in Table 7-3. For validation purposes, two cases will be considered here, simulation with open-circuited VCM and the simulation with short-circuited VCM.

### 7.5.2 Model Validation Test 1: Open-Circuited VCM

The extended model is simulated assuming sinusoidal excitation of 3V amplitude between 5Hz-100Hz. Experimental tests are performed under similar conditions to the simulation in order to allow for comparison of data. The frequency domain results from simulation are plotted alongside the experimental test results. In the first experiment, control is off ( $f_{act} =$

0) and the VCM terminals are left open because the intention of this test is to verify the proposed model before performing the control action. The results from both the simulation and experiments are depicted in the graphs of Figure 7-7. They reveal a very close match between the theoretical model predictions and the experimental results. Perhaps the most important discrepancy between the two plots is the mismatch in the level of attenuation that exists in the frequency range 40Hz - 60Hz in all the four plots. The reason for this mismatch is that in the simulation, the damping value of ATMD was randomly chosen as  $c_2 = 0.5 \text{ Ns/m}$  however in reality the VCM introduced more damping.

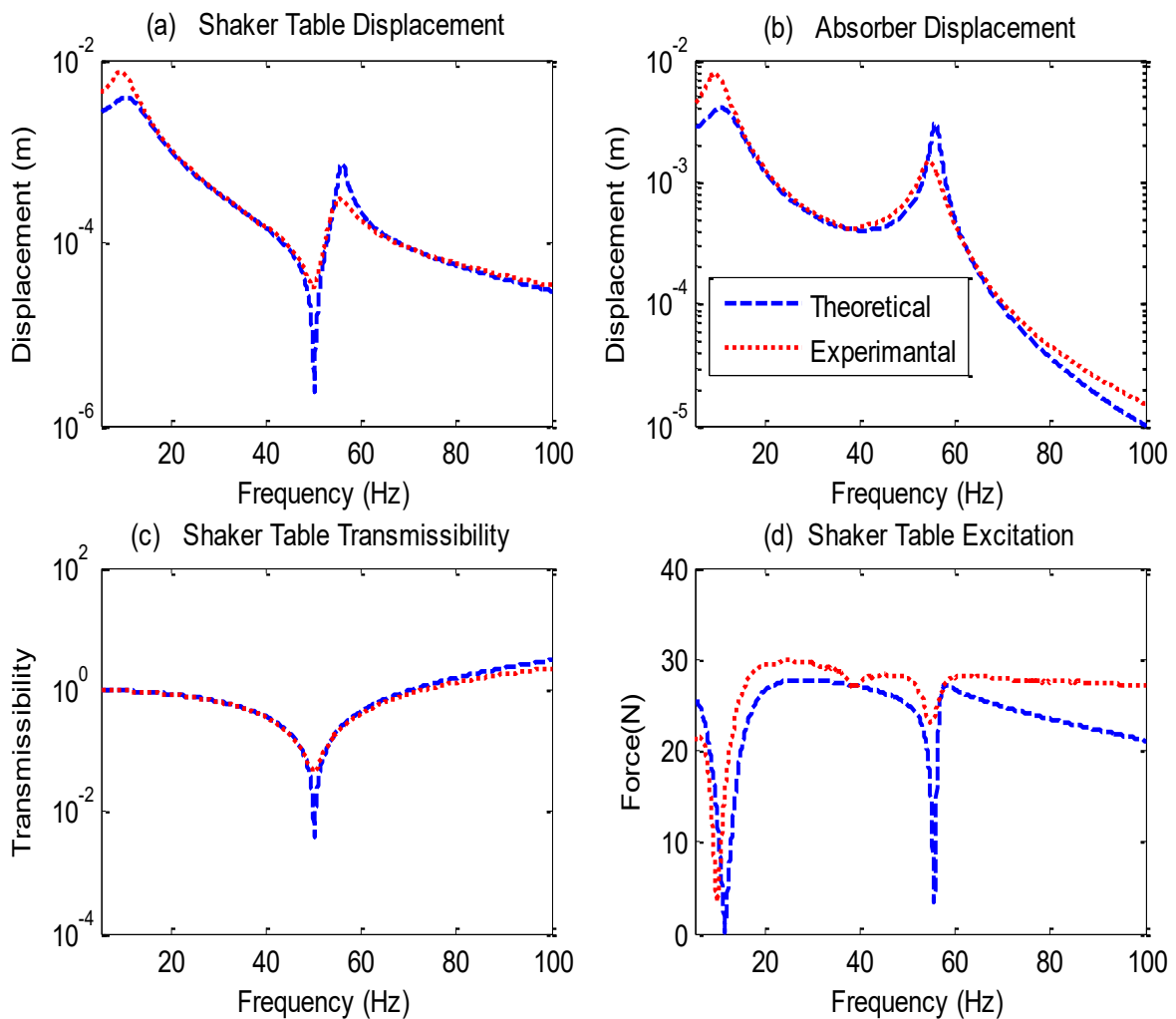


Figure 7-7 Theoretical model results vs experimental results with open circuited VCM

The experimental results shows less attenuation at 50Hz which the original tuning of the ATMD indicating to a higher damping coefficient  $c_2$  introduced by the VCM. By reverse fitting the theoretical simulation to that of the experimental response, the value of the damping coefficient was obtained ( $c_2 = 7 \text{ Ns/m}$ ) and the model parameters were updated to match the real system response. A new simulation was carried out with ( $c_2 = 7 \text{ Ns/m}$ ). The graphs of Figure 7-8 show the response of the updated theoretical model alongside the experimental results.

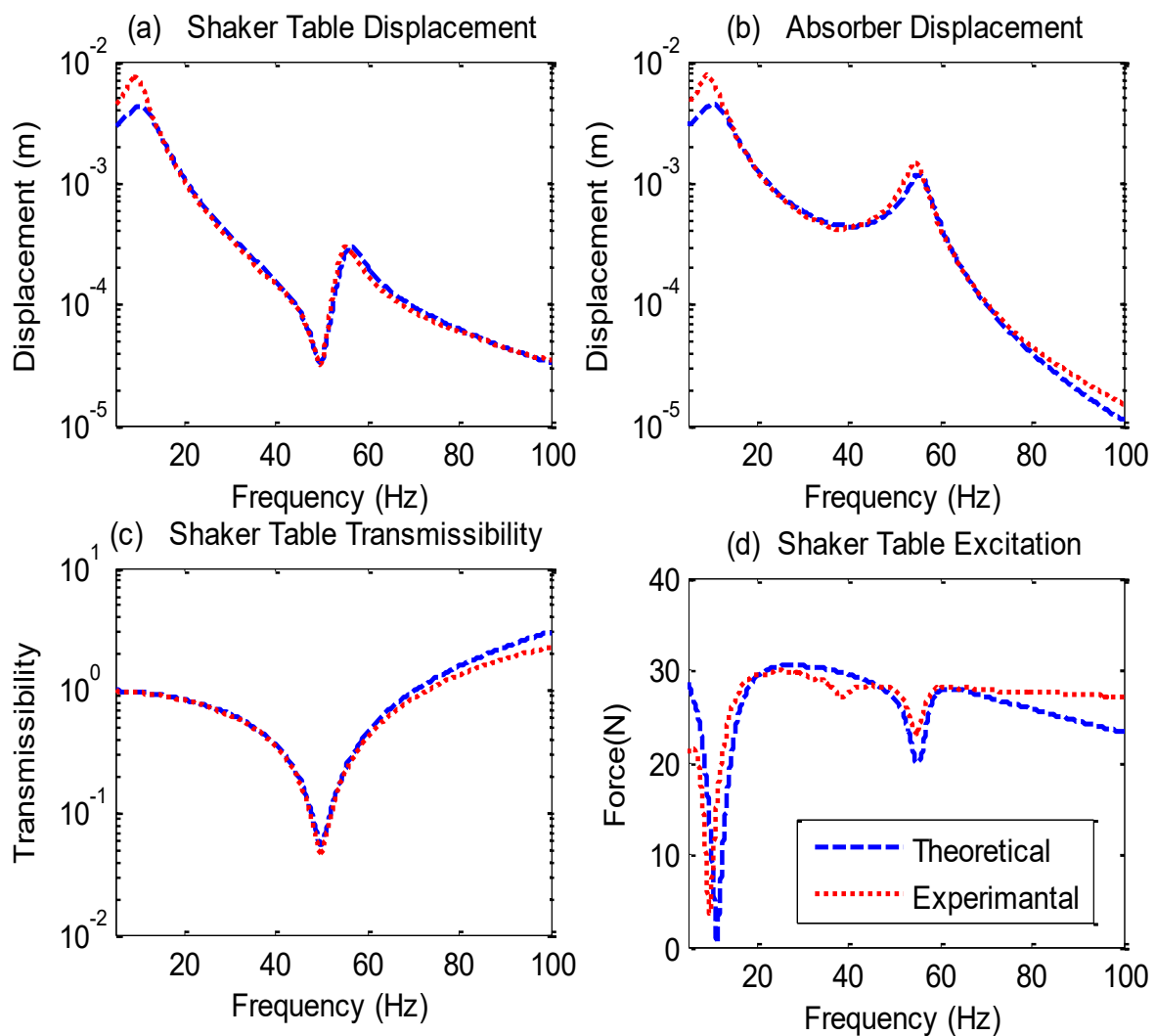


Figure 7-8 Updated theoretical model results vs experimental results with open circuited VCM ( $c_2 = 7 \text{ Ns/m}$ )

### 7.5.3 Model Validation Test 2: Short-Circuited VCM

This section discusses the experimental verification of the model when the VCM terminals are shorted. The experimental results are shown in Figure 7-9 alongside the results predicted by simulation. The first observation that can be made is that less attenuation is achieved in the shaker table displacement compared to the theoretical expected results at 50Hz. It can be implied that further damping in the ATMD is incurred due to the electromechanical interaction of the VCM components when its terminals are shorted. The extra damping is due to the eddy current losses and the Joule losses in the VCM.

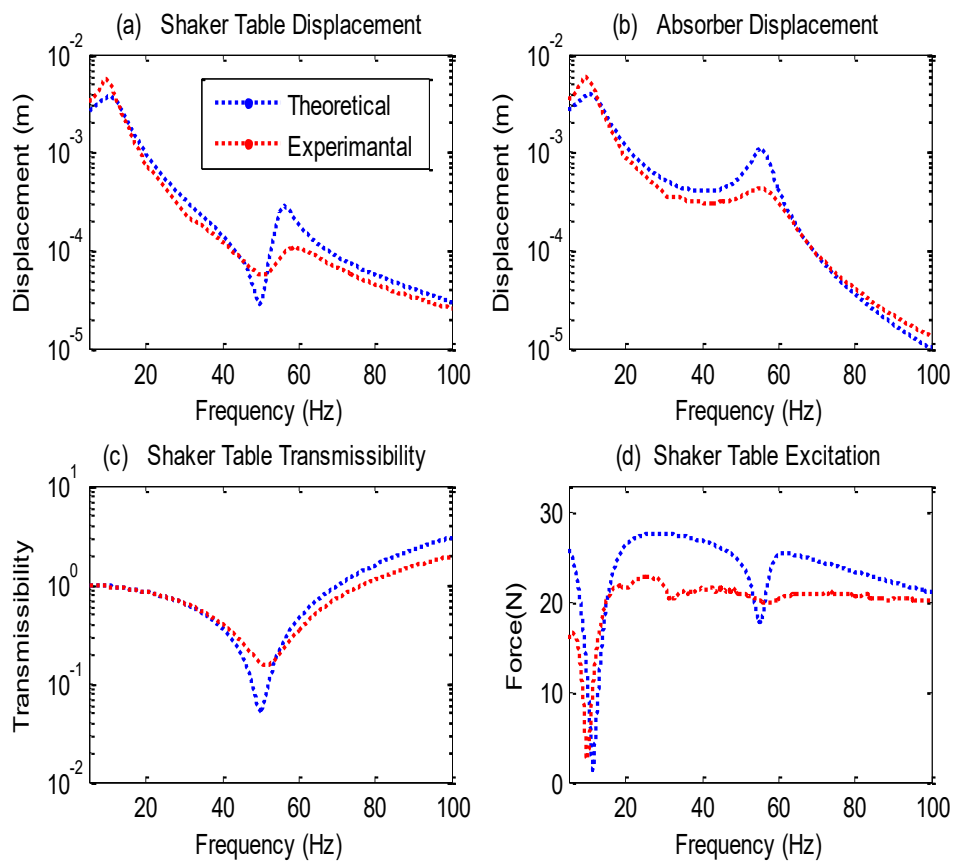


Figure 7-9 Model verification with short circuited VCM

The new value of the damping coefficient is determined by reverse fitting of the theoretical simulation so they align with those obtained experimentally. Referring to Figure 7-10, the value of damping was implied to be  $c_2 = 20.5 \text{ Ns/m}$ .

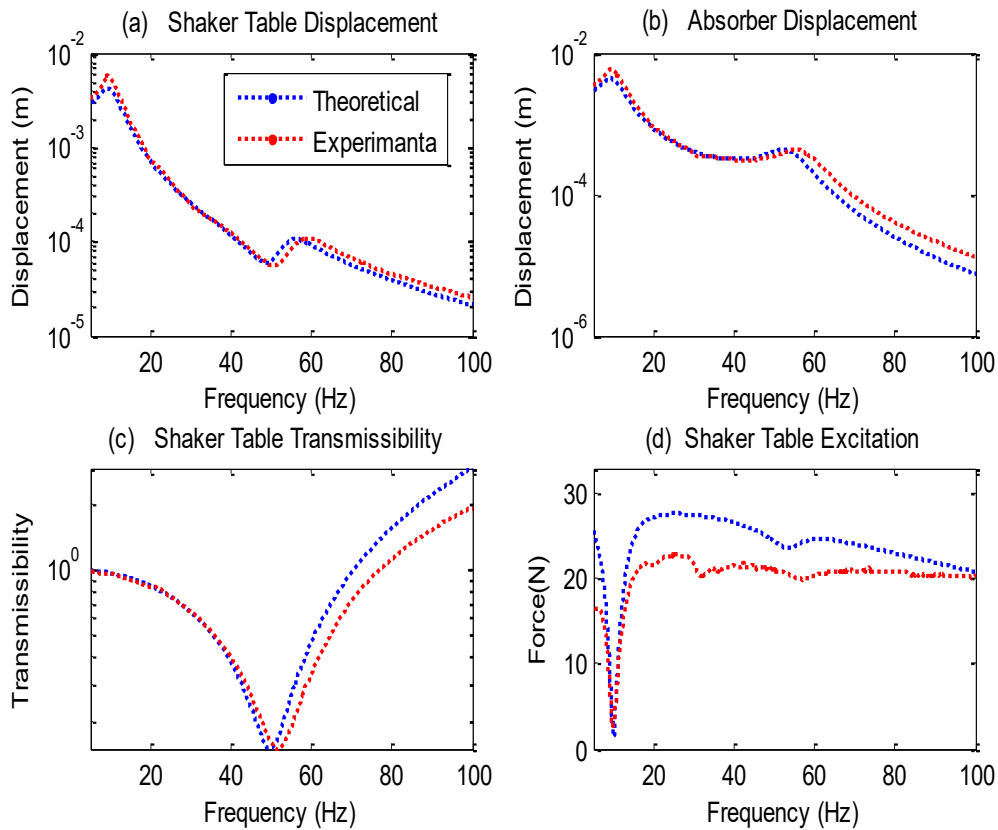


Figure 7-10 Short-circuited VCM with damping  $c_2 = 20.5 \text{ Nm/s}$

On the other hand, it can be observed that there has been a slight variation of the resonant frequency of the ATMD system manifested by a slight frequency shift observed on the graphs of the experimental results. In fact this change in the tuning frequency of the ATMD was not observed in the previous case. The change in frequency to a higher value is attributed to the inductance of the VCM. The effect of the motor inductance is analogous to the effect of the mass in the mechanical system. This conclusion is further elaborated in the next section.

#### 7.5.4 Model Validation Test 3: Powered VCM

The slight variation in the resonant frequency of the ATMD that was indicated to in the previous section is now illustrated with emphasis on the voltage drop across the motor coil. A new test was carried out similar to the previous test; however the VCM terminals are not shorted but powered through a power amplifier. A LabVIEW code is designed to control the voltage across the VCM terminals throughout the test. The code was implemented on the

FPGA of a compact RIO with a loop iteration time of  $20\mu\text{s}$ . In the code, the current through the VCM ( $i_{vcm}$ ) is measured using a low noise non-contact current probe with a wide frequency bandwidth range of DC to 5MHz capable of detecting 10mA to 20A peak to peak. The time derivative of the electrical current signal in the VCM is taken and then a voltage proportional to  $-L_{vcm} \frac{di_{vcm}}{dt}$  is delivered to the VCM via a power amplifier. This delivered voltage shall compensate for any voltage dropped across the VCM coil assuming its inductance doesn't change. Figure 7-11 shows the results obtained in Test 1, Test 2, and Test3. It is revealed that when the voltage drop across the coil was compensated actively, the slight variation in the resonant frequency of the ATMD disappeared.

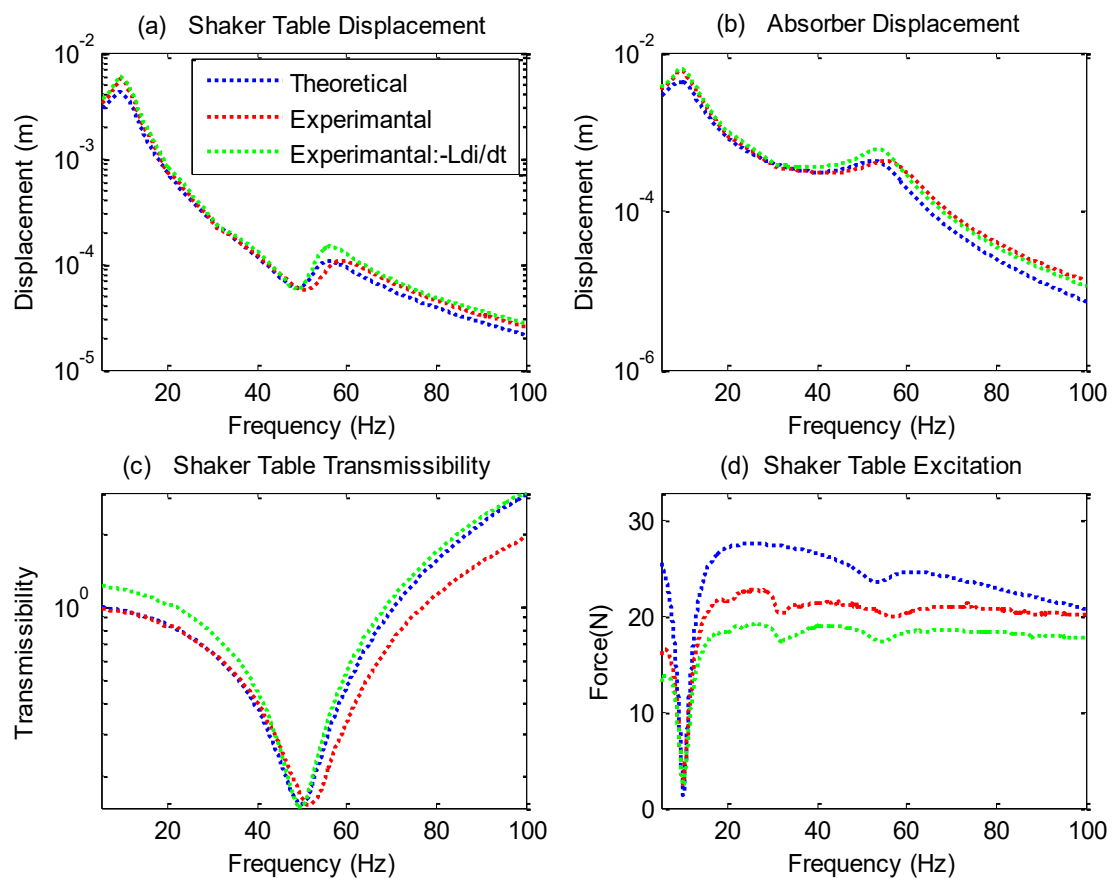


Figure 7-11 Updated theoretical model results vs experimental results with short circuited VCM

## 7.6 Active Damping Control Simulation with Test Rig Model

In this section, the validated model of the test rig with the VCM is now extended to incorporate the control action. The equations that describe the model dynamics are represented in equation system 7-4 and its state-space representation is shown below.

$$\begin{cases}
 m_1 \ddot{x}_1 + k_1 x_1 + c_1 \dot{x}_1 + k_2(x_1 - x_2) + c_2(\dot{x}_1 - \dot{x}_2) = F_{sha} - f_{act} \\
 m_2 \ddot{x}_2 + k_2(x_2 - x_1) + c_2(\dot{x}_2 - \dot{x}_1) = f_{act} \\
 F_{sha} = k_{sha} i_{sha} \\
 V_{sha} = R_{sha} i_{sha} + L_{sha} \frac{di_{sha}}{dt} + k_{sha}(\dot{x}_1) \\
 V_{vcm} = R_{vcm} i_{vcm} + L_{vcm} \frac{di_{vcm}}{dt} + k_{vcm}(\dot{x}_1 - \dot{x}_2) \\
 i_{ref} = \frac{f_{act}}{k_{vcm}} \\
 e = i_{ref} - i_{vcm} \\
 PID = k_p e + k_i \int e dt + k_d \frac{d}{dt}(e) \\
 V_{vcm} = PID(e)
 \end{cases} \quad 7-4$$

$$\begin{bmatrix} \dot{x}_1 \\ \dot{x}_2 \\ \dot{x}_3 \\ \dot{x}_4 \\ \dot{x}_5 \\ \dot{x}_6 \\ \dot{x}_7 \\ \dot{x}_8 \end{bmatrix} = \begin{bmatrix} 0 & 0 & 0 & 0 & 1 & 0 & 0 & 0 \\ 0 & 0 & 0 & 0 & 0 & 1 & 0 & 0 \\ 0 & 0 & 0 & 0 & 0 & 0 & 1 & 0 \\ 0 & 0 & 0 & 0 & 0 & 0 & 0 & 1 \\ -\frac{(k_1 + k_2)}{m_1} & \frac{k_2}{m_1} & 0 & 0 & \frac{-(c_1 + c_2)}{m_1} & \frac{c_2}{m_1} & \frac{-k_{vcm}}{m_1} & \frac{k_{sha}}{m_1} \\ \frac{k_2}{m_2} & \frac{-k_2}{m_2} & 0 & 0 & \frac{c_2}{m_2} & \frac{-c_2}{m_2} & \frac{k_{vcm}}{m_2} & 0 \\ \frac{0}{m_2} & \frac{0}{m_2} & \frac{-k_i}{L_{vcm} + k_d} & 0 & \frac{-k_{vcm}}{L_{vcm} + k_d} & \frac{k_{vcm}}{L_{vcm} + k_d} & \frac{-R_{vcm} - k_p}{L_{vcm} + k_d} & 0 \\ 0 & 0 & 0 & 0 & \frac{-k_{sha}}{L_{sha}} & 0 & 0 & \frac{-R_{sha}}{L_{sha}} \end{bmatrix} \begin{bmatrix} x_1 \\ x_2 \\ x_3 \\ x_4 \\ x_5 \\ x_6 \\ x_7 \\ x_8 \end{bmatrix} + \begin{bmatrix} 0 & 0 & 0 & 0 \\ 0 & 0 & 0 & 0 \\ 0 & 0 & 0 & 0 \\ 0 & 0 & 0 & 0 \\ \frac{1}{m_1} & 0 & 0 & 0 \\ 0 & 0 & 0 & 0 \\ 0 & \frac{k_i}{L_{vcm} + k_d} & \frac{k_p}{L_{vcm} + k_d} & \frac{k_d}{L_{vcm} + k_d} \\ \frac{1}{L_{sha}} & 0 & 0 & 0 \end{bmatrix} \begin{bmatrix} V_{sha} \\ q_{ref} \\ \dot{q}_{ref} \\ \ddot{q}_{ref} \end{bmatrix} \quad 7-5$$

In this representation, it is assumed that the actuator force is obtained by either control method and the equations of the control method are not included in the state-space model. The state variable definitions are presented in Table 7-2 and the values of Table 7-3 represent those of the test rig simulations.

Table 7-2 State-Space model parameters

Parameter	Component	Variable	State-Space	Inputs	
<b>Displacement</b>	Shaker table	$x_1$	$\dot{x}_1$	Shaker	$V_{sha}$
	Absorber mass	$x_2$	$\dot{x}_2$		
<b>Electrical Charge</b>	VCM: Actual	$q_{vcm}$	$\dot{x}_3$		
	Shaker	$q_{sha}$	$\dot{x}_4$		
<b>Velocity</b>	Shaker table	$\dot{x}_1$	$\dot{x}_5$	VCM	$q_{ref}$
	Absorber mass	$\dot{x}_2$	$\dot{x}_6$		$\dot{q}_{ref}$
<b>Electrical Current</b>	VCM: Actual	$\dot{x}_3 = \dot{q}_{vcm}$	$\dot{x}_7$		$\ddot{q}_{ref}$
	Shaker	$\dot{x}_4 = \dot{q}_{sha}$	$\dot{x}_8$		

Table 7-3 Electromechanical model parameters of the test rig

Mechanical	Shaker V406 series	VCM	Gain Scheduling Control
$m_1 = 2.1 [kg]$	$V_{sha} = 3 \sin(\omega T) [V]$	$k_{vcm} = 8 [N/A]$	$\gamma = m_2(\omega^2 - \omega_0^2)$ $\alpha = m_2\left(\frac{\omega_0^2}{\omega^2} - 1\right)$ $\beta = -c_2$
$m_2 = 0.4125 [kg]$	$L_{sha} = 1.8 [mH]$	$L_{vcm} = 1.3 [mH]$	
$c_1 = 5 [Ns/m]$	$R_{sha} = 1.2 [\Omega]$	$R_{vcm} = 2.7 [\Omega]$	
$c_2 = 7 [Ns/m]$	$k_{sha} = 11.1 [N/A]$	$k_p = 100$	
$k_1 = 12300 [N/m]$	$f = 5 - 100 [Hz]$	$k_i = 1$	
$k_2 = 40714 [N/m]$		$k_d = 0$	

In the control strategy, the actuator force is generated by either gain scheduling or LQ control. In a VCM, electrical current generates the force depending on the value of the motor constant. The motor constant is a feature of the motor that depends mainly on the design and physical arrangement of the motor. A fast current control loop is designed by employing a PID controller to control the actual current in the VCM so it tracks a reference current. The reference current signal is determined by taking the division between the required actuator

force and the motor constant. In the model, the constants  $k_p$ ,  $k_i$ , and  $k_d$  represent the PID controller's gains. The term  $i_{ref}$  refers to the reference current that is inversely proportional to the control force by  $k_{vcm}$  determined by the active damping control strategy. Subsequently, the terms  $q_{ref}$ ,  $\dot{q}_{ref}$ ,  $\ddot{q}_{ref}$  are related to the reference electrical charge for the purpose of state-space representation. The schematic model in Figure 7-12 represents the current control strategy.

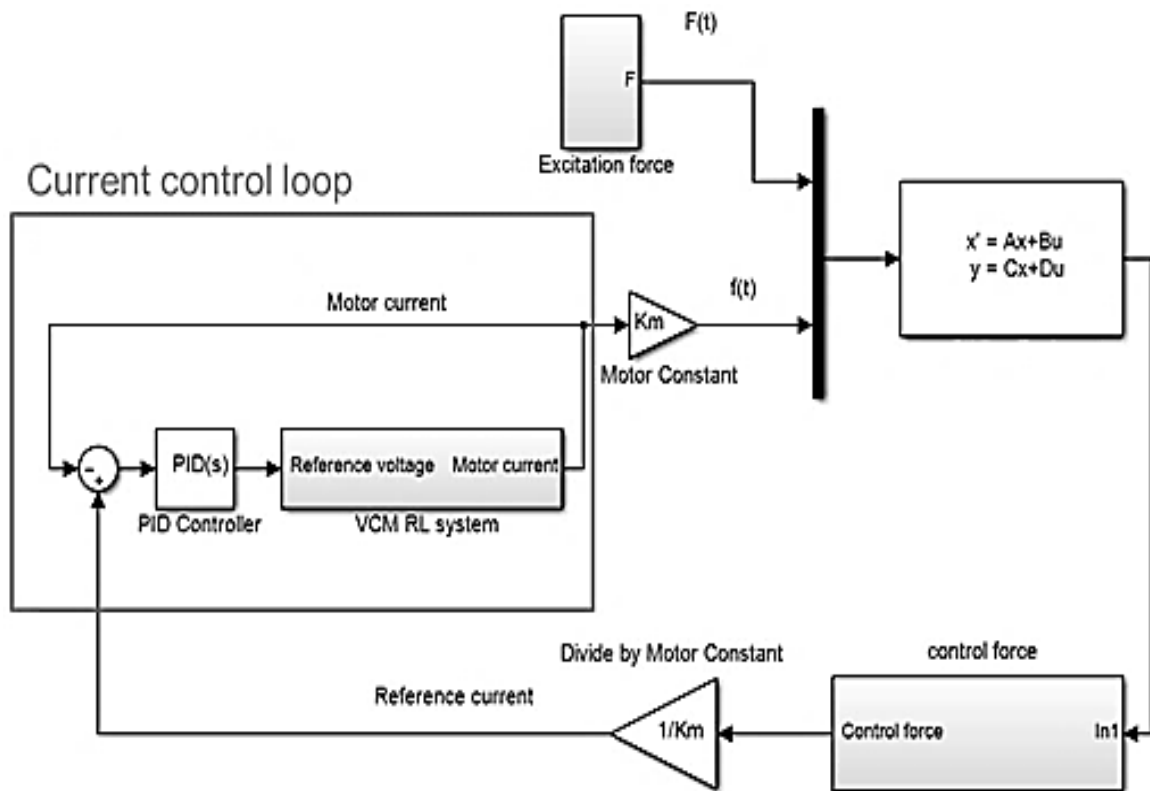


Figure 7-12 Control system representation

The simulation is carried out for 60 seconds and the excitation frequency is varied between 45Hz and 55Hz with a 1Hz step after each 5 seconds of simulation time. The plots of Figure 7-13 show the time domain simulation results with the theoretical model for the active damping of the shaker table.

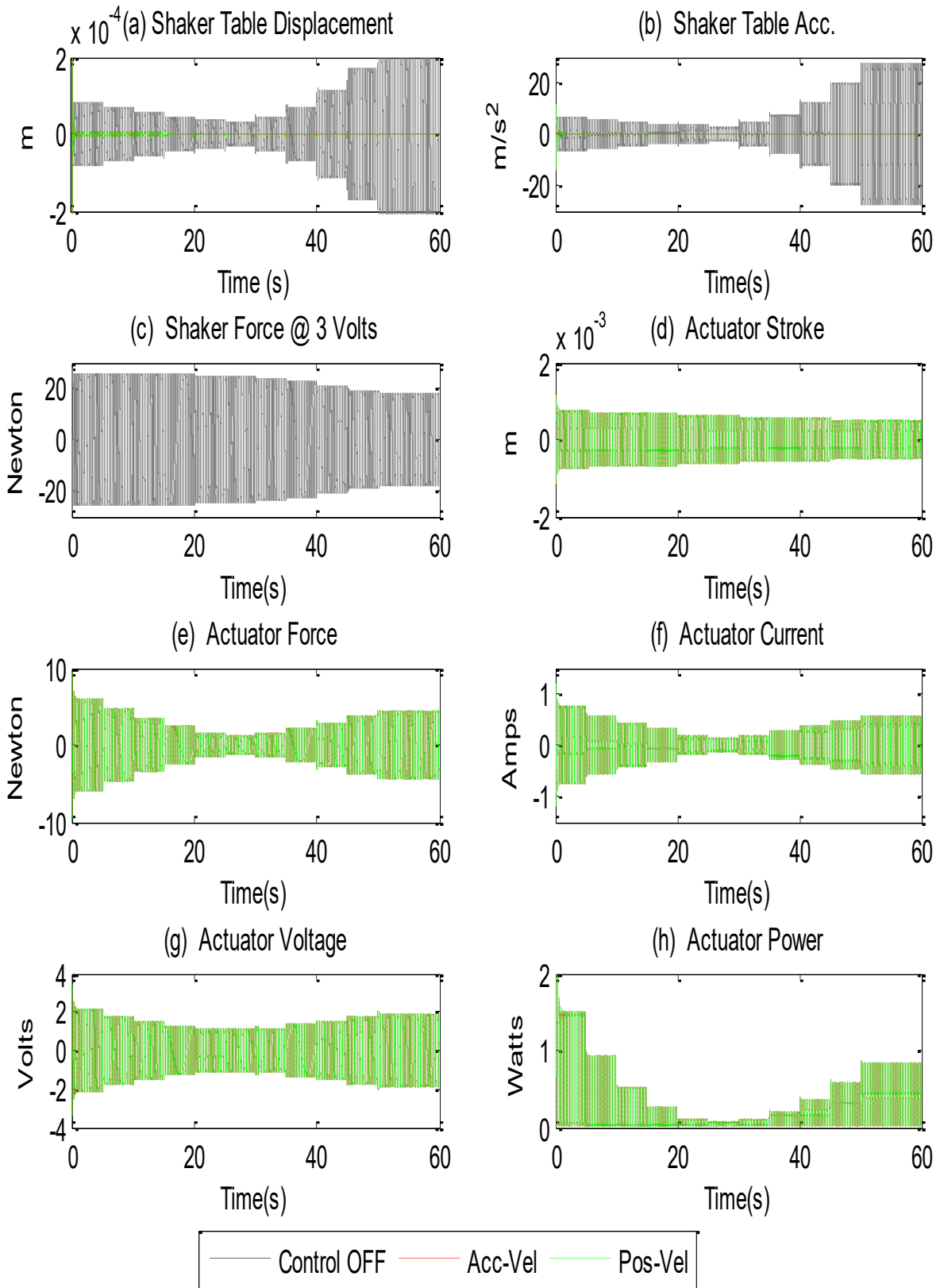


Figure 7-13 Time domain simulation results for the active damping control of the designed rig

In (a) and (b), when control is off, the ATMD only attenuates the vibration at its tuned frequency (50Hz). Theoretically the ATMD should cancel the vibration of the shaker table completely at 50 Hz when it has no damping, however in this case the vibration in the shaker table is not fully cancelled due to the existence damping in the VCM, nevertheless the vibration is minimum at this frequency. After 50Hz, the magnitude of the shaker table vibration grows larger as the frequency of excitation shifts rightwards away from 50Hz to reach a maximum value at the combined resonance of the entire shaker-rig system which occurs around 56Hz. With active control on, it is revealed that a far better performance is obtained with active control for all the frequencies between 45Hz and 55Hz with both position and acceleration feedback. The theoretical actuator force, stroke, voltage, current, and power consumption to perform active control of vibration for the shaker table are also determined. The predicted power consumption of the VCM decreases from a maximum value at 45Hz to a minimum at 50Hz then increases again with frequency.

## 7.7 Theoretical Study 1: Time Delays and Stability

In section 6.10, it was illustrated theoretically that time delays have direct effect on the stability of the control system. The previous study on time delays was conducted with a generic actuator force for the Stirling engine model. This section is dedicated for the study of the effect of time delays on stability of the gain scheduling control strategy with both position or acceleration and velocity feedback utilising the validated shaker rig model. The equation that relates the reference electrical current,  $i_{ref}$  and the actuator force,  $f_{act}$  with delays is defined in 7-6

$$i_{ref} = \frac{f_{act}}{k_{vcm}} = \frac{1}{k_{vcm}} (\alpha s^2 + \beta s + \gamma) (x_1 - x_2) (1 - \tau s) \quad 7-6$$

Equation 7-6 is incorporated into  $W(s)$  which relates the shaker table displacement with the shaker excitation force for the model represented in equations 7-3 and 7-5

$$W(s) = \frac{X_1(s)}{F_{sha}(s)} = \frac{b_4s^4 + b_3s^3 + b_2s^2 + b_1s^1 + b_0s^0}{a_7s^7 + a_6s^6 + a_5s^5 + a_4s^4 + a_3s^3 + a_2s^2 + a_1s^1 + a_0s^0} \quad 7-7$$

The coefficients of  $W(s)$  are presented in appendix C.  $W(s)$  applies for any 2DOF vibration system equipped with a linear VCM for active vibration control with the proposed gain scheduling control law. The poles of  $W(s)$  are investigated for different time delays as the excitation frequency is varied. The study was carried out for time delay between 0s and 200 $\mu$ s and excitation frequencies between 45Hz and 55Hz.

### 7.7.1 Gain Scheduling with Relative Position/Acceleration and Velocity Feedback

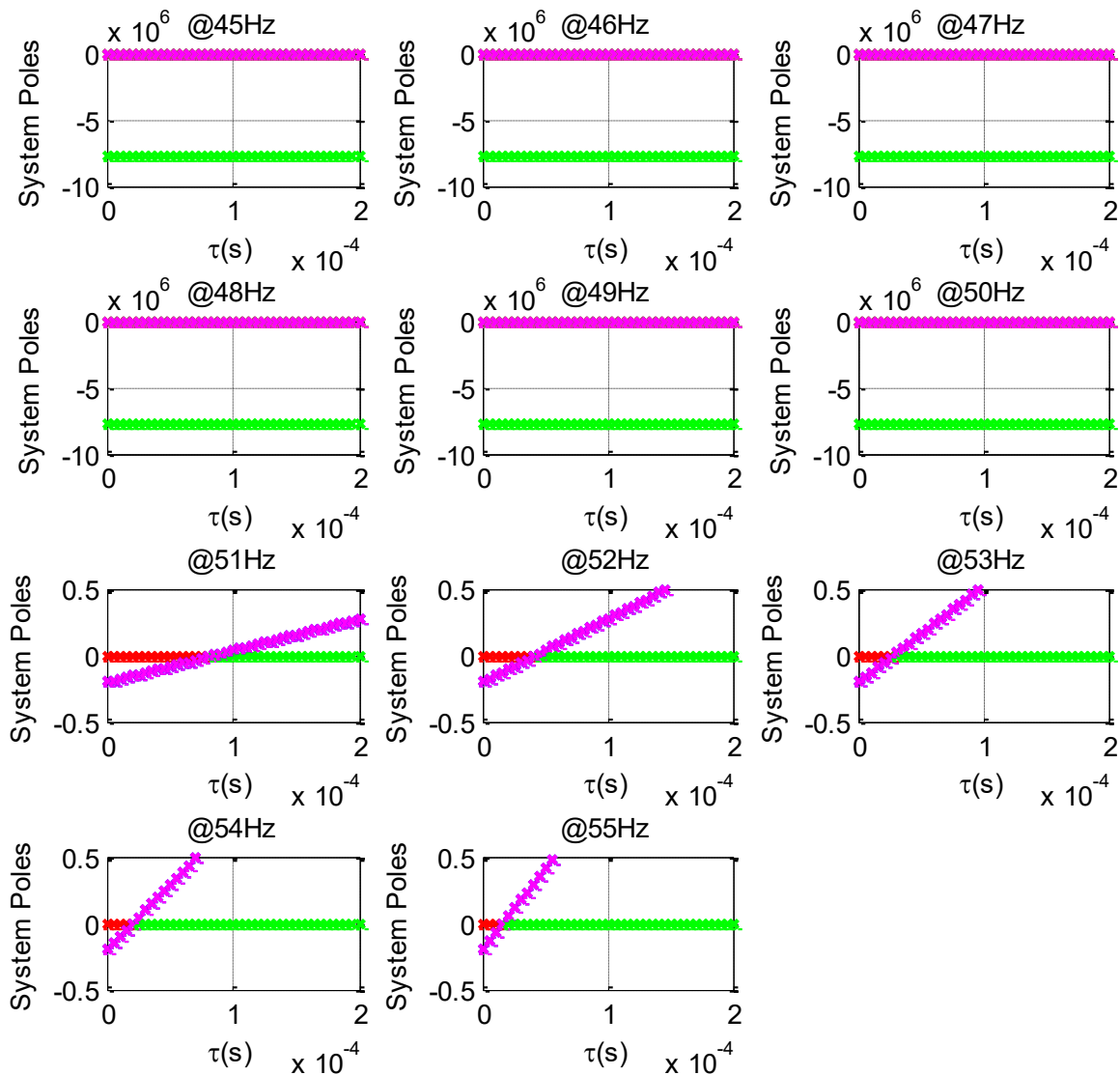


Figure 7-14 Position of the closed-loop poles with gain scheduling control: position and velocity feedback control with ATMD tuned at 50Hz

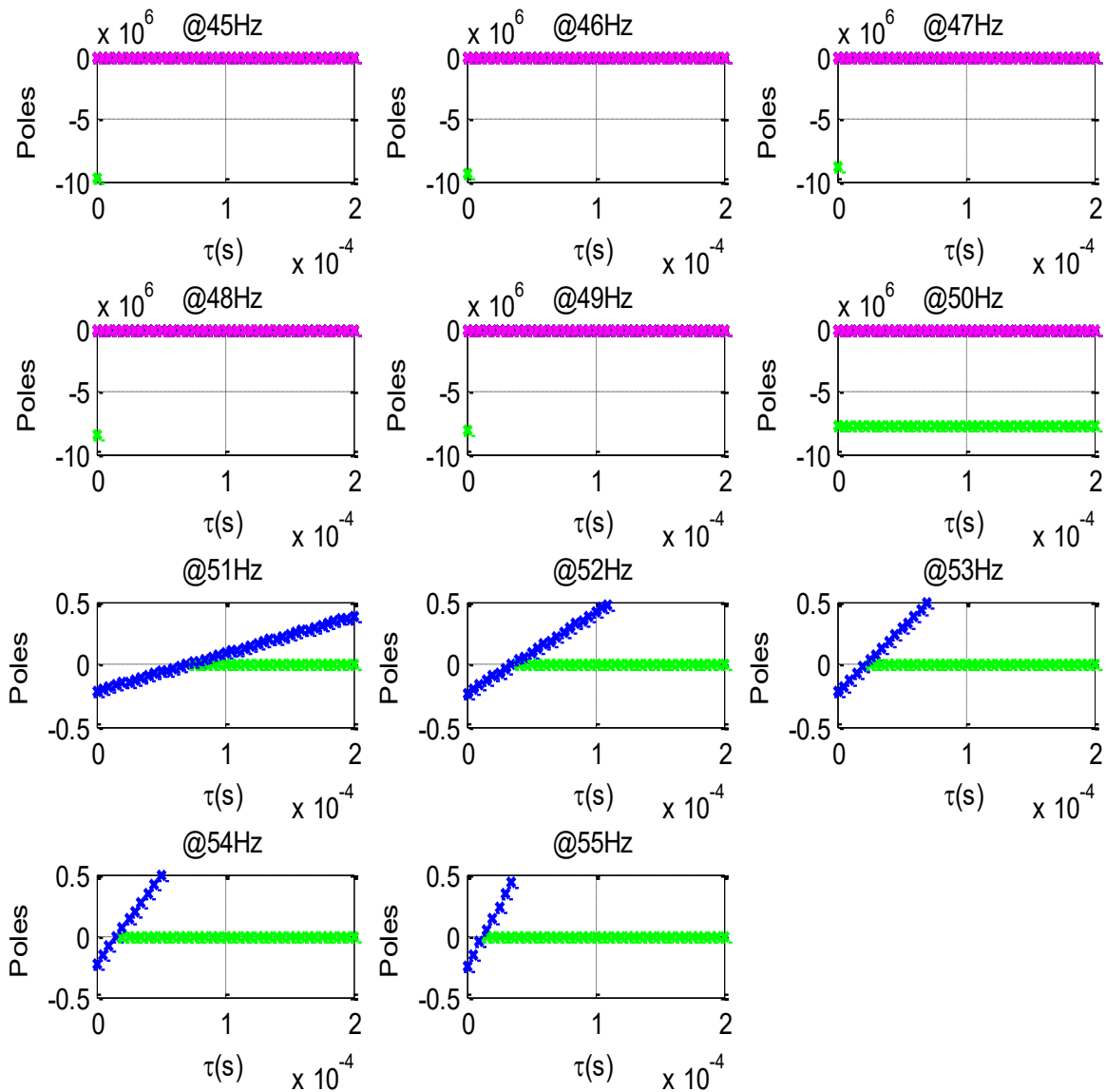


Figure 7-15 Position of the closed-loop poles with gain scheduling control: Acceleration and velocity feedback control with ATMD tuned at 50Hz

The graphs presented in the Figure 7-14 and Figure 7-15 reveal that when the ATMD is passively tuned at 50Hz, delays between 0s and 200 $\mu$ s do not destabilise the system before 50Hz since the real part of all the system poles are negative. As the excitation frequency drifts above the original resonance of the ATMD, the control strategy becomes unstable shortly after a certain time delay margin which decreases consistently with the increase in the excitation frequency. Those results are similar to the previous results obtained in the study for the Stirling engine model.

### 7.7.2 Time Delay Tackling with Changing the Original Tuning of the ATMD

Upon the examination of the system poles, the instability with gain scheduling and zero-placement control method occurs after the frequency has passed the passive resonance of the ATMD. Recall that the operational range is between 45Hz-55Hz, hence if the original tuning of the ATMD is shifted to 55Hz the system may maintain stability when the frequency of excitation is below 55Hz. The graphs of the Figure 7-16 and Figure 7-17 depict the closed-loop poles of the system after shifting the passive tuned frequency of the ATMD to 55Hz.

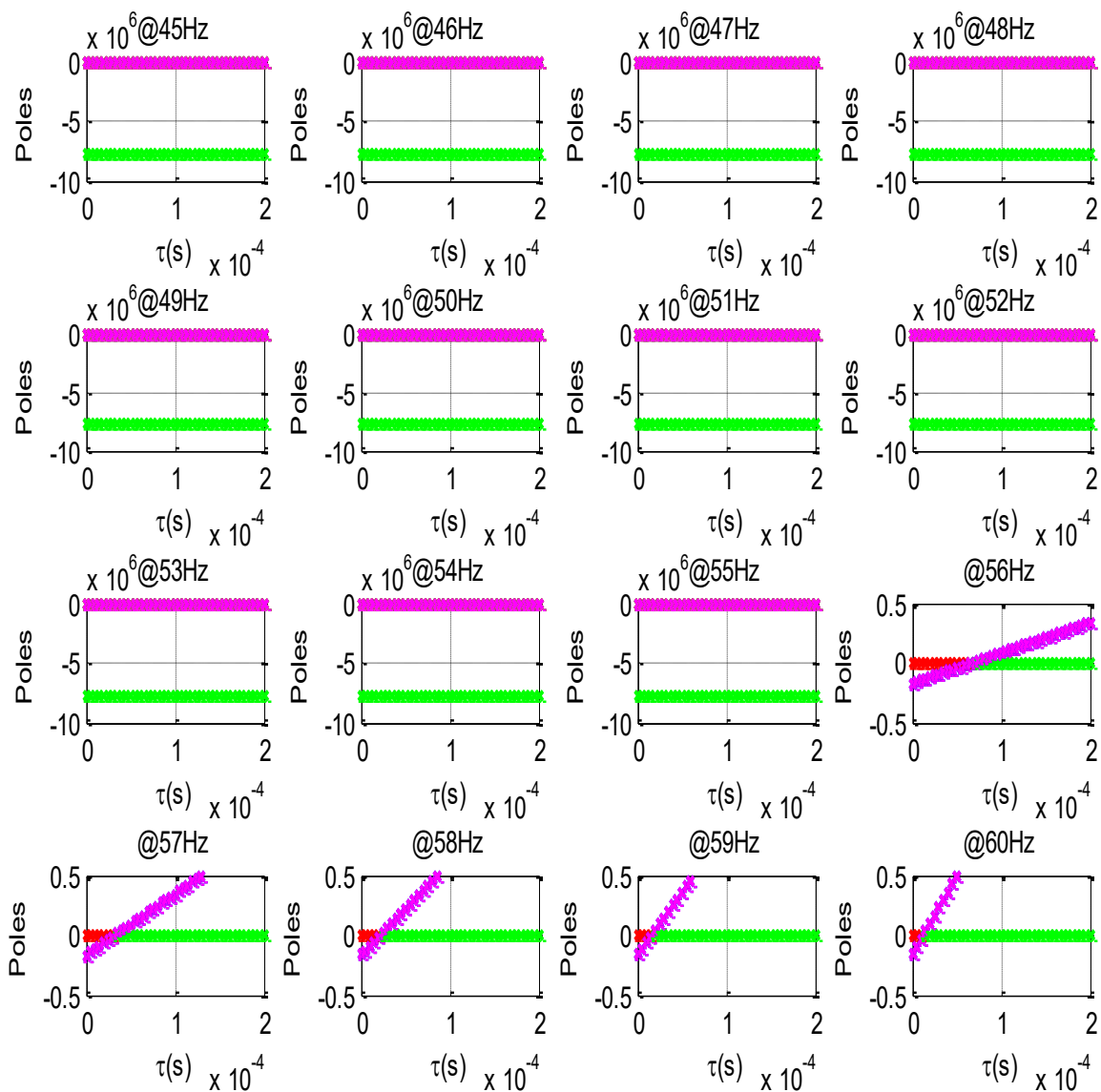


Figure 7-16 ATMD tuned at 55Hz with Position control

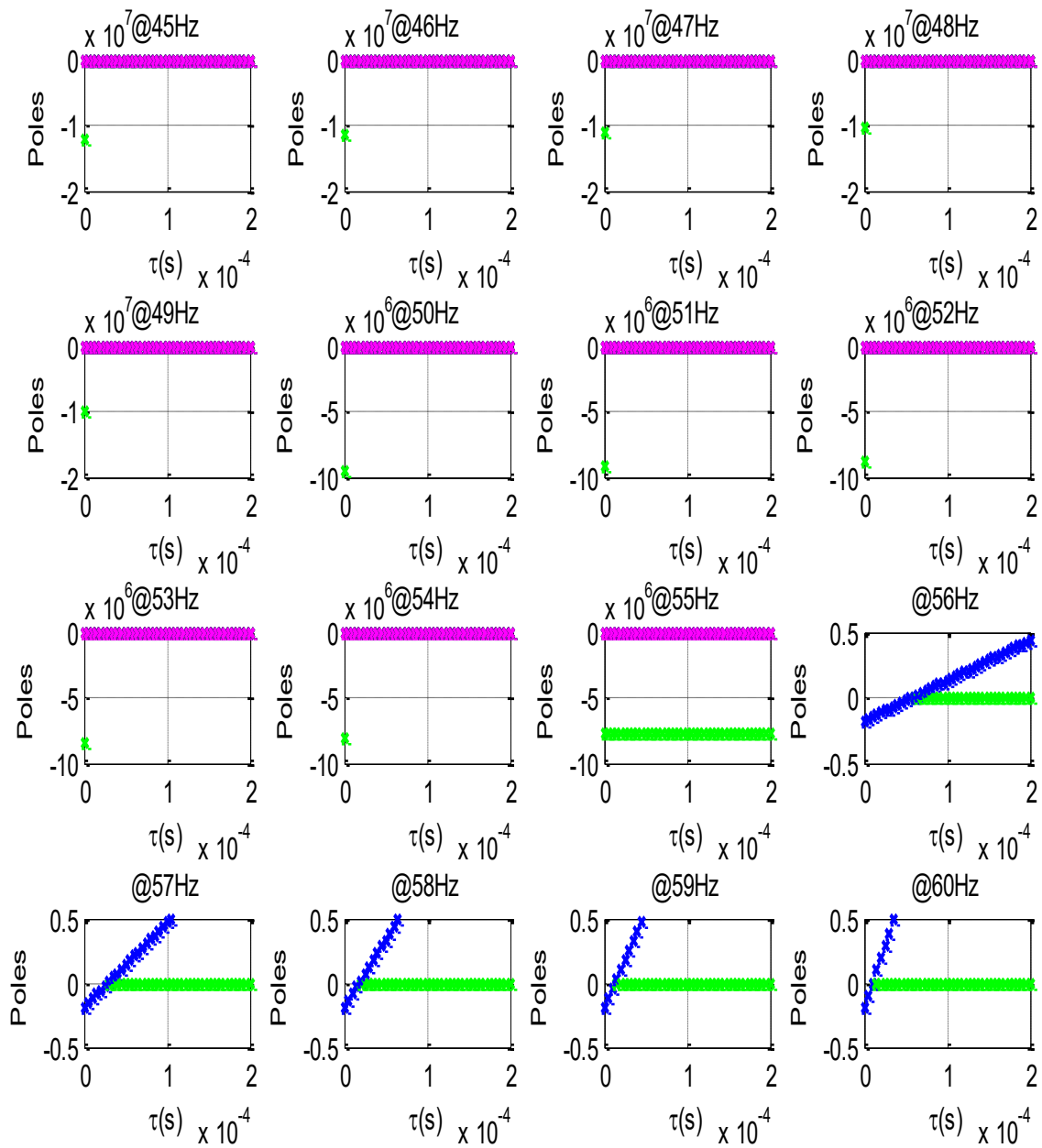


Figure 7-17 ATMD tuned at 55Hz with Acceleration control

The results reveal that the predictions are correct and indeed the system only becomes unstable after 55Hz. The results prove that this approach treats the effect of delays on the control system stability within the frequency operational range. One drawback with this approach is incurred considering the associated higher power requirement. For the actuator to shift the resonance frequency from 55Hz to 45Hz, it requires more power than shifting from 50Hz to 45Hz.

## 7.8 Active Damping Control Implementation

This section is dedicated for the experimental implementation that demonstrates the concept of active vibration control with an ATMD for the gain scheduling control law using the shaker rig. The main focus will be on the shaker table acceleration and the actuator parameters. The real power consumed by the actuator is also emphasised in the tests. Furthermore, experimental tests provide a change to validate the simulation predictions of the shaker rig model.

### 7.8.1 Test Setup

The scaled rig introduced earlier is now used for the experimental tests as shown in Figure 7-18.

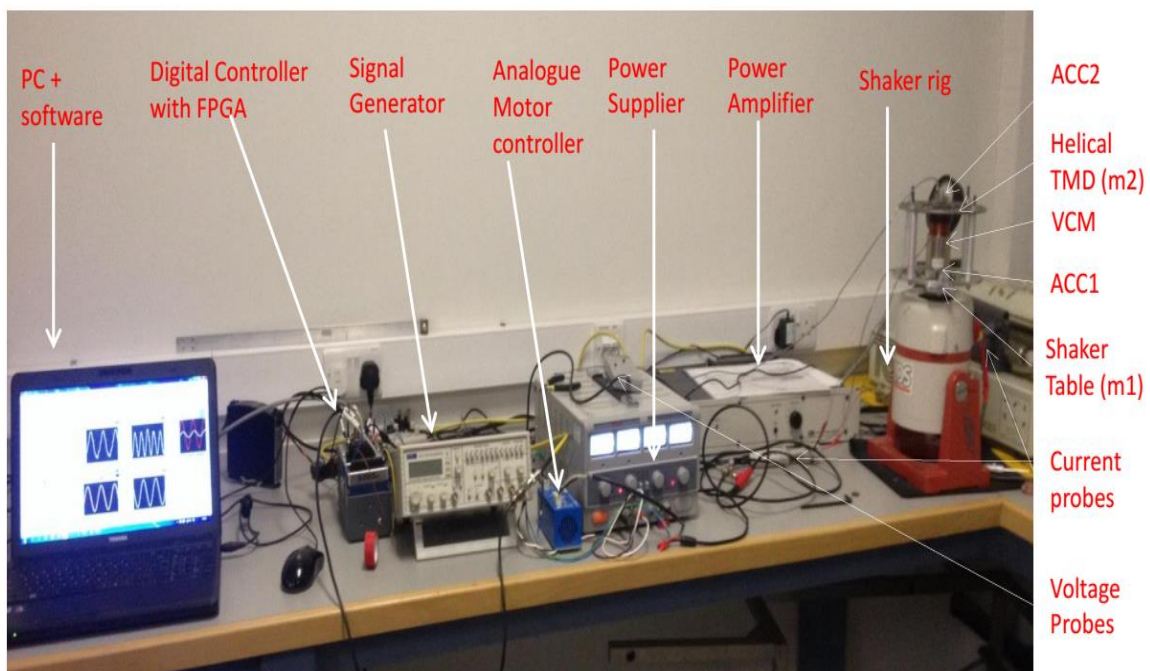


Figure 7-18 Active damping shaker-absorber rig

The rig comprises an ATMD system employing a VCM motor placed axially between the helical spring and the shaker table. The shaker generates a sinusoidal excitation with variable frequency and amplitude controlled with suitable vibration software. Originally, the ATMD is tuned to attenuate the vibration of the shaker table at 50Hz without any control

intervention. The shaker table acts like the primary mass whose vibration needs to be damped. For the Stirling engine, the first resonant frequency of the composite system occurs at approximately 2Hz and the second one is at 54.8Hz. For the shaker rig system, the first resonant frequency occurs at around 11.8 Hz and the second one is at 56Hz. The difference between the composite resonant modes in the Stirling engine and the shaker rig is due to the unequal scaling of the spring masses and stiffness. For both systems however, the original tuning of the absorbers is 50Hz. In fact the first resonant mode doesn't affect the operation as long as it is far below 50Hz.

### **7.8.2 Hardware and Software**

The electromagnetic shaker (V406 series) is a permanent magnet shaker manufactured by Bruel & Kjaer and is capable of delivering a sine vector force up to 196N with a wide frequency range 5Hz – 9 kHz and continuous max peak to peak displacement of 17.6mm. In the experiments, the shaker is powered by a 1.3 KVA power amplifier which is controlled by a small voltage signal with range  $\pm 2$  volts. In order to measure the shaker force during operation, the shaker current is measured using low noise non-contact current probes with a wide frequency bandwidth range from DC to 5MHz capable of detecting 10mA to 20A peak to peak. A differential voltage probe with a wide frequency bandwidth range of DC to 15MHz and continuous input range of  $\pm 1000V$  and output range  $\pm 7V$  is used for the purpose of measuring the voltage across the VCM terminals.

The VCM (GVCM-051-051-01 appendix D) is powered and controlled with a servo linear drive amplifier TA105 capable of delivering a max current of 2A peak to peak control by a fast proportional current controller. During operation, the active damping control method determines a reference current that is delivered to the servo drive and then compared with the actual current in the VCM which is measured internally.

For control system prototyping, an embedded CompactRIO (CRIO) 9024 controller featuring an 800 MHz real-time processor that runs LabVIEW with real-time applications is used for control, logging, and data analysis. The CRIO can be powered up with a 9V to 35V VDC power supply. It also features a user-defined FPGA circuitry in its chassis that controls each I/O module.

Two LabVIEW codes were designed and implemented simultaneously on the CRIO real time engine and the FPGA respectively. The FPGA code is executed with a 20 $\mu$ s loop rate where the measurement and control takes place. The RT code runs with a 100ms loop rate and communicates to the FPGA code via direct memory access FIFOs. The RT code is used mainly for data logging and communicating information that don't require high loop rate.

Two analog input modules (NI 9234, NI 9205) and one analog output module (NI 9263) were used to process the measurements. Acceleration data of the shaker table and the TMD were obtained from two accelerometers with dynamic range of  $\pm 71g$  mounted in the middle of the shaker table and the TMD respectively. The acceleration signals were sampled at a rate of 50KS/s using an AC coupled input stage of a 24-bit Analogue-to-Digital converter. The relative acceleration between the shaker table and the ATMD is then run through a low pass filter to remove any noise. The signals were then integrated digitally twice to obtain the relative velocity and relative position respectively. A two second order high pass filter stages were implemented after each integration stage in order to remove any DC offset resulting from the integration. The signal that is proportional to the relative position is then multiplied with a frequency gain that is altered autonomously. The excitation frequency is determined by measuring the frequency of the exciting voltage on the shaker. The relative velocity signal is also multiplied by an autonomous velocity gain to remove the effect of damping introduced by the VCM in the ATMD. The control code outputs the desired current to the VCM amplifier via an analogue output channel with a 16-bit resolution at 50 KHz sampling rate.

## 7.9 Relative Position and Velocity feedback

The experimental tests considered the gain scheduling with zero-placement control law. In this section, position and velocity feedback is considered.

### 7.9.1 Test 1: Active Damping Control Implementation

In this test, the shaker excitation frequency is varied linearly from 40Hz to 60Hz in a time interval of 1 minute. The active vibration control is only operated in the frequency range between 45Hz and 55Hz. A second order Butterworth low pass filter stage with a cut-off frequency of 200Hz is added to remove any measurement noise from the accelerometers. On the other hand, two second order Butterworth high pass filters are implemented with a 1Hz cut-off frequency to remove any post-integration DC offset. In addition to that, based on the model validation in validation Test 2, the velocity gain is chosen accordingly  $\beta = -14 \text{Ns/m}$ . Figure 7-19 contains a schematic that describe the applied control strategy. Table 4-1 summarises the parameters that are adopted for this test.

Table 7-4 Test 1 Parameters

Parameter	Symbol	Value	Unit
Shaker Excitation	$V_s$	$4 \sin 2\pi f_{exc} T$	[V]
Excitation Frequency	$f_{exc}$	40 - 60	[Hz]
Test time	T	60	[S]
FPGA loop rate	Ts	20e-6	[S]
ATMD resonance	$f_{ATMD}$	50	[Hz]
Position feedback gain	$\gamma$	$4\pi^2 m_{ATMD} (f_{exc}^2 - f_{ATMD}^2)$	[Ns <sup>2</sup> /m]
Velocity feedback gain	$\beta$	-14	[Ns/m]
VCM reference current	$i_{ref}$	$\frac{1}{k_{vcm}} ((\gamma(\ddot{x}_1 - \ddot{x}_2) + \beta(x_1 - x_2))$	[A]
“Control ON”	$f_{control}$	45 - 55	[Hz]
Low pass cut-off	$f_{Lp}$	200	
High pass cut-off	$f_{Hp}$	1	

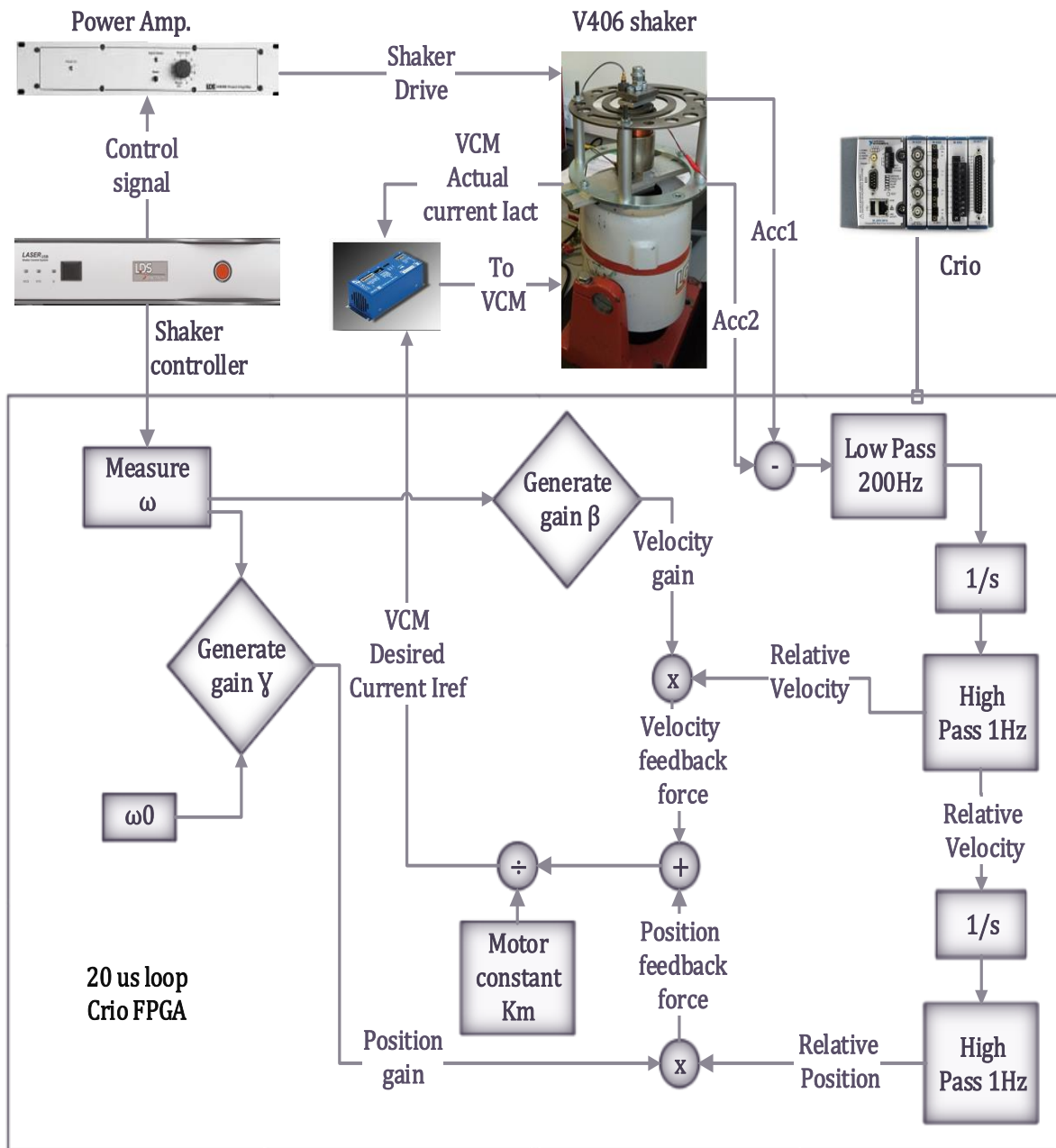


Figure 7-19 Active damping control model

The graphs of Figure 7-20 present the experimental measurements of the shaker excitation and the shaker table acceleration for the test rig with passive TMD (black) and the actively controlled ATMD (red).

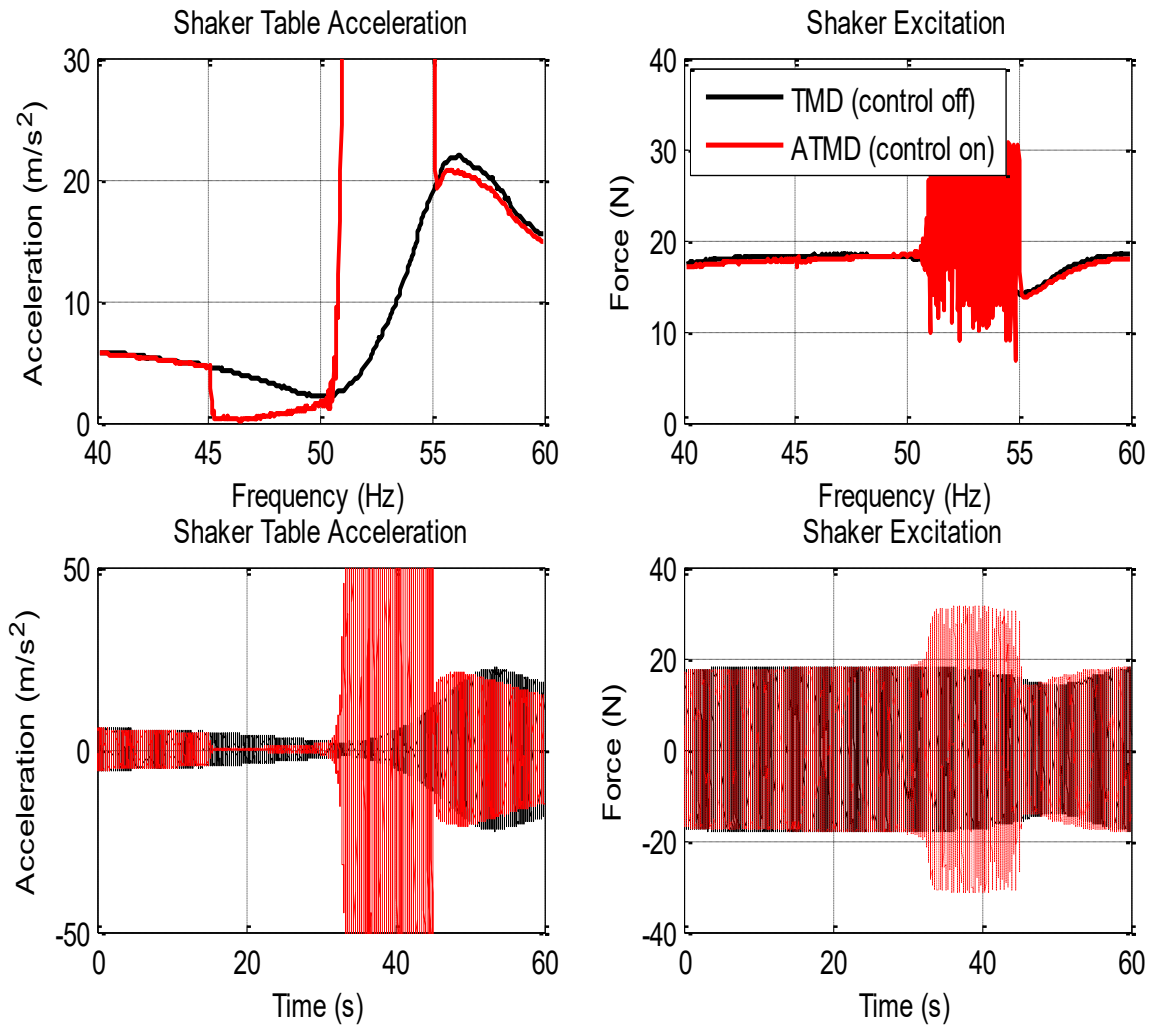


Figure 7-20 Test1: Shaker table excitation and acceleration

The VCM voltage, current, and power consumption measurements for the ATMD are plotted in Figure 7-21 and Figure 7-22 respectively. Both the desired and actual current and power consumption are plotted.

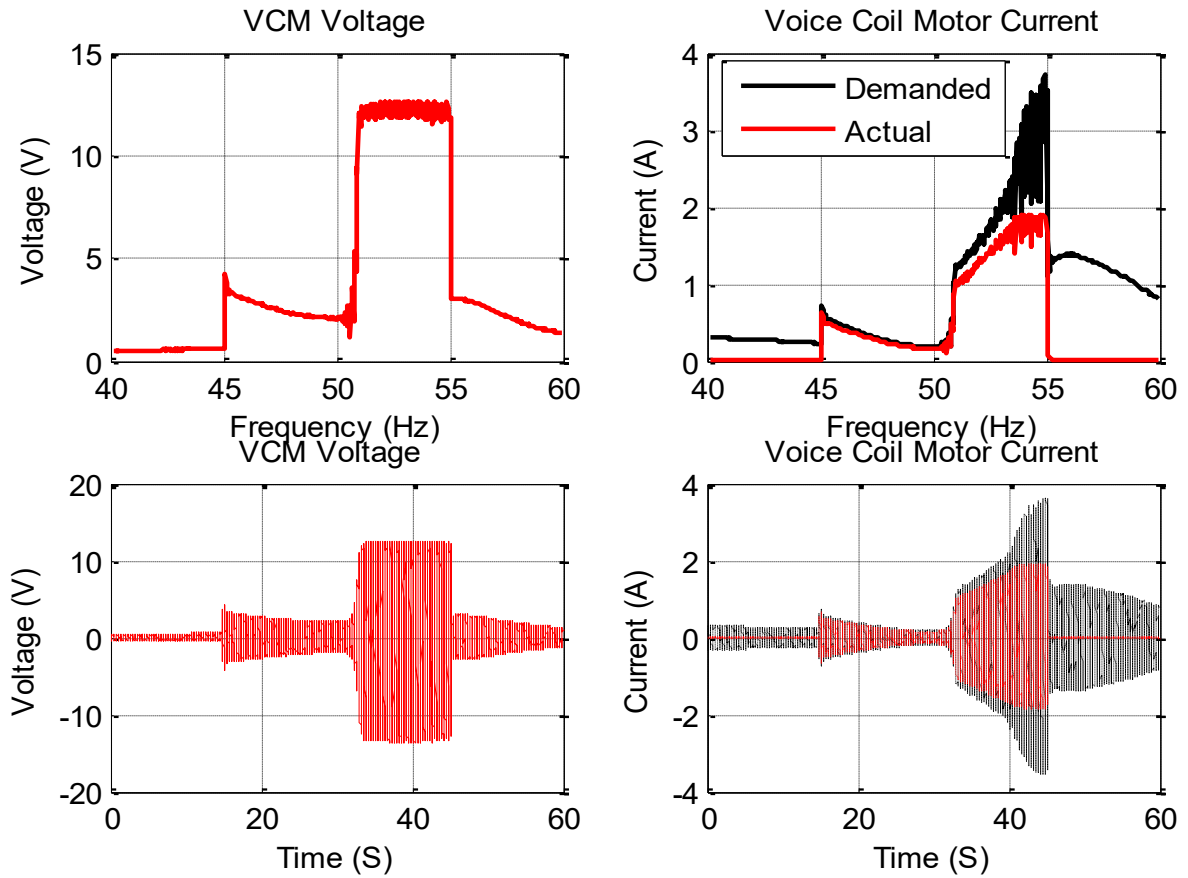


Figure 7-21 Test1: VCM voltage and Current with active control

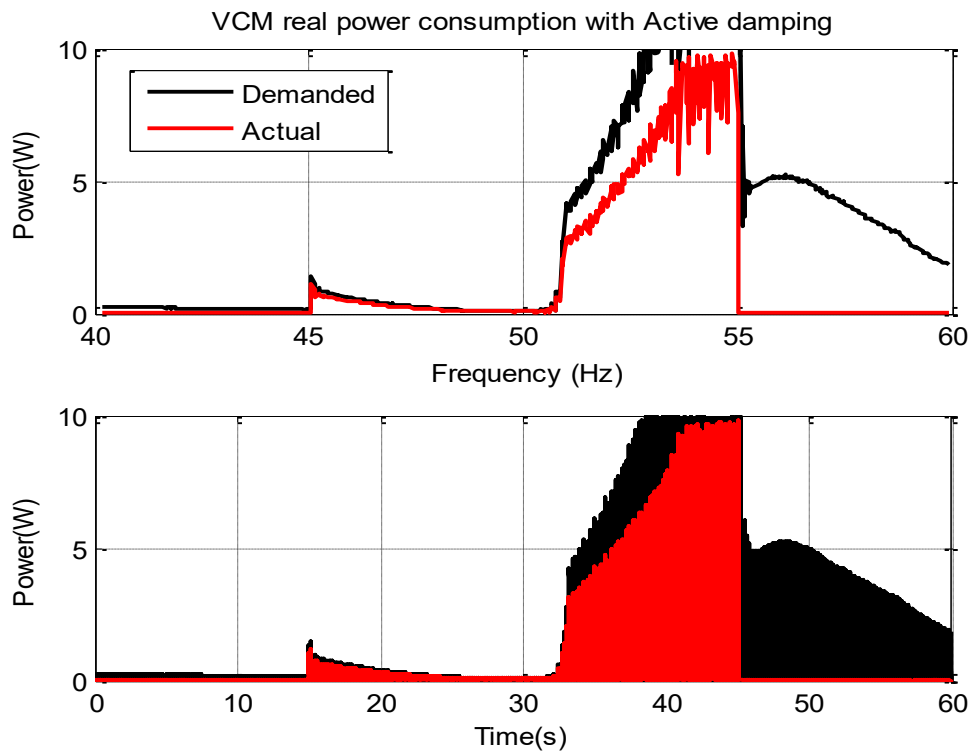


Figure 7-22 Test1: VCM Real power consumption with active control

Referring to Figure 7-20, the shaker table acceleration with the passive case (black) is only attenuated at 50Hz which is the original resonance of the ATMD. It is evident that the attenuation level doesn't cancel the vibration of the shaker table completely due to the damping in the VCM. The following discussion elaborates upon the active control (red) with ATMD whereby the response is analysed in four different intervals.

1. [40-45]Hz: For the ATMD, the control is off in this interval and therefore the response of the shaker table acceleration is similar to that of the passive TMD response plotted in black. The current delivered to the VCM is zero in this interval due to the control being off. A small voltage appears across the terminals of the VCM in this interval due to the generated back EMF but this voltage is negligible.
2. [45-50]Hz: In the case of the passive TMD (black), the amplitude of the shaker table acceleration starts decreasing to reach a minimum at 50Hz. When control is on (red), the amplitude of the shaker table acceleration drops to minimum immediately at 45Hz due to the effect of the control action. As excitation frequency increases, it is revealed that the shaker table acceleration grows a little instead of being at minimum. The reason for this discrepancy is not known but it is likely to be attributed to the damping coefficient in the VCM. The prediction is that the value of damping coefficient is not chosen correctly. This affects the velocity feedback gain which has a direct effect on the level of attenuation of the shaker table. A more thorough investigation on the value of damping in the ATMD is presented later.

The maximum amplitudes of the voltage (4V), current (0.65A), and power (1.13W) occur at 45Hz. These amplitudes decrease gradually as the frequency reaches 50Hz.

3. [50-55]Hz: The control action is still on in this interval and the shaker table acceleration is expected to be attenuated in this interval as well. However, the system becomes unstable after 50Hz and the amplitudes of the acceleration reach larger

magnitudes as the frequency of excitation moves from 50Hz towards 55Hz. Similarly, the VCM voltage, current, and power reach larger values in this interval. The instability in the system caused higher demand in the VCM current due to the large acceleration amplitudes. In fact the servo controller current output is saturated after 53Hz as it reached its maximum output limit of 2A. This is evident in the graphs of Figure 7-21 and Figure 7-22 where the actual current and power do not track the demanded ones. The source of instability in the control system is attributed to time delays/phase shifts resulting from filtering and will be discussed later. The effect of delays in instability was presented earlier in this chapter.

4. [55-60]Hz: This is the case when control is turned off in the system. No current is delivered to the VCM and hence the response of the shaker table acceleration is similar to that when the system is passive.

Another important observation in this test is related to the damping coefficient in the ATMD system. Previous theoretical study with the gain scheduling control strategy showed that a velocity feedback gain is capable of altering the damping in the ATMD. Precisely, the value of the velocity feedback gain must be chosen in such a way that reduces the damping while ensuring a stable control. In this test, it was observed that the VCM not only introduces damping into the ATMD but this damping is not constant. In fact, it was observed that the damping coefficient varies with frequency. This was implied from the level of attenuation on the shaker table which was not consistent in the range between [45Hz-55Hz]. This calls for further investigation on the value of the damping coefficient in the ATMD.

### 7.9.2 Test 2: Time Delays Mitigation and Characterisation of Damping Coefficient in the ATMD

Test 1 showed that the instability occurred after the excitation frequency passes the resonant frequency of the ATMD (50Hz) as described in the theoretical study on the effect of time delays on the stability of the control system. Since the nominal operation of the engine is assumed to be between 45Hz and 55Hz, the idea is that if instability occurs at frequencies beyond the original resonance of the ATMD, it is possible to avoid this situation by shifting the original resonance of the absorber up to 55Hz. In this test, the intention is to illustrate the proposed remedy experimentally by conducting the test while the original resonance of the ATMD is passively tuned to 55Hz.

Another outcome of this test is the characterisation of the damping coefficient of the VCM. It was shown previously that damping in the TMD has a direct effect on the level of attenuation in the primary mass whose vibration to be cancelled. In the validation section of the test rig model with short circuited VCM, the value of the damping coefficient in the ATMD due to the VCM core losses and eddy currents was determined ( $c_2 = 14 \text{ Ns/m}$ ). A major drawback is associated with this method since it only considers two cases whereby the ATMD is tuned at a single resonant frequency; however, the aim is to perform the active damping for a wider range of frequency operation. Furthermore, the results of implementation Test 1 showed that the level of attenuation on the shaker table is not consistent as revealed in the frequency range between 45Hz-55Hz.

The following describes a novel procedure of characterising the damping of the ATMD using active damping of vibration control. The test was carried out where the excitation frequency is varied manually from 45Hz to 55Hz in 0.5Hz steps. Meanwhile the value of velocity gain was varied up or down with each increment of frequency until the minimum value of the shaker table acceleration is observed. The minimum acceleration is associated with the

minimum damping in the system. The following illustrates the findings of the required velocity gain needed in order to remove damping from the ATMD system. The values of  $\beta$  are then used for the shaker rig's ATMD with all the following tests.

The attributes of this test are identified in Table 7-5.

Table 7-5 Test 2 Parameters

Parameter	Symbol	Value	Unit
Shaker Excitation	$V_{sha}$	$4 \sin 2\pi f_{exc} T$	[V]
Excitation Frequency	$f_{exc}$	40 - 60	[Hz]
Test time	T	60	[S]
FPGA loop rate	Ts	20e-6	[S]
ATMD resonance	$f_{ATMD}$	55	[Hz]
Position feedback gain	$\gamma$	$4\pi^2 m_{ATMD} (f_{exc}^2 - f_{ATMD}^2)$	[Ns <sup>2</sup> /m]
Velocity feedback gain	$\beta$	Yet to be identified	[Ns/m]
VCM reference current	$i_{ref}$	$\frac{1}{k_{vcm}} ((\gamma(\ddot{x}_1 - \ddot{x}_2) + \beta(x_1 - x_2)))$	[A]
“Control ON”	$f_{control}$	45 - 55	[Hz]
Low pass cut-off	$f_{Lp}$	200	
High pass cut-off	$f_{Hp}$	1	

The value of the optimum velocity feedback gain is obtained as per the following graph.

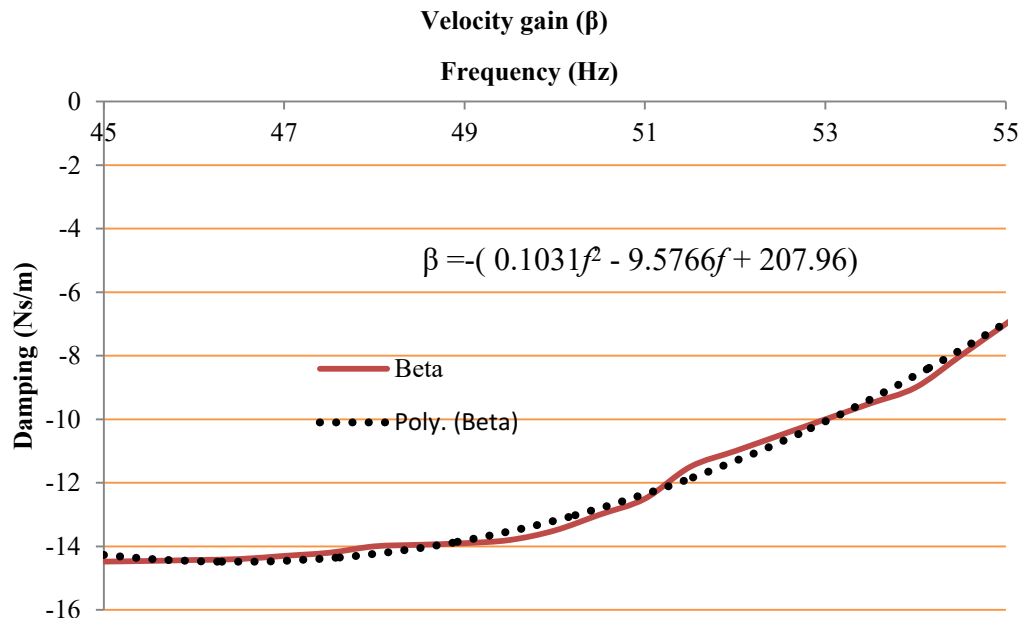


Figure 7-23 Velocity gain against excitation frequency

By examining the acceleration profile of the shaker table in Figure 7-24, it is revealed that the active control succeeds in attenuating the vibration of the shaker table mass across the entire range of frequency between 45Hz and 55Hz when the ATMD is originally tuned at 55Hz while the system is stable in the between 45-55Hz.

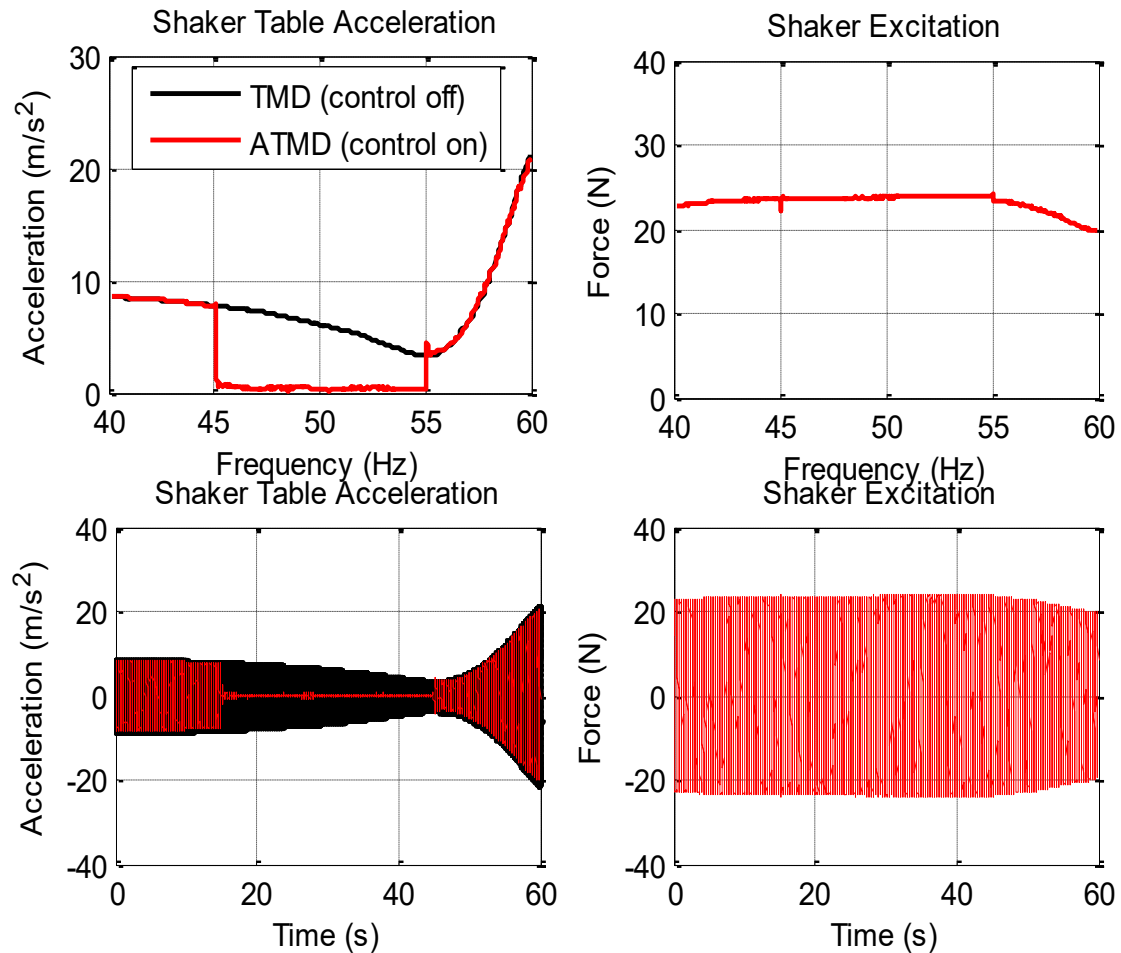


Figure 7-24 Results of Test 2

The graph of Figure 7-25 shows two plots corresponding to the responses of the shaker table acceleration with the passive TMD that was originally tuned at 50Hz and the response with the ATMD that was originally tuned at 55Hz. It is shown that the ATMD extends the envelope of attenuation significantly compared to the passive TMD. The ATMD achieves an average attenuation of 88% across the range between 45Hz-55Hz compared to the TMD attenuation which is only effective at 50Hz.

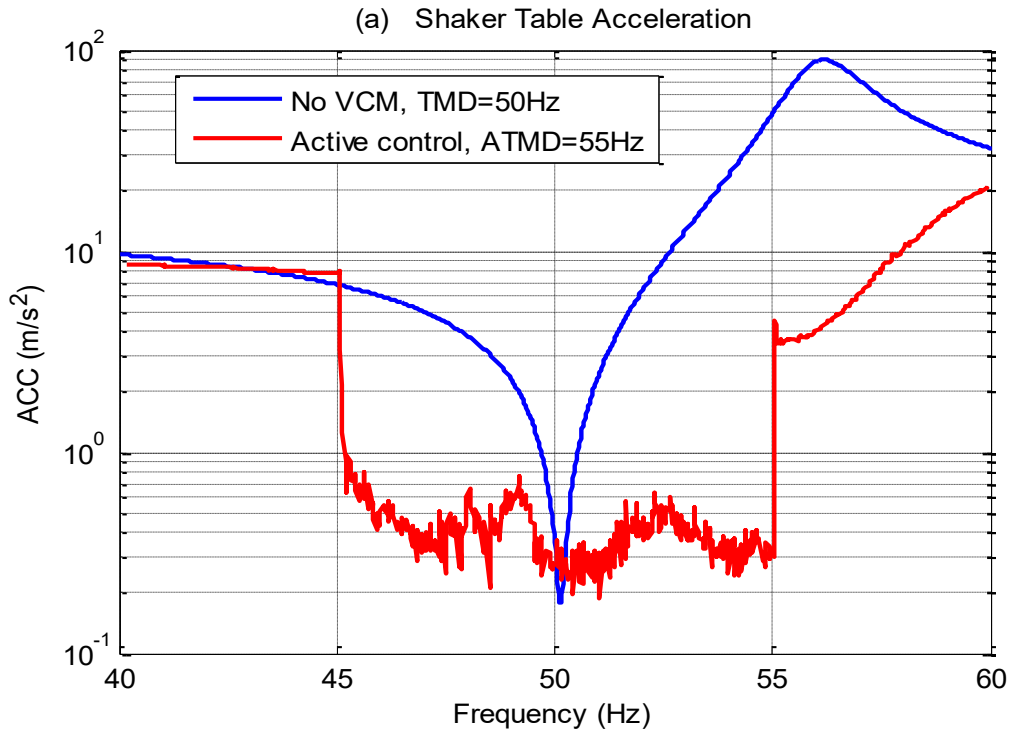


Figure 7-25 Response of the shaker table acceleration with ATMD (originally tuned at 55Hz) vs TMD (originally tuned at 50Hz)

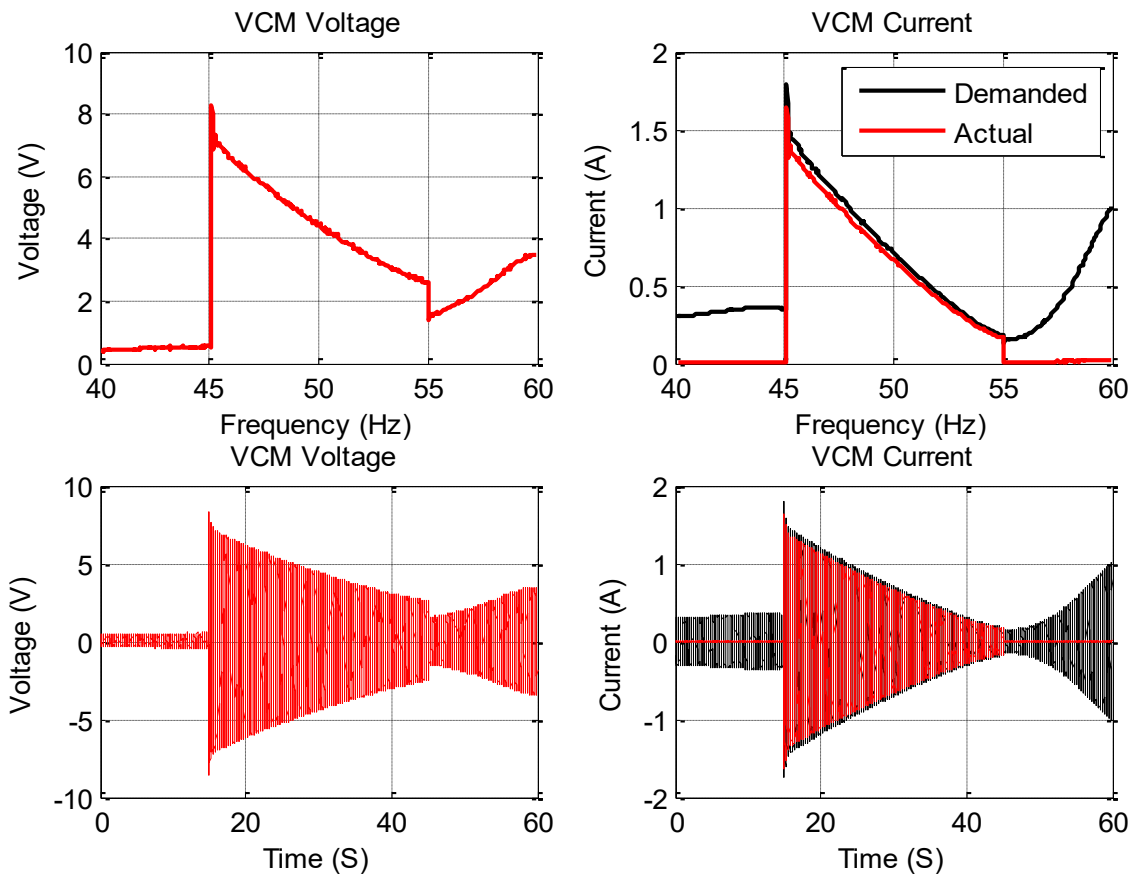


Figure 7-26 VCM voltage and Current with TMD tuned at 55Hz

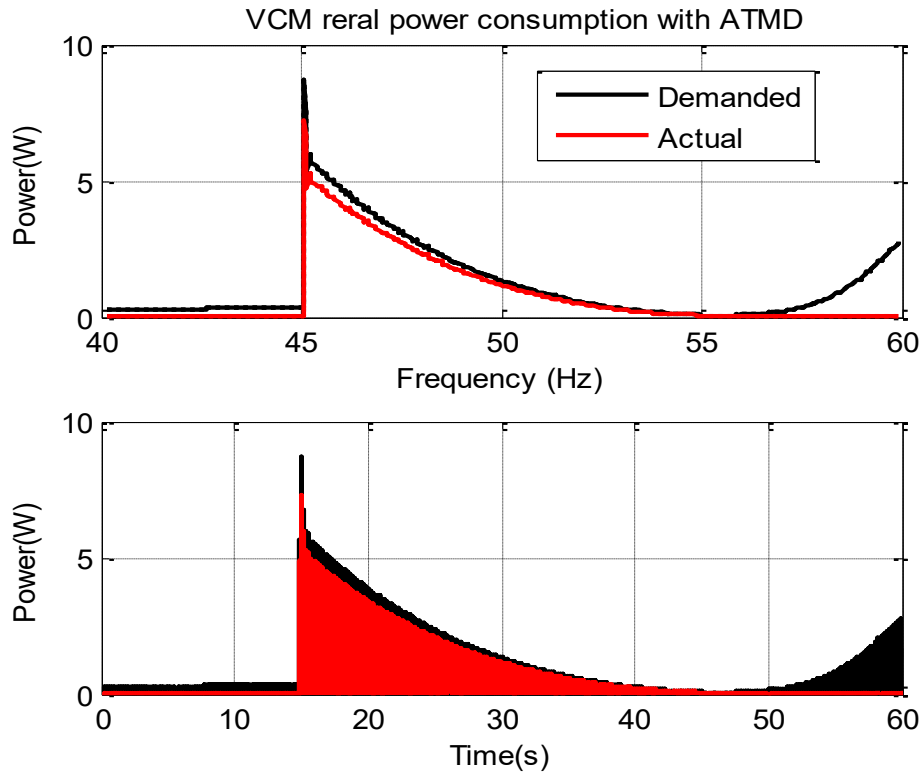


Figure 7-27 VCM Active power consumption with TMD tuned at 55Hz

For Test 2, the electrical requirements of the VCM, plotted in Figure 7-26, show that the maximum voltage, current, and power requirement occur at 45Hz and that greater power input is required compared to Test 1. The reason is that, in this test, the VCM requires power to shift the tuning of the ATMD from 55Hz rather than from 50Hz. Note that since the feedback gains vary quadratically with frequency, the value of the demanded current also increased quadratically rather than linearly.

It can be concluded that the proposed method of shifting the original resonance of the ATMD up to 55Hz has succeeded in avoiding the instability encountered in the range between 50Hz-55Hz. This however does incur more power consumption for active control. The following thus considers another method of mitigating the effect of time delays/phase shift on the stability of the control system but with more efficient power consumption.

### 7.9.3 Theoretical Study: Phase Delays Evaluation and Compensation

#### 7.9.3.1 Phase Shifts Due to Low Pass Filtering

The system under study is a linear-time invariant system with sinusoidal excitation and the steady state solution of this system is known. In practice, the control implementation generally requires filtering of input signals from noise, anti-aliasing, and for DC component elimination that induce inevitable group delay. Furthermore, sensor measurement, non-collocated sensor/actuator pair in addition to processing times can induce more time delays. Reasons for these delays can be related to geometrical arrangements, computational time in analog digital converters (ADCs) and in digital to analog converters (DACs). These delays represent a phase shift in periodic signals that postpones feedback signals. The theoretical study on delays in an earlier section showed that the instability of the control system is dependent upon a delay margin and the excitation frequency. These theoretical findings were verified experimentally in Test 1. Furthermore, following an observation of the system with delays, a remedy based on changing the original resonance of the ATMD was proposed, simulated, and experimentally validated in Test 2. Despite the successful remedy, there exist two main drawbacks with this approach. Firstly, this solution treats the consequence of delays without compensation and secondly more power consumption is incurred. In here, a thorough investigation of the source of time delays in the implementation code is carried out in order to propose a method of compensating delays. Compensation of delays does not only maintain a stable system, but also provides a more efficient control. By visualising the control model presented in Figure 7-19, it can be noticed that filter stages introduce phase shifts into the signal chain which may affect stability of the control system. To investigate further, the continuous Laplace domain transfer function,  $TF_{LP}(s)$ , which represents the low pass filter plant is shown below

$$TF_{LP}(s) = \frac{0.0001551s^2 + 15.7s + 1.579e06}{s^2 + 1777s + 1.579e06} \quad 7-8$$

The phase angle equation of the 2<sup>nd</sup> order Butterworth filter is determined using the following equation (Waters, 1991)

$$\phi_{LP}(f_{exc}) = -\tan^{-1} \left[ \frac{1}{\zeta} \left( 2 \frac{f_{exc}}{f_{LP}} + \sqrt{4 - \zeta^2} \right) \right] - \tan^{-1} \left[ \frac{1}{\zeta} \left( 2 \frac{f_{exc}}{f_{LP}} - \sqrt{4 - \zeta^2} \right) \right] \quad 7-9$$

$f_{LP}$ ,  $f$ , and  $\zeta$  represent the cut-off frequency, the excitation frequency, and the damping ratio of the filter respectively.

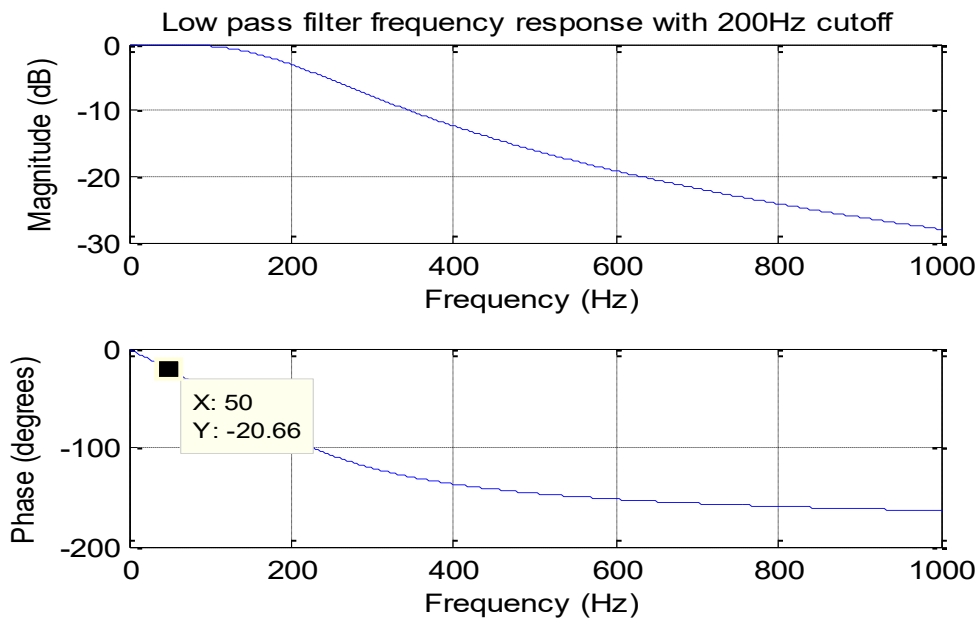


Figure 7-28 Low pass Butterworth filter response with cut-off frequency of 200Hz

Figure 7-28 shows the frequency response of the 2<sup>nd</sup> order low pass filter. Referring to the phase angle plot in the frequency range of 45-55Hz, the phase angles at 45Hz and 55Hz are  $-18.53^\circ$  and  $-22.82^\circ$  respectively. Those two phase shifts can be seen as positive phase delay of 1.143ms and 1.152ms at 45Hz and 55Hz respectively in accordance with the following relationship that associates time delay ( $\tau$ ), the phase shift  $\phi$ , and the excitation frequency  $f_{exc}$ .

$$\tau = \frac{\phi^\circ}{360^\circ \times f_{exc}} \quad 7-10$$

It is observed that the phase shifts introduced by the low pass filter with 200Hz cut-off frequency generates a phase shift that is translated as a signal shift in the time domain with a minimum value of 1.143ms at 45Hz and a maximum of 1.152ms at 55Hz.

### 7.9.3.2 Phase Shifts Due to High Pass Filtering

The continuous Laplace domain transfer function,  $TF_{HP}(s)$ , which represents the 2<sup>nd</sup> order high pass filter plant is expressed as

$$TF_{HP}(s) = \frac{s^2 - 0.0003948s - 7.792e - 08}{s^2 + 8.886s + 39.48} \quad 7-11$$

The phase angle equation of the 2<sup>nd</sup> order high pass Butterworth filter is determined using the following equation (Waters, 1991)

$$\phi_{HP}(f_{exc}) = \pi - \tan^{-1} \left[ \frac{1}{\zeta} \left( 2 \frac{f_{exc}}{f_{HP}} + \sqrt{4 - \zeta^2} \right) \right] - \tan^{-1} \left[ \frac{1}{\zeta} \left( 2 \frac{f_{exc}}{f_{HP}} - \sqrt{4 - \zeta^2} \right) \right] \quad 7-12$$

This expression is similar to that of the low pass filter but advanced by a  $\pi$  radian. The high pass filter is associated with negative phase shift. The frequency response of the high pass filter used with 1Hz cut-off frequency is depicted in Figure 7-29.

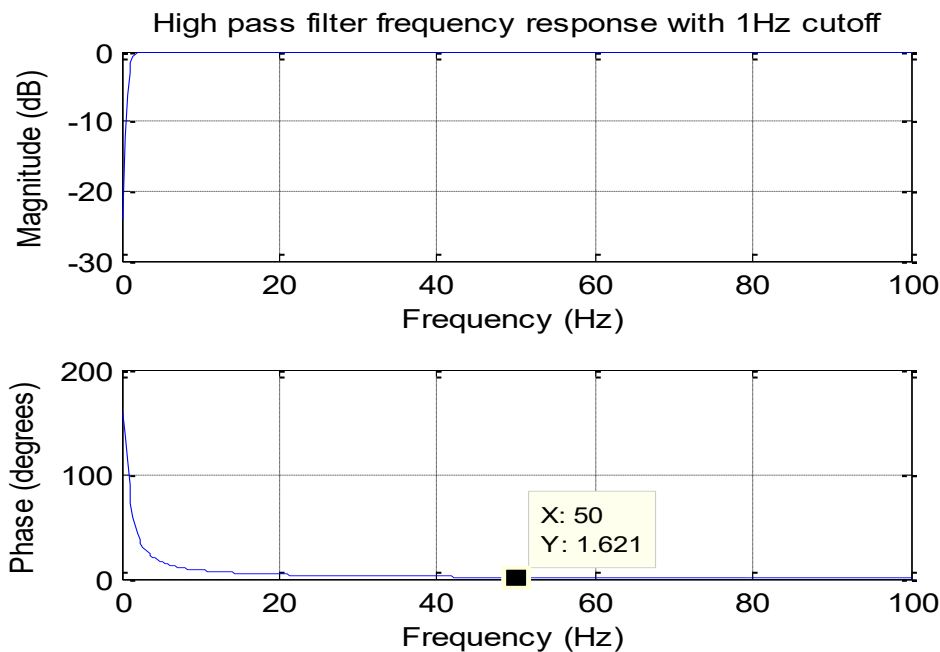


Figure 7-29 High pass Butterworth filter response with cut-off frequency of 1Hz

The phase angles at 45Hz and 55Hz are  $1.801^0$  and  $1.473^0$  respectively. Those phase shifts contribute to a max negative phase delay of  $-0.10006\text{ms}$  at 45Hz and minimum phase delay  $-0.07439\text{ms}$  at 55Hz. Since there are two high pass filters in the code, they contribute to advancing the signal by  $0.20012\text{ms}$  at 45Hz and  $0.148\text{ms}$  at 55Hz. The group delay is then estimated by adding the individual delays of each filter.

### 7.9.3.3 Delay Compensation

Phase shift manipulation can be also utilized for delay compensation as per the following explanation. Referring the time delay margin identified in the investigation of the effect of time delays on control stability in section 7.7, the comparison shows that the amount of group phase shifts generated by the different filter types in the implementation code is larger than the identified time margin, justifying the control instability exhibited in the experiments of Test 1. Based on the above explanation, it was found that a low pass filter contributes to positive phase delay between the filtered and original signal whereas a high pass filter corresponds to positive phase delay. Therefore, by careful choice of the cut-off frequencies, it is possible to compensate for the incurred group phase shifts. The following discusses the derivation of the phase shift relationship between the high pass and the low pass filter cut-off frequencies. The aim is to obtain an analytic solution that relates the cut-off frequencies to the phase shift and then solve it to obtain a zero group phase shift. By adding the phase equations of the phase shift and equating to zero, the following equality is obtained

$$\frac{\zeta f_{exc} (f_{HP} + f_{LP}) (-f_{exc}^2 + f_{HP} f_{LP})}{\zeta^2 f_{exc}^2 f_{HP} f_{LP} - (f_{HP} f_{LP})^2 + (f_{exc} f_{HP})^2 + (f_{exc} f_{LP})^2 - f_{exc}^2} = 0 \quad 7-13$$

Assuming that cut-off frequency of one filter is known, the following shows the non-trivial solution that relates the excitation frequency to the cut-off frequencies

$$f_{exc}^2 = f_{LP} f_{HP} \quad 7-14$$

As shown, the solutions are independent of the damping ratio  $\zeta$  of the filter.

### 7.9.4 Test 3: Experimental Implementation with Phase Shift Compensation

The compensation of phase delays resulting from the filtering is achieved by adaptively altering the low pass filter coefficients so that its cut-off frequency is chosen according to the above explanation. The following schematic model represents that of Test 3.

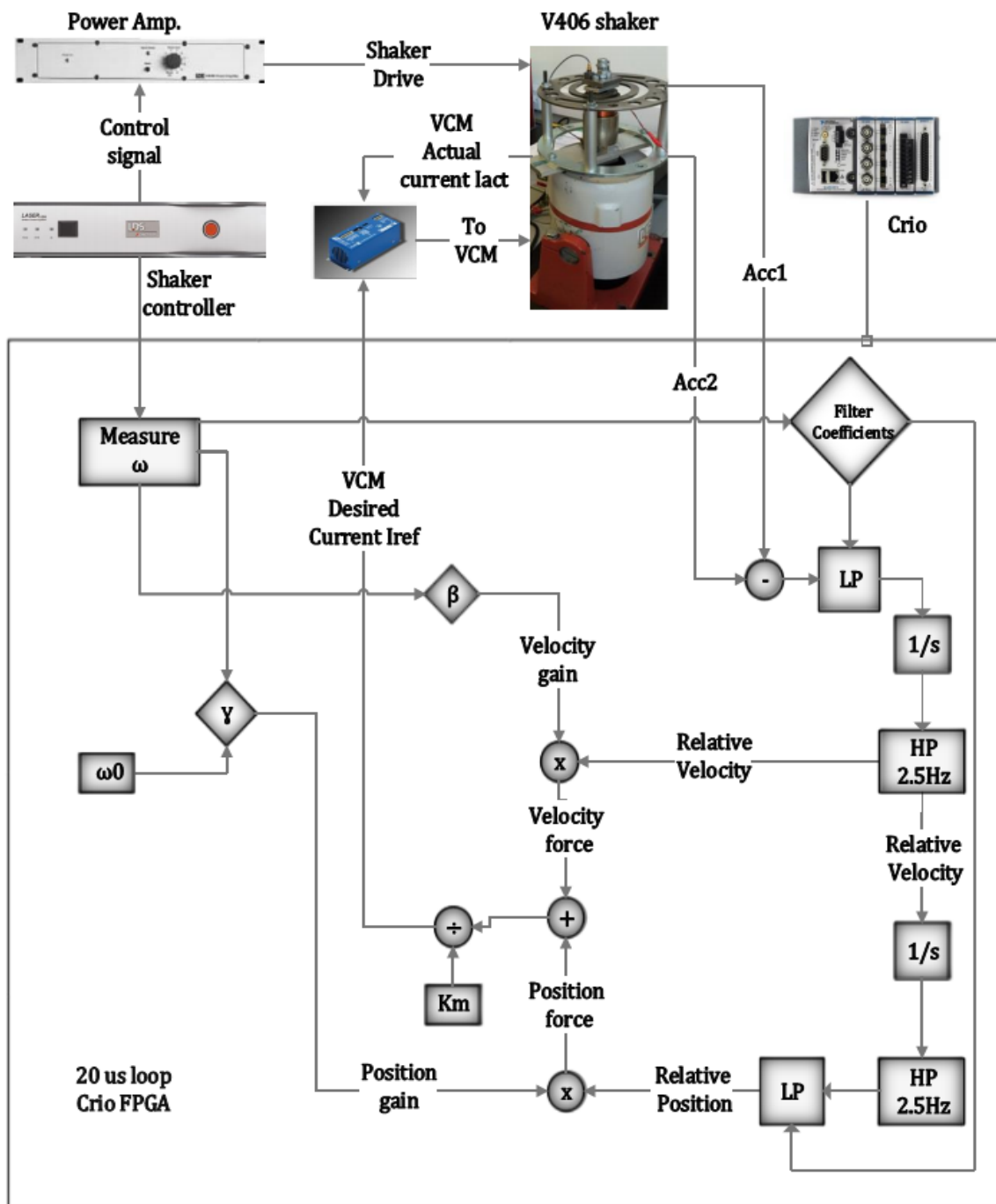


Figure 7-30 Schematic Diagram of the control model of Test 3

The attributes of Test 3 are provided in Table 7-6.

Table 7-6 Test 3 Parameters

Parameter	Symbol	Value	Unit
<b>Shaker Excitation</b>	$V_s$	$4 \sin 2\pi f_{exc} T$	[V]
<b>Excitation Frequency</b>	$f_{exc}$	40 - 60	[Hz]
<b>Test time</b>	T	60	[s]
<b>FPGA loop rate</b>	Ts	20e-6	[s]
<b>ATMD resonance</b>	$f_{ATMD}$	50	[Hz]
<b>Position feedback gain</b>	$\gamma$	$4\pi^2 m_{ATMD} (f_{exc}^2 - f_{ATMD}^2)$	[Ns <sup>2</sup> /m]
<b>Velocity feedback gain</b>	$\beta$	$-(0.103 f_{exc}^2 - 9.58 f_{exc} + 208)$	[Ns/m]
<b>VCM reference current</b>	$i_{ref}$	$\frac{1}{k_{vcm}} ((\gamma(\ddot{x}_1 - \ddot{x}_2) + \beta(x_1 - x_2)))$	[A]
<b>“Control ON”</b>	$f_{control}$	45 - 55	[Hz]
<b>Low pass cut-off</b>	$f_{Lp}$	$f_{exc}^2 / f_{HP}$	
<b>High pass cut-off</b>	$f_{Hp}$	2.5	

The test was performed and delay compensation is implemented in the code as described above. For the shaker table acceleration, the active damping succeeded in attenuating its vibration between 45Hz and 55Hz with stable control action across the entire range. Comparing the results with that of Test 1, it has been made clear that delays were the source of instability encountered in the test. The compensation of phase delays has successfully improved the system response while maintaining stability of the control after 50Hz.

In Test 2, delays were mitigated by shifting the ATMD original resonant frequency to 55Hz so that it lies outside the range of operation. This workout was successful, however it incurred extra power consumption as indicated in the section of Test 1. In this test, the ATMD original resonant frequency is tuned back to 50Hz and the test results proved to be successful. By comparing the electrical requirements of this test with that of Test 2, it is revealed that less power is required to perform the active damping for the same excitation level.

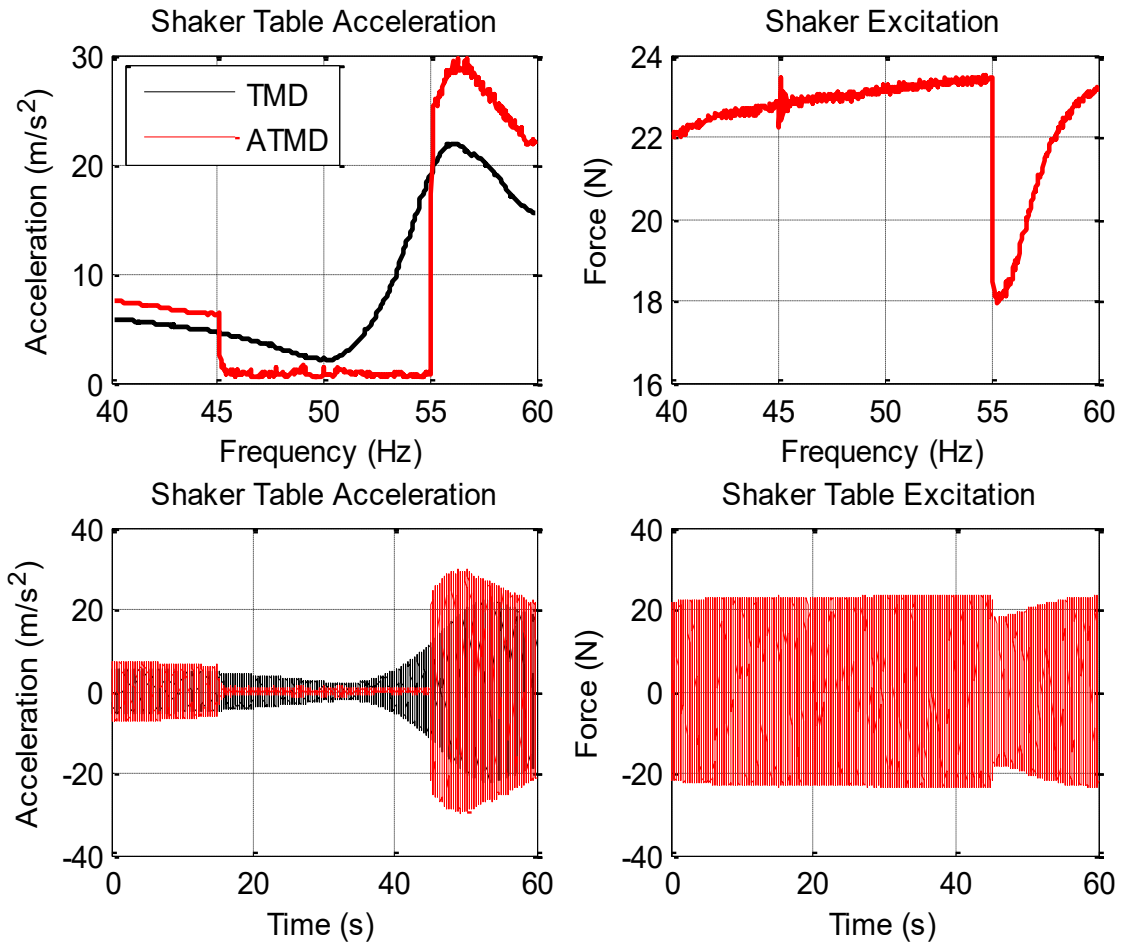


Figure 7-31 Shaker table excitation and acceleration with TMD tuned at 50Hz with delay cancelation

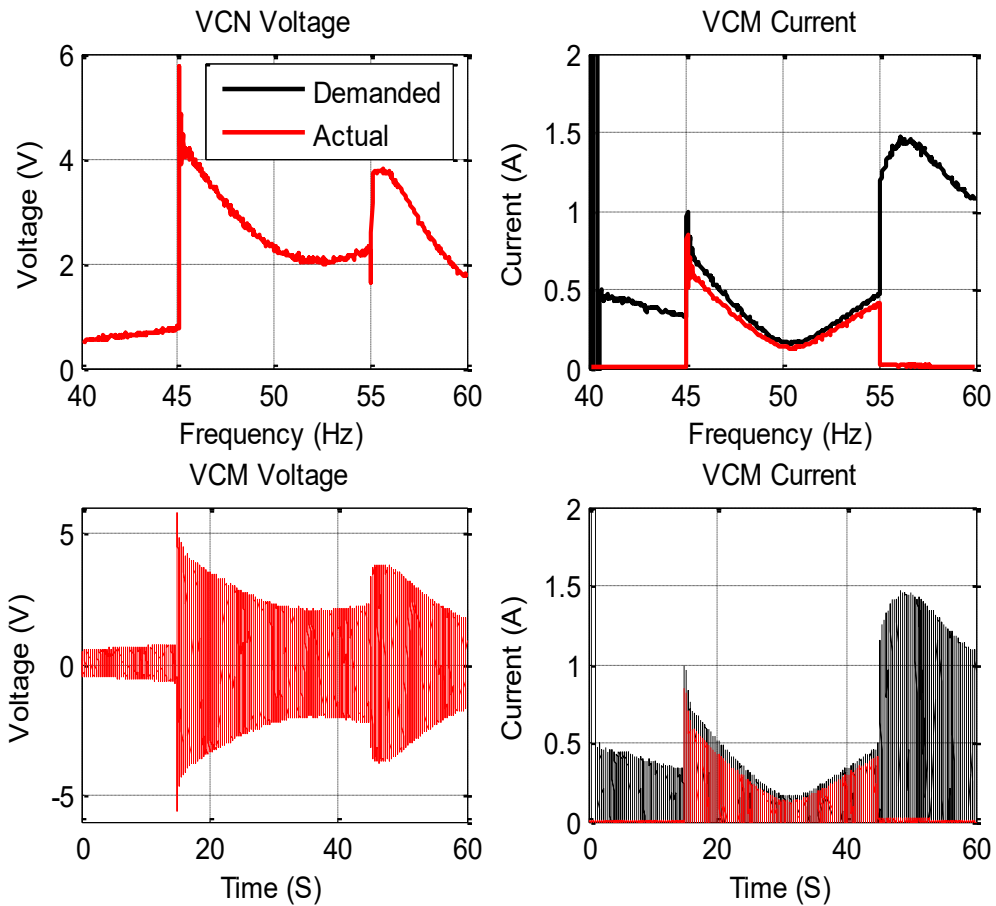


Figure 7-32 VCM voltage and Current with TMD tuned at 50Hz with delay cancellation

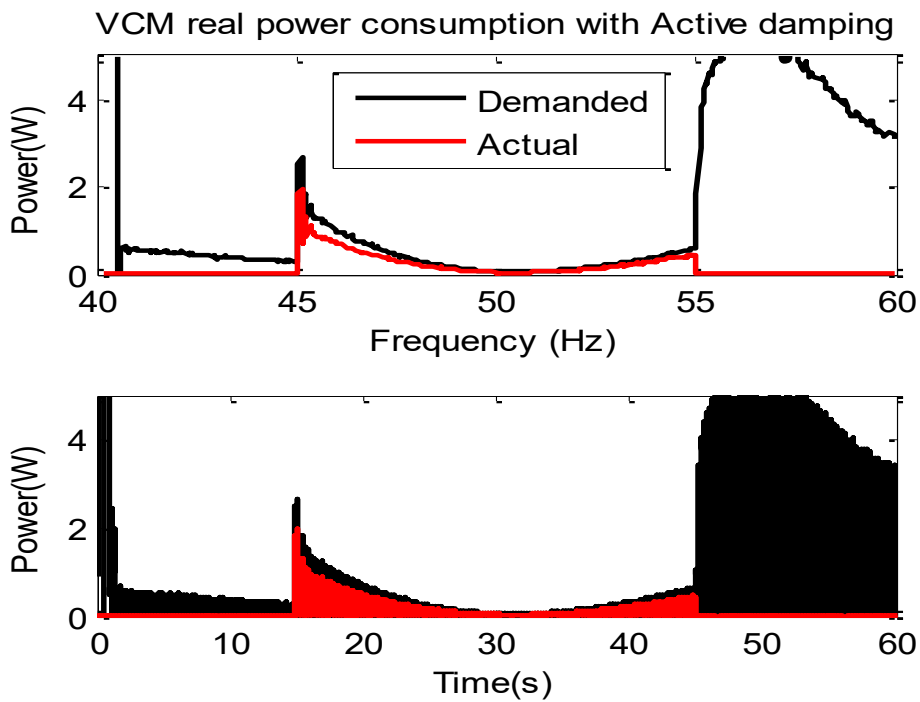


Figure 7-33 VCM power consumption with TMD tuned at 50Hz with delay cancellation

## 7.10 Test 4: Absolute Position and Velocity feedback

The model diagram in Figure 7-34 represents that of the gain scheduling control with absolute displacement measurement of the ATMD dynamic mass only.

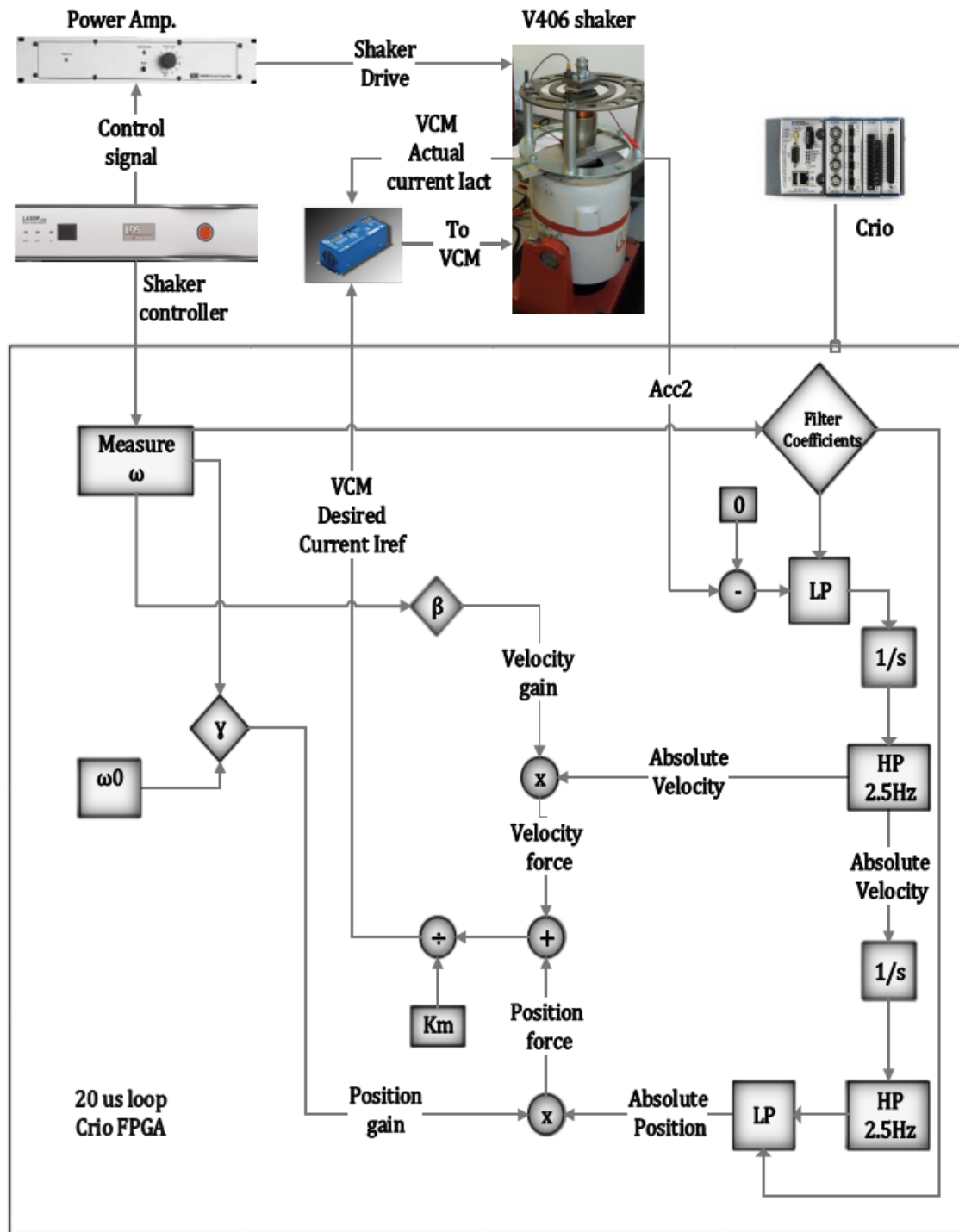


Figure 7-34 Schematic Diagram of the control model of Test 4

While assuming absolute measurement, it was observed from the theoretical analysis on the gain scheduling control law that the transfer function that relates the shaker table displacement with the excitation force has the same zeros as the transfer function resulting from assuming relative measurement. The use of absolute measurements could be more efficient in the sense that only one sensor is required to perform the control. Consequently, this allows for lower computational power requirements as well as more packed physical arrangement of the system. The intention in this test is to experimentally illustrate the concept of active vibration control with absolute measurement of the states. The results of this test are presented in the following set of figures. It is revealed that the feedback of absolute measurement of the ATMD position and velocity succeeds in reducing the vibration of the shaker table. The results are quite similar to those of Test 3.

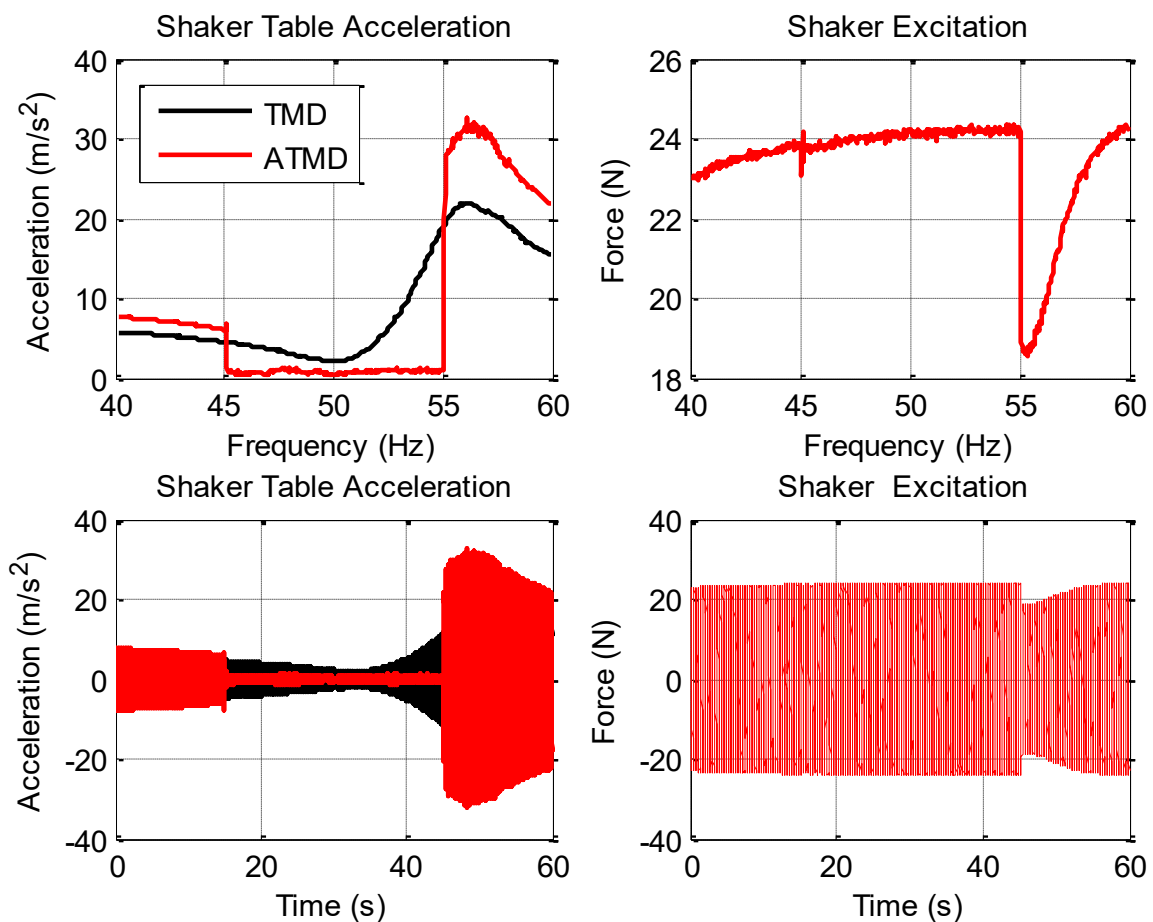


Figure 7-35 Shaker table excitation and acceleration

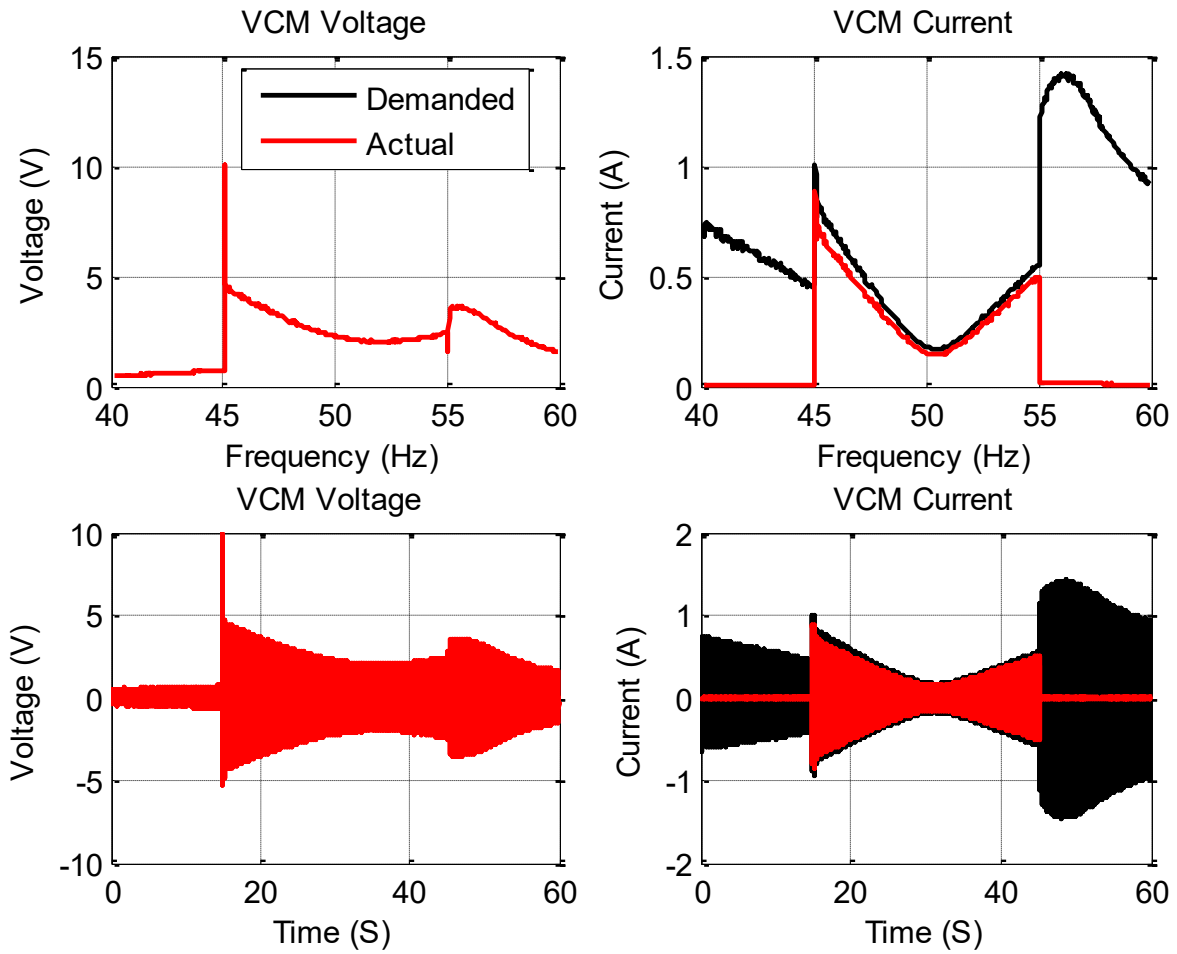


Figure 7-36 VCM voltage and Current of Test 4

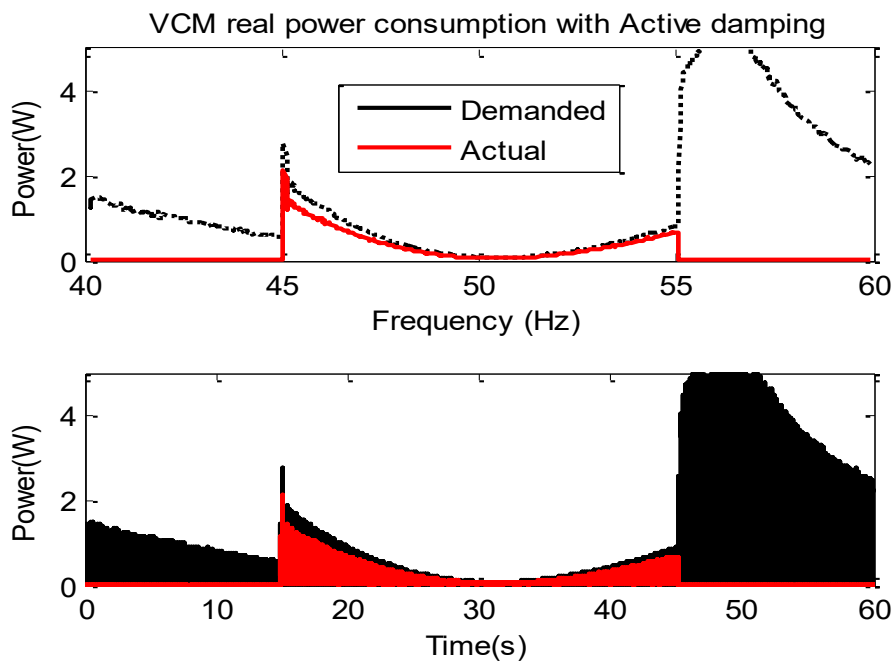


Figure 7-37 VCM real power consumption of Test 4

## 8 Stirling Engine Active Control Analysis

In the very first stages of this work, a vibration model of the Stirling engine was proposed. A set of simulations were carried out based on the proposed model and then it was validated experimentally within certain operating conditions. The validated model was then selected for further simulation with different control techniques for the mitigation of the engine case vibration.

A scaled test rig emulating the behaviour of the Stirling engine was built for the purpose of testing the proposed control strategies for the active vibration control. An electromechanical model was proposed for the test rig featuring the dynamics of an electromagnetic shaker and an ATMD with a VCM actuator. The system comprised the shaker table subject to harmonic excitation. An ATMD with a helical spring was mounted horizontally on top of the shaker table. A VCM is placed axially between the shaker table and the helical spring. The simulation of the proposed shaker rig model showed successful results. Following the successful simulation, a set of experimental tests were carried out with active control using the real test rig.

The experimental results revealed that the proposed model predictions match very well with real results and the tests illustrated the success of the control implementation. The actuator electrical specifications to deliver the required actuation force were extracted within the context of the shaker rig.

This section is dedicated to the extension of the original model of the Stirling. The idea is to apply the model parameters of the Stirling engine within the electromechanical model of the shaker rig. The same control strategies will be applied as before however, a different VCM will be used to deliver a larger force since larger excitation force exists.

## 8.1 Extended Model of the Stirling Engine

In here, the model that represents the vibration characteristics of the Stirling engine that was presented in chapter 5 is considered for development. The model dynamics of a VCM are added to the engine model. In the simulation, the excitation force is assumed to be harmonic with 1000N and 3000N amplitudes and frequency that varies between 45Hz and 55Hz. The active control force delivered by the VCM is determined in the simulation code according to the gain scheduling control with position/acceleration and velocity feedback. It is assumed that the engine behaves a 2DOF featuring an engine case whose vibration to be reduced with the aid of an ATMD originally tuned at 50Hz. The VCM forms an integral part of the ATMD and is controlled with a current control technique employing a conventional PID controller. The system of dynamics equations that describe the electromechanical system of the Stirling engine and the ATMD is expressed in system 8-1.

$$\left\{ \begin{array}{l} m_1 \ddot{x}_1 + k_1 x_1 + c_1 \dot{x}_1 + k_2(x_1 - x_2) + c_2(\dot{x}_1 - \dot{x}_2) = F_{exc} - f_{act} \\ m_2 \ddot{x}_2 + k_2(x_2 - x_1) + c_2(\dot{x}_2 - \dot{x}_1) = f_{act} \\ V_{vcm} = R_{vcm} i_{vcm} + L_{vcm} \frac{di_{vcm}}{dt} + k_{vcm}(x_1 - x_2) \\ i_{ref} = \frac{f_{act}}{k_{vcm}} \\ e = i_{ref} - i_{vcm} \\ PID = k_p e + k_i \int e dt + k_d \frac{d}{dt}(e) \\ V_{vcm} = PID(e) \end{array} \right. \quad 8-1$$

A state-space model is proposed for the entire model in 8-2 based on the definitions presented in Table 8-1

$$\begin{bmatrix} \dot{x}_1 \\ \dot{x}_2 \\ \dot{x}_3 \\ \dot{x}_4 \\ \dot{x}_5 \\ \dot{x}_6 \end{bmatrix} = \begin{bmatrix} 0 & 0 & 0 & 1 & 0 & 0 \\ 0 & 0 & 0 & 0 & 1 & 0 \\ 0 & 0 & 0 & 0 & 0 & 1 \\ \frac{-(k_1 + k_2)}{m_1} & \frac{k_2}{m_1} & 0 & \frac{-(c_1 + c_2)}{m_1} & \frac{c_2}{m_1} & \frac{-k_{vcm}}{m_1} \\ \frac{k_2}{m_2} & \frac{-k_2}{m_2} & 0 & \frac{c_2}{m_2} & \frac{-c_2}{m_2} & \frac{k_{vcm}}{m_2} \\ 0 & 0 & \frac{-k_i}{L_{vcm} + k_d} & \frac{-k_{vcm}}{L_{vcm} + k_d} & \frac{k_{vcm}}{L_{vcm} + k_d} & \frac{-R_{vcm} - k_p}{L_{vcm} + k_d} \end{bmatrix} \begin{bmatrix} x_1 \\ x_2 \\ x_3 \\ x_4 \\ x_5 \\ x_6 \end{bmatrix} + \begin{bmatrix} 0 & 0 & 0 & 0 \\ 0 & 0 & 0 & 0 \\ 0 & 0 & 0 & 0 \\ 0 & 0 & 0 & 0 \\ \frac{1}{m_1} & 0 & 0 & 0 \\ 0 & 0 & 0 & 0 \\ 0 & \frac{k_i}{L_{vcm} + k_d} & \frac{k_p}{L_{vcm} + k_d} & \frac{k_d}{L_{vcm} + k_d} \end{bmatrix} \begin{bmatrix} F_{exc} \\ q_{ref} \\ \dot{q}_{ref} \\ \ddot{q}_{ref} \end{bmatrix} \tag{8-2}$$

Table 8-1 Stirling Engine electromechanical system variables

Parameter	Component	State-Space Variable	Inputs	
Displacement	Engine case	$\dot{x}_1 = x_1$	Engine	$F_{exc}$
	ATMD mass	$\dot{x}_2 = x_2$		
Electrical Charge	VCM: Actual	$\dot{x}_3 = q_{vcm} = x_3$		
Velocity	Engine case	$\dot{x}_4 = \dot{x}_1 = x_4$	VCM	$q_{ref}$
	ATMD mass	$\dot{x}_5 = \dot{x}_2 = x_5$		$\dot{q}_{ref}$
Electrical Current	VCM: Actual	$\dot{x}_6 = \dot{q}_{vcm} = x_6$		$\ddot{q}_{ref}$

The schematic diagram presented in Figure 8-1 shows the simulation model of the Stirling engine with the control strategy according to the state-space system presented earlier. The “Stirling Engine” subsystem block in the schematic of Figure 8-1 contains the state-space model of the Stirling engine in system 8-2. The excitation force is connected to the first input of the state-space model and the control current to the VCM is connected to the third input. The system outputs all the states and the control is performed accordingly.

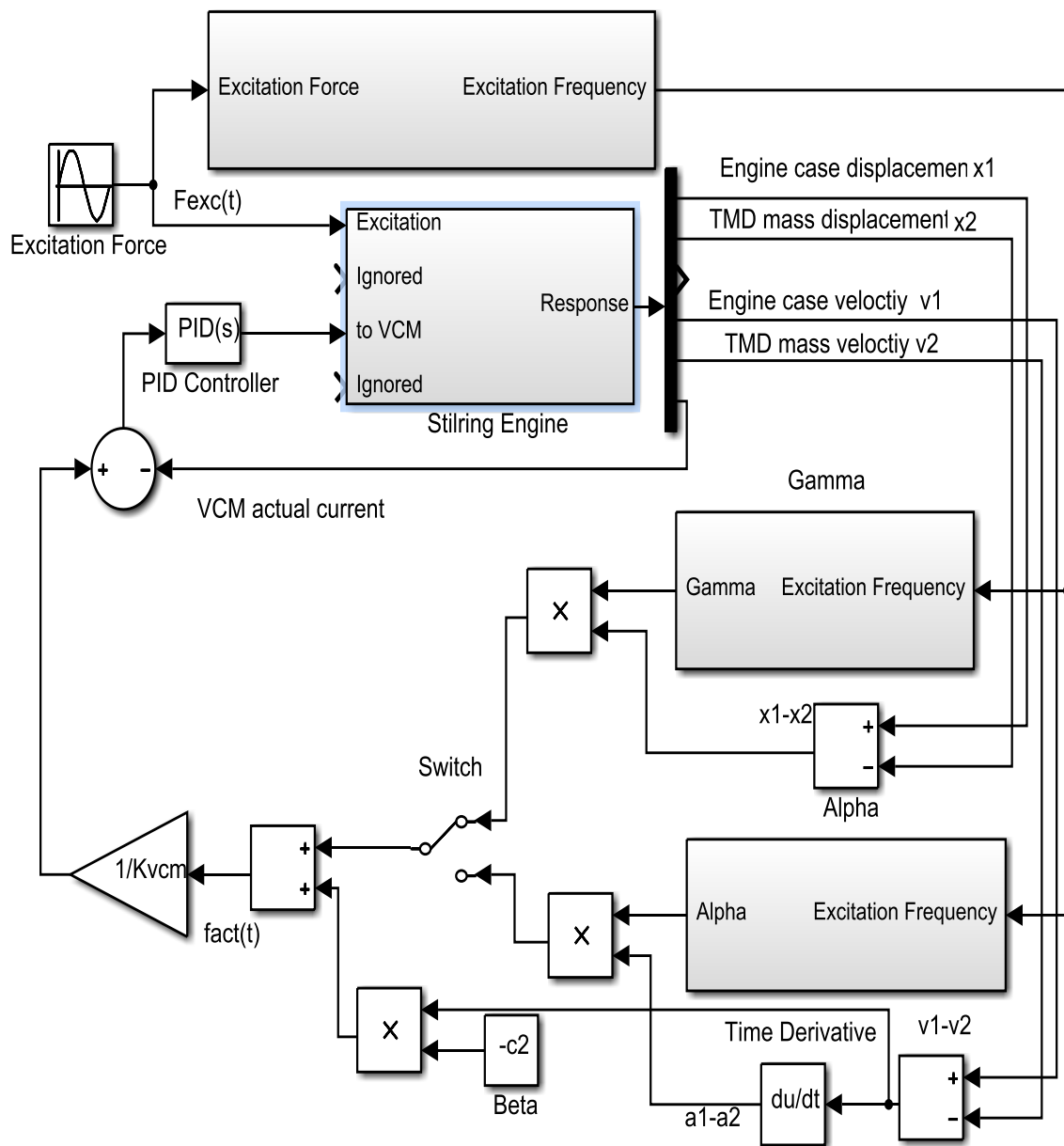


Figure 8-1 Schematic model diagram for the active damping control of the Stirling engine

## 8.2 Simulation of the Electromechanical Model

For the simulation, the values of Table 8-2 are adopted. The VCM is chosen based on the force and stroke requirements that were extracted in the control simulation of the engine system in chapter 6. The VCM introduces additional mass in the ATMD which lowers its resonant frequency slightly below 50Hz. The ATMD was retuned removing some dynamic mass. Previously, the damping introduced by the VCM was characterised experimentally and in the active control experiments an adaptive velocity feedback gain was implemented to remove the effect of this damping. In this section, there are no means to characterise the damping that will be introduced by the suggested VCM due to the fact that the motor is not available in our lab and an exact model of the VCM doesn't exist. Therefore, in here, damping will be assumed constant.

Table 8-2 Electro-mechanical Simulation parameters

Stirling Engine	VCM LVCM-095-089-01	Simulation
$m_1 = 41.38 + m_{VCM} [kg]$	$R_{vcm} = 3 [\Omega]$	$f_{exc} = 45 - 55 [Hz]$
$m_2 = 8.862 + m_{coil} [kg]$	$L_{vcm} = 2.1 [mH]$	T: 55 [s]
$c_1 = 200 [Ns/m]$	$k_{vcm} = 22.2 [N/A]$	$T_s = 1e - 5 [s]$
$c_2 = 2.7 Ns/m$	$m_{VCM} = 4.15 [kg]$	
$k_1 = 8369.4 [N/m]$	$m_{coil} = 0.621 [kg]$	
$k_2 = 935930 [N/m]$	$k_p = 200$	
$F_{exc}(t) = 1000 \sin f_{exc} T [N]$		

The results of the simulation are shown in Figure 8-2. It is revealed that for 1000N excitation, the proposed active control law is capable of attenuating the vibration of the engine case to amplitudes below  $20\mu m$  in the frequency range of 45-55Hz with either the acceleration or position and velocity feedback. Key requirements such as the voltage, current and power consumptions that the actuator requires to achieve the active damping are identified.

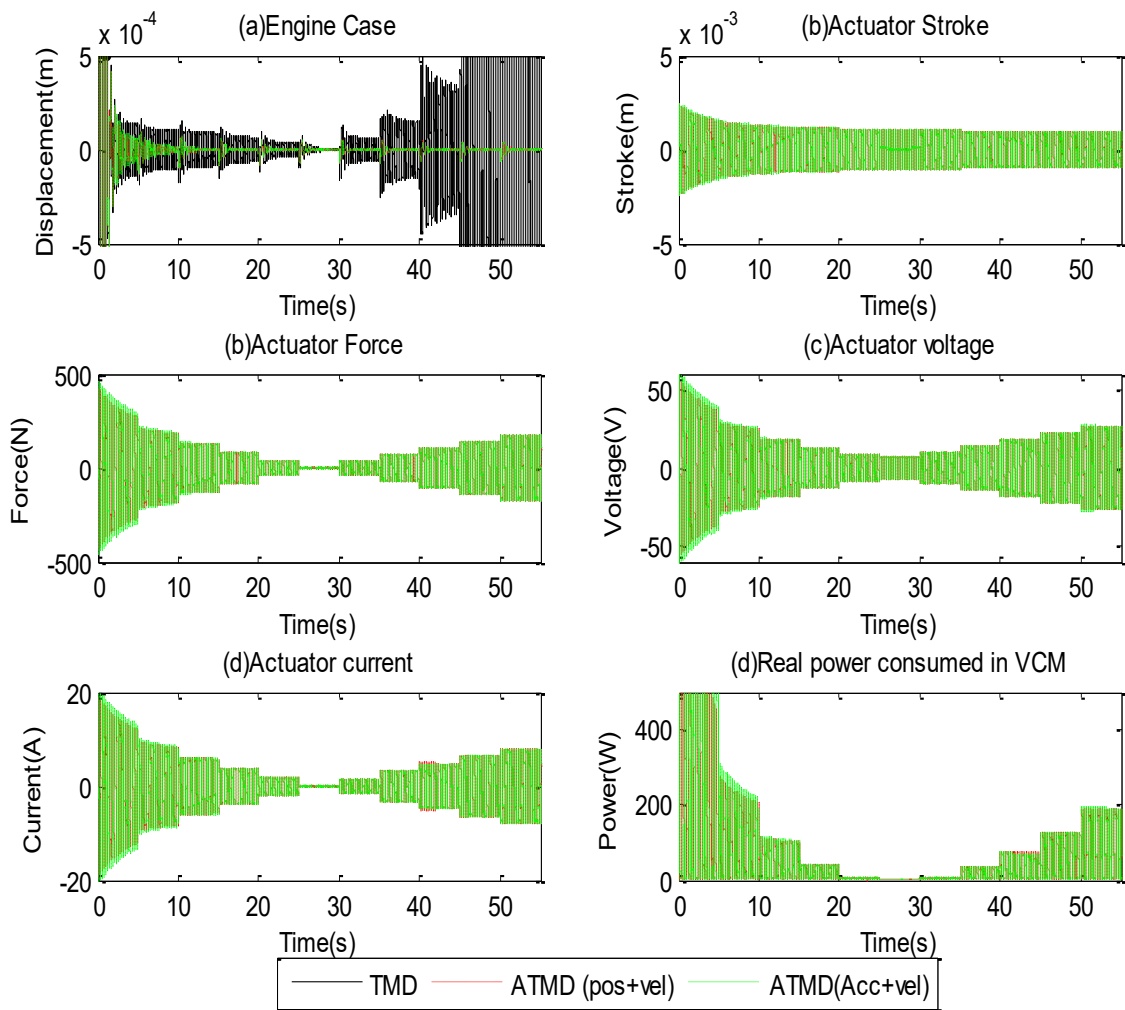


Figure 8-2 Simulation results of the active damping control for the Stirling engine

### 8.3 Discussion on Power Consumption

Perhaps the most important parameter to study is the electrical power that the VCM consumes to perform the active control. Referring to the Figure 8-2, the VCM consumes high power in the first 5 seconds associated with the high transients. The existence of high transients corresponds to the immediate retuning of the ATMD resonant frequency from 50Hz to 45Hz. In reality this doesn't happen because the excitation frequency varies smoothly from between 47-53Hz. For now, the transient can be ignored and the interval between 10 seconds and 45 seconds will be considered. This interval corresponds to excitation frequency interval 47-53Hz. The following graphs depict the power consumption of the VCM for 1000N and 3000N excitation forces respectively.

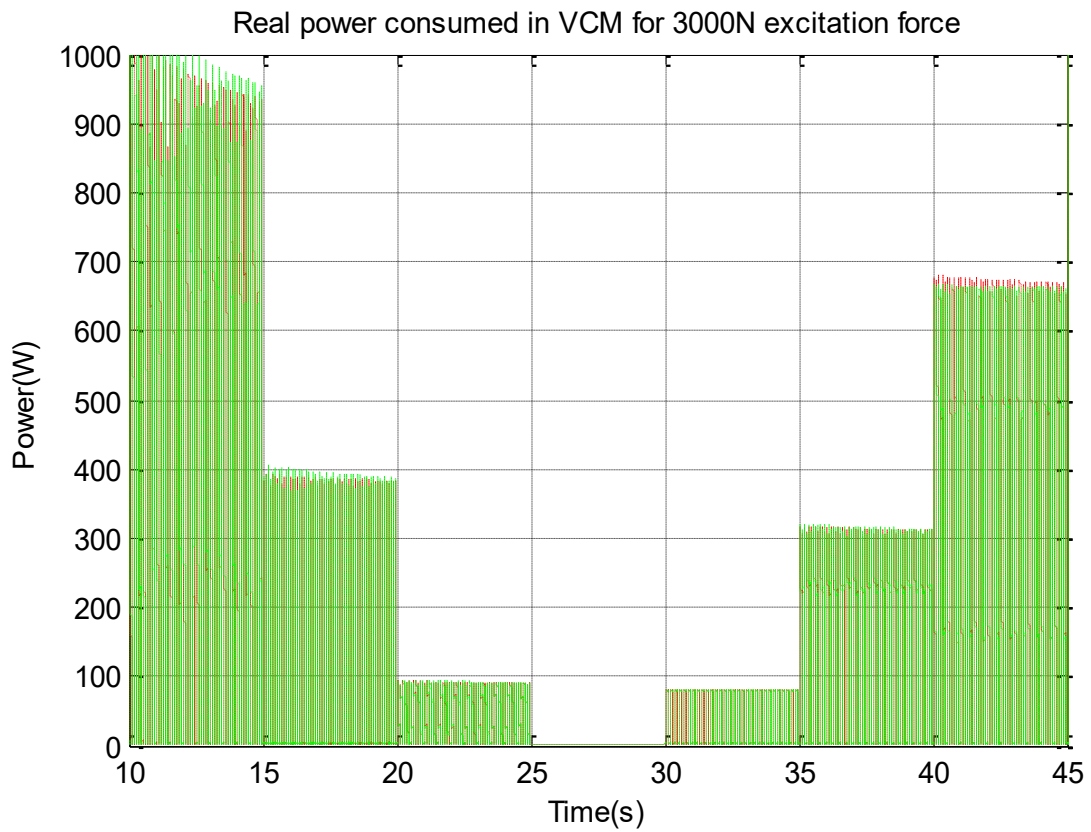
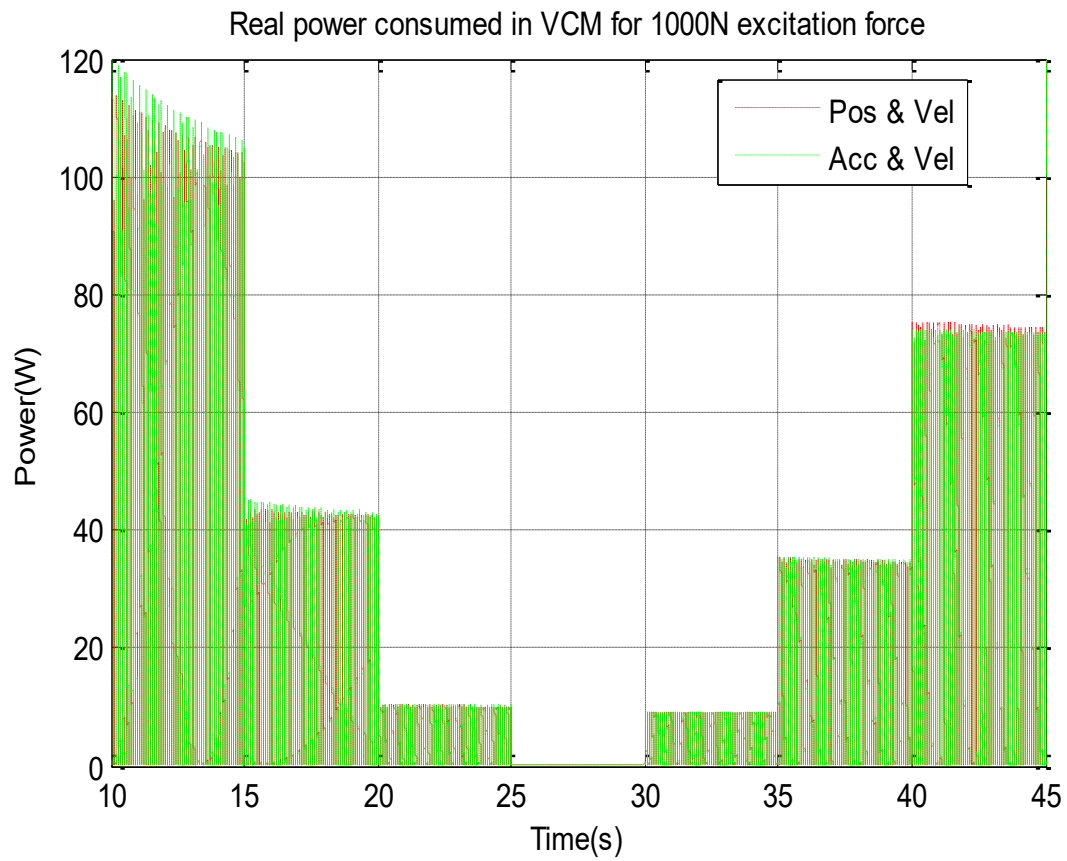


Figure 8-3 Close-up view of the real power consumption of the VCM for 1kN and 3kN excitation forces

Referring to the graphs and recalling, two main observations can be made:

1. The power consumption doesn't vary linearly with the change in the excitation frequency. There is no significant difference between performances of the two control strategies.
2. The power levels vary by the square of the excitation force ratio.

The question that comes to mind is that if the Stirling engine is generating 1KW of power, how much power is it willing to lose for powering up the VCM? Assuming that a max of 10% (100W) of the engine power generation will be lost to power the VCM, two scenarios is taken into account:

1. If the engine case excitation is 1000N, it is then feasible to do the active damping with the VCM because the max power consumption of the VCM is 100W at 47Hz and is lower for other frequencies in the range of 47-53Hz.
2. If the engine case excitation is 3000N, it is not feasible to perform active damping with this VCM. According to the graph in Figure 8-3, the max power consumption of the VCM is 9 times larger at 47Hz for 3000N excitation force. This means that the Stirling engine will need to give out almost its entire power generation.

The following discusses a potential solution that can be used in order to perform the active damping when the excitation force is 3000N. The VCM that was used in the simulation has a motor constant  $k_{vcm} = 22.2 [N/A]$ , if a larger motor constant is used, the demanded electrical current will be lower for the same demanded force, hence a lower power requirement. Table 8-3 contains data for a VCM from Moticont that has much higher motor constant. This motor is chosen for simulation with 3KN excitation and the required power is obtained.

Table 8-3 GVCM-095-089-02S06 parameters

<b>VCM</b> <b>GVCM-095-089-02S06</b>
$R_{vcm} = 3 \text{ } [\Omega]$
$L_{vcm} = 1.9 \text{ } [mH]$
$k_{vcm} = 51.6 \text{ } [N/A]$
$m_{VCM} = 4.10 \text{ } [kg]$
$m_{coil} = 0.710 \text{ } [kg]$

The following simulation results show the VCM power requirement with 3000N excitation force for the GVCM-095-089-02S06.

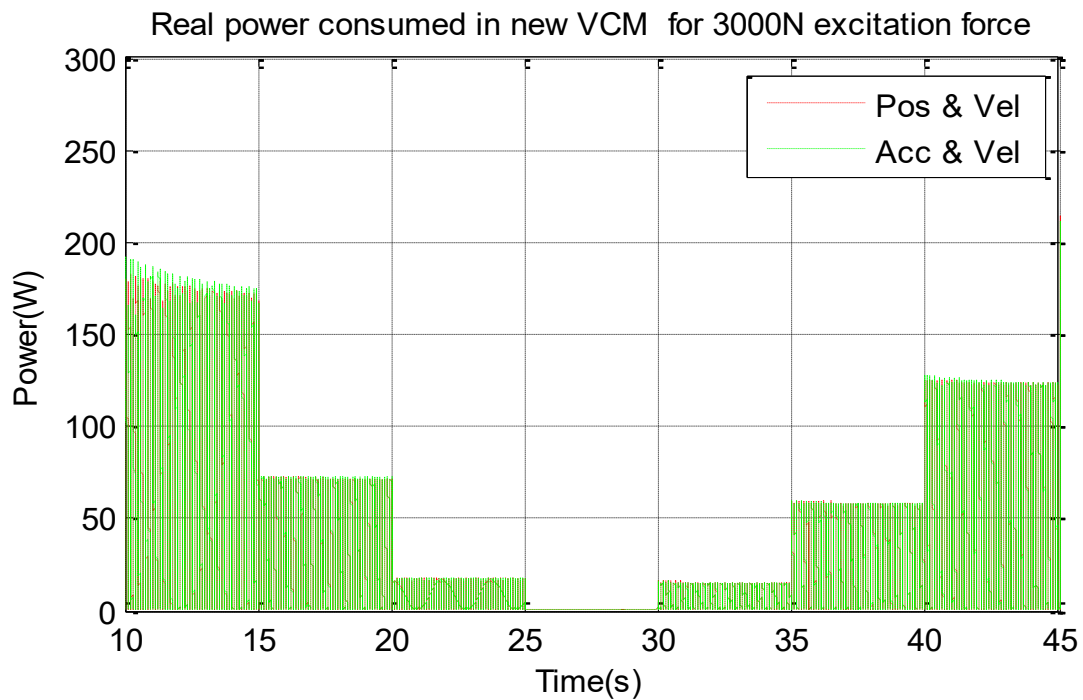


Figure 8-4 Real power consumption of the VCM for 3kN excitation force and VCM motor constant  $k_{vcm} = 51.6 \text{ } [N/A]$

In Figure 8-4, it can be seen that the power consumption has been reduced significantly when a VCM with higher motor constant is used. Assuming that engine can generate 1.2KW of power and assuming that 10% of this power will be used in the active control implementation, if the original engine efficiency is 30%, this would be reduced to 27%.

## 8.4 General Equations for Active Vibration Control with a VCM

This section is dedicated to the derivation of the general actuator force, actuator current, and actuator real power consumption equations for any 2DOF electromechanical system whose vibration to be cancelled actively using a VCM and following the proposed control strategies. The availability of those expressions allows studying the actuator requirements for any 2DOF system. Therefore, having any validated 2DOF model, the actuator requirement can be estimated based on those equations by substituting the relevant parameters.

### 8.4.1 Gain Scheduling with Zero Placement Position & Velocity Feedback

Considering position and velocity feedback gains, the transfer function that relates the actuator force to the excitation force is derived from the proposed model. It is expressed in the Laplace domain as follows

$$F_{act}(s) = \frac{m_2(\beta k_p - k_{vcm}^2)s^3 + \gamma k_p m_2 s^2}{a_5 s^5 + a_4 s^4 + a_3 s^3 + a_2 s^2 + a_1 s + a_0} F_{exc}(s) \quad 8-3$$

The electrical current drawn by the VCM actuator is then expressed as

$$I_{act}(s) = \frac{F_{act}(s)}{k_{vcm}} = \frac{1}{k_{vcm}} \frac{m_2(\beta k_p - k_{vcm}^2)s^3 + \gamma k_p m_2 s^2}{a_5 s^5 + a_4 s^4 + a_3 s^3 + a_2 s^2 + a_1 s + a_0} F_{exc}(s) \quad 8-4$$

The power consumed by the VCM can then be expressed as

$$\begin{aligned} P_{act}(s) &= R_{vcm} I_{act}(s)^2 \\ &= R_{vcm} \left[ \frac{1}{k_{vcm}} \frac{m_2(\beta k_p - k_{vcm}^2)s^3 + \gamma k_p m_2 s^2}{a_5 s^5 + a_4 s^4 + a_3 s^3 + a_2 s^2 + a_1 s + a_0} F_{exc}(s) \right]^2 \end{aligned} \quad 8-5$$

Where

$$\begin{aligned}
a_5 &= L_{vcm}m_1m_2 \\
a_4 &= L_{vcm}c_1m_2 + L_{vcm}c_2(m_1 + m_2) + m_1m_2(R_{vcm} + k_p) \\
a_3 &= L_{vcm}c_1c_2 + m_1(-k_{vcm}^2 + c_2(R_{vcm} + k_p) + L_{vcm}k_2 + \beta k_p) \\
&\quad + m_2(-k_{vcm}^2 + \beta k_p + (R_{vcm} + k_p)(c_1 + c_2) + L_{vcm}(k_1 + k_2)) \\
a_2 &= c_1(-k_{vcm}^2 + L_{vcm}k_2 + \beta k_p + c_2(R_{vcm} + k_p)) + L_{vcm}k_1c_2 \\
&\quad + m_2((R_{vcm} + k_p)(k_1 + k_2) + \gamma k_p) + m_1(k_p(\gamma + k_2) + R_{vcm}k_2) \\
a_1 &= c_1(k_p(\gamma + k_2) + R_{vcm}k_2) + k_1(k_p(\beta + c_2) - k_{vcm}^2 + L_{vcm}k_2 + R_{vcm}c_2) \\
a_0 &= k_1k_p(\gamma + k_2) + R_{vcm}k_1k_2
\end{aligned}$$

#### 8.4.2 Gain Scheduling with Zero Placement Acceleration & Velocity Feedback

Now assuming the acceleration and velocity feedback, the following equations are derived

$$F_{act}(s) = \frac{\alpha k_p m_2 s^4 + m_2(\beta k_p - k_{vcm}^2)s^3}{a_5 s^5 + a_4 s^4 + a_3 s^3 + a_2 s^2 + a_1 s + a_0} F_{exc} \quad 8-6$$

$$I_{act}(s) = \frac{F_{act}(s)}{k_{vcm}} = \frac{1}{k_{vcm}} \frac{\alpha k_p m_2 s^4 + m_2(\beta k_p - k_{vcm}^2)s^3}{a_5 s^5 + a_4 s^4 + a_3 s^3 + a_2 s^2 + a_1 s + a_0} F_{exc}(s) \quad 8-7$$

$$\begin{aligned}
P_{act}(s) &= R_{vcm} I_{act}(s)^2 \\
&= R_{vcm} \left[ \frac{1}{k_{vcm}} \frac{\alpha k_p m_2 s^4 + m_2(\beta k_p - k_{vcm}^2)s^3}{a_5 s^5 + a_4 s^4 + a_3 s^3 + a_2 s^2 + a_1 s + a_0} F_{exc}(s) \right]^2 \quad 8-8
\end{aligned}$$

Where

$$\begin{aligned}
a_5 &= L_{vcm}m_1m_2 \\
a_4 &= L_{vcm}c_1m_2 + (L_{vcm}c_2 + \alpha k_p)(m_1 + m_2) + m_1m_2(R_{vcm} + k_p) \\
a_3 &= c_1(L_{vcm}c_2 + \alpha k_p) + m_1(-k_{vcm}^2 + c_2(R_{vcm} + k_p) + L_{vcm}k_2 + \beta k_p) \\
&\quad + m_2(-k_{vcm}^2 + \beta k_p + (R_{vcm} + k_p)(c_1 + c_2) + L_{vcm}(k_1 + k_2)) \\
a_2 &= c_1(-k_{vcm}^2 + L_{vcm}k_2 + \beta k_p + c_2(R_{vcm} + k_p)) \\
&\quad + m_2(R_{vcm} + k_p)(k_1 + k_2) + m_1k_2(k_p + R_{vcm}) + k_1(L_{vcm}c_2 + \alpha k_p) \\
a_1 &= c_1k_2(k_p + R_{vcm}) + k_1(k_p(\beta + c_2) - k_{vcm}^2 + L_{vcm}k_2 + R_{vcm}c_2) \\
a_0 &= k_1k_2(R_{vcm} + k_p)
\end{aligned}$$

### 8.4.3 LQ control

For the LQ control, full-state feedback is assumed. The resulting equations are

$$F_{act}(s) = \frac{b_4s^4 + b_3s^3 + b_2s^2 + b_1s + b_0}{a_5s^5 + a_4s^4 + a_3s^3 + a_2s^2 + a_1s + a_0} \quad 8-9$$

$$I_{act}(s) = \frac{F_{act}(s)}{k_{vcm}} = \frac{1}{k_{vcm}} \frac{b_4s^4 + b_3s^3 + b_2s^2 + b_1s + b_0}{a_5s^5 + a_4s^4 + a_3s^3 + a_2s^2 + a_1s + a_0} \quad 8-10$$

$$\begin{aligned} P_{act}(s) &= R_{vcm} I_{act}(s)^2 \\ &= R_{vcm} \left[ \frac{1}{k_{vcm}} \frac{b_4s^4 + b_3s^3 + b_2s^2 + b_1s + b_0}{a_5s^5 + a_4s^4 + a_3s^3 + a_2s^2 + a_1s + a_0} F_{exc}(s) \right]^2 \end{aligned} \quad 8-11$$

Where

$$b_4 = -\mathbf{K}\mathbf{x}k_p m_1 m_2$$

$$b_3 = -F_{exc}(s)(k_{vcm}^2) - \mathbf{K}\mathbf{x}k_p (c_2(m_1 + m_2) + c_1 m_2)$$

$$b_2 = -\mathbf{K}\mathbf{x}k_p (c_1 c_2 + m_1 k_2 + m_2 (k_1 + k_2))$$

$$b_1 = -\mathbf{K}\mathbf{x}k_p (c_1 k_2 + c_2 k_1)$$

$$b_0 = -\mathbf{K}\mathbf{x}k_p k_1 k_2$$

$$a_5 = L_{vcm} m_1 m_2$$

$$a_4 = L_{vcm} c_1 m_2 + L_{vcm} c_2 (m_1 + m_2) + m_1 m_2 (R_{vcm} + k_p)$$

$$\begin{aligned} a_3 &= L_{vcm} c_1 c_2 + m_1 (-k_{vcm}^2 + c_2 (R_{vcm} + k_p) + L_{vcm} k_2) \\ &\quad + m_2 (-k_{vcm}^2 + (R_{vcm} + k_p) (c_1 + c_2) + L_{vcm} (k_1 + k_2)) \end{aligned}$$

$$\begin{aligned} a_2 &= c_1 (-k_{vcm}^2 + L_{vcm} k_2 + c_2 (R_{vcm} + k_p)) \\ &\quad + m_2 (R_{vcm} + k_p) (k_1 + k_2) + m_1 k_2 (k_p + R_{vcm}) + L_{vcm} k_1 c_2 \end{aligned}$$

$$a_1 = c_1 k_2 (k_p + R_{vcm}) + k_1 (k_p c_2 - k_{vcm}^2 + L_{vcm} k_2 + R_{vcm} c_2)$$

$$a_0 = k_1 k_2 (R_{vcm} + k_p)$$

Where upper case vectors  $\mathbf{K}$  and  $\mathbf{x}$  represent the LQ control gains and the systems states variables respectively.

## 9 Discussion, Future Work, and Conclusion

### 9.1 Discussion

New grid connection/disconnection regulations for small scale generators have imposed challenging design constraints in FPSE/LA generators when the machine is grid connected. The  $\beta$ -type Stirling engine is directly affected by the new regulations that require a wider frequency bandwidth for the electrical grid operation, particularly, broadening the original 50Hz operation to 47Hz-53Hz. During the normal operation of this engine, its case is subjected to internal harmonic excitation at 50Hz. currently, this engine is equipped with a passive TMD designed to damp the vibration of the engine at 50Hz only. The installed TMD is only effective when the frequency is 50Hz, and hence it is not possible for it to cope with the new frequency range introduced in the new regulations. The use of active vibration control techniques has proven to be a potential solution for numerous vibration problems in various areas including machine induced and structural vibrations.

This research work considered modeling, simulation, and implementation of an ATMD for the purpose of controlling the vibration in the FPSE/LA with the aim of broadening its frequency range of operation from 50Hz to 47Hz-53Hz. The research was conducted by dividing it into three main parts:

- Theoretical modelling & simulation of the mechanical system
- Integration of the mechanical model with the electrical actuation and the control element
- Experimental validation and implementation of the models and control system

To begin with, based on preliminary knowledge of the  $\beta$ -type Stirling engine parameters that were provided by the manufacturer, a simplified vibration model based on 2DOF system was developed to emulate the response of the Stirling engine and the internally mounted passive TMD. The response of the simulated model was later analysed with emphasis on specific frequencies of interest. In terms of the experimental validation of the proposed model, the simulation results were compared against data sets from the manufacturer and against experimental test results that were carried out in the university lab benefiting from an electromagnetic shaker. The theoretical and experimental results matched very well around particular operating frequencies.

For active vibration control of the engine, two control techniques, Gain scheduling with zero placement and LQ control were investigated. The two control strategies were integrated into the original model of the engine assuming a generic actuator situated between the engine case and the absorber. The control model was then simulated and analysed in the time and frequency domains. The results showed that both strategies are capable of minimizing the vibration of the Stirling engine case within the required vibration magnitudes and bandwidth despite of the different modes of operation of each control technique. The availability of the simulation data allowed the extraction of certain specification regarding the type of actuator that could be installed efficiently to achieve the required forces and strokes.

The gain scheduling control law was tested experimentally using a scaled test rig. A VCM motor was chosen and the model of the VCM was proposed and integrated with the 2DOF vibration model with the addition of the control law. The scaled rig comprised an electrodynamic shaker and an ATMD with a VCM. The experimental tests with an ATMD succeeded in mitigating the vibration of the rig between 45Hz and 55Hz. The ATMD attenuated around 88% of the vibration in the new frequency range compared to the passive TMD at a single frequency. The concept of active damping with the scaled rig can be

extended to the Stirling engine system following the successful experimental validation of the proposed Stirling engine model.

In addition to that, the effect of time delays for active control with a 2DOF system were investigated thoroughly and the general characteristic equations of the transfer function that relate the shaker table displacement to the excitation force were obtained with the two control techniques.

Furthermore, equations that relate the required actuator force and the power demand are obtained in relation to the excitation force for any general 2DOF vibration system that employs a VCM to perform active vibration control.

The research found that in order to reduce the power consumption with the active damping for the Stirling engine, a VCM with a large motor constant is needed.

A comparison of the operation and performance under different scenarios was then carried out. The results showed that while both of the control strategies was successful in fulfilling the main objective, they have different modes of operation and requirements summarized in the following comparative table

Table 9-1 Comparison of the control strategies

	Gain Scheduling	LQ
Active Damping	Both control techniques succeed in attenuating the vibration of the engine from a theoretical point of view. The force requirements have approximately the same magnitude in both control techniques. The implementation results illustrated that gain scheduling control was successful	
Model Dynamics	Requires knowledge of the excitation frequency and no accurate model of the Stirling engine is required. No need to access the full states of the system.	Requires accurate modeling and access to the full dynamic states of the system. For practical considerations, a state-observer is needed estimate the states.
Operation	Tracks excitation frequency to alter that of the ATMD. The control could be achieved with lower complexity and computational power. This type of control would not suitable for this application when knowledge of the excitation frequency and magnitude	It provides a single gain matrix that works over a wider bandwidth. Complex control and more computational power are more likely considering the involvement of matrix operations and the requirement of a state observer.

	<p>is unavailable. Works with either relative or absolute state measurements.</p> <p>A control force that is proportional to either acceleration or position feedback is capable of altering the frequency of the TMD. A force that is only proportional to velocity is not capable of altering the natural frequency of the TMD, but can affect its damping coefficient.</p>	<p>Suitable for this application if precise information about the excitation is unavailable.</p> <p>Full state feedback force is required (position and velocity depending on the model). There is no direct intuition on how the control force affects the natural frequency of the TMD, however in general terms; the control gain produces a response that resembles that of the gain scheduling control with position and velocity feedback.</p>
Gain Tuning	<p>Online calculation of the gains is required; however it is fairly straight forward. The gain calculation follows an analytical formula that is obtained easily by associating the relevant equations. Different gains are required depending on whether a position or acceleration feedback is used. Velocity gain is needed to achieve maximum attenuation when the TMD possesses damping inherently.</p>	<p>A single gain matrix is determined offline however accurate model of the engine dynamics is required. The optimal control state and input force matrix coefficients are tuned following a heuristic procedure rather than an analytical equation which makes optimal control harder to obtain. Adaptive gain matrix is required where the system dynamics such as mass or stiffness change with time</p>
Noise Resistance	<p>The control performance is hindered by the existence of noise.</p>	<p>The control performance is slightly affected by the noise providing the existence of a state observer with accurate dynamics of the engine.</p>
Time Delays	<p>Could be destabilized after a certain time delay depending on excitation frequency.</p>	<p>Could be destabilized but allows for more time delay irrespective of excitation frequency.</p>

The implementation using a scaled rig focused on the gain scheduling control strategy. The first test was carried out with the ATMD tuned at 50Hz. The control succeeded in mitigating the vibration of the rig between 45Hz-50Hz with around 90% attenuation achieved across the proposed bandwidth compared to the TMD operation at 50Hz only. This control technique became unstable between 50Hz-55Hz as a result of existing phase delays in the system. A novel working solution was devised by shifting the ATMD frequency to 55Hz so that the required range of operation is always below the original resonance of the ATMD. This solution incurs more power consumption. Specifically, the VCM is required to shift the

frequency down from 55Hz to 45Hz rather than from 50Hz if excitation frequency was 45Hz. During the first test, a further observation was made concerning the damping coefficient of the ATMD which was found to be dependent of the excitation frequency. Knowledge of damping is crucial since it is directly proportional to the velocity feedback. As a result, the velocity feedback gain was made to change adaptively with the excitation frequency in the later tests.

The simulation predicted the control instability after 50Hz due to phase delays and this was demonstrated in the first test. A further investigation of the implementation code showed that phase delays occur due to the low pass and high pass filtering stages. As a result, a dual filtering technique was followed based on gain scheduling of the filter coefficients to compensate for phase delays. This technique is more expected to be more efficient than the previous one because the ATMD is not passively tuned at 55Hz. A further test was carried out with delay compensation. The test revealed successful results and the problem of instability was solved. Furthermore, the power consumption of the motor was reduced following this method.

The previous set of tests was carried out assuming a relative measurement of the position and velocity which required two acceleration sensors. A new test was successfully performed while taking absolute measurement of the absorber position and velocity using one single sensor instead of two.

The extrapolation of the test results to the Stirling engine was discussed from a power consumption perspective. Assuming that the engine can only give away 10% of its power generation, it was found out that in order to perform the active damping in the Stirling engine a higher power requirement is needed. In order to reduce the amount of power needed, a VCM with larger motor constant is capable of performing the active damping with lower power rating. Assuming that the original efficiency of the Stirling engine without active

control is 30%, this would be reduced to 27% as a result of the active damping implementation.

Finally, it can be now said that the active damping control for vibration in the Stirling engine is successfully proven as a potential solution that can increase the range of operation of this engine.

## 9.2 Conclusions

In this work, an active vibration control strategy employing an ATMD with a linear voice coil actuator is proposed and tested experimentally for the mitigation of the vibration problem in the  $\beta$ -type Stirling engine with the aid of a scaled test rig. A simple gain scheduling with zero placement control law utilizing both position and velocity feedback succeeded in mitigating 88% of the vibration of the test rig structure for a wide bandwidth between 45Hz and 55Hz compared to a passive system that is only operational at 50Hz only.

An LQG control method with a state observer based on the proposed model of the engine was also tested theoretically and it was capable of reducing the vibration of the engine with similar outcome to the gain scheduling control strategy despite the difference in their principle of operation.

A thorough theoretical and experimental investigation on the effect of phase delays on control stability with both control techniques showed that after a critical time delay margin dependent of the excitation frequency the control system becomes unstable. The critical delay margin has a larger tolerance with LQG control compared to that with the gains scheduling one.

Three methods for mitigating the effect of phase delays on stability were proposed and verified experimentally with the gain scheduling control method. It was found that it is possible to successfully mitigate the effect of delays on the stability of the control system. The introduction of damping into that ATMD system improves the time delay margin

allowing for more room of operation with a phase-delayed ATMD. The second method incorporated retuning the original resonance of the ATMD which ensured stable control for excitation frequencies below the resonance of the ATMD. A third technique incorporating a dual-filtering technique of delay compensation provided a successful and lower power-consuming solution compared to the other two.

A novel experimental procedure benefiting from the test rig is used for evaluating the stiffness and dynamic mass of a spring mass system based on an optimization technique. Furthermore, the damping introduced by the VCM actuator was found to vary with frequency non-linearly and a novel experimental procedure was followed for determining the damping coefficient in the ATMD used in the test rig by benefiting from the active control experiment. The discussion of power consumption found that a larger VCM with a higher motor constant is required in order to perform the active control for the actual Stirling engine which may experience excitation force magnitudes of 3.2 KN. Specifically, it was found that if the engine is willing to grant 10% of its assumed 1.2KW generated electrical power to power the VCM, a hypothetical 30% efficiency of the engine will be affected by around 3%.

The proposed control laws are not restricted to this type of Stirling engine. In fact this study can be generalised for other types of Stirling engines. Furthermore, other systems that can be modelled as a 2DOF system can benefit from this study as well.

### **9.3 Future Work**

- In the implementation section of this work, the main focus was on the gain scheduling with zero placement control. Furthermore, in this work, it was assumed that the excitation frequency is known. The simulation with LQ control showed promising results, however due to time and resource limitation, the LQ control could not be tested experimentally. Hence, this research could be furthered by testing the LQ control techniques with adding a state observer. The LQ control could also be

extended to consider the case where information about the disturbance/excitation is unknown.

- The modelling of the damping in the VCM was carried out experimentally and a quadratic fit is obtained to describe the change in damping as a function of excitation frequency. The theoretical modelling of damping in the VCM could be a rewarding future orientation of this research. The modelling of the damping in the system allows for a more accurate evaluation of the power consumption of the proposed active control technique. The available experimental equipment in our labs allows for the practical investigation and validation of the VCM models.
- The promising theoretical results that were consolidated with experimental results warrant a future direction of this research featuring the implementation of the proposed active vibration control techniques in the Stirling engine while using a bigger VCM. The proposed control laws can be extended for other types of the Stirling engine such as  $\alpha$  and  $\gamma$  type Stirling engines. In fact the proposed control laws and the derived equations for the active control could be applied to any 2DOF system that operates with similar functionality as the Stirling engine.
- This work considered the conversion of the existing TMD into an ATMD with a VCM. A future work might consider the same control laws but with a different design of the TMD. In fact as active control was proven to achieve far better performance than a passive control method, the possibility is made open for a different design of the TMD that has a lower mass and a more compact form. This also allows for lowering the stiffness in the ATMD.

The excitation force acting on the Stirling engine studied in this work is assumed to be sinusoidal of known magnitude and the scope of this work. A future trend of this research may consider the modeling and validation of the excitation force attributes

that act on this engine. This requires complicated modeling of the Stirling engine internal dynamics that involve mechanics, thermodynamics, and electromagnetism. This allows for better prediction and more accurate control of the vibration in the engine. It is agreed within the Stirling engine society that experimental trials of this type of engines are very costly and time consuming, hence modeling of this engine is a rewarding contribution.

- The study investigated the vibration control of the engine under normal operation conditions but without considering the case when a load is connected. A further research could consider the modeling of the effect of loading of the Stirling engine integrated with the active control operation. By benefiting from the electrical analogy presented in this work, the conversion from mechanical energy to electrical energy could also be integrated to the entire system. This allows for more accurate power consumption and efficiency predictions.
- Semi-active control could be investigated. The gain scheduling control law aimed at tuning the natural frequency so it follows the frequency of excitation. In order to improve the power consumption and the efficiency of the engine, a study could be carried out to investigate the use of semi-active devices that are capable of changing stiffness/damping in response to a control signal while consuming much less power than a fully active system.
- The study on the effect of time delays on the control law was carried out for this engine based on a 2DOF model that comprised that active control law with gain scheduling and the model of the VCM. The values of the masses, stiffnesses, and damping coefficients, in addition to the parameters of the VCM were known which allowed for a numerical estimation of the critical time delay margin. A future work

might consider finding an analytical solution of the time delay margin based on the proposed model with symbolic parameters.

## 10 References

- Abdel-Rohman, M. and Leipholz, H.H., 1983. Active control of tall buildings. *Journal of Structural Engineering*.
- Alkhatib, R. and Golnaraghi, M.F., 2003. Active structural vibration control: a review. *Shock and Vibration Digest*, 35(5), p.367.
- Anthony, D.K., Elliott, S.J. and Keane, A.J., 2000. Robustness of optimal design solutions to reduce vibration transmission in a lightweight 2-D structure, part i: Geometric design. *Journal of Sound and Vibration*, 229(3), pp.505-528.
- Bani-Hani, K., Ghaboussi, J. and Schneider, S.P., 1999. Experimental study of identification and control of structures using neural network. Part 1: Identification. *Earthquake engineering & structural dynamics*, 28(9), pp.995-1018.
- Battaini, M., Casciati, F. and Faravelli, L., 1998. Fuzzy control of structural vibration. An active mass system driven by a fuzzy controller. *Earthquake Engineering and Structural Dynamics*, 27(11), pp.1267-1276.
- Beale, W.T., Wood, J.G. and Gedeon, D.R., Sunpower, Inc., 1980. *Spring and resonant system for free-piston Stirling engines*. U.S. Patent 4,183,214.
- Berchowicz, D.M., 1983, August. The development of a 1 kW electrical output free piston Stirling engine alternator unit. In *Proc., Intersoc. Energy Convers. Eng. Conf.;*(United States) (Vol. 2, No. CONF-830812-). Sunpower, Inc., Athens, Ohio.
- Bin-Nun, U., 2008. Reduction of Self Induced Vibration in Rotary Stirling Cycle Coolers.
- Black, B., Lopez, M. and Morcos, A., 1993. Basics of voice coil actuators. *PCIM-VENTURA CA-*, 19, pp.44-44.
- Boldea, I. and Nasar, S.A., 1997, May. Linear electric actuators and generators. In *Electric Machines and Drives Conference Record, 1997. IEEE International* (pp. MA1-1). IEEE.
- Carter, A.K., 1998. Transient motion control of passive and semiactive damping for vehicle suspensions.
- Chang, C.C. and Yang, H.T., 1995. Control of buildings using active tuned mass dampers. *Journal of engineering mechanics*.

Chang, C.C. and Yu, L.O., 1998. A simple optimal pole location technique for structural control. *Engineering structures*, 20(9), pp.792-804.

Chang, J.C. and Soong, T.T., 1980. Structural control using active tuned mass dampers. *Journal of the Engineering Mechanics Division*, 106(6), pp.1091-1098.

Chen, P., Zhai, J., Zhang, X., Zhang, H.T. and Ding, H., 2013. Research on Active Vibration Control of Thin-Walled Workpiece in Milling Based on Voice Coil Motor. In *Intelligent Robotics and Applications* (pp. 503-512). Springer Berlin Heidelberg.

Cheng, C.H. and Yu, Y.J., 2010. Numerical model for predicting thermodynamic cycle and thermal efficiency of a beta-type Stirling engine with rhombic-drive mechanism. *Renewable Energy*, 35(11), pp.2590-2601.

Cheng, T.H. and Oh, I.K., 2009. Coil-based electromagnetic damper and actuator for vibration suppression of cantilever beams. *Journal of Intelligent Material Systems and Structures*, 20(18), pp.2237-2247.

Chung, L.L., Lin, R.C., Soong, T.T. and Reinhorn, A.M., 1989. Experimental study of active control for MDOF seismic structures. *Journal of Engineering Mechanics*, 115(8), pp.1609-1627.

Chung, L.L., Reinhorn, A.M. and Soong, T.T., 1988. Experiments on active control of seismic structures. *Journal of Engineering Mechanics*, 114(2), pp.241-256.

Datta, T.K., 2003. A state-of-the-art review on active control of structures. *ISET Journal of earthquake technology*, 40(1), pp.1-17.

de Marneffe, B., 2007. Active and passive vibration isolation and damping via shunted transducers. *These, Faculté des Sciences Appliquées, Université Libre de Bruxelles*.

Dorf, R.C. and Bishop, R.H., 1998. Modern control systems.

Ehrgott, R.C. and Masri, S.F., 1992. Modeling the oscillatory dynamic behaviour of electrorheological materials in shear. *Smart Materials and Structures*, 1(4), p.275.

Fan, K., Liu, Y. and Chu, C., 2006. Design Analysis of Voice Coil Motor for Active Vibration Isolation. *JOURNAL-CHINESE SOCIETY OF MECHANICAL ENGINEERS*, 27(5), p.501.

Fang, X. and Chen, W., 1999. Fuzzy control technology and the application to vehicle semi-active suspension. *Chinese Journal of Mechanical Engineering*, 35, pp.98-100.

Franchek, M.A., Ryan, M.W. and Bernhard, R.J., 1996. Adaptive passive vibration control. *Journal of Sound and Vibration*, 189(5), pp.565-585.

Fuller, C.C., Elliott, S. and Nelson, P.A., 1996. *Active control of vibration*. Academic Press.

Gordaninejad, F., Saiidi, M., Hansen, B.C. and Chang, F.K., 1998, June. Control of bridges using magnetorheological fluid (MRF) dampers and a fiber-reinforced composite-material column. In *5th Annual International Symposium on Smart Structures and Materials* (pp. 2-11). International Society for Optics and Photonics.

Guo, T., Liu, Z. and Cai, L., 2012. An improved force feedback control algorithm for active tendons. *Sensors*, 12(8), pp.11360-11371.

Hansen, C. and Snyder, S., 1996. *Active control of noise and vibration*. CRC Press.

Harris, C.M., 1988. *Shock and vibration handbook*. McGraw-Hill.

Harris, C.M. and Piersol, A.G., 2002. *Harris' shock and vibration handbook*(Vol. 5). New York: McGraw-Hill.

Harris, C.M. and Beyer, R.T., 1988. Shock and Vibration Handbook, edited by Cyril M. Harris. *The Journal of the Acoustical Society of America*, 84(3), pp.1126-1126.

Holliday, E.S., Sunpower, Inc., 2014. *Driving an active vibration balancer to minimize vibrations at the fundamental and harmonic frequencies*. U.S. Patent 8,800,302.

Housner, G.W., Bergman, L., Caughey, T.K., Chassiakos, A.G., Claus, R.O., Masri, S.F., Skelton, R.E., Soong, T.T., Spencer, B.F. and Yao, J.T., 1997. Structural control: past, present, and future. *Journal of engineering mechanics*, 123(9), pp.897-971.

Hrovat, D., Barak, P. and Rabins, M., 1983. Semi-active versus passive or active tuned mass dampers for structural control. *Journal of Engineering Mechanics*, 109(3), pp.691-705.

Jenkins, M.D., Nelson, P.A., Pinnington, R.J. and Elliott, S.J., 1993. Active isolation of periodic machinery vibrations. *Journal of Sound and Vibration*, 166(1), pp.117-140.

Jeon, D., Park, C. and Park, K., 1999. Vibration suppression by controlling an MR damper. *International Journal of Modern Physics B*, 13(14n16), pp.2221-2228.

Johnson, W., Long, R., Nelson, M. and Mascareñas, D., 2012. Embedded Active Vibration Cancellation of a Piston-Driven Cryocooler for Nuclear Spectroscopy Applications. In *Topics in Modal Analysis I, Volume 5* (pp. 377-384). Springer New York.

JP Den Hartog, 1985. *Mechanical vibrations*. Courier Corporation.

Karnopp, D., 1995. Active and semi-active vibration isolation. *Journal of Vibration and Acoustics*, 117(B), pp.177-185.

Karnopp, D., 1990. Design principles for vibration control systems using semi-active dampers. *Journal of Dynamic Systems, Measurement, and Control*, 112(3), pp.448-455.

Karnopp, D.C., 1973. Active and passive isolation of random vibration(Automatic control theory application to random vibration passive and active isolators synthesis, considering vehicle suspension systems and electrohydraulic damper). *Isolation of mechanical vibration, impact, and noise*, pp.64-86.

Karnopp, D., 1989. Permanent magnet linear motors used as variable mechanical dampers for vehicle suspensions. *Vehicle System Dynamics*, 18(4), pp.187-200.

Karnopp, D., Crosby, M.J. and Harwood, R.A., 1974. Vibration control using semi-active force generators. *Journal of Manufacturing Science and Engineering*, 96(2), pp.619-626.

Kim, Y.B., Hwang, W.G., Kee, C.D. and Yi, H.B., 2001. Active vibration control of a suspension system using an electromagnetic damper. *Proceedings of the Institution of Mechanical Engineers, Part D: Journal of Automobile Engineering*, 215(8), pp.865-873.

Korkmaz, S., 2011. A review of active structural control: challenges for engineering informatics. *Computers & Structures*, 89(23), pp.2113-2132.

Li, C., Liu, Y. and Wang, Z., 2003. Active multiple tuned mass dampers: A new control strategy. *Journal of Structural Engineering*, 129(7), pp.972-977.

Liu, J., Xia, K. and Zhu, C., 2009, December. The state-of-the-art review of structural control strategy. In *E-Learning, E-Business, Enterprise Information Systems, and E-Government, 2009. EEEE'09. International Conference on*(pp. 211-213). IEEE.

Liu, Y.H. and Wu, W.H., 2013. Active Vibration Isolation Using a Voice Coil Actuator with Absolute Velocity Feedback Control. *International Journal of Automation and Smart Technology*, 3(4), pp.221-226.

Liu, Y., Waters, T.P. and Brennan, M.J., 2005. A comparison of semi-active damping control strategies for vibration isolation of harmonic disturbances. *Journal of Sound and Vibration*, 280(1), pp.21-39.

Liu, Y., 2004. *Semi-active damping control for vibration isolation of base disturbances* (Doctoral dissertation, University of Southampton).

Luo, N., Rodellar, J., de la Sen, M. and Vehí, J., 2002. Decentralized active control of a class of uncertain cable-stayed flexible structures. *International Journal of Control*, 75(4), pp.285-296.

Makris, N., Hill, D., Burton, S. and Jordan, M., 1995, May. Electrorheological fluid damper for seismic protection of structures. In *Smart Structures & Materials' 95* (pp. 184-194). International Society for Optics and Photonics.

Marques, R.F., Rade, D.A. and CUNHA, S.S., 2001. Assessment of an active dynamic vibration absorber. In *Proceedings of SPIE, the International Society for Optical Engineering* (Vol. 4359, pp. 32-36). Society of Photo-Optical Instrumentation Engineers.

Mead, D.J., 1999. *Passive vibration control*. John Wiley & Sons Inc

Meirovitch, L., 1990. *Dynamics and control of structures*. John Wiley & Sons.

Messner, W.C., Tilbury, D.M. and Hill, A.P.R., 1999. *Control Tutorials for MATLAB® and Simulink®*. Addison-Wesley.

Microgen Engine Corporation, 2013, Stirling Engine, How it Works. Available: <http://www.microgen-engine.com> [2013]

Moheimani, S.R., 2003. A survey of recent innovations in vibration damping and control using shunted piezoelectric transducers. *Control Systems Technology, IEEE Transactions on*, 11(4), pp.482-494.

Morison, J. and Karnopp, D., 1973. Comparison of optimized active and passive vibration absorbers. In *Joint Automatic Control Conference* (No. 11, pp. 932-938).

Nagashima, I., 2001. Optimal displacement feedback control law for active tuned mass damper. *Earthquake engineering & structural dynamics*, 30(8), pp.1221-1242.

Ogata, K. and Yang, Y., 1970. Modern control engineering.

Olson, H.F., 1958. *Dynamical analogies* (pp. 27-29). Princeton, NJ: Van Nostrand.

Pare, T.E. and How, J.P., 1999. Hybrid H<sub>2</sub> control design for vibration isolation. *Journal of sound and vibration*, 226(1), pp.25-39.

Pinkaew, T. and Fujino, Y., 2001. Effectiveness of semi-active tuned mass dampers under harmonic excitation. *Engineering Structures*, 23(7), pp.850-856.

Poel, G.W., 2010. *An exploration of active hard mount vibration isolation for precision equipment*. University of Twente.

Preumont, A., Achkire, Y. and Bossens, F., 2000. Active tendon control of large trusses. *AIAA journal*, 38(3), pp.493-498.

Preumont, A., 2012. *Vibration control of active structures: an introduction*(Vol. 50). Springer Science & Business Media.

Qiu, J., Ji, H. and Zhu, K., 2009. Semi-active vibration control using piezoelectric actuators in smart structures. *Frontiers of Mechanical Engineering in China*, 4(3), pp.242-251.

Qiu, S., Augenblick, J.E., Peterson, A.A. and White, M.A., Stirling Technology Company, 2005. *Active balance system and vibration balanced machine*. U.S. Patent 6,933,629.

Ram, Y.M. and Inman, D.J., 1999. Optimal control for vibrating systems. *Mechanical systems and signal processing*, 13(6), pp.879-892.

Rao, S.S., *Mechanical Vibrations*,(1990).

Rauch, J.S., Mechanical Technology Incorporated, 1983. *Vibration absorber for a free piston Stirling engine*. U.S. Patent 4,400,941.

Rodellar, J., Barbat, A.H. and Casciati, F., 1999. *Advances in structural control*. International Center for Numerical Methods in Engineering (CIMNE).

Ross Jr, R.G., 2003, July. Vibration suppression of advanced space cryocoolers: an overview. In *Smart Structures and Materials* (pp. 1-12). International Society for Optics and Photonics.

Ross, B., 1995. Status of the emerging technology of Stirling machines. *Aerospace and Electronic Systems Magazine, IEEE*, 10(6), pp.34-39.

Ross, A., 1993. *Making stirling engines*. Ross Experimental.

Sciulli, D., 1997. Dynamics and control for vibration isolation design.

Shaw, J., 1999. Active vibration isolation by adaptive control. In *Control Applications, 1999. Proceedings of the 1999 IEEE International Conference on* (Vol. 2, pp. 1509-1514). IEEE.

Sievers, L.A. and von Flotow, A.H., 1992. Comparison and extensions of control methods for narrow-band disturbance rejection. *Signal Processing, IEEE Transactions on*, 40(10), pp.2377-2391.

Simpson, J. and Schweiger, J., 1998, June. Industrial approach to piezoelectric damping of large fighter aircraft components. In *5th Annual International Symposium on Smart Structures and Materials* (pp. 34-46). International Society for Optics and Photonics.

Soong, T.T., 1987. *Active structural control in civil engineering*.

Soong, T.T. and Cimellaro, G.P., 2009. Future directions in structural control. *Structural control and health monitoring*, 16(1), pp.7-16.

Soong, T.T. and Dargush, G.F., 1997. *Passive energy dissipation systems in structural engineering*. Wiley.

Spanos, J.T., Rahman, Z.H. and von Flotow, A.H., 1993, September. Active vibration isolation on an experimental flexible structure. In *1993 North American Conference on Smart Structures and Materials* (pp. 674-680). International Society for Optics and Photonics.

Spencer, B.F., Dyke, S.J., Sain, M.K. and Carlson, J.D., 1996. Dynamical model of a magnetorheological damper. In *Analysis and Computation (1996)*(pp. 361-370). ASCE.

Spencer Jr, B.F. and Nagarajaiah, S., 2003. State of the art of structural control. *Journal of structural engineering*.

Spencer Jr, B.F. and Soong, T.T., 1999, August. New applications and development of active, semi-active and hybrid control techniques for seismic and non-seismic vibration in the USA. In *Proceedings of international post-SMiRT conference seminar on seismic isolation, passive energy dissipation and active control of vibration of structures* (pp. 23-25). Cheju, Korea.

Symans, M.D. and Constantinou, M.C., 1999. Semi-active control systems for seismic protection of structures: a state-of-the-art review. *Engineering structures*, 21(6), pp.469-487.

Thomson, W.T. and Dahleh, M.D., 1981. *Theory of Vibration with Applications* Prentice-Hall. New Jersey.

Tong, W., 2014. *Mechanical design of electric motors*. CRC Press.

Vipperman, J.S., Burdisso, R.A. and Fuller, C.R., 1993. Active control of broadband structural vibration using the LMS adaptive algorithm. *Journal of Sound and Vibration*, 166(2), pp.283-299.

Von Flotow, A.H., 1988, December. An expository overview of active control of machinery mounts. In *Decision and Control, 1988., Proceedings of the 27th IEEE Conference on* (pp. 2029-2032). IEEE.

Walker, G., 1980. Stirling engines.

Wang, A.P. and Lin, Y.H., 2007. Vibration control of a tall building subjected to earthquake excitation. *Journal of Sound and Vibration*, 299(4), pp.757-773.

Waters, A., 1991. *Active filter design* (p. 161). McGraw-Hill.

Watters, B.G., Coleman, R.B., Duckworth, G.L. and Berkman, E.F., 1988, December. A perspective on active machinery isolation. In *Decision and Control, 1988., Proceedings of the 27th IEEE Conference on* (pp. 2033-2038). IEEE.

Wu, X. and Griffin, M.J., 1997. A semi-active control policy to reduce the occurrence and severity of end-stop impacts in a suspension seat with an electrorheological fluid damper. *Journal of Sound and Vibration*, 203(5), pp.781-793.

Yan, N., Wang, C.M. and Balendra, T., 1999. Optimal damper characteristics of ATMD for buildings under wind loads. *Journal of Structural Engineering*, 125(12), pp.1376-1383.

Yao, J.T., 1972. Concept of structural control. *Journal of the Structural Division*, 98(7), pp.1567-1574.

# 11 Appendix A

## 11.1 Passive Tuned Mass Damper (TMD)

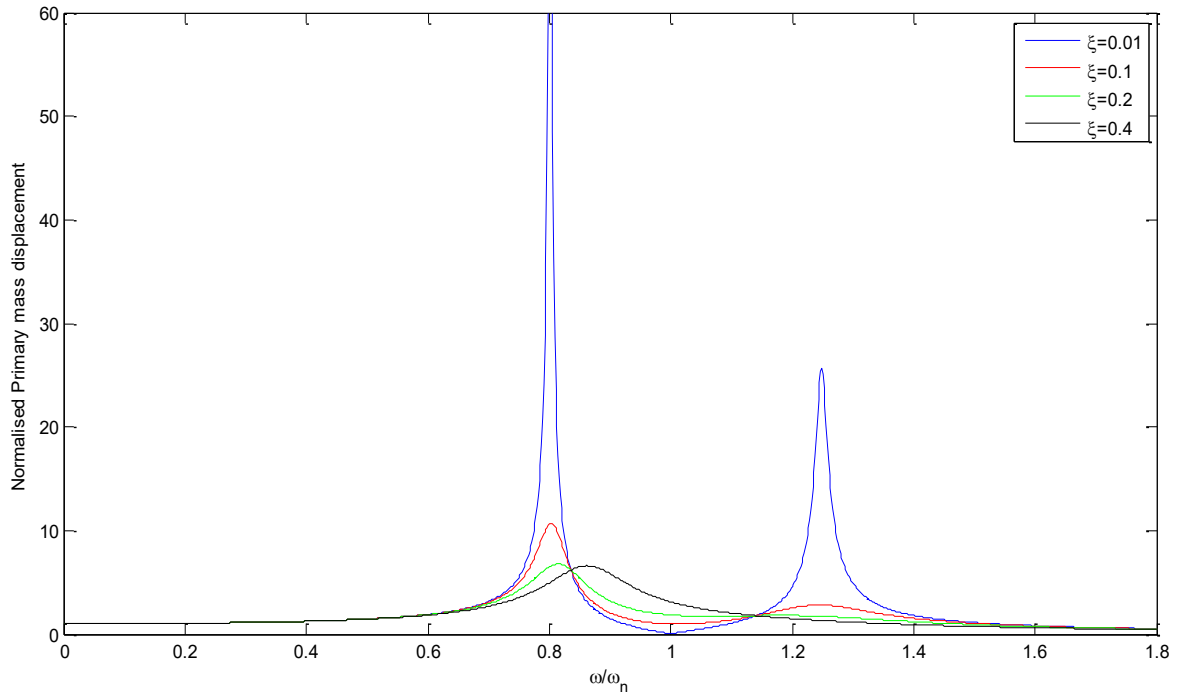


Figure 11-1 Normalised amplitude of vibration of the primary mass as a function of the frequency ratio for several values of damping ratios assuming negligible damping in the primary mass and  $\mu=0.2$

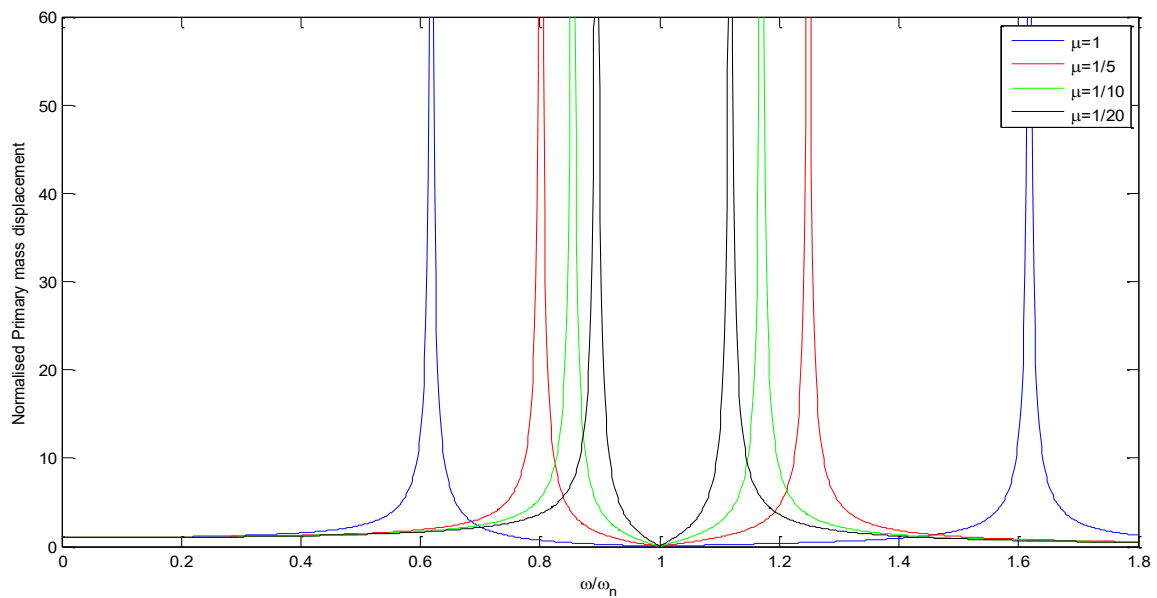


Figure 11-2: Normalised amplitude of vibration of the primary mass as a function of the frequency ratio for several values of mass ratios assuming negligible damping in the primary mass and  $\zeta=0$

## 11.2 Frequency Domain Simulation of Active Damping with Zero-Placement Control

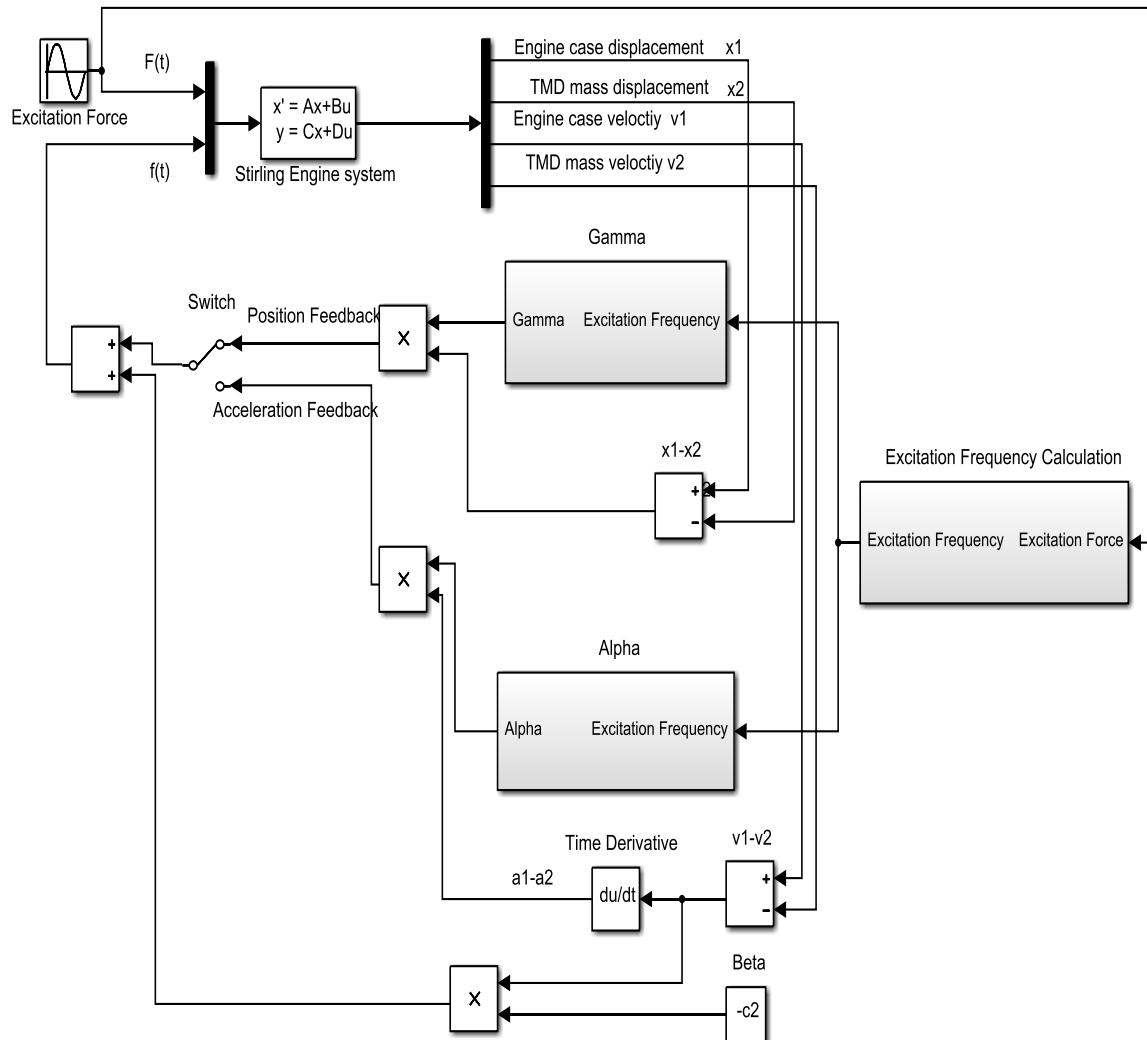


Figure 11-3 SIMULINK model used to simulate the control of the engine vibration with ATMD

### 11.3 Position Gain Feedback ( $\gamma$ )

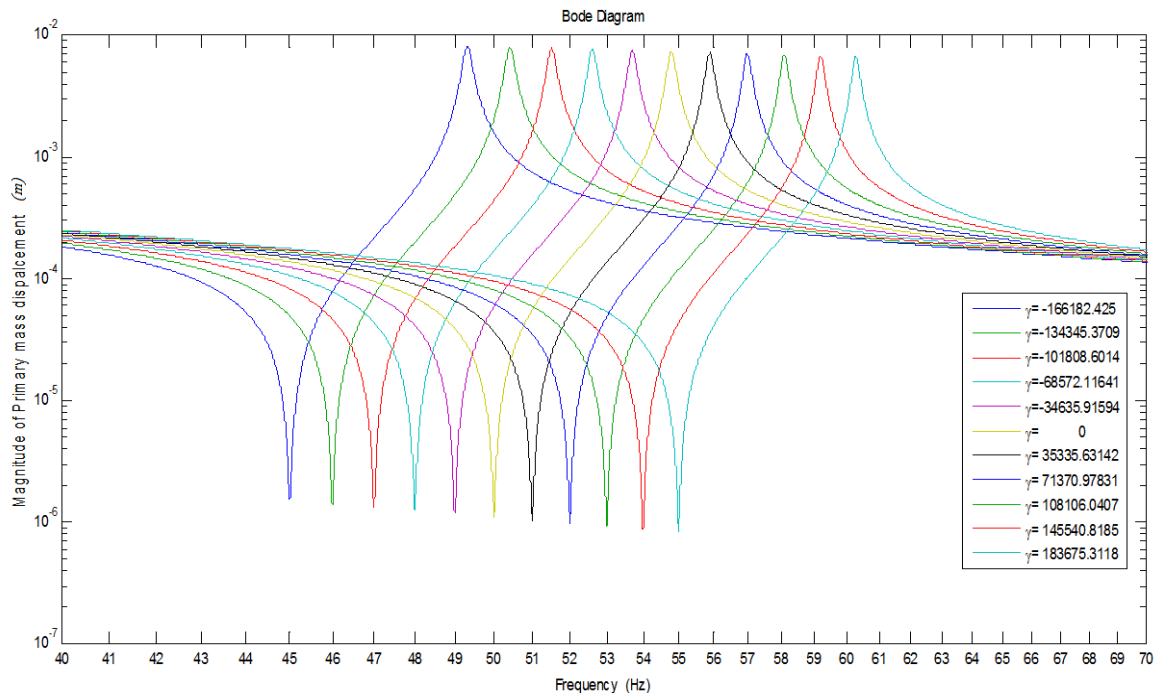


Figure 11-4 Frequency response of the primary mass displacement with position feedback

### 11.4 Acceleration feedback ( $\alpha$ )

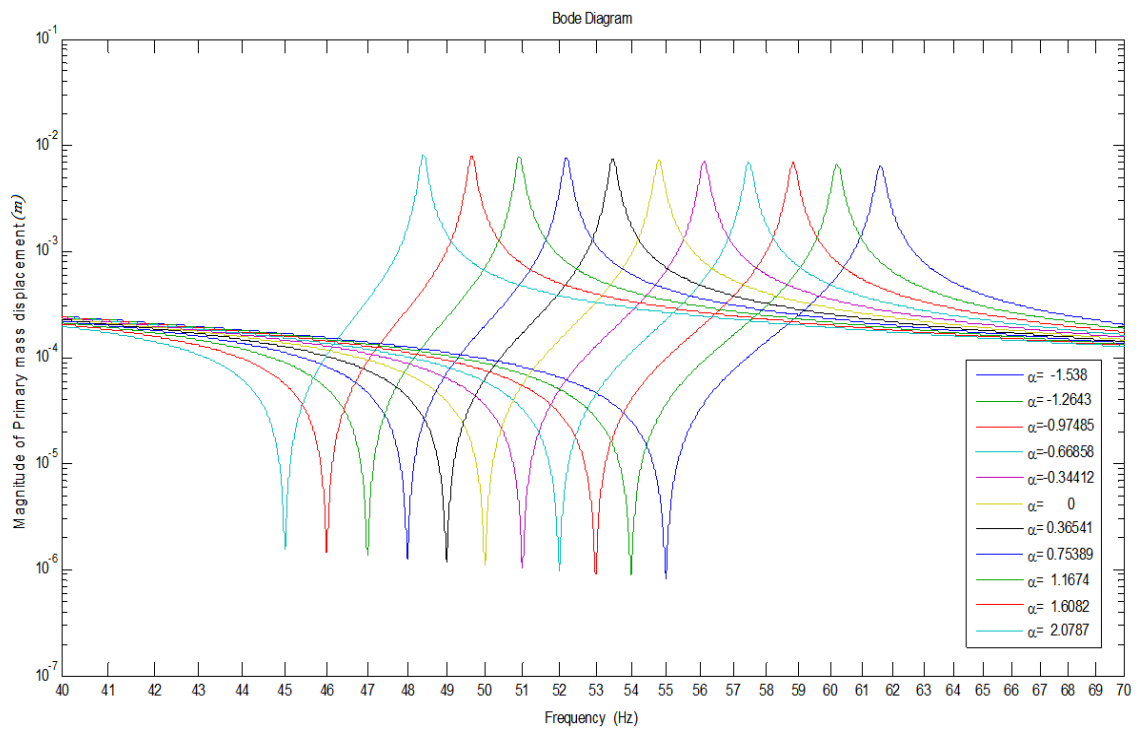


Figure 11-5 Frequency response of the primary mass with acceleration feedback

## 11.5 Position and Velocity feedback ( $\gamma\beta$ )

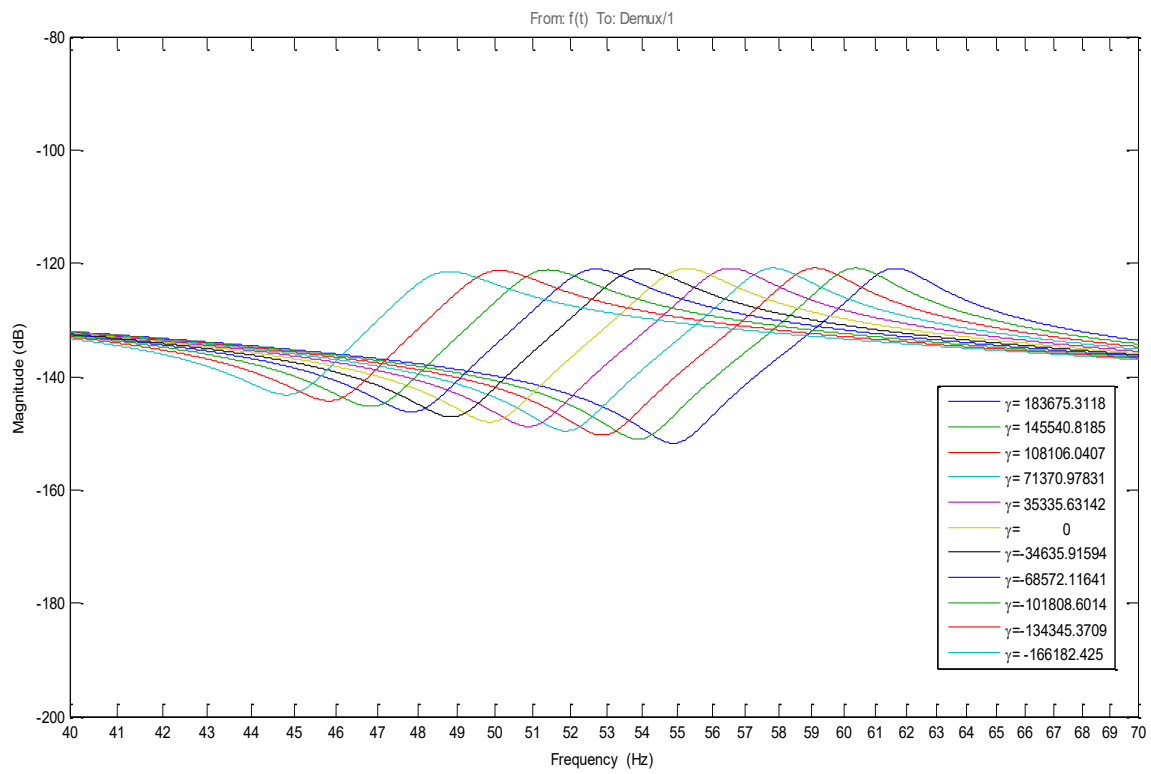


Figure A-6 Frequency response of the primary mass displacement with position and positive velocity feedback

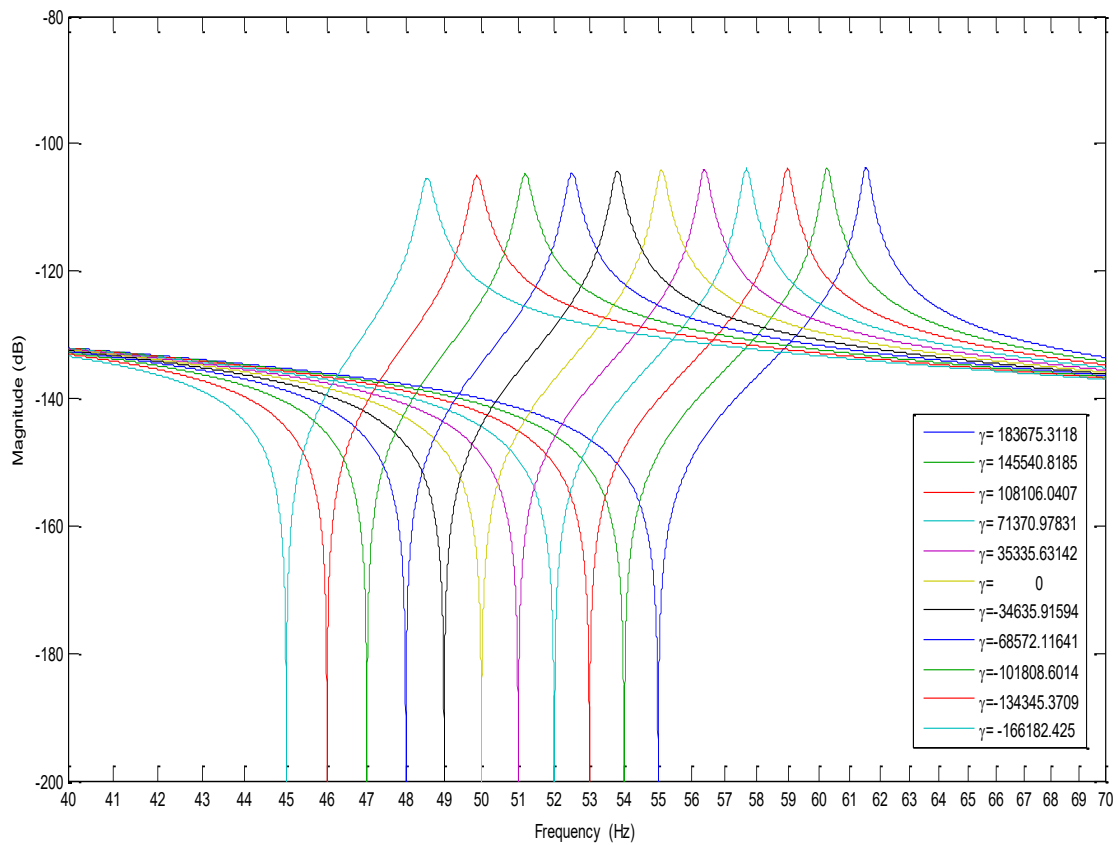


Figure 11-6 Frequency response of the primary mass displacement with position and negative velocity feedback

## 11.6 Acceleration and Velocity feedback ( $\alpha\beta$ )

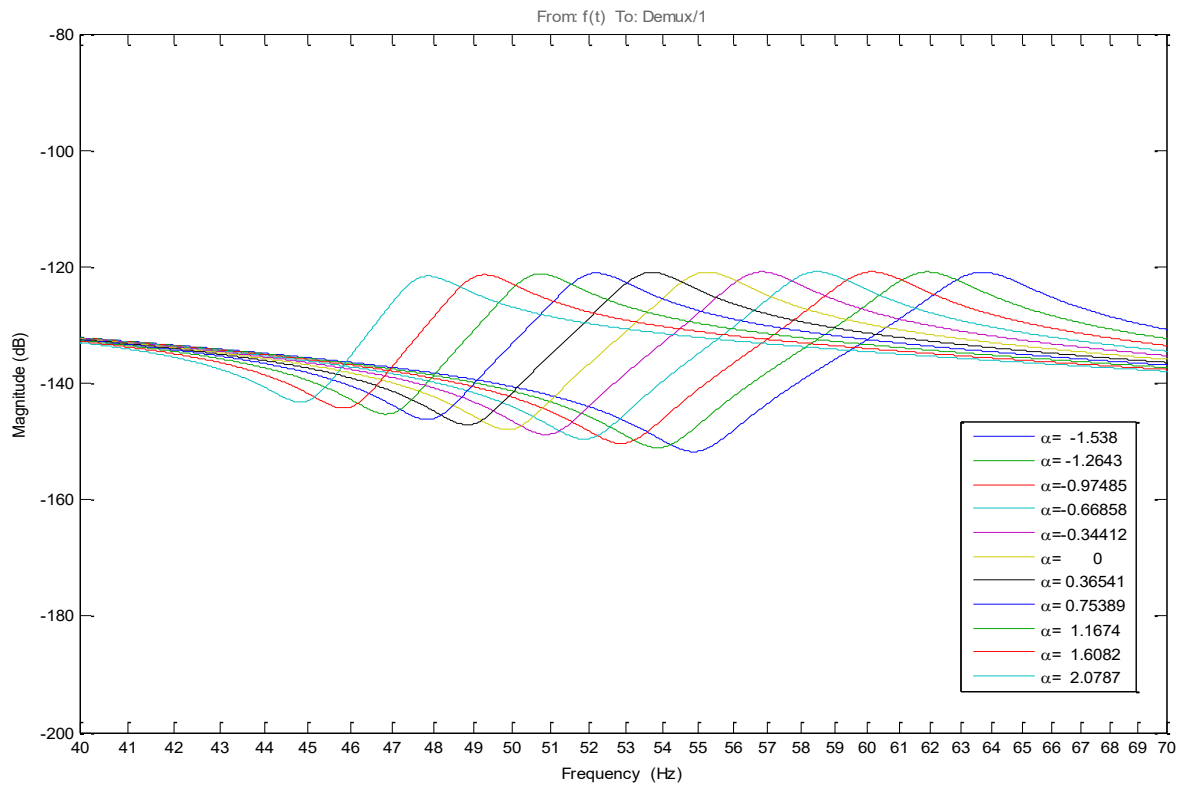


Figure 11-7 Frequency response of the primary mass displacement with position and with positive velocity feedback

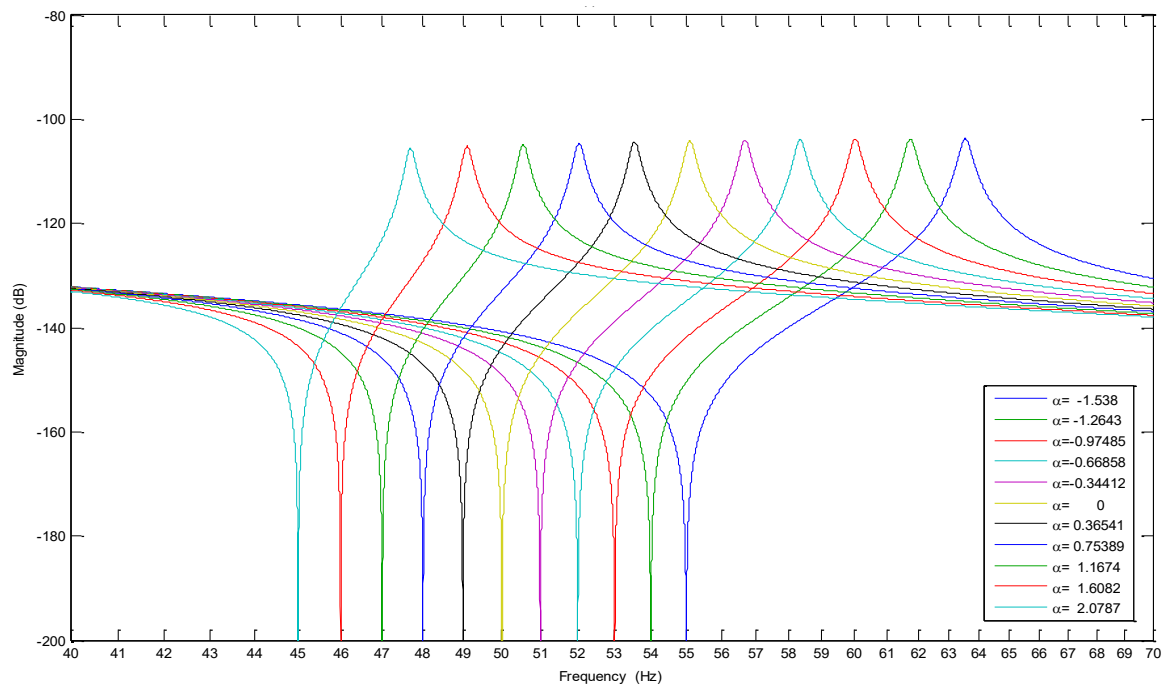


Figure 11-8 Frequency response of the primary mass displacement with acceleration and negative velocity feedback

## 11.7 Electrical Charge Feedback

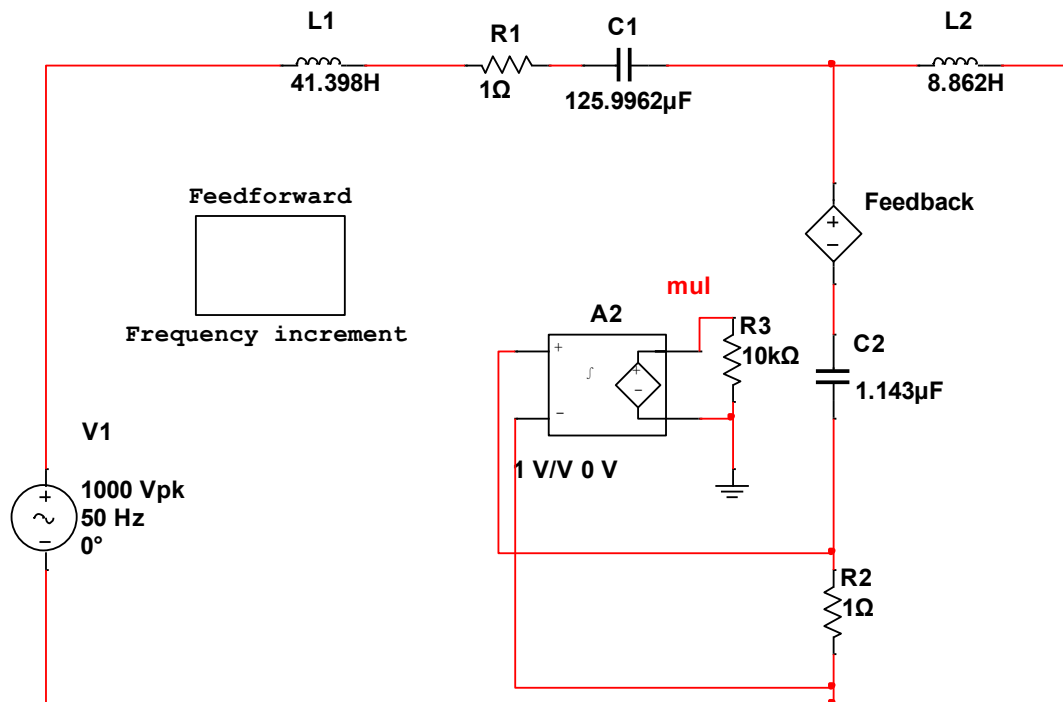


Figure 11-9 Gain scheduling control strategy for the analogous electrical circuit with electrical charge feedback

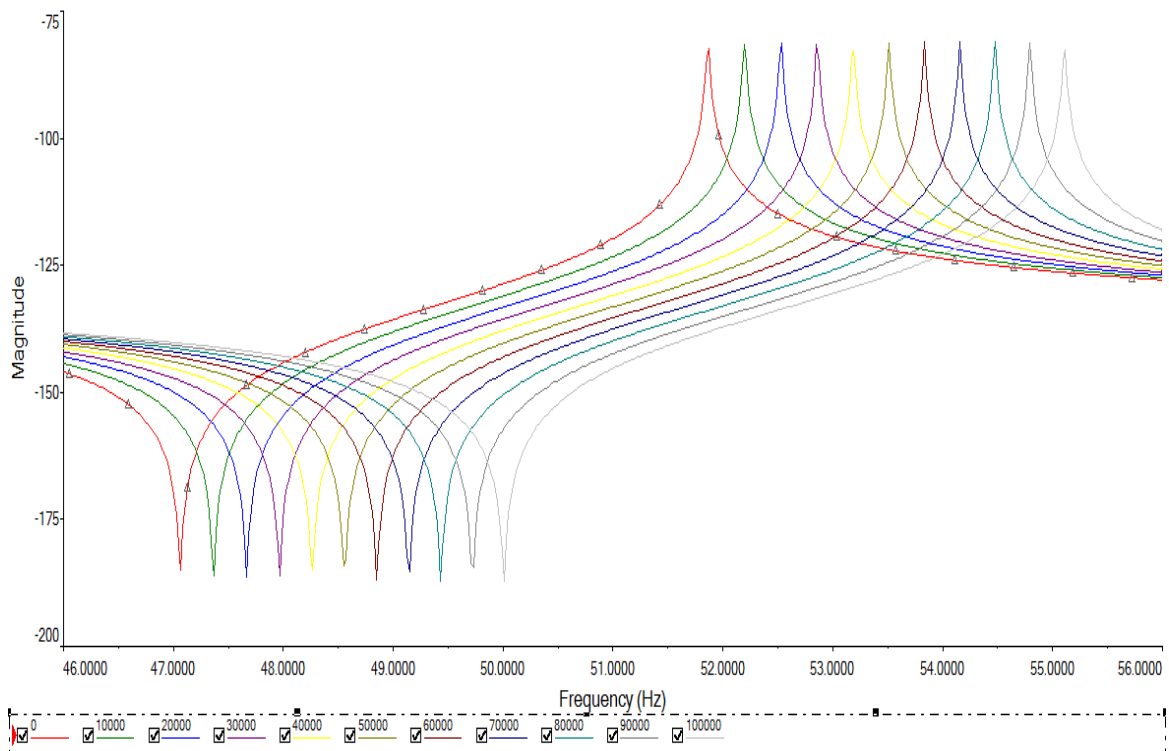


Figure 11-10 Frequency response of the electrical analog system with electrical charge (Q) feedback

## 11.8 Rate of change of the electrical current feedback

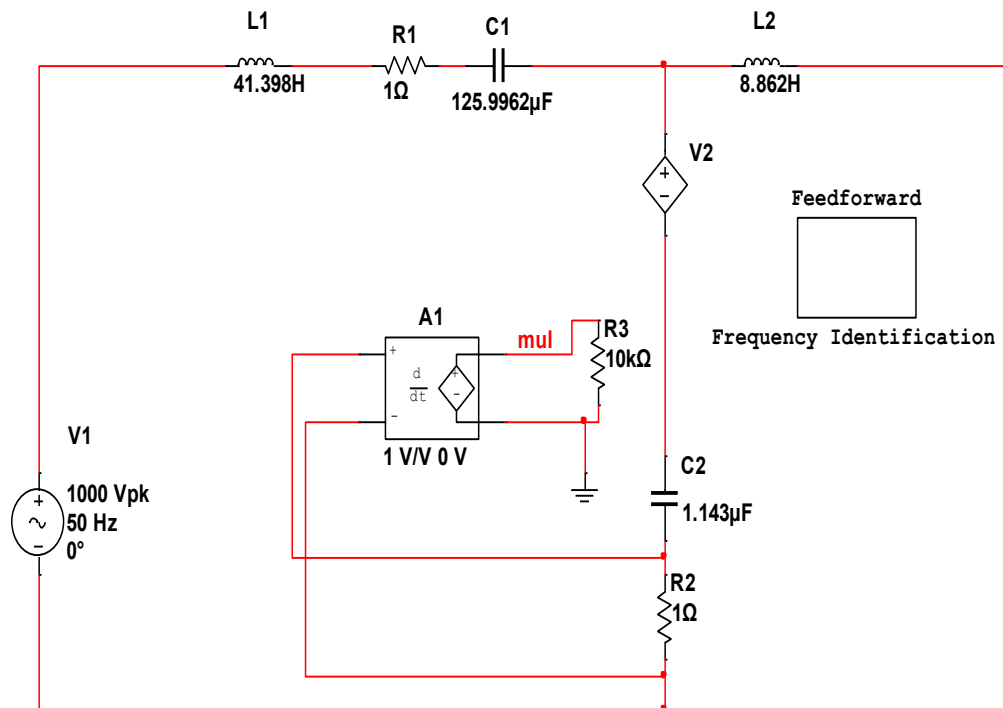


Figure A-12 Gain Scheduling control strategy for the analogous electrical circuit with acceleration feedback

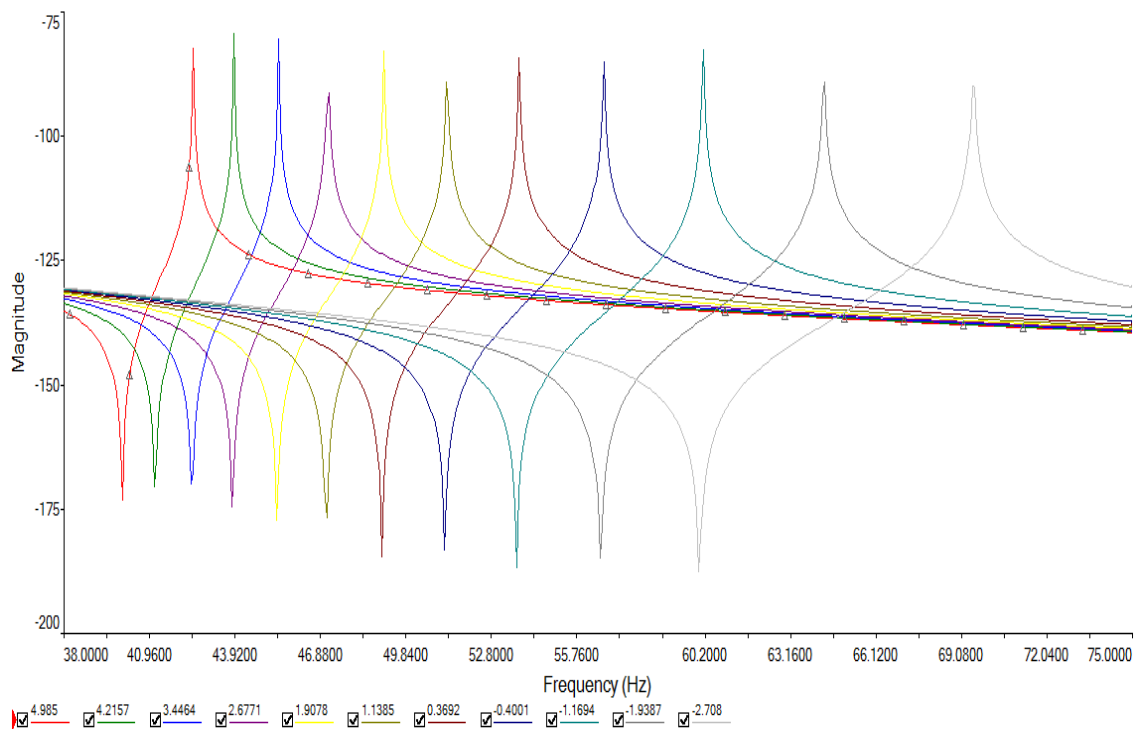


Figure 11-11 Frequency Response with current rate of change feedback gains

## 11.9 Electrical current and electrical charge feedback

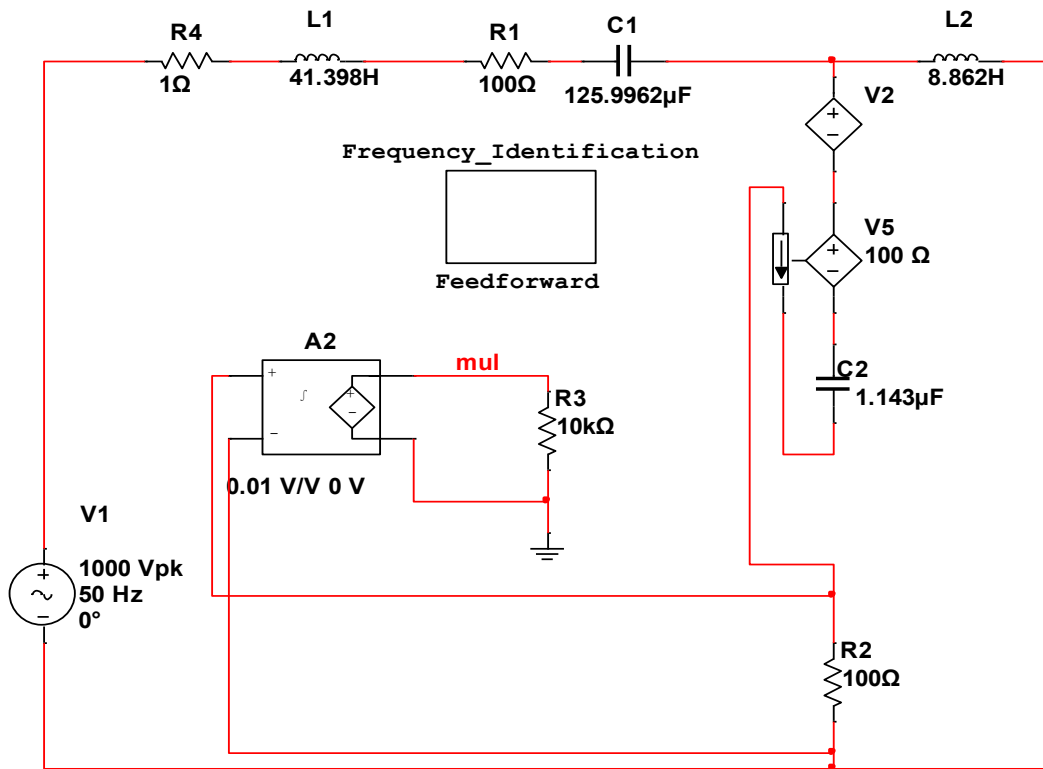


Figure 11-12 Multisim Model with electrical charge and electrical current gain scheduling control strategy

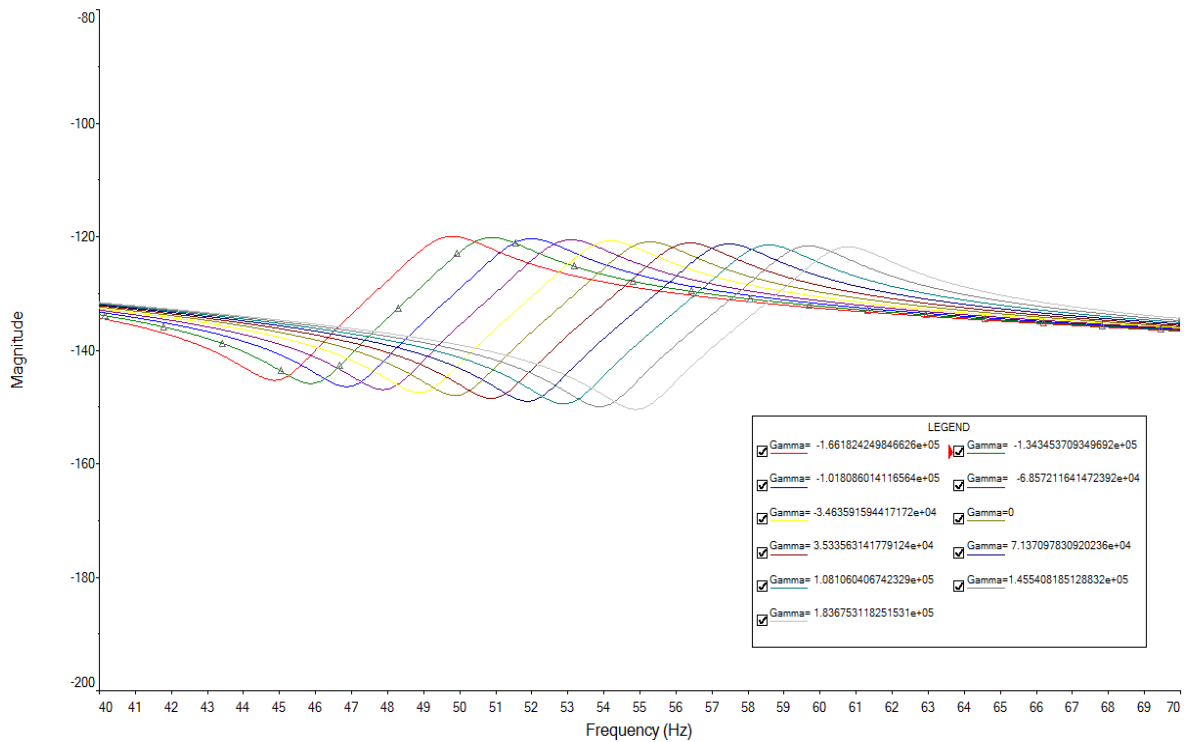


Figure 11-13 Frequency response with charge feedback and with positive current feedback gain

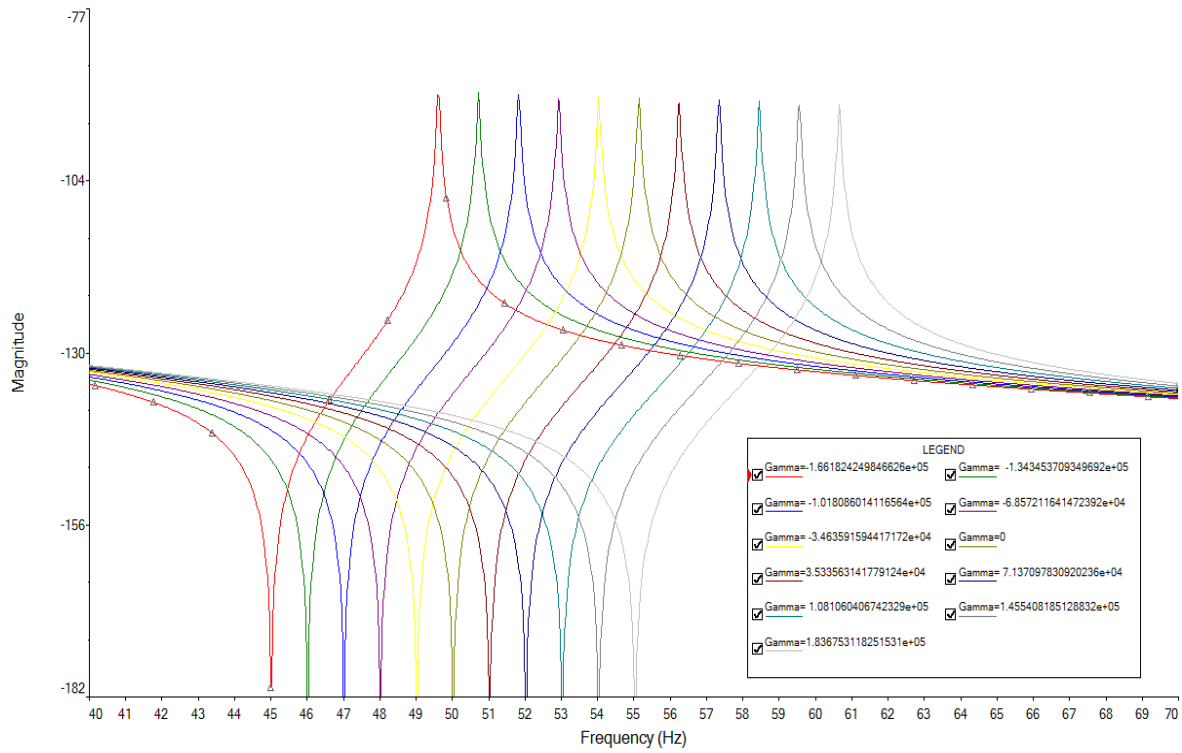


Figure 11-14 Frequency response with charge and negative current feedback gain

## 11.10 Electrical current and rate of change of current feedback

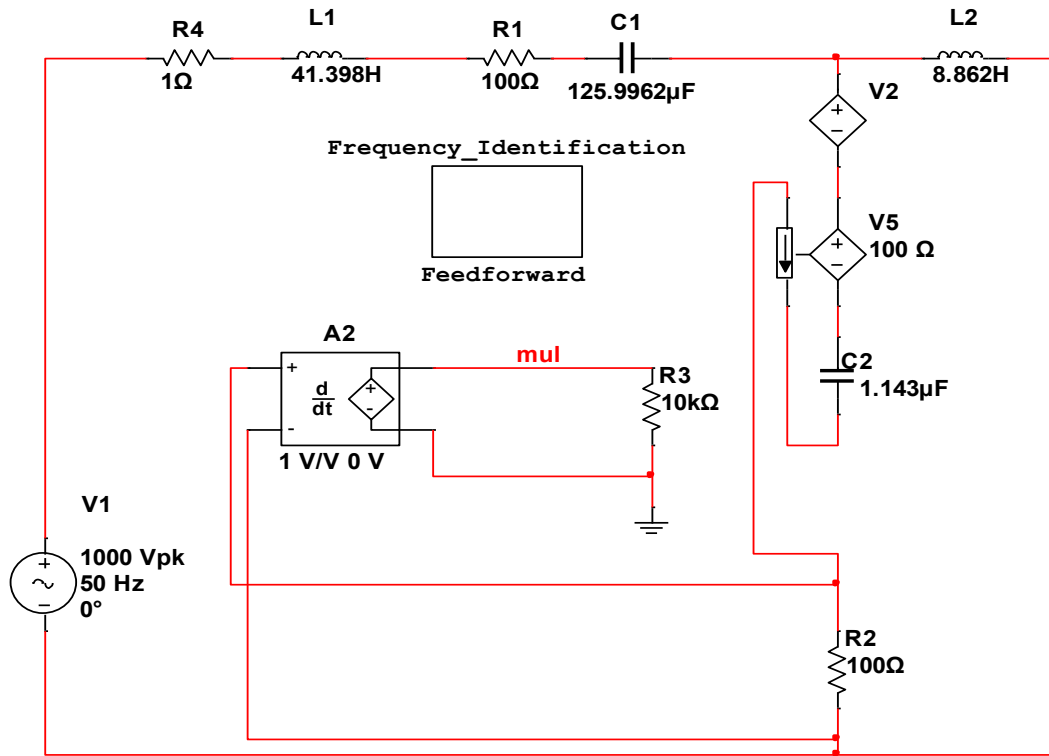


Figure 11-15 Multisim Model with rate of change of electrical charge and electrical current scheduling control strategy

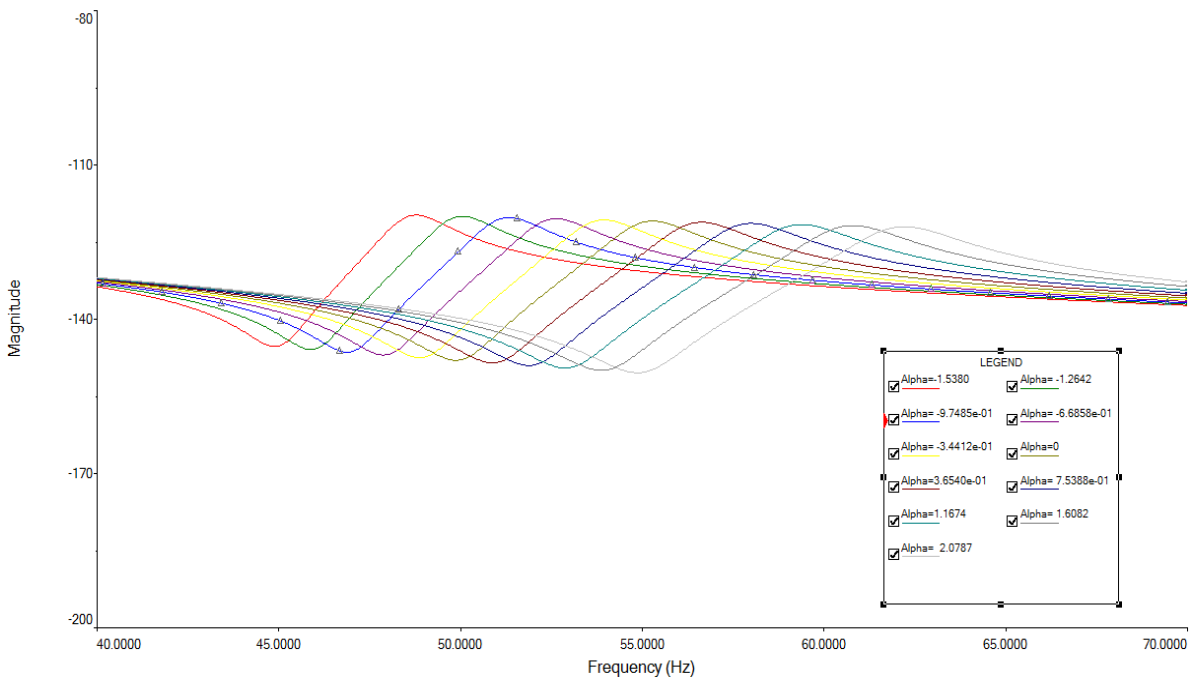


Figure 11-16 Frequency response with rate of current and with positive rate of change of current feedback gain

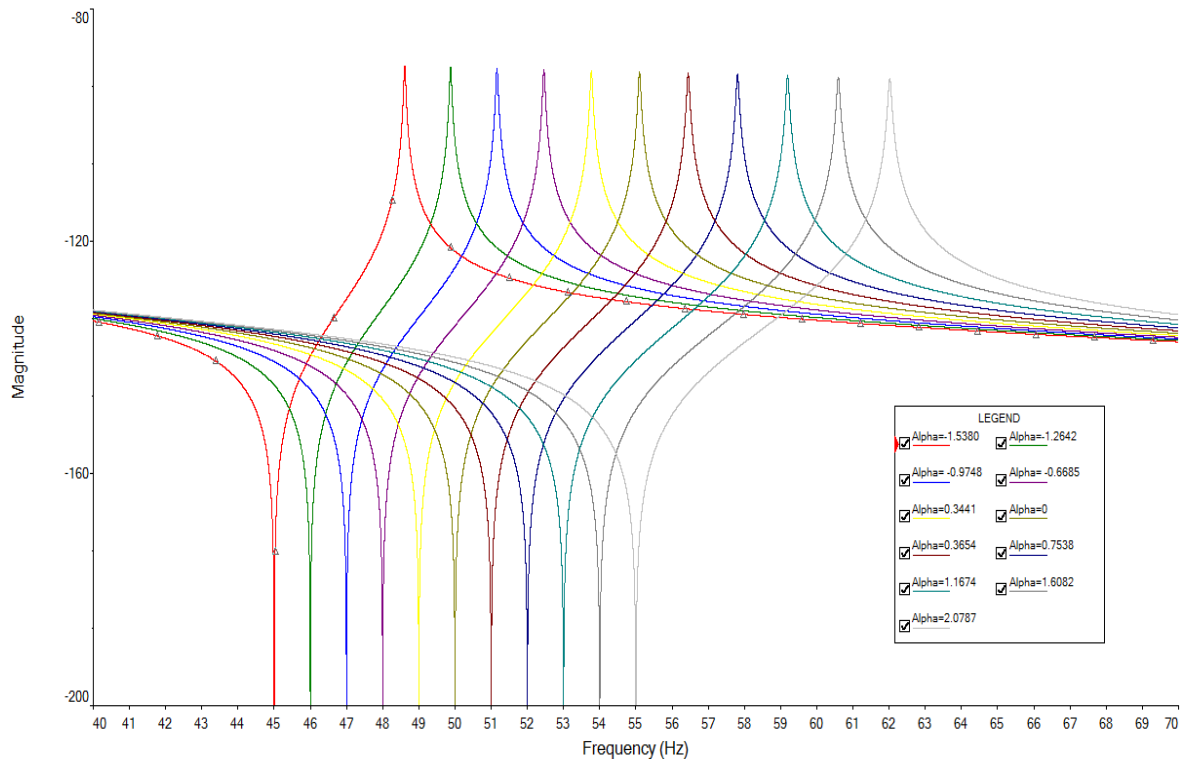


Figure 11-17 Frequency response with current and negative rate of change of current feedback

## 12 Appendix B

### 12.1 Time domain Simulation of Stirling Engine with Active Control

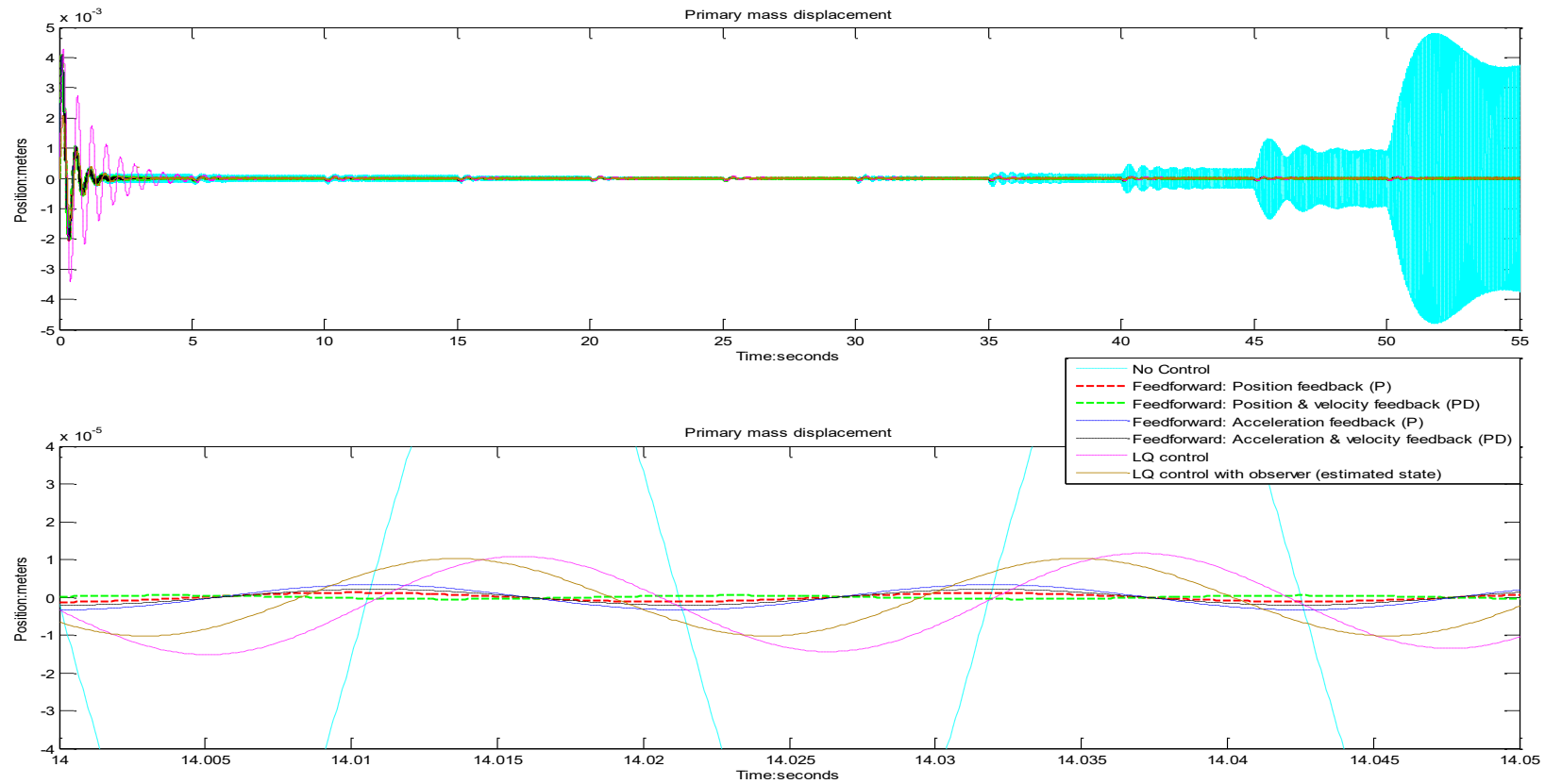


Figure 12-1 Time domain simulation results of the primary mass displacement

## 13 Appendix C

### 13.1 Delay Equations with Shaker Rig Model for Gain Scheduling Control

#### Strategy

$$W(s) = \frac{X_1(s)}{F_{Sha}(s)} = \frac{b_5 s^5 + b_4 s^4 + b_3 s^3 + b_2 s^2 + b_1 s^1 + b_0 s^0}{a_7 s^7 + a_6 s^6 + a_5 s^5 + a_4 s^4 + a_3 s^3 + a_2 s^2 + a_1 s^1 + a_0 s^0}$$

$$b_5 = -\alpha \tau k_d$$

$$b_4 = k_d m_2 + m_2 L_{vcm} + \alpha k_d - \alpha \tau k_p - \beta \tau k_d$$

$$b_3 = c_2 k_d + k_p m_2 + c_2 L_{vcm} + m_2 R_{vcm} + \alpha k_p + \beta k_d - \alpha \tau k_i - \beta \tau k_p - \gamma \tau k_d$$

$$b_2 = c_2 k_i + k_2 k_p + k_2 R_{vcm} + \beta k_i + \gamma k_p - \gamma \tau k_i$$

$$b_1 = c_2 k_i + k_2 k_p + k_2 R_{vcm} + \beta k_i + \gamma k_p - \gamma \tau k_i$$

$$b_0 = k_2 k_i + \gamma k_i$$

$$a_7 = -\alpha \tau k_d m_1 - \alpha \tau k_d m_2$$

$$a_6 = \alpha k_d m_1 + \alpha k_d m_2 + k_d m_1 m_2 + m_1 m_2 L_{\text{vcm}} - \alpha \tau c_1 k_d - \alpha \tau k_p m_1 - \alpha \tau k_p m_2 - \beta \tau k_d m_1 - \beta \tau k_d m_2$$

$$a_5 = \alpha c_1 k_d + \alpha k_p m_1 + \alpha k_p m_2 + \beta k_d m_1 + \beta k_d m_2 + c_1 k_d m_2 + c_2 k_d m_1 + c_2 k_d m_2 + k_p m_1 m_2 + c_1 m_2 L_{\text{vcm}} + c_2 m_1 L_{\text{vcm}}$$

$$+ c_2 m_2 L_{\text{vcm}} + m_1 m_2 R_{\text{vcm}} - \alpha \tau c_1 k_p - \beta \tau c_1 k_d - \alpha \tau k_1 k_d - \alpha \tau k_i m_1 - \alpha \tau k_i m_2 - \beta \tau k_p m_1 - \beta \tau k_p m_2 - \gamma \tau k_d m_1$$

$$- \gamma \tau k_d m_2$$

$$a_4 = \alpha c_1 k_p - k^2 m_2 - k^2 m_1 + \beta c_1 k_d + \alpha k_1 k_d + \alpha k_i m_1 + \alpha k_i m_2 + \beta k_p m_1 + \beta k_p m_2 + \gamma k_d m_1 + \gamma k_d m_2 + R_{\text{vcm}} c_2 m_1$$

$$+ c_1 c_2 k_d + c_1 k_p m_2 + c_2 k_p m_1 + c_2 k_p m_2 + c_1 c_2 L_{\text{vcm}} + k_1 k_d m_2 + k_2 k_d m_1 + k_2 k_d m_2 + k_i m_1 m_2 + c_1 m_2 R_{\text{vcm}} + c_2 m_2 R_{\text{vcm}}$$

$$+ k_1 m_2 L_{\text{vcm}} + k_2 m_1 L_{\text{vcm}} + k_2 m_2 L_{\text{vcm}} - \alpha \tau c_1 k_i - \beta \tau c_1 k_p - \gamma \tau c_1 k_d - \alpha \tau k_1 k_p - \beta \tau k_1 k_d - \beta \tau k_i m_1 - \beta \tau k_i m_2$$

$$- \gamma \tau k_p m_1 - \gamma \tau k_p m_2$$

$$a_3 = -c_1 k^2 + \alpha c_1 k_i + \beta c_1 k_p + \gamma c_1 k_d + \alpha k_1 k_p + \beta k_1 k_d + \beta k_i m_1 + \beta k_i m_2 + \gamma k_p m_1 + \gamma k_p m_2 + c_1 c_2 k_p + c_1 k_2 k_d$$

$$+ c_2 k_1 k_d + c_1 k_i m_2 + c_2 k_i m_1 + c_2 k_i m_2 + c_1 c_2 R_{\text{vcm}} + k_1 k_p m_2 + k_2 k_p m_1 + k_2 k_p m_2 + c_1 k_2 L_{\text{vcm}} + c_2 k_1 L_{\text{vcm}} + k_1 m_2 R_{\text{vcm}}$$

$$+ k_2 m_1 R_{\text{vcm}} + k_2 m_2 R_{\text{vcm}} - \beta \tau c_1 k_i - \gamma \tau c_1 k_p - \alpha \tau k_1 k_i - \beta \tau k_1 k_p - \gamma \tau k_1 k_d - \gamma \tau k_i m_1 - \gamma \tau k_i m_2$$

$$a_2 = -k_1 k^2 + \beta c_1 k_i + \gamma c_1 k_p + \alpha k_1 k_i + \beta k_1 k_p + \gamma k_1 k_d + \gamma k_i m_1 + \gamma k_i m_2 + c_1 c_2 k_i + c_1 k_2 k_p + c_2 k_1 k_p + k_1 k_2 k_d$$

$$+ k_1 k_i m_2 + k_2 k_i m_1 + k_2 k_i m_2 + c_1 k_2 R_{\text{vcm}} + c_2 k_1 R_{\text{vcm}} + k_1 k_2 L_{\text{vcm}} - \gamma \tau c_1 k_i - \beta \tau k_1 k_i - \gamma \tau k_1 k_p$$

$$a_1 = \gamma c_1 k_i + \beta k_1 k_i + \gamma k_1 k_p + c_1 k_2 k_i + c_2 k_1 k_i + k_1 k_2 k_p + k_1 k_2 R_{\text{vcm}} - \gamma \tau k_1 k_i$$

$$a_0 = \gamma k_1 k_i + k_1 k_2 k_i$$

# 14 Appendix D

## 14.1 Experimental Testing

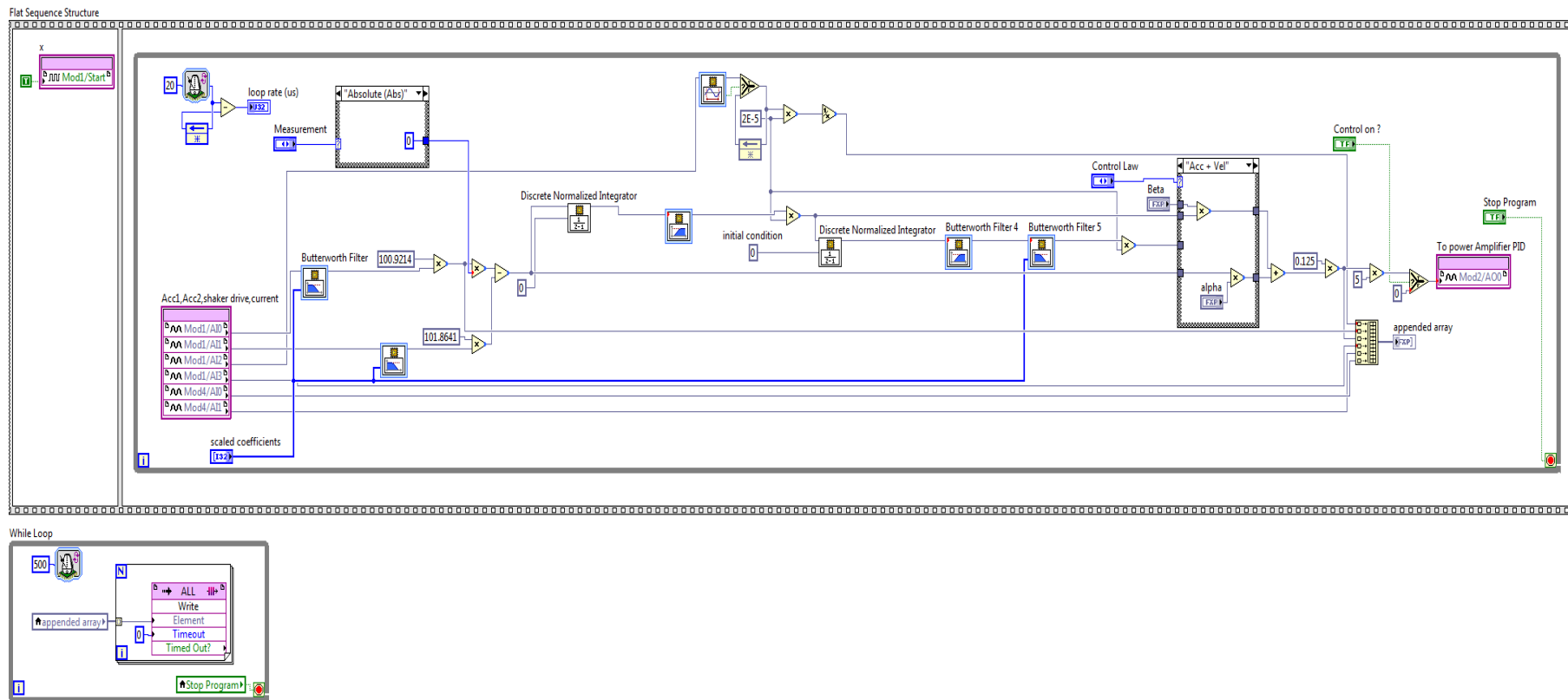


Figure 14-1 LabVIEW FPGA code

Active Tuned Mass Damper - Feedforward Control- ALI-V1.0

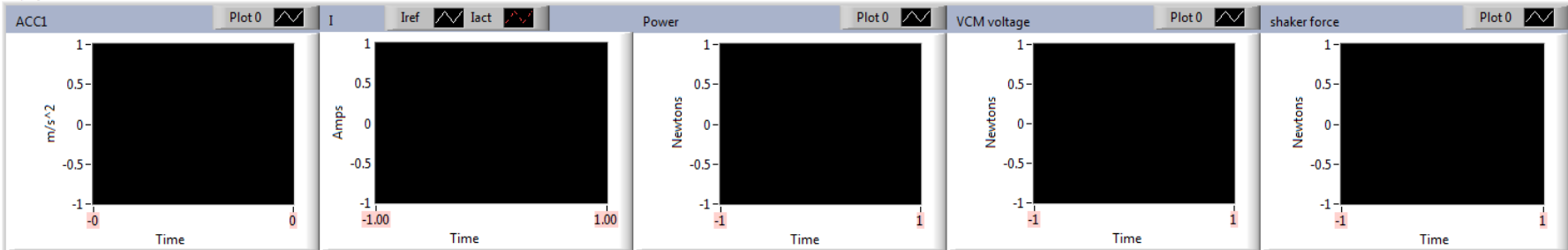
Code Operation

Control interface for Code Operation:

- Stop Program:** STOP button with a red square indicator.
- Log:** Record button with a red circle indicator.
- Control on ?:** OK button with a green checkmark indicator.

External status indicators: Stop (red circle), Log (red circle), Control (red circle).

Display



Control Action Parameters

Control Law: Acc + Vel

Measurement: Relative

Alpha %: 0

Gamma %: 0

Shaker Force Constant (N/A): 11.1

Absorber mass (Kg): 0.4033

Absorber Stiffness N/m: 39804

Beta Coefficients

Beta Coeff 2: 0.0076

Beta Coeff 1: 0.6654

Beta Coeff 0: -59.321

output cluster

System performance and configuration parameters:

- Gamma: 0
- Beta: 0
- Alpha: 0
- Elements Remaining FIFO: 0
- RT loop time (ms): 0
- Control loop rate (us): 0
- Absorber Tuned Frequency (Hz): 0

EXCITATION FREQUENCY (Hz) gauge showing a value around 200 Hz.

Figure 14-2 LabVIEW Real time front panel

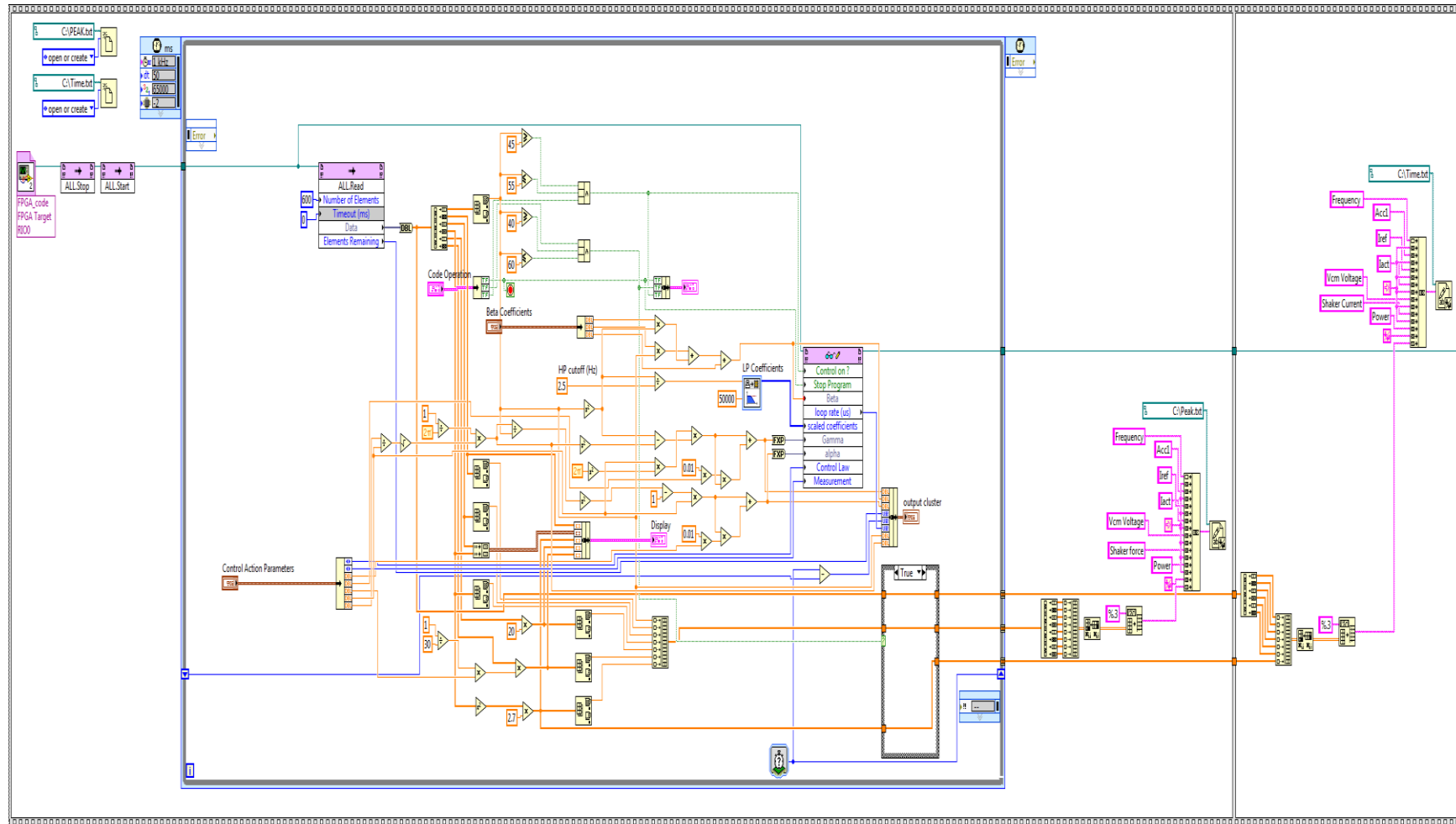


Figure 14-3 LabVIEW Real time block diagram

INTERMITTENT FORCE @10% DUTY CYCLE	88.6 N	19.9 LB
CONTINUOUS FORCE	28.0 N	6.3 LB
FORCE CONSTANT	8.0 N/A	1.8 LB/A
BACK EMF CONSTANT	8.0 V/M/S	0.20 V/IN/S
STROKE	19.1 mm	0.75 IN
COIL CLEARANCE PER SIDE	0.38 mm	0.015 IN
COIL ASSY MASS	162 GR	5.7 OZ
BODY MASS	668 GR	23.6 OZ
COIL RESISTANCE	2.7 Ohms	
COIL INDUCTANCE @ 1000 Hz	1.3 mH	
MAX CONTINUOUS POWER	33 W	
MAX TOTAL SHAFT SIDE LOAD	22 N	5 LB
LINEAR BEARING TYPE	RECIRCULATING BALL	

Figure 14-4 VCM parameters GVCM-051-051-01